DNA–Ligand Interactions: A Biophysical Study of 9-Hydroxyellipticine, Hoechst 33258 and a Meso-Substituted Porphyrin Derivative Binding to DNA.

Matthew Arif Ismail

Submitted for the degree of PhD to the Department of Chemistry, University of Warwick, Coventry, CV4 7AL, UK.

December 1998

Contents

Acknowledgements v

Declaration vi

Abstract vii

Abbreviations viii

1 Introduction 1

2 DNA 3
2.1 DNA geometry 3
2.2 DNA–ligand interactions 6
2.3 Biological function of DNA 11

3 Spectroscopic Techniques 14
3.1 Introduction 14
3.2 Normal absorption spectroscopy 14
3.3 Linear dichroism spectroscopy 17
3.3.1 Stretched film linear dichroism 18
3.3.2 Flow linear dichroism 22
3.4 Circular dichroism spectroscopy 23
3.5 Fluorescence spectroscopy 26
3.5.1 Fluorescence polarisation anisotropy 28
3.6 Resonance light scattering spectroscopy 29
3.6.1 Scope and limitations of resonance light scattering 31

4 Spectroscopic Studies of Porphyrin Binding to DNA 34
4.1 Introduction 34
4.2 Experimental 38
4.2.1 Materials 38
4.2.2 Spectroscopic titrations 38
4.2.3 Melting curves 41
4.2.4 Linear dichroism 42
4.2.5 Competition binding 42
4.2.6 Spectroscopy 43
4.2.7 Molecular modelling 44
4.3 Results 45
4.3.1 Normal absorption titrations 45
4.3.2 Circular dichroism titrations 50
4.3.3 Resonance light scattering titrations 56
4.3.4 Film linear dichroism 62
4.3.5 Flow linear dichroism 66
4.3.6 Competition binding 75

4.3.7 Normal absorption melting curves 77
4.3.8 Circular dichroism melting curves 79
4.3.9 Molecular modelling 82
4.4 Discussion 89
4.4.1 Interaction of *t*-H_2P with ct-DNA 89
4.4.2 Interaction of *t*-H_2P with poly[d(G-C)]$_2$ 91
4.4.3 Interaction of *t*-H_2P with poly[d(A-T)]$_2$ 93
4.5 Conclusions 95

5 Spectroscopic Studies of Hoechst 33258 Binding to DNA 97
5.1 Introduction 97
5.2 Experimental 100
5.2.1 Materials 100
5.2.2 Spectroscopic titrations 100
5.2.3 Linear dichroism 101
5.2.4 Spectroscopy 102
5.3 Results 103
5.3.1 Normal absorption titrations 103
5.3.2 Circular dichroism titrations 105
5.3.3 Fluorescence titrations 108
5.3.4 Resonance light scattering titrations 112
5.3.5 Linear dichroism 115
5.4 Discussion 119
5.4.1 Interaction of Hoechst with poly[d(G-C)]$_2$ 119
5.4.2 Interaction of Hoechst with poly[d(A-T)]$_2$ 121
5.5 Conclusions 123

6 Spectroscopic Studies of 9-hydroxyellipticine Binding to DNA 125
6.1 Introduction 125
6.2 Experimental 128
6.2.1 Materials 128
6.2.2 Spectroscopic titrations 128
6.2.3 Linear dichroism 130
6.2.4 Spectroscopy 130
6.3 Results 131
6.3.1 Normal absorption titrations 131
6.3.2 Film linear dichroism 133
6.3.3 Flow linear dichroism 137
6.3.4 Resonance light scattering titrations 141
6.4 Discussion 145
6.5 Conclusions 148

7 Conclusions 149

References 152

Appendices

A1 Porphyrin Molecular Modelling 160
A2 9-Hydroxyellipticine Film Linear Dichroism 164
A3 Biopolymers Paper: Spectroscopic Studies of 9-Hydroxyellipticine Binding to DNA 166

Acknowledgements

I am indebted to Dr Alison Rodger for the opportunity to conduct this research and for her invaluable support and advice that has accompanied me through the work. In addition, I would like to thank Dr Mark Rodger for allowing me to spend time with his research group in Reading and for his expert assistance with the molecular modelling.

I am grateful to my fellow research group, in particular Dr Karen Sanders and Andrew Parkinson, for constructive comments regarding the work. I would also like to thank my parents for their support during the preparation of this thesis.

Declaration

The observations and recommendations in this thesis are those of the author except where acknowledgement has been made to results and ideas previously published. The work was undertaken at the Department of Chemistry, University of Warwick and the Department of Chemistry, University of Reading between November 1995 and November 1998 and has not been previously submitted for a degree at any institution.

Abstract

The binding of 9-hydroxyellipticine (9-OHE), Hoechst-33258 (Hoechst) and *trans*-bis-(4-*N*-methylpyridiniumyl)diphenylporphyrin (*t*-H_2P) to DNA has been studied by means of spectroscopic techniques. The binding modes of *t*-H_2P to calf thymus DNA (ct-DNA), poly[d(G-C)]$_2$ and poly[d(A-T)]$_2$ were dependent on ionic strength, ligand load on DNA and the base composition at the binding site. At low ionic strength, flow linear dichroism (*LD*) data suggested *t*-H_2P binds to ct-DNA and poly[d(A-T)]$_2$ in an orientation consistent with groove binding and to poly[d(G-C)]$_2$ in an orientation consistent with partial intercalation. Interpretation of the spectroscopic data was facilitated by molecular modelling. At high ionic strength, circular dichroism (*CD*) and resonance light scattering (*RLS*) measurements indicated the formation of extended *t*-H_2P aggregates on DNA. In addition, the approximate, average transition moment polarisations of *t*-H_2P were assigned from stretched film *LD* data to facilitate interpretation of the flow *LD* data.

The interaction of Hoechst with poly[d(G-C)]$_2$ and poly[d(A-T)]$_2$ was studied with *CD*, *LD*, *RLS* and fluorescence spectroscopy. The mode of Hoechst binding to poly[d(G-C)]$_2$ was ligand load independent. The collective spectroscopic data suggested a binding mode in which part of the molecule intercalates and part lies extensively stacked in the poly[d(G-C)]$_2$ major groove. Hoechst binding to poly[d(A-T)]$_2$ was ligand load dependent. The molecule was observed to bind as dimers or small oligomers at the lower ligand loads studied, with extended aggregates being formed as the concentration of bound Hoechst was increased. *LD* measurements suggested a binding orientation inconsistent with minor groove binding thus it was concluded that the molecule stacked in the major groove.

9-OHE binding to ct-DNA, poly[d(G-C)]$_2$ and poly[d(A-T)]$_2$ was studied with *LD*, *RLS* and normal absorption spectroscopy. Binding by intercalation was shown to occur with each of the three DNAs. The intercalated mode was shown to be complemented at high ligand load by a stacked binding mode. *LD* data pertaining to the stacked mode were inconsistent with minor groove binding in which the 9-OHE plane lies at 45° to the helix axis, thus it was concluded that the stacking occurred in the major groove. The stacked binding mode occurred most readily on poly[d(G-C)]$_2$. The flow *LD* data were complemented with film *LD* measurements from which the approximate, average transition moment polarisations were assigned.

Abbreviations

9-OHE	9-hydroxyellipticine
α	angle between a transition polarisation and the orientation axis
A	absorbance
$A_{\|\|}$	absorbance of parallel plane polarised light
A_l	absorption of left circularly polarised light
A_r	absorption of right circularly polarised light
AT	adenine and thymine DNA base pair
A_x	X polarised absorbance spectrum
A_y	Y polarised absorbance spectrum
A_z	Z polarised absorbance spectrum
$A_\perp$	absorbance of perpendicular polarised light
β	constant of proportionality
χ	angle between absorbing and emitting transition moments
c	velocity of light
C	concentration
C_{abs}	absorption cross section
CD	circular dichroism
C_{sca}	scattering cross section
ct-DNA	calf thymus DNA
D	dielectric constant
DAPI	4',6-diamidino-2-phenylindole
DNA	deoxyribonucleic acid
ε	extinction coefficient
E	energy
FPA	fluorescence polarisation anisotropy
Γ	rate of fluorescence emission
GC	guanine and cytosine DNA base pair
h	Planck's constant
H_2TMPyP	meso-tetrakis(4-*N*-methylpyridiniumyl)porphyrin
Hoechst	Hoechst 33258
I	intensity of light
ICD	induced circular dichroism
k	wave vector of light
K	rate of non-radiative electronic decay
λ	wavelength
l	path length
L	sample thickness
L_b	concentration of bound ligand
LD	linear dichroism
LD^r	reduced linear dichroism
m	magnetic dipole transition moment

μ	electric dipole transition moment
n_L	linking number
NMR	nuclear magnetic resonance
n_T	twisting number
n_W	writhing number
PE	polyethylene
poly[d(A-T)]$_2$	duplex DNA of alternating adenine and thymine base pairs
poly[d(G-C)]$_2$	duplex DNA of alternating guanine and cytosine base pairs
PPP	Pariser-Parr-Pople
PVA	polyvinyl alcohol
θ	angle between macroscopic and molecular orientation axes
Q	quantum yield
ρ	*ICD* intensity
r	ligand/DNA mixing ratio
R	rotational strength
RLS	resonance light scattering
σ	polarisability
S	orientation parameter
T	transmittance
t-H_2P	trans-bis-(4-*N*-methylpyridiniumyl)diphenylporphyrin
T_a	DNA annealing temperature
TEM	Trial and Error Method
T_m	DNA melting temperature
TMAP	meso-tetrakis(4-*N*-trimethylaniliniumyl)porphyrin
TθOPP	meso-tetrakis[4(3-(trimethylammonio)propyl)-oxy]phenyl]porphyrin
UV	ultraviolet
ν	frequency
X	propagation direction of incident light
z	molecular orientation axis
Z	macroscopic orientation axis

1 Introduction

Deoxyribonucleic acid (DNA) has fascinated scientists since its discovery in the late 19th century. Early studies of DNA were motivated by the mystery surrounding the biological function of the molecule. This pioneering work culminated in the discovery of the structure of DNA by Watson and Crick in 1953.[1] The elucidation of the DNA structure initiated subsequent investigations that were to lead to a molecular level understanding of the biological function of DNA as the carrier of genetic information.[2] Intrinsic to the function of DNA are interactions with a diverse variety of molecules within biological cells. An understanding of the chemistry of DNA–ligand interactions in terms of structure, function and dynamics is therefore important to comprehend the role of DNA in biology. The structural details of DNA and the basic principles of DNA–ligand interactions are described in Chapter 2.

An understanding of DNA–ligand interactions enables the development of applications that exploit those interactions. For example, medical conditions such as cancer are potentially treatable at the level of DNA since many of the defective genes responsible for the various diseases have been identified and located in the human genome. Medical applications such as gene therapy and antisense therapy constitute potential molecular level treatments for genetic diseases.

The work presented in this thesis involves the study of the interactions of 9-OHE (Figure 6.1b), Hoechst (Figure 5.1) and *t*-H_2P (Figure 4.1a) with DNA. Although none of the ligands are naturally occurring, each has potential clinical application either directly or

as a model for the development of structural analogues with therapeutic activity. Porphyrins are composed of four pyrrole rings linked by methene bridges to form a tetrapyrrole ring[3] and *t*-H_2P is a tetra meso-substituted derivative with a dicationic charge. Porphyrins constitute a commonly recurring structural motif in nature as evidenced by haemoglobin and myoglobin, the oxygen transporting proteins in vertebrates, and the photoreceptor chlorophyll.[4] 9-OHE, well established as having anticancer properties,[5] and Hoechst are studied to provide detailed structural information on their DNA binding and thus enhance their suitability as models for the design of DNA binding analogues. The results of the DNA–ligand binding studies are described and discussed in Chapters 4, 5, 6 and 7.

The experimental study of DNA–ligand interactions requires a means of detecting and characterising the DNA–ligand complexes. Spectroscopic techniques that are sensitive to the electronic properties of the sample molecules are employed as the method of choice to study the DNA–ligand systems in this work. Polarised light spectroscopy is sensitive to the average orientations of the electronic transition moments of DNA and ligand but interpretation of the spectra in terms of binding geometries requires a knowledge of the polarisation of these transition moments. Thus the properties of the electronic transition moments of 9-OHE and *t*-H_2P were also investigated in addition to their DNA binding. The spectroscopic techniques employed in this work are described in Chapter 3. Molecular modelling was also used for the DNA–porphyrin system to aid interpretation of the spectroscopic data on a molecular level.

2 DNA

2.1 DNA geometry

The basic structure of DNA was established by Watson and Crick to be a right handed double helix composed of two complementary strands. Each strand comprises a polynucleotide chain of alternating phosphate and 2-deoxyribose sugar groups linked by 3' and 5' phosphodiester bonds, and a purine or pyrimidine base attached to C1 of the sugar (Figure 2.1). The bases of physiological DNA are any of either adenine, thymine, cytosine or guanine. The complementary strands of a DNA double helix (one runs 3' → 5' and the other 5' → 3') interact through a unique pattern of hydrogen bonds between either adenine and thymine (AT) or guanine and cytosine (GC) to form base pairs (Figure 2.1).[2, 6, 7]

When DNA adopts a right handed double helix, in which Watson–Crick base pairs lie in the centre of the helix approximately perpendicular to the helix axis, the B-DNA conformation (Figure 2.2) arises. In B-DNA, the glycosidic bonds linking base to sugar are not diametrical opposites, resulting in a major and minor groove that span the length of the helix. The structure is stabilised in solution by hydrophilic interactions between the negatively charged phosphate groups and the surrounding solvent, and by hydrophobic π-stacking interactions between adjacent bases.[2] Although the B-form is the most abundant DNA polymorph, other conformations can exist under appropriate conditions. Z-DNA or A-DNA, for example, are two alternative conformations. Z-DNA

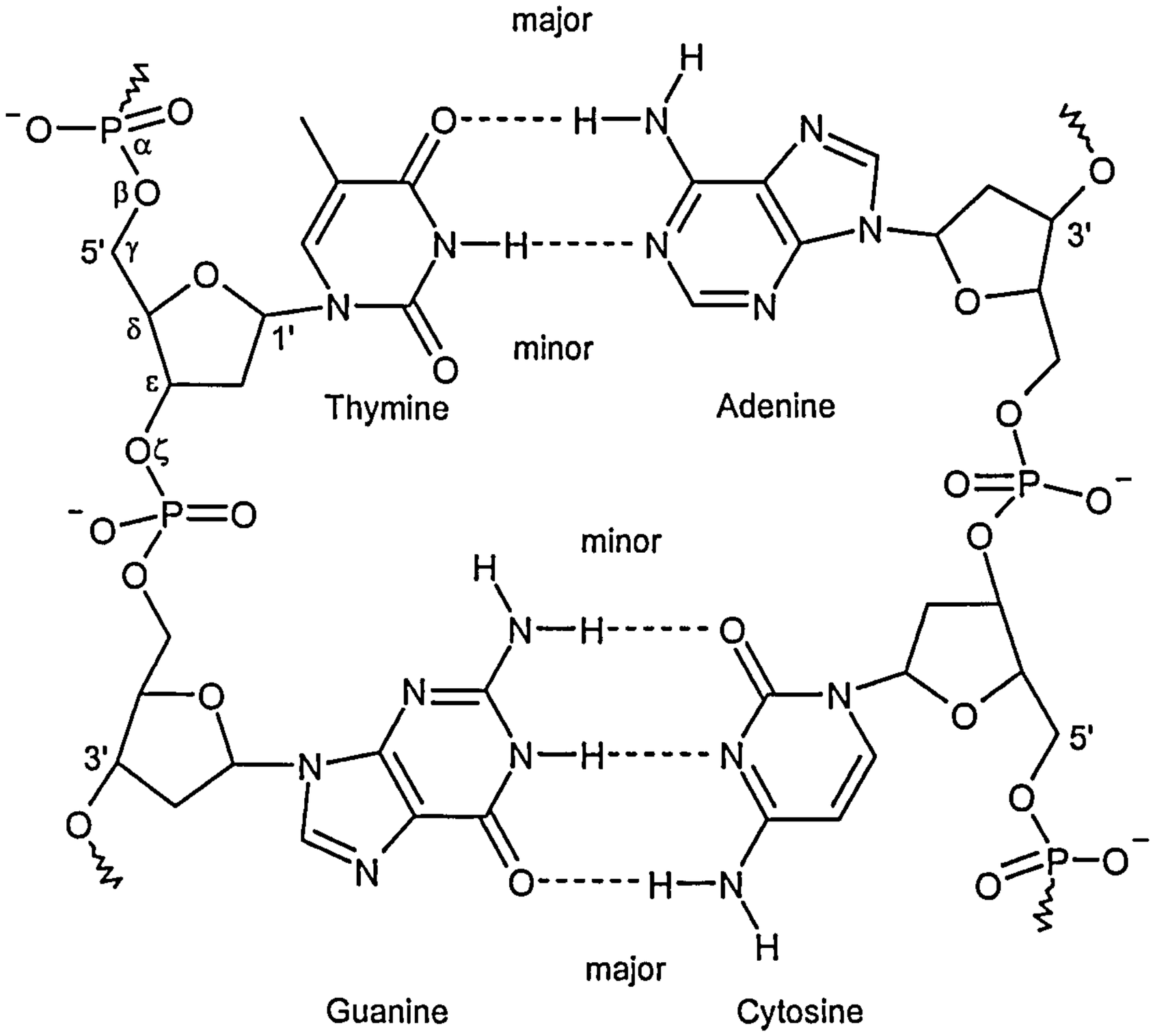

Figure 2.1 Structure of DNA. The backbone is composed of 2-deoxyribose sugar units linked via 3' and 5' phosphodiester bonds. Hydrogen bonding interactions between Watson–Crick base pairs are shown along with definitions of backbone torsion angles.

is a left handed helix in which the glycosidic bond connecting base to sugar alternates between the *anti* and *syn* conformations to give a dinucleotide repeat in which the phosphate backbone zigzags the length of the helix. A-DNA (Figure 2.2) is a right handed helix but differs from the B-form in that the sugar adopts the $C_{3'}$-endo conformation, resulting in a 19° tilt of the Watson–Crick base pairs away from the normal to the helix axis.[4] The formation of A-DNA is favoured under conditions of low humidity. A given DNA conformation may be described in terms of several geometric parameters including backbone torsion angles (Figure 2.1) and the relative orientations of adjacent base pairs. Some structural parameters of various DNA polymorphs are compared in Table 2.1.

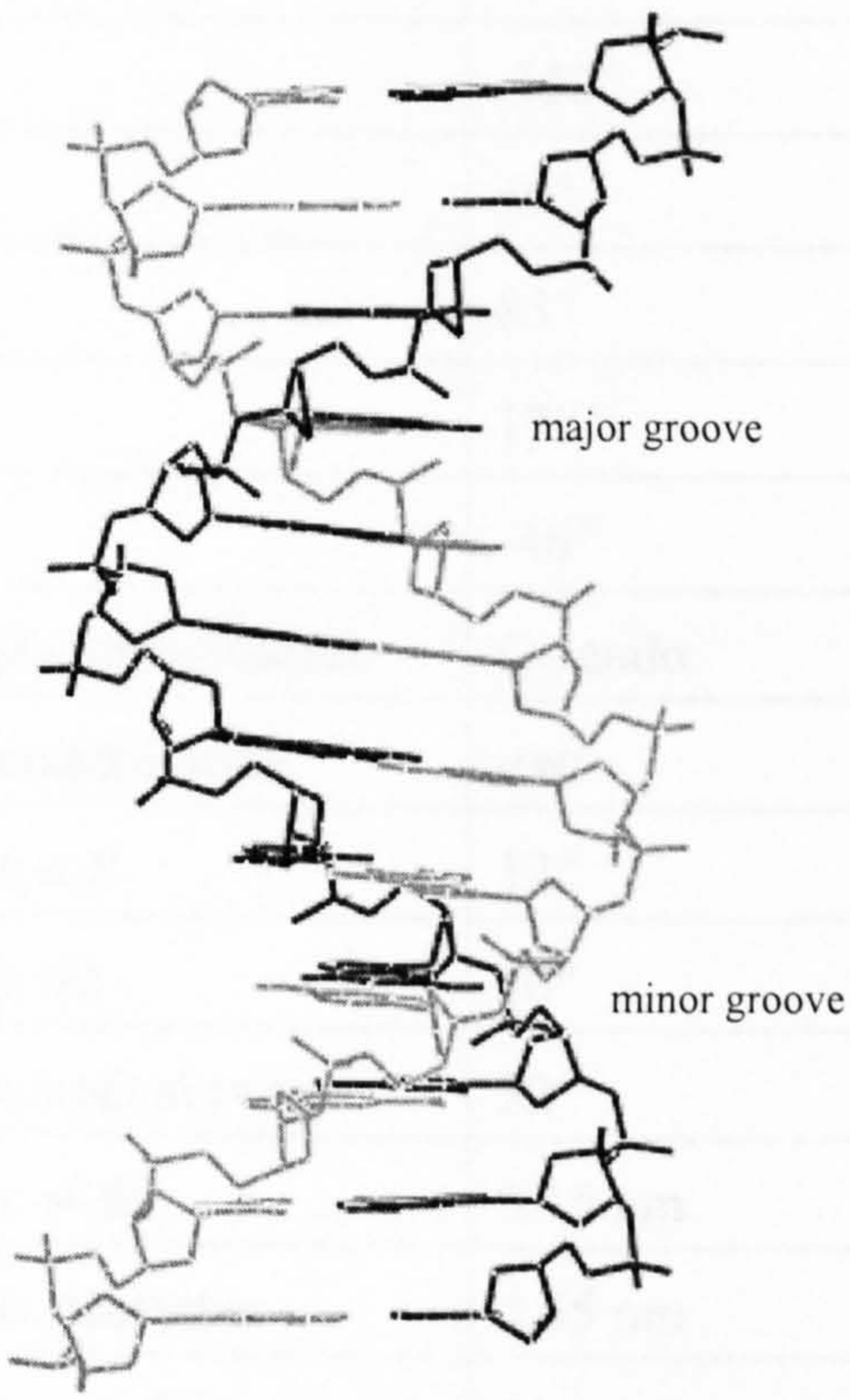

(a)

(b)

Figure 2.2 (a) B-DNA and (b) A-DNA conformations viewed parallel and perpendicular to the helix axis.

Parameter	A-DNA	B-DNA	Z-DNA
α	-85°	-47°	60°/160°
β	-152°	-146°	-175°/-135°
γ	46°	36°	178°/57°
δ	83°	156°	140°/95°
ε	178°	155°	-95°/-110°
ζ	-46°	-95°	-35° – 85°
sugar conformation	$C_{3'}$-endo	$C_{2'}$-endo	$C_{3'}$-endo/$C_{2'}$-endo
glycosidic bond	*anti*	*anti*	*anti* (C, T), *syn* (G)
base roll	12°	0°	1°
base tilt	20°	5°	9°
base helical twist	32°	36°	11°/50°
base slide	0.15 nm	0 nm	0.2 nm
helix diameter	2.55 nm	2.37 nm	1.84 nm
bases per helix turn	11	10.4	12
base rise per base pair	0.23 nm	0.33 nm	0.38 nm
major groove	narrow, deep	wide, deep	flat
minor groove	broad, shallow	narrow, deep	narrow, deep

Table 2.1 Geometric parameters for A-, B- and Z-DNA.[6, 7] Z-DNA repeats in dinucleotide units.

2.2 DNA–ligand interactions

The ability to interact uniquely with many different types of molecules underpins much of the biological function and malfunction of DNA. The specific focus in this work, however, is on the study of the non-covalent binding of small cationic molecules to DNA. Non-covalent interactions are fundamental to many biological structures and mechanisms. They are generally classified as either hydrogen bonds, electrostatic

interactions or van der Waals forces. Hydrogen bonds in DNA–ligand systems typically occur between a hydrogen that is covalently attached to either a nitrogen or oxygen (hydrogen donor) and a nitrogen or oxygen with a partial negative charge (hydrogen acceptor). An important feature of hydrogen bonds is that their stability is geometry dependent. A linear alignment of donor, hydrogen and acceptor atoms, as observed in Watson–Crick base pairs of DNA, permits the optimum interaction energy for the hydrogen bond. Electrostatic interactions occur between oppositely charged groups on, for example, DNA and ligand. The strength of the electrostatic attraction, F, is governed by Coulomb's law

$$F = \frac{q_1 q_2}{r^2 D} \tag{2.1}$$

where q_1 and q_2 are the two opposite charges, r is the distance between the charges and D is the dielectric constant of the medium ($D = 80$ for water). Van der Waals forces depend on the temporal asymmetry inherent in the electric charge distribution of atoms. A similar asymmetry is induced into the electric fields of adjacent atoms resulting in a net attraction between those atoms. The force of the attraction increases as the distance between the atoms decreases until the van der Waals contact distance (where closer contact would result in dominant charge–charge repulsions of adjacent electron clouds) is reached. Hydrophobic interactions are also an important stabilising force in polar media such as water and describe the tendency of non-polar groups to associate in polar environments.[3]

The double helical structure of B-DNA presents several possible target sites for ligand binding (most DNA binding ligands are cationic). Planar aromatic molecules such as

ethidium (Figure 2.3) may intercalate between the base pairs of DNA. This binding mode is stabilised by hydrophobic π-stacking interactions between the intercalated ligand and adjacent DNA bases. Intercalation forces the base pairs apart causing an overall increase in the length of the DNA duplex. Partial untwisting of the duplex also occurs in the presence of an intercalated ligand. Furthermore, intercalating ligands may cause the unwinding of condensed DNA. The capacity to induce DNA structural changes is a property that confers therapeutic activity on many DNA intercalating drugs.

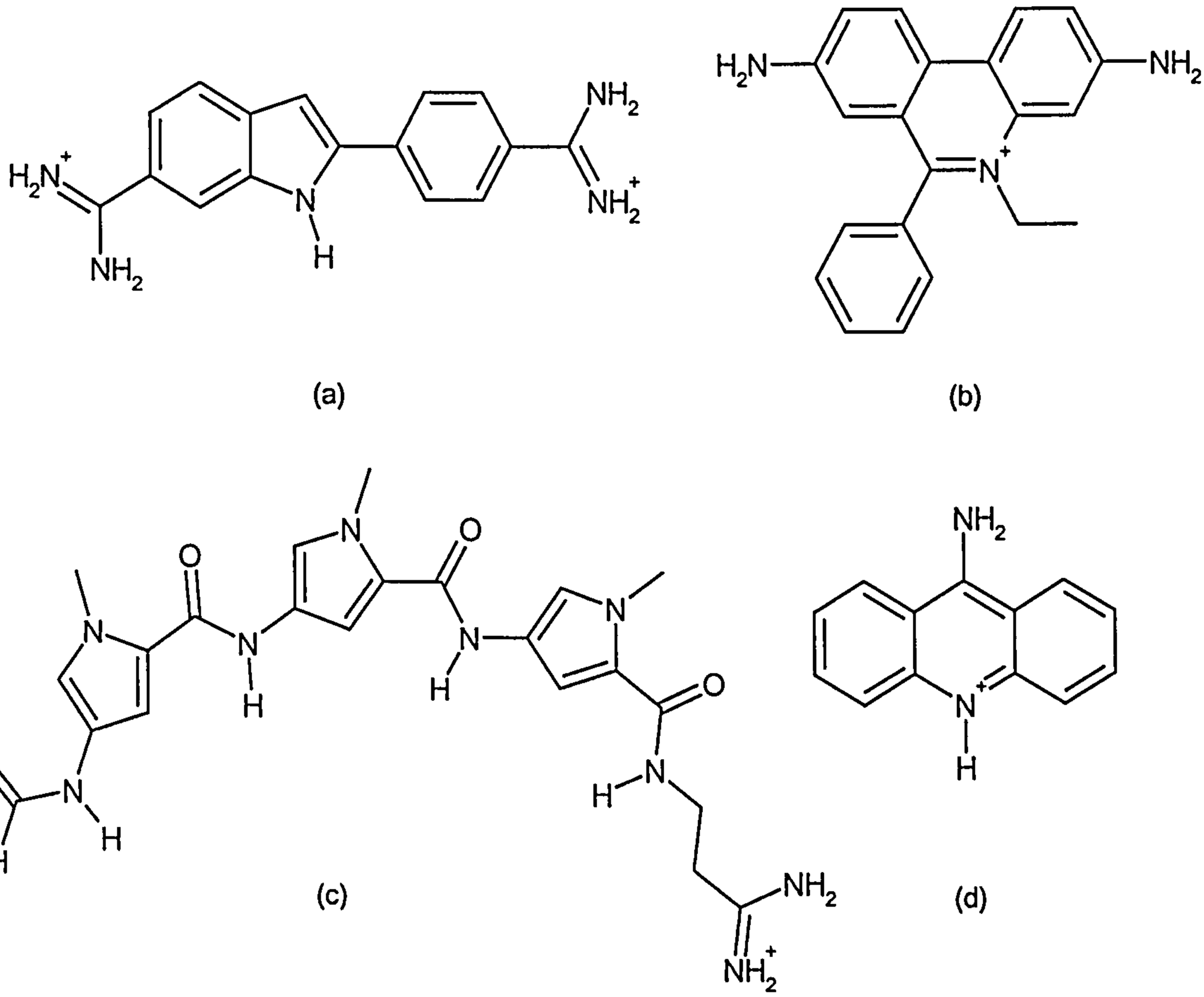

Figure 2.3 (a) 4',6-diamidino-2-phenylindole (DAPI), (b) ethidium, (c) distamycin and (d) 9-aminoacridine (pH 7).

Molecules composed of planar aromatic groups connected by bonds with some degree of rotational freedom, and that are too large to intercalate, may bind in the B-DNA minor groove.[7] Many minor groove binders, such as distamycin (Figure 2.3), are crescent shaped since this permits the bound ligand to follow the pitch and curvature of the groove. Minor groove binding modes are stabilised by hydrophobic interactions, hydrogen bonding, van der Waals forces and electrostatic interactions with the floor and walls of the groove. Minor groove binding ligands exhibit strong base sequence discrimination, a tendency that is usually determined by a preference for the deep electrostatic potential of AT rich tracts.[8] Moreover, the guanine exocyclic amino group at C2 sterically hinders efficient minor groove binding to sequences rich in GC.

The major groove is wider than the minor groove and can accommodate larger ligands such as the DNA binding domains of proteins.[4] In GC rich sequences ligands may preferentially bind in the major groove since its electrostatic potential is more negative[7] than the sterically blocked minor groove.

External binding to the DNA backbone may occur for molecules that are not well suited to intercalation or groove binding. Counter ion binding occurs through electrostatic interactions with the anionic phosphate groups of the backbone. The bound counter ions partially screen the charge–charge repulsions between adjacent phosphate groups leading to increased stabilisation and shortening of the duplex. Furthermore, polyamines, such as spermine, that contribute to the control of DNA condensation *in vivo* may do so through a mechanism that involves interaction with the backbone.

When the mode of binding is highly cooperative, or when the concentration of bound ligand is high, stacking interactions may occur between adjacently bound ligands. Stacked binding modes are thought to arise through either of three general mechanisms. The first of these involves the formation of a DNA–ligand complex in which the bound ligand perturbs the local structure of the host DNA, creating a binding site to which subsequent ligands have an increased affinity. The second also involves a DNA structural change but one that is disfavoured while only one ligand is bound, occurring only upon binding of a subsequent ligand. Alternatively, stabilising ligand–ligand interactions could promote the formation of stacks of ligands. Stacked ligands may occupy almost any non–intercalated binding site including the major and minor grooves and external binding to the phosphate backbone.

Certain DNA binding ligands may exhibit multiple binding modes, where different binding regimes are observed that are specific to the environment to which the ligand is exposed. For example, ligands commonly bind in different geometries to AT and GC base sequences. The relative concentrations of DNA and ligand or the ionic strength of the environment may also influence the mode of binding. 4',6-diamidino-2-phenylindole (DAPI; Figure 2.3), for example, binds to the minor groove of AT rich sequences, the major groove of GC rich sequences and adopts a stacked binding mode at higher ligand concentrations.[9]

2.3 Biological function of DNA

The biological function of DNA comprises both the preservation and utilisation of genetic information. The former is achieved through DNA replication and the latter by means of the control of the synthesis of proteins. The capability of DNA to perform these functions is a direct consequence of the unique ability of proteins and other molecules to recognise specific DNA structural features.[4]

Intrinsic to sequence recognition are local structural deviations from the Watson–Crick ideal that are specific to base composition. The degree of base roll or twist, for example, varies subtly with the sequence of bases along a DNA duplex. Also, kinks and bends may be induced into the duplex such as the kink observed at a run of four or more adenine bases. Recognition may then occur through the sensing of specific structural features at the target sequence. Hydrogen bonding is also fundamental to the recognition of target binding sites. The major and minor grooves of B-DNA, as well as the different bases, present unique patterns of hydrogen bond donors and acceptors through which site specific interactions may occur. The minor groove contains hydrogen bond acceptors at N3 on adenine and guanine, and O2 on thymine and cytosine, and a hydrogen bond donor at the C2 amino group on guanine (Figure 2.1). In the major groove, N7 on guanine and adenine, O6 on guanine and O4 on thymine, can act as hydrogen bond acceptors and the amino groups at C6 on adenine and C4 on cytosine are potential hydrogen bond donors (Figure 2.1). Since the major groove is wider and exhibits more defined structural features than the minor groove, proteins often interact with specific DNA sequences via the major groove.[4]

DNA exhibits one further structural property on which the biological function of the molecule depends. The double helix can be bent or arced without significantly perturbing the local structure of the molecule. This topological property permits the formation of circular and supercoiled DNAs which are essential to enable a large amount of DNA to fit into the micrometre dimensions of a biological cell. A superhelix can be formed by unwinding a linear double helix by a given number of turns then joining its ends to create circular DNA. The resulting structure may then adopt a circular shape with an unwound loop, or a negative supercoil in which the number of turns of superhelix corresponds to the number of turns by which the helix was initially unwound (a positive supercoil results from an initial increased winding). The superhelical structure is energetically favoured over the partially unwound circle since it permits a greater degree of base pairing. A DNA supercoil may be described in terms of the number of helical turns (linking number), n_L, the number of Watson–Crick helical turns (twisting number), n_T, and the number of superhelical turns (writhing number), n_W, which are related by

$$n_L = n_T + n_W \tag{2.2}$$

Since the superhelix is energetically favoured, changes in n_L usually lead to changes in the degree of supercoiling rather than in the number of Watson–Crick turns. Furthermore, interconversion between DNAs with different n_L values (topoisomers) requires strand cleavage. Although equation 2.2 strictly holds only for short plasmid DNAs, the relationship is still a good approximation for other DNAs.

In eukaryotic cells the first stage of DNA condensation (eukaryotic DNA is linear) is achieved through the formation of nucleosomes. Nucleosomes are the repeating units of chromatin and comprise 140 base pairs coiled around an octamer of histone proteins (two

each of four different types), with linker regions of DNA connecting the units and a fifth histone protein bound on the outside of the coil. Chromatin then adopts a higher order structure in conjunction with other proteins to form chromosomes. The degree of supercoiling is mediated by enzymes known as topoisomerases which act by altering the linking number of DNA through strand cleavage and subsequent rejoining.[4]

3 Spectroscopic Techniques

3.1 Introduction

DNA and many DNA binding ligands absorb light in the near UV (190 – 380 nm) and visible (380 – 700 nm) regions of the electromagnetic spectrum. Light of these wavelengths is sufficiently energetic to perturb the valence electrons of a chromophore (a discrete molecular unit with isolated electronic structure) and can thus be used to probe the $\pi \rightarrow \pi^*$ or $n \rightarrow \pi^*$ transitions of DNA and DNA–ligand systems.

Light can be described in terms of the properties of a wave as comprising oscillating electric and magnetic fields with wavelength, λ, and frequency, ν, and in terms of a particle as possessing discrete packets of energy called photons. Thus a typical UV–visible spectrum will characterise the wavelength dependent absorption of a molecule that has occurred as a series of unique absorption events involving single photons. Although the interactions that occur when light is incident on a molecule are described by quantum mechanics, the emphasis in this work is on the interpretation of optical spectra in terms of the macroscopic electronic properties of molecules and the changes in these properties that occur upon interaction with DNA.

3.2 Normal absorption spectroscopy

Normal absorption spectroscopy (or UV–visible spectroscopy) measures the amount of light of a given wavelength absorbed by a group of molecules. If the energy of an

incident photon corresponds to the difference in energy between two electronic states of a molecule then the photon may be absorbed and a redistribution of electron density between those states is induced. The increase in energy of a molecule upon the absorption of a photon is[7]

$$\Delta E = h\nu = \frac{hc}{\lambda} \tag{3.1}$$

where ΔE is the energy absorbed by the molecule, h is Planck's constant, ν is the frequency of light and c is the velocity of light.

The rearrangement of electron density during an electronic transition can be characterised in terms of a net linear displacement of charge, or transition polarisation. The magnitude and direction of a given transition polarisation is described by the electric dipole transition moment, μ, a vector of defined length and direction within the framework of the molecule. The probability that absorption will occur depends on the relative alignment of the transition moment and the electric field of the incident light. This probability is maximised when the transition moment and electric field are aligned in parallel.[7]

The Beer-Lambert law[7] relates the transmittance, T, of a sample of molecules to their concentration, C, by

$$\log_{10}\left(\frac{1}{T}\right) = \log_{10}\left(\frac{I_0}{I}\right) = \varepsilon C l = A \tag{3.2}$$

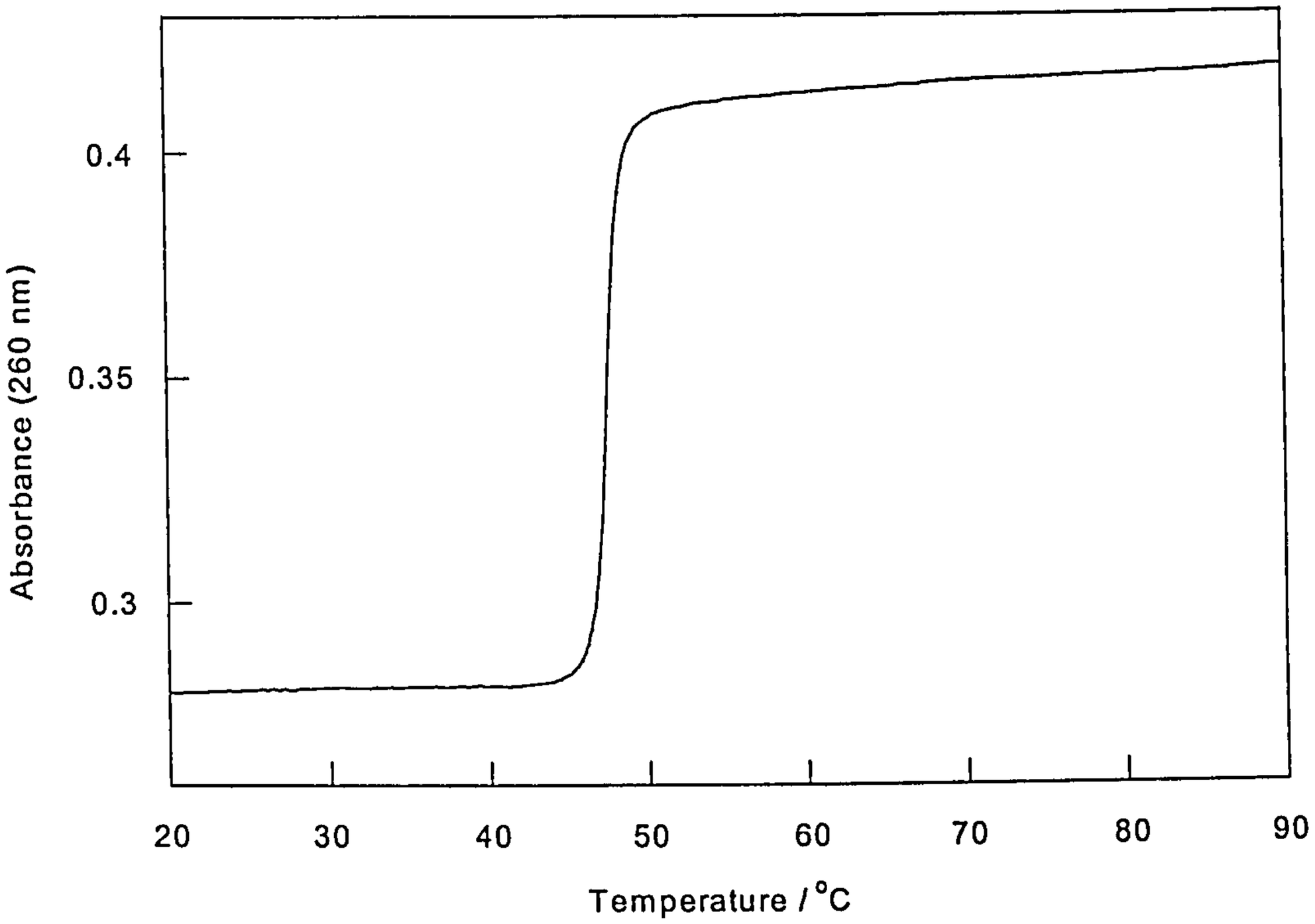

Figure 3.1 DNA melting curve of poly[d(A-T)]$_2$ (40 μM) and NaCl (20 mM). The 260 nm DNA absorbance is monitored as a function of temperature.

where l is the sample path length, ε is the extinction coefficient, A is the sample absorbance, I_0 is the intensity of light incident on the sample and I is the intensity of light emergent from the sample.

Normal absorption spectroscopy is sensitive to a number of aspects of DNA and DNA–ligand systems. When applied to free DNA in solution the technique can probe the extent of base stacking since the DNA absorption at 260 nm increases as the bases unstack. Thus measurement of the hyperchromic shift at 260 nm as a function of temperature for a sample of DNA results in a melting curve (Figure 3.1) characteristic of the double stranded to single stranded transition. The DNA melting temperature, T_m, is defined as the temperature at which half the DNA is a duplex and is approximately the temperature corresponding to the midpoint between the upper and lower plateaus in the

DNA melting curve.[4] Moreover, the degree of duplex stabilisation due to the presence of a ligand can be determined by observing the effect of the bound ligand on T_m.

The interaction of a ligand with DNA will often produce a change in the normal absorption spectrum characteristic of the type of binding. For example, red shifts and hypochromicity in the absorption bands of intercalators are usually observed upon DNA binding. The effect on the absorption spectroscopy of groove binders is usually less dramatic upon binding to DNA. Conversely, significant hypochromicity may be observed in the absorption bands of drugs that are interacting with one another in a DNA groove.

3.3 Linear dichroism spectroscopy

LD is the difference in anisotropic absorption of light polarised in planes parallel ($A_{\|}$) and perpendicular ($A_{\perp}$) to the direction of orientation.[7]

$$LD = A_{\|} - A_{\perp} \tag{3.3}$$

An isotropic collection of molecules will have no *LD*, whilst a group of molecules whose transition moments are macroscopically oriented will absorb differing amounts of parallel and perpendicular plane polarised light, producing a non-zero *LD* spectrum. For a perfectly oriented molecule the measured *LD* would equal $A_{\|}$ (> 0) for a transition polarised exactly parallel to the orientation direction or $-A_{\perp}$ (< 0) for a transition polarised exactly perpendicular to the orientation direction. Thus qualitative information about the orientation of molecules in space can be extracted from the sign of the *LD*. A more quantitative picture of molecular alignment can be obtained from the reduced *LD* (*LD*^{r}),[7]

$$LD^r = \frac{A_{\parallel} - A_{\perp}}{A} \tag{3.4}$$

where A is the normal isotropic absorption and constitutes an average over all possible orientations.

Macroscopic orientation of molecules may be achieved in a number of ways. Small molecules are suited to orientation in stretched polymer films, liquid crystals or by adsorption onto quartz whereas DNA may be oriented by viscous drag (flow orientation) or an electric field, for example. In this work stretched polymer films and flow orientation are used to orient molecules for *LD*.

3.3.1 Stretched film linear dichroism

Stretched film *LD* provides information about the polarisation directions of the transition moments of DNA binding ligands. When a small molecule is dissolved in a polymer film matrix such as polyvinyl alcohol (PVA) or polyethylene (PE), orientation of that molecule can be achieved by stretching the film. The degree of orientation attained is imperfect and an orientation distribution results. The distribution can be discussed in terms of an axis framework which relates the macroscopic (laboratory) axes, such as the stretch direction of the film, to the molecular axes of the system (Figure 3.2).[7]

The solute molecules typically align within the film such that a minimum cross sectional area is presented to the orienting force. If the resulting orientation is uniaxial then the

orientation distribution is defined such that the surface of a cone centred about the macroscopic orientation axis, *Z*, defines the maximum probability of finding a specific molecular axis at a given angle from *Z* (Figure 3.3).[7]

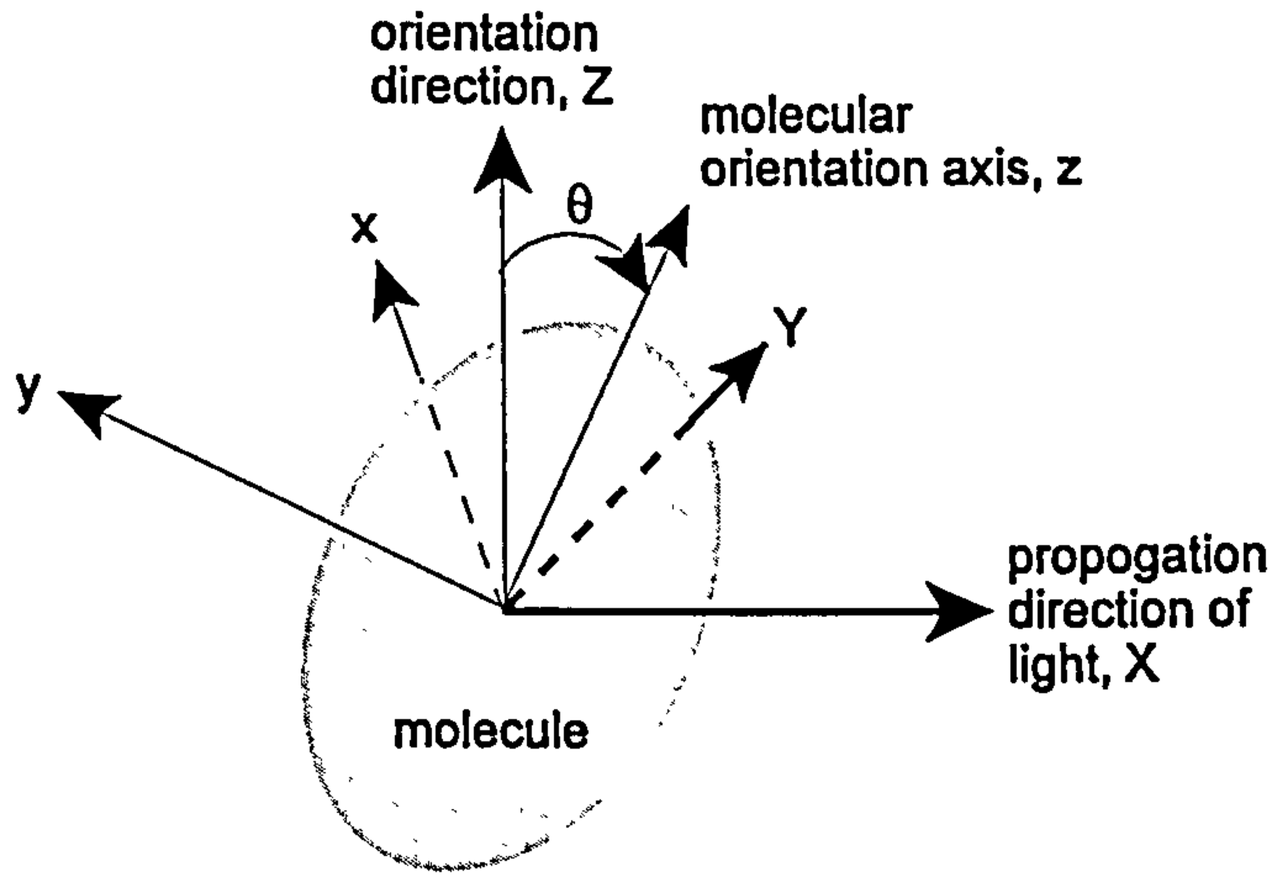

Figure 3.2 Macroscopic {X, Y, Z} and molecular {x, y, z} axis systems.

If the sample molecule also has an identifiable unique 'long' axis about which all orientations are rotationally averaged then that molecule can be described as rod-like, where the molecular orientation axis, *z*, corresponds to the long axis of the molecule. The molecular orientation axis is defined as the molecular axis with maximum value of

$$\langle \cos^2 \theta \rangle \tag{3.5}$$

where θ is the angle between *z* and *Z* (Figure 3.2) and ⟨ ⟩ denotes an average over all the sample molecules.[7] DNA binding ligands with C_{2v} or D_{2h} symmetry and a long axis are examples of rod like molecules.

The degree of orientation can be described in terms of the average orientation parameter, *S*, for a uniaxially oriented rod within a stretched film. *S* can be determined from the LD^r.

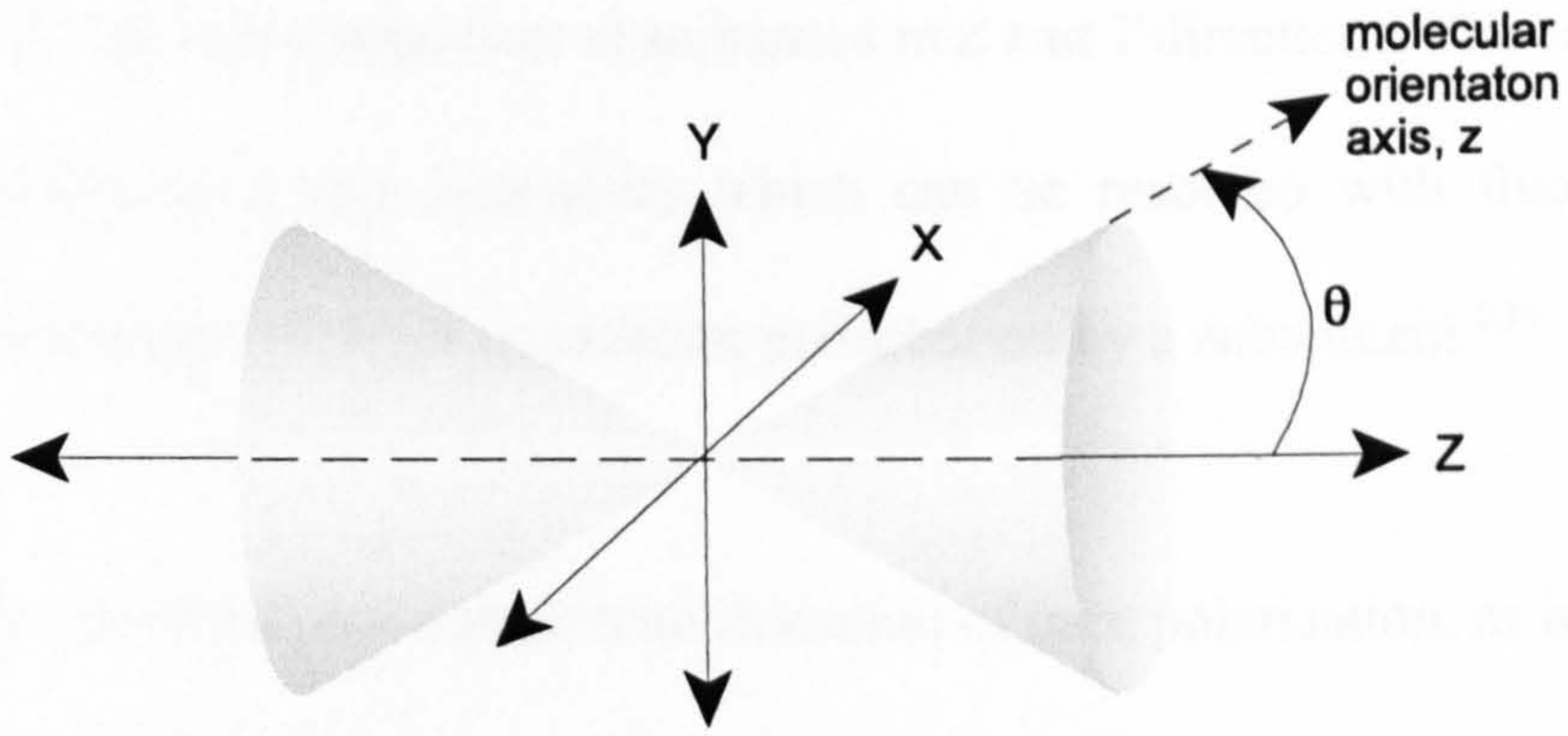

Figure 3.3 Uniaxial orientation relative to a macroscopic axis system.

For a transition of pure *z* polarisation[7]

$$LD^r = 3S_{zz} \tag{3.6}$$

where

$$S_{zz} = \frac{1}{2}\left(3\langle\cos^2\theta\rangle - 1\right) \tag{3.7}$$

In a uniaxially oriented system $S_{xx} = S_{yy}$ and $S_{xx} + S_{yy} + S_{zz} = 0$ thus S_{yy} is determined from

$$S_{zz} + 2S_{yy} = 0 \tag{3.8}$$

where S_{xx}, S_{yy} and S_{zz} are the orientation parameters for the *x*, *y* and *z* molecular axes respectively. The angle between the polarisation direction of a transition moment and the orientation direction, α, for a planar molecule with no out-of-plane transitions ($A_x(\lambda) = 0$), can then be computed from

$$\frac{A_y(\lambda)}{A_z(\lambda)} = -\frac{LD^r(\lambda) - 3S_{zz}}{LD^r(\lambda) - 3S_{yy}} = \frac{\sin^2\alpha}{\cos^2\alpha} = \tan^2\alpha \tag{3.9}$$

where $A_y(\lambda)$ and $A_z(\lambda)$ are component absorbances in Z and Y directions. The calculated α value is subject to a sign ambiguity which can be resolved with fluorescence polarisation anisotropy (FPA) or orientation perturbation by a substituent.[7,10]

When the molecule of interest contains no transition of pure polarisation, as is the case for many DNA binding ligands, the 'Trial and Error Method' (TEM) may be used to deconvolute an absorbance spectrum composed exclusively of in-plane transitions into its Z ($A_{||}$) and Y ($A_{\perp}$) components.[7,11] The technique is most effective for high symmetry molecules but may also be applicable to low symmetry systems if the component absorbance spectra contain peaks known to derive from a single transition. The component spectra A_y and A_z are calculated by forming the linear combinations

$$A_z(\lambda) \propto A_z(\lambda) - \delta_z A_y(\lambda) \tag{3.10}$$

and

$$A_y(\lambda) \propto A_y(\lambda) - \delta_y A_z(\lambda) \tag{3.11}$$

by incrementally varying δ to give an entirely positive spectrum that has good shape and has no feature known to belong to the corresponding orthogonal spectrum. An assignment of transition polarisations made with the TEM can then be corroborated with, for example, theoretical Pariser-Parr-Pople (PPP) calculations.[12]

3.3.2 Flow linear dichroism

Flow *LD* when applied to DNA systems is sensitive to the orientation of the nucleobases and of DNA bound ligands relative to the helix axis. Structural information regarding the geometry of a bound ligand can thus be extracted from a flow *LD* spectrum. The DNA sample in solution is exposed to a hydrodynamic shear force and becomes macroscopically oriented by the resulting viscous drag. Experimentally this is achieved using a Couette flow cell[7,13,14] (Figure 3.4) where the sample is contained by two concentric cylinders, one of which rotates to provide a constant flow of solution through the narrow gap between the cylinders. The flow must be laminar to avoid light scattering and loss of orientation.

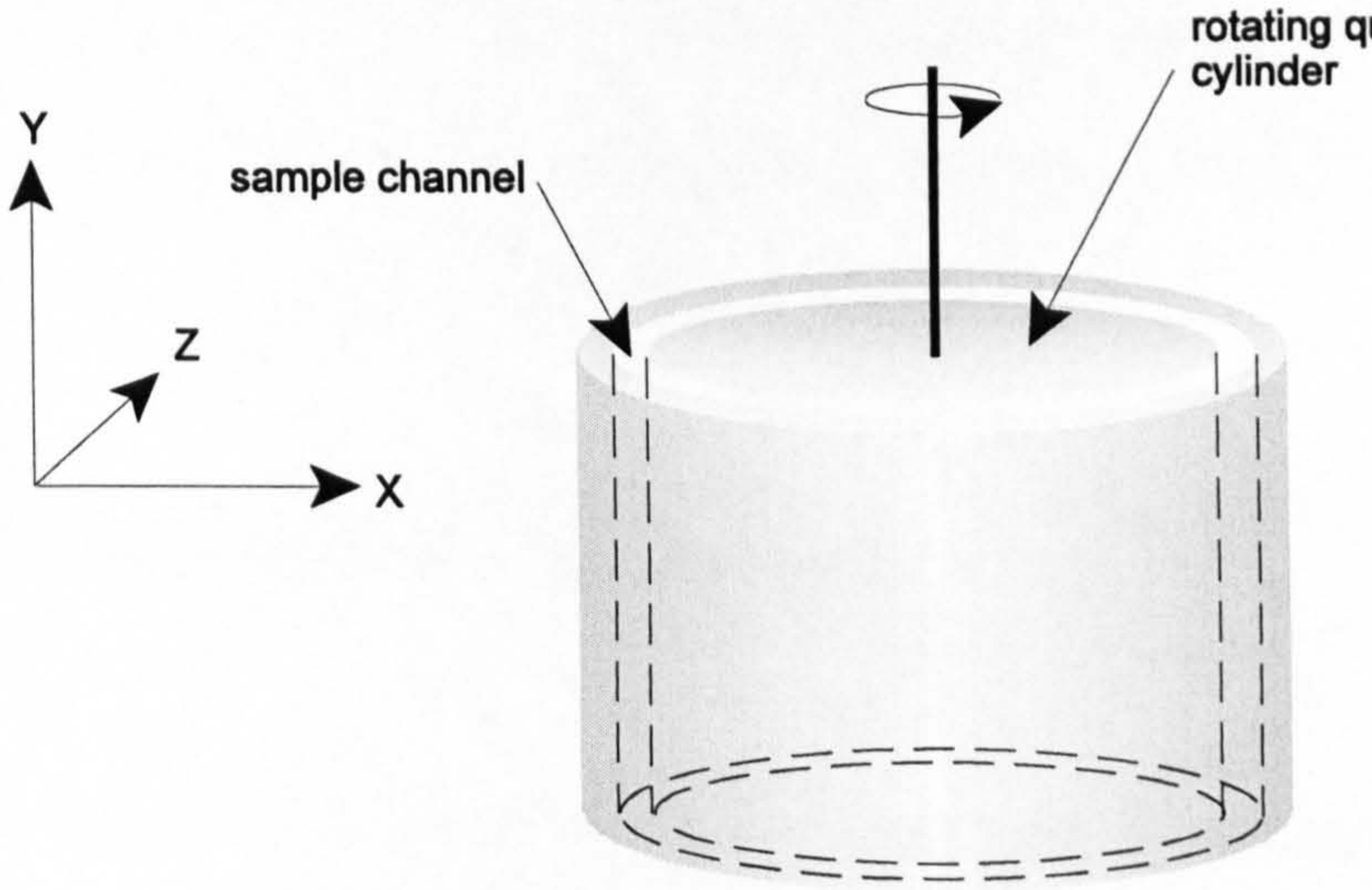

Figure 3.4 Couette flow cell for the orientation of nucleic acids. Light is propagated in the X direction (perpendicular to the flow direction). $A_{\parallel}$ is absorbance of XZ polarised light and and $A_{\perp}$ is absorbance of XY polarised light.

Flow *LD* of effectively rod-like DNA such as the B-form duplex produces uniaxial orientation about the helix axis for which the LD^r may be expressed as[7, 14]

$$LD^r = S\frac{3}{2}\left(3\langle\cos^2\alpha\rangle - 1\right) \tag{3.12}$$

where α refers to the angle between a transition moment and the DNA helix axis and $\langle\rangle$ denotes an ensemble average over the orientation distribution function. For the transitions of the DNA bases, which are predominantly $\pi \rightarrow \pi^*$ in-plane polarised, a value for α of 86° has been calculated.[7,15,16] Thus if $\alpha = 86°$ for the in-plane $\pi \rightarrow \pi^*$ transitions of the DNA bases then S can be determined from the magnitude of the LD^r at 260 nm using equation 3.12. Once S has been determined, α may be computed for the transition moments of DNA bound ligands with known polarisations. The value of α for a bound ligand can then be used to help identify the mode of binding. The in-plane transitions of a bound intercalator would be expected to have negative LD^r of similar magnitude to that of the DNA bases since the ligand and bases would be co-planar. A bound ligand in the minor groove of B-DNA would have positive LD and $\alpha \approx 45°$ for a long axis polarised transition that followed the pitch of the groove.

3.4 Circular dichroism spectroscopy

CD is the difference in absorption of left (A_l) and right (A_r) circularly polarised light.[7]

$$CD = A_l - A_r \tag{3.13}$$

CD measures the difference in helical redistribution of electron density that occurs in chiral chromophores upon excitation with left or right circularly polarised light. The origin of the helical electron motion lies in the non-perpendicular and non-coplanar polarisations of μ and the magnetic dipole transition moment, m, that is unique to chiral

chromophores. Helical transitions are then a consequence of the linear charge displacement induced by the electric field vector of the exciting light, combined with the circular displacement of charge induced by the magnetic field vector of the exciting light.[7]

CD is sensitive to asymmetry. In biological systems any structural change involves a change in asymmetry, thus *CD* is uniquely suited to the study of biomolecular systems. Many aspects of such systems may be probed by *CD* and these include the study of DNA or protein conformational changes and the interaction of ligands with biomolecules.

The *CD* of DNA (Figure 3.5) above 190 nm is due almost exclusively to the $\pi \rightarrow \pi^*$ transitions of the nucleobases. Although the bases themselves are achiral in isolation, a combination of their helical arrangement in space in duplex DNA (permitting electronic coupling between the transitions of adjacent bases) and the *CD* induced (*ICD*) by the intrinsically chiral deoxyribose sugar produces a *CD* spectrum that constitutes a convolution of all the transitions of the bases.[7] The form of the spectrum is dependent on the both the base composition and conformation of the DNA being probed. The *CD* spectrum of B-form ct-DNA, for example, has a positive band at 275 nm and a negative band at 240 nm with the zero at 258 nm. Other DNA conformations also have characteristic *CD* signatures since variations in the precise relative orientations of the bases between the different polymorphs are reflected in the *CD* spectrum.

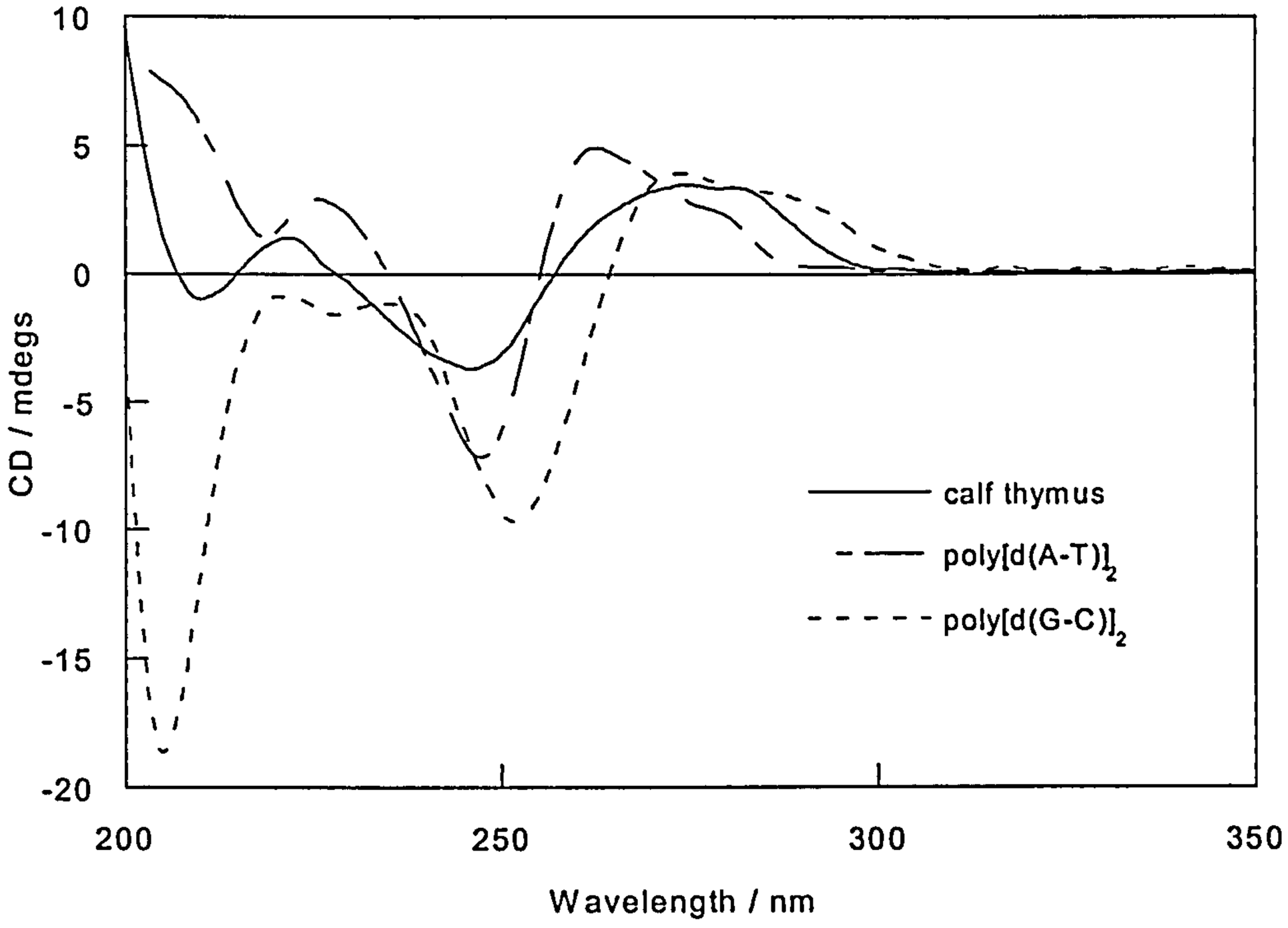

Figure 3.5 *CD* spectra of various B-DNA sequences (40 μM DNA, 1 mM phosphate, 20 mM NaCl).

Although many DNA binding ligands are achiral, investigation of DNA–ligand interactions is still possible by *CD*. The bound ligand may perturb the structure of the host DNA resulting in a change in the *CD* signature of that DNA, and the ligand itself will acquire *ICD* enabling its transitions to be probed directly. The *ICD* originates from the coupling of the ligand transitions with those of the DNA bases or the imposition of a chiral conformation on the ligand by the DNA binding site.[7] The presence of *ICD* at the wavelength of an achiral ligand transition therefore implies DNA binding.

In principle, from a knowledge of the transition moments of the DNA and ligand the orientation of the ligand on the DNA may be computed from the experimental *CD* spectrum. In practice, however, DNA–ligand spectra are normally interpreted empirically. When *CD* spectra of DNA–ligand systems are measured as a function of

some variable, such as ionic strength, ligand/DNA mixing ratio, *r*, or temperature, any change in the behaviour of the system is reflected in the *CD* spectrum. A change in the intensity of the ligand *ICD* usually mirrors a change in the amount of bound ligand, whereas a variation in shape of the ligand *ICD* reflects a change in binding mode.

Stacking interactions between DNA bound ligands can also be detected in the *CD* spectrum. The occurrence of stacking interactions results in electronic coupling between the ligand transition moments.[17] This coupling is apparent in the *CD* spectrum as anomalously large signals at the absorption wavelength of the ligand transitions and is commonly referred to as exciton *CD*. The strength of the coupling depends on the individual oscillator strengths of the coupled transition moments and their relative orientation and energies.

If the shape of the *CD* spectrum remains constant over a range of ligand/DNA mixing ratios (implying the operation of a single binding mode) a binding constant may be determined since the *CD* intensity is proportional to the amount of bound ligand

$$L_b = \beta \rho \tag{3.14}$$

where L_b is the concentration of bound ligand, ρ is the intensity of the *ICD* and β is a proportionality constant.[7,13]

3.5 Fluorescence spectroscopy

Fluorescence spectroscopy measures the radiative decay of the electronically excited state of a molecule following the absorption of UV–visible light. Fluorescence is characterised

by the quantum yield, Q, a measure of the proportion of absorbed light that is then emitted as fluorescence[18]

$$Q = \frac{\Gamma}{\Gamma + K} \tag{3.15}$$

where Γ is the rate of emission of the fluorophore and K is the rate of non-radiative decay of the electronically excited state. The extent to which a molecule is fluorescent is determined by a combination of the efficiency of non-radiative decay processes such as intersystem crossing and internal conversion (Figure 3.6) and the environment to which the molecule is exposed.

The environment dependence of fluorescence may be exploited in the study of DNA–ligand interactions since the change in environment on binding to DNA may lead to a change in the fluorescence properties of the ligand. An enhancement in the

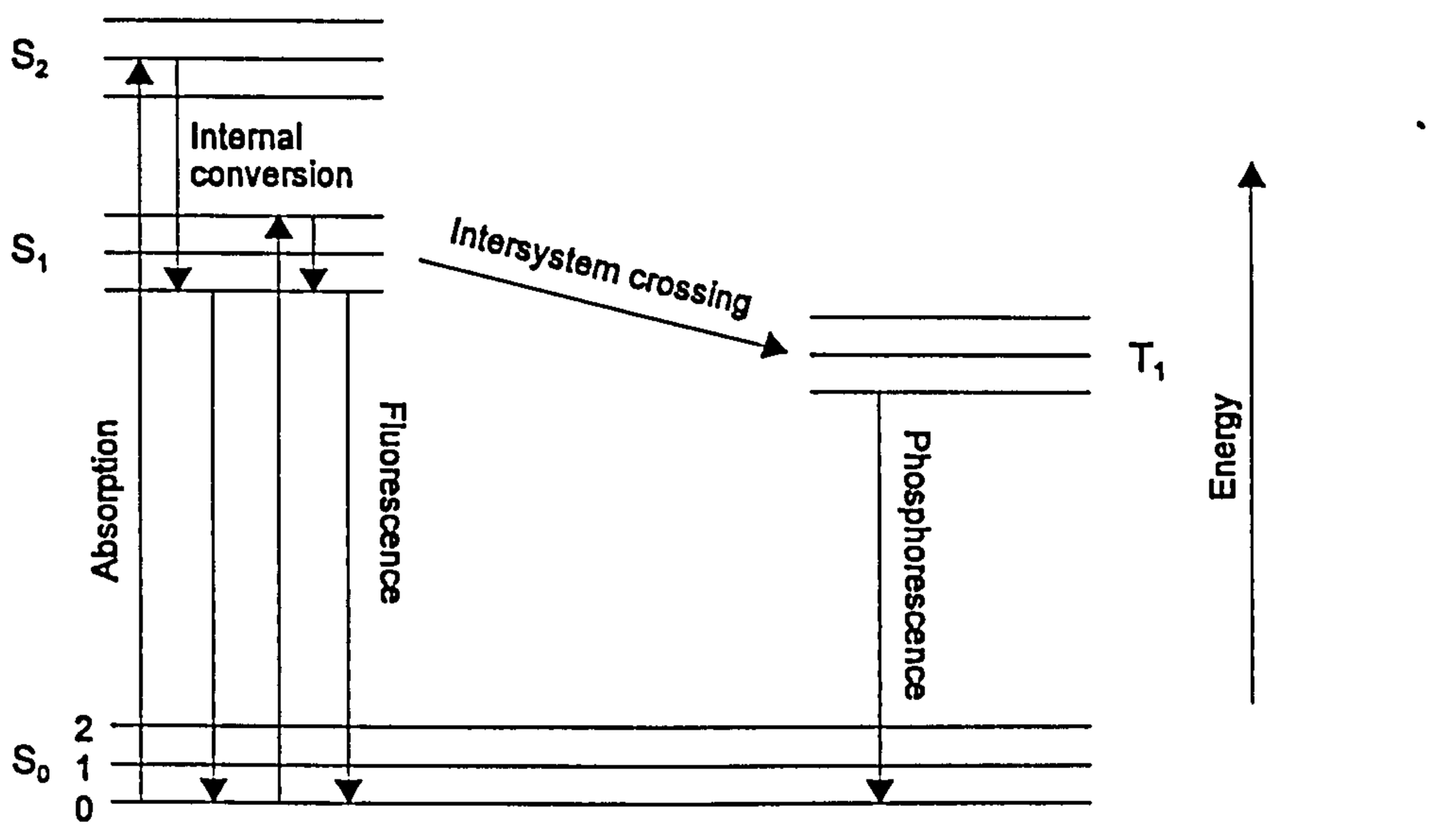

Figure 3.6 Jablonski diagram. S_0, S_1 and S_2 denote the ground state and first and second excited singlet states respectively. T_1 denotes the first excited triplet state. 0, 1 and 2 denote vibrational levels.[18]

fluorescence intensity of intercalators such as ethidium, for example, is detectable as the hydrophobic environment of the intercalation site prevents fluorescence quenching by the solvent. Wavelengths shifts and quenching may also be observed in the ligand fluorescence spectrum if ligand–ligand interactions are occurring.

3.5.1 Fluorescence polarisation anisotropy

Fluorescence polarisation anisotropy (FPA) measures the mobility of a chromophore by probing the extent to which the polarisation of emitted plane polarised light is the same as that absorbed. The technique exploits the requirement of molecules to absorb and emit light according to the polarisation direction of their transition moments. FPA is defined as[7]

$$FPA = \frac{I_{VV} - I_{VH}}{I_{VV} - I_{VH}} \tag{3.16}$$

where I_{VV} is intensity of fluorescence emission measured with vertical excitation and emission polarisers and I_{VH} is the intensity of fluorescence emission measured with a vertical excitation polariser and a horizontal emission polariser. When applied to an oriented sample of molecules FPA may be used to resolve sign ambiguities arising from the $\cos^2 \alpha$ dependence of transition moment polarisation assignments by *LD*. In the absence of depolarisation effects arising from chromophore rotation or contact energy transfer during the lifetime of the excited state[7]

$$FPA = \frac{1}{5}\left(3\cos^2 \chi - 1\right) \tag{3.17}$$

where χ is the angle between the absorbing and emitting transition moments.

3.6 Resonance light scattering spectroscopy

When light is incident on a collection of polarisable molecules the electrons of those molecules oscillate and radiate light in all directions. In a homogeneous sample the secondary waves interfere destructively except in the propagation direction of the incident light. Conversely, in an inhomogeneous sample, such as a solution of aggregated molecules, light will be scattered in directions other than the propagation direction since the polarisability of the aggregates and solution are different. When light is scattered by particles that are significantly smaller then the wavelength of the incident light, as for an uncondensed DNA–ligand system, Rayleigh scattering is observed where the intensity of scattered light is proportional to λ^{-4}.[19]

If the wavelength of the incident light corresponds to the absorption band energy of an aggregated chromophore an enhanced *RLS* is observed.[20–23] The origin of the *RLS* is explained by the theory of resonance enhanced Rayleigh scattering.[24,25] When light passes through a solution of aggregates energy is removed from the incident beam by absorption and scattering by the aggregates. The ratio of the rate of energy absorption from the incident light to the intensity of the incident light is the absorption cross section, C_{abs}. If the size of the aggregates is considerably smaller than the wavelength of the incident light in the solvent, λ_m, then[22]

$$C_{abs} = k_m \sigma_i \tag{3.18}$$

where k_m is the magnitude of the wave vector of the light in the solvent ($k_m = 2\pi/\lambda_m$) and σ_i is the imaginary part of the polarisability of the aggregate. The absorbance of the sample is then related to C_{abs} by[22]

$$A = 2.3^{-1}\left(\frac{N}{V}\right)C_{abs}L \tag{3.19}$$

where N/V is the number of aggregates per unit volume and L is thickness of the sample. The ratio of the rate of energy loss due to scattering out of the incident light to the intensity of the incident light is the scattering cross section, C_{sca}, and is related to the polarisability of the aggregate by[22]

$$C_{sca} = \frac{k_m^4}{6\pi}\left|\sigma^2\right| = \frac{k_m^4}{6\pi}\left(\sigma_r^2 + \sigma_i^2\right) \tag{3.20}$$

where σ_r is the real part of the polarisability of the aggregate. Since an absorption band corresponds to a maximum in σ_i, and σ_r and σ_i are related such that σ_r is also anomalously large within an absorption band, a maximum in $|\sigma^2|$ results and leads to an enhanced light scattering.

In practice, several factors contribute to the observed *RLS*. For monomers or oligomers the effect of the enhanced scattering is weak and cannot be detected above the increased absorption of the species. For aggregated chromophores however, an extremely large *RLS* is observable within their absorption band. Strong electronic coupling between the chromophores of the aggregate is an important prerequisite for an enhanced *RLS*. The strength of the coupling is dependent on factors such as the magnitude of the extinction

coefficient and relative spatial orientation of the constituent chromophores of the aggregate. For these reasons, the bases of uncondensed duplex DNA (which have $\varepsilon < 10^4$), although extensively stacked, exhibit no *RLS* since the extent of the electronic coupling is restricted to short range interactions between neighbouring base pairs. Thus DNA scatters light as a collection of small oligomers and the *RLS* enhancement is weak. Conversely, for systems where the electronic coupling is strong, as in porphyrin aggregates for example ($\varepsilon \approx 2 \times 10^5$), long range electronic coupling can occur leading to delocalisation of electron density across the entire particle. Thus σ is large for systems of this type and they exhibit a correspondingly large *RLS* enhancement the magnitude of which increases with aggregate size (and concentration).

Experimentally, *RLS* spectra may be measured on a standard fluorimeter set to scan synchronously across excitation and emission wavelengths. The *RLS* is then detected at 90° to the exciting light on samples of typically micromolar concentrations. The *RLS* spectrum appears as a dip at the wavelength of the absorption band of a monomeric chromophore or a large peak corresponding to the absorption wavelength of an aggregated chromophore.

3.6.1 Scope and limitations of resonance light scattering

When applied to DNA–ligand systems, *RLS* can detect the stacking interactions between bound ligands that often occur as a result of highly cooperative binding modes. Since *RLS* is sensitive to the size of an aggregated chromophore, the technique can differentiate an extended stack from ligands bound as monomers, dimers or oligomers. Although *CD*

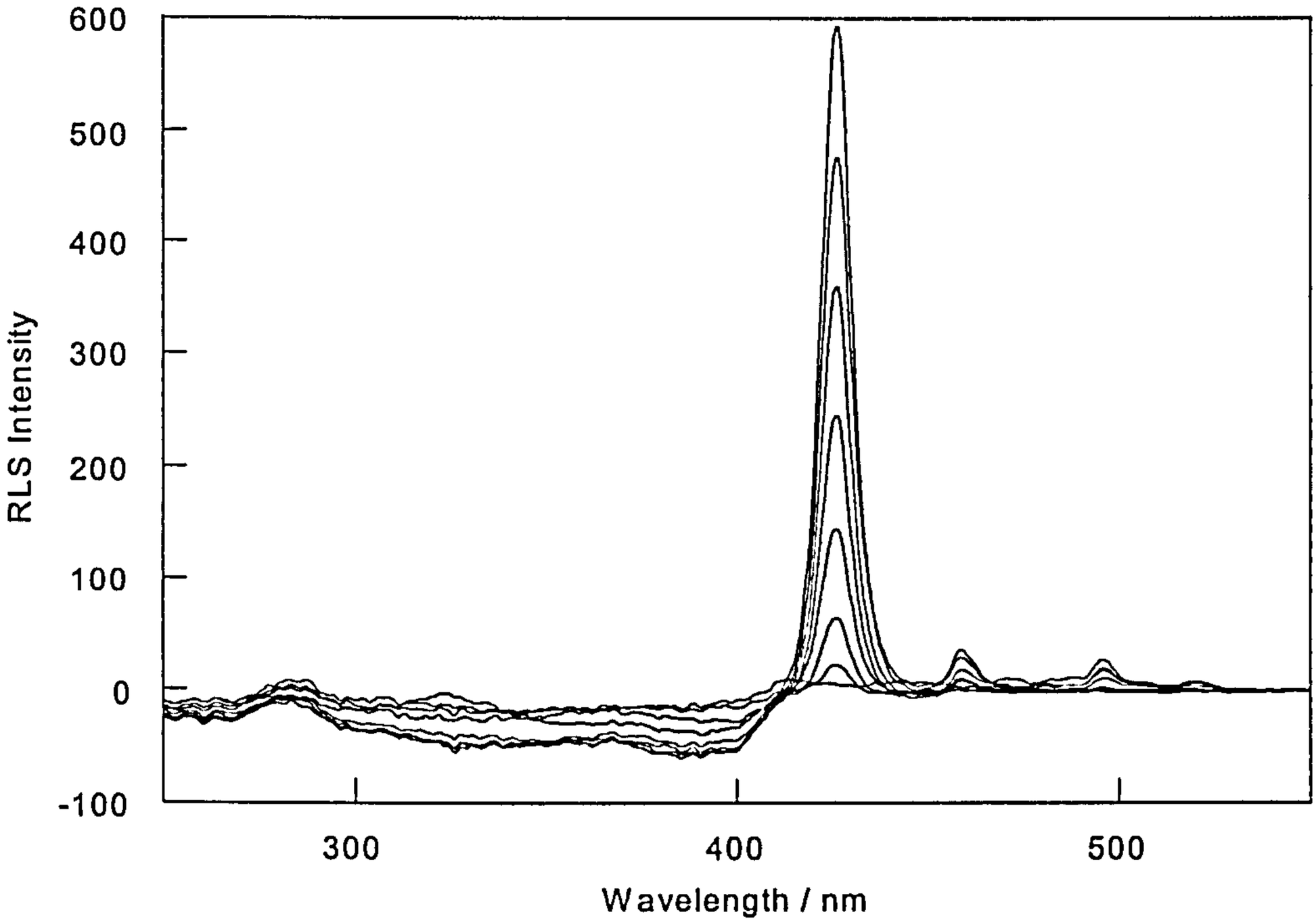

Figure 3.17 *RLS* spectra of 9-aminoacridine (6 – 20 μM; signal intensity at 426 nm increases with concentration), poly[d(G-C)]$_2$ (40 μM) and phosphate buffer (1 mM; pH 7).

and fluorescence spectroscopies can also detect ligand–ligand interactions these techniques are not sensitive to the extent of the stack. Furthermore, *RLS* can in principal probe complex systems since it usually responds to the aggregated component of the system only.[21] *RLS* has also been applied as an analytical technique to determine nanogram amounts of proteins[26] and nucleic acids[24,25] by measuring the state of aggregation of bound porphyrin arrays.

When applied to very large particles such as condensed or aggregated DNA, the *RLS* signal is barely detectable above conventional Rayleigh light scattering. Moreover, *RLS* is limited to molecules that are either non-fluorescent or that fluoresce at wavelengths well away from the wavelength of *RLS* detection. For example, 9-aminoacridine is a known intercalator (intercalation does not permit interaction between adjacently bound

ligands) but when a sample of 9-aminoacridine and DNA is scanned synchronously (Figure 3.7) peaks appear in the *'RLS'* spectrum that actually arise from fluorescence rather than chromophore stacking. Thus the possibility exists that synchronous scanning can detect fluorescence in addition to or instead of the *RLS*. Appropriate control experiments are therefore required to correctly interpret *RLS* spectra of fluorescent molecules.

4 Spectroscopic Studies of Porphyrin Binding to DNA

4.1 Introduction

DNA–porphyrin interactions have been extensively studied due to their potential utility in chemical and biological applications.[27] For example, porphyrins are now well established as photosensitisers in the photodynamic therapy of tumours where photochemically activated porphyrin promotes the formation of singlet oxygen and subsequent DNA cleavage.[28] Porphyrins have also been established as potential DNA binding chemotherapeutic and antiviral agents.[27,29] Structural studies of DNA–porphyrin interactions are therefore important to elucidate the mode of action of porphyrin based drugs.

Investigations of DNA–porphyrin interactions have focused on the binding of cationic tetra meso-substituted porphyrin derivatives to DNA,[30–36] with specific emphasis on meso-tetrakis(4-*N*-methylpyridiniumyl)porphyrin (H_2TMPyP; Figure 4.1b) and its metal derivatives.[37–47] Intercalation, outside binding and outside binding with self-stacking were initially proposed by Fiel *et al.* as three possible porphyrin binding modes.[30,31] Intercalation is generally observed at GC binding sites for free base porphyrins that do not readily self-stack, and for square planar metalloporphyrins such as those with Cu^{2+} or Ni^{2+} metal ions.[30,32] Outside binding generally occurs at AT binding sites. Free base porphyrins with bulky peripheral substituent groups, or metal derivatives with axial ligands such as those with Co^{3+}, Mn^{3+} or Fe^{3+} metal ions, exhibit outside binding modes

since insertion between the base pairs is sterically blocked.[41] Intercalation and outside binding modes are ionic strength dependent. H_2TMPyP, for example, have been shown to preferentially intercalate into 5'-CG-3' sites[43] at low ionic strength but to bind externally to AT tracts at high ionic strength.[44] The charge on the porphyrin core may also be an important determinant in the formation of intercalated vs outside bound DNA complexes.[45] The influence of the location and number of charges on the DNA–porphyrin binding mode has also been studied.[46,47] Partial intercalation constitutes an extension to the Fiel model of porphyrin binding to DNA. An X-ray crystal structure of a DNA–porphyrin complex was recently reported in which the hemiintercalated porphyrin flipped out a cytosine base from the central helical stack.[48]

Porphyrins such as the dicationic *t*-H_2P[20,49,50] (Figure 4.1a) and the tetracationic *meso*-tetrakis[4(3-(trimethylammonio)propyl)-oxy]phenyl]porphyrin (TθOPP)[51–53] self-stack on the surface of DNA at both GC and AT binding sites. Most of the characterisation of porphyrin binding to DNA has focused on monomer binding, and where a stacked binding mode has been examined no information regarding the exact binding geometry is available. The purpose of this study therefore, was to examine in detail the DNA binding geometries of the self-stacking porphyrin *t*-H_2P. For both *t*-H_2P and TθOPP the stacked binding mode is favoured at high ionic strength (such as in biological systems) or high ligand/DNA mixing ratios. Both porphyrins also show a greater tendency to stack on poly[d(G-C)]$_2$ than on poly[d(A-T)]$_2$,[49] although in the case of TθOPP, binding to poly[d(A-T)]$_2$ is favoured over binding to poly[d(G-C)]$_2$.[51] In addition to the stacked binding mode, *t*-H_2P has also been suggested to be capable of intercalating into DNA under conditions of low ionic strength and a low ligand/DNA mixing ratio.[46,47] The

kinetic and thermodynamic properties of *t*-H_2P aggregation in the presence of DNA have also recently been reported.[54,55]

In this work, the binding of *t*-H_2P to ct-DNA, poly[d(A-T)]$_2$ and poly[d(G-C)]$_2$ is examined with several spectroscopic techniques. The presence of stacked porphyrins bound to DNA can be detected with *CD*, where the interaction between adjacently bound porphyrins on DNA gives rise to large exciton *CD* signals at the Soret band wavelength of the porphyrin.[20] Although *CD* can detect the presence of porphyrin–porphyrin interactions on DNA, information regarding the extent of the stack cannot be extracted. *RLS* is sensitive not only to porphyrin–porphyrin interactions but also to the extent of stacking of an array of chromophores. *RLS* was initially applied by Pasternack *et al.* to probe the self–assembly of *t*-H_2P on DNA[20] and subsequently applied to probe the extent of stacking of anionic sulfonatophenyl-porphyrin derivatives[21] and chlorophyll α[56] in solution. The technique was later applied to study the self-assembly of metal complexes with terpyridine ligands bound to DNA.[57,58]

Flow *LD* has previously been applied to differentiate the intercalated binding geometry of H_2TMPyP to ct-DNA, where the plane of the porphyrin ring lies parallel to the plane of the bases, from the outside binding mode of its Zn^{2+} derivative, in which the porphyrin plane is inclined at 62 – 67° to the helix axis.[42] The technique has also been employed to characterise the binding of a series of Co^{3+} porphyrins to ct-DNA, poly[d(A-T)]$_2$ and poly[d(G-C)]$_2$, where binding angles of 45°, 45 – 50° and 30 – 40° respectively were established.[41] To facilitate interpretation of the flow *LD* results presented in this work the transition polarisations of *t*-H_2P were determined with stretched film *LD*. The electronic

spectrum of tetraphenyl porphyrin in stretched polymer films has been previously investigated[59,60] along with the effect of various symmetries on the transition moment polarisations in porphyrin derivatives.[61]

In addition to the experimental data, molecular models of possible DNA–porphyrin complexes were constructed to visualise the possible DNA–porphyrin complexes and to facilitate interpretation of the spectroscopic results in terms of molecular structure. Molecular modelling has been used previously to examine minor groove bound complexes of H_2TMPyP and a porphyrin derivative with bulky trimethylanilinium substituents (TMAP).[62] A significant DNA structural change was shown to be required for TMAP to bind in the minor groove. Lipscomb *et al.* also used molecular modelling to investigate the relative energetics of CuTMPyP binding by hemiintercalation to DNA and binding by conventional intercalation.[48]

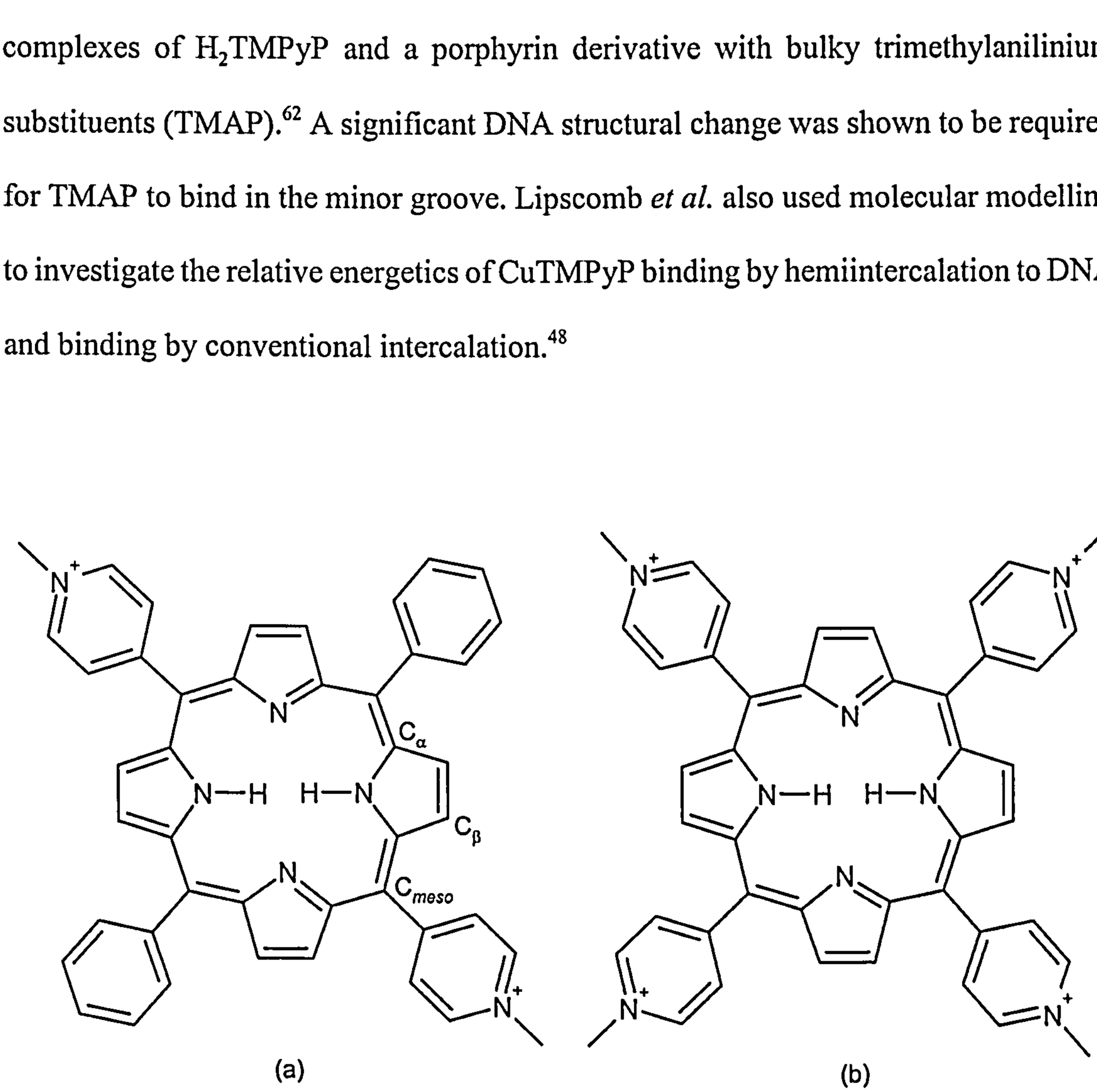

Figure 4.1 Structures of (a) *t*-H_2P and (b) H_2TMPyP at pH 7.

4.2 Experimental

4.2.1 Materials

t-H_2P was purchased as the chloride salt from MidCentury Chemicals, Illinois, and used without further purification. Solution concentrations were determined in 18.2 MΩ water (pure water) using $\varepsilon = 2.4 \times 10^5\ M^{-1}\ cm^{-1}$ for the Soret absorption maximum at 418 nm.[49] All *t*-H_2P solutions were stored in the dark until required. Synthetic DNAs were purchased from Pharmacia Biotech and used without further purification. The DNA was then rehydrated at room temperature by stirring in pure water for approximately 1 hour. Solution concentrations were determined for poly[d(G-C)]$_2$ in pure water using $\varepsilon = 8400$ $mol^{-1}\ dm^3\ cm^{-1}$ at 256 nm and for poly[d(A-T)]$_2$ in 20 mM NaCl using $\varepsilon = 6600\ mol^{-1}\ dm^3\ cm^{-1}$ at 262 nm. ct-DNA was purchased from Sigma Chemical Company and used without further purification. The DNA was rehydrated by stirring overnight in pure water at room temperature. Solution concentrations were determined in pure water using $\varepsilon = 6600\ mol^{-1}\ dm^3\ cm^{-1}$ at 258 nm. All DNA samples were stored at −20°C until required.

4.2.2 Spectroscopic titrations

For experiments involving DNA, phosphate buffers were first prepared. Anhydrous monobasic and dibasic sodium phosphates were obtained from Sigma Chemical Company and used without further purification. Stock solutions (0.2 M) of each phosphate were prepared and mixed in the ratio 39 parts monobasic sodium phosphate to 61 parts dibasic sodium phosphate to 100 parts pure water to give a pH 7 phosphate

buffer (0.1 M).[63] This solution was then diluted by a factor of two to give a stock solution (50 mM) for experimental use. The pH of the final solution was verified with a pH meter. The buffer was stored at 4°C but allowed to warm to room temperature before use.

Spectroscopic titrations were performed in which *CD*, *RLS* and normal absorption spectra were collected as a function of both salt concentration and *t*-H_2P concentration for each DNA sequence. For salt titrations involving ct-DNA, poly[d(G-C)]$_2$ and poly[d(A-T)]$_2$, an initial solution was prepared containing DNA (40 μM), *t*-H_2P (5 μM) and phosphate buffer (1 mM). The concentration of NaCl was then adjusted from 0 – 100 mM in increments of 20 mM for ct-DNA and poly[d(G-C)]$_2$, and from 20 – 100 mM for poly[d(A-T)]$_2$ (poly[d(A-T)]$_2$ requires 20 mM salt for duplex formation), and spectra recorded after each addition of salt. The concentrations of DNA, *t*-H_2P and buffer were held constant after each salt addition by adding an identical volume of a solution containing the other components at double the required concentration. The necessary volume of NaCl required for each concentration adjustment was computed from the relationship

$$[\mathrm{NaCl}] = \frac{V_{\mathrm{NaCl}}}{V_i + 2V_{\mathrm{NaCl}}}[\mathrm{NaCl}]_{\mathrm{stock}} \qquad (4.1)$$

then, rearranging to give

$$V_{\mathrm{NaCl}} = \frac{V_i[\mathrm{NaCl}]}{[\mathrm{NaCl}]_{\mathrm{stock}} - 2[\mathrm{NaCl}]} \qquad (4.2)$$

where V_{NaCl} is the required volume of salt, [NaCl] is the required concentration of salt, V_i is the initial volume of solution and $[NaCl]_{stock}$ is the concentration of salt stock solution. Since a large number of titrations were performed computer spreadsheets (Table 4.1) were written to automate the required calculations. This approach both reduced the frequency of numerical errors and facilitated the rapid modelling of experimental variables such as concentration of stock solutions and required solution volumes.

	B	C	D	E
2	$[NaCl]_{stock}$ / mM =	1000		
3	Initial volume / μL =	2000		
4	Required [NaCl] / mM	Total NaCl Volume / μL	Total Volume / μL	Additional NaCl Volume / μL
5	0	=($C$3*B5)/($C$2-2*B5)	=$C$3+2*C5	=$C$5
6	20	=($C$3*B6)/($C$2-2*B6)	=$C$3+2*C6	=C6-C5
7	40	=($C$3*B7)/($C$2-2*B7)	=$C$3+2*C7	=C7-C6
8	60	=($C$3*B8)/($C$2-2*B8)	=$C$3+2*C8	=C8-C7
9	80	=($C$3*B9)/($C$2-2*B9)	=$C$3+2*C9	=C9-C8
10	100	=($C$3*B10)/($C$2-2*B10)	=$C$3+2*C10	=C10-C9
11			Total	=SUM(E5:E10)

Table 4.1 Spreadsheet for the calculation of salt titration parameters. The formulae in column C are based on equation 4.2.

An important consideration when preparing solutions for the titrations is the order of addition of reagents. Since high concentrations of certain porphyrins can aggregate DNA, high local concentrations of *t*-H_2P in the presence of DNA were avoided by adding the DNA last to a well mixed solution of pure water, buffer and *t*-H_2P. NaCl was then added incrementally during the course of the titration. A reference titration was also performed in which NaCl (0 – 200 mM in 20 mM increments) was added to a solution of *t*-H_2P (5 μM) only.

For the titrations involving variable *t*-H_2P concentration, initial solutions containing DNA (40 μM), phosphate buffer (1 mM) and NaCl (20 mM) were prepared. The concentration of *t*-H_2P was then adjusted from 1 – 8 μM in 1 μM increments. The volume and concentration of solutions were controlled as described previously using equation 4.2 and a spreadsheet adapted from that detailed in Table 4.1.

4.2.3 Melting curves

Normal absorption melting curves were collected for poly[d(A-T)]$_2$ and poly[d(G-C)]$_2$ in the presence of *t*-H_2P. Samples were prepared containing DNA (40 μM), NaCl (20 mM), phosphate buffer (1 mM) and either 1 μM, 4 μM or 8 μM *t*-H_2P. Reference samples were also prepared containing either DNA (40 mM) only, *t*-H_2P (8 μM) only or phosphate buffer (1 mM) only. Each sample was then heated from 20 – 90°C at a ramp rate of 0.1 °C min^{-1}. The absorbance at 260 nm was measured every 0.2°C and averaged for 10 s. The samples were then cooled from 90 – 20°C using the same temperature control and absorbance measurement parameters as for the heating.

CD melting curves were also measured for the high mixing ratio DNA–porphyrin systems. Samples were prepared containing either poly[d(A-T)]$_2$ or poly[d(G-C)]$_2$ (40 μM), NaCl (20 mM), phosphate buffer (1 mM) and *t*-H_2P (8 μM). The samples were then heated from 20 – 90°C at a ramp rate of 40°C hour^{-1} and the *CD* at 260 nm monitored. In addition, a wavelength spectrum was collected at 10°C increments and averaged over four scans. Reference melting curves were measured on samples containing DNA (40 μM), NaCl (20 mM) and phosphate buffer (1 mM) only.

4.2.4 Linear dichroism

Flow *LD* spectra were collected over an identical range of concentrations and conditions as for the salt and *t*-H_2P titrations. Solutions for *LD* were prepared individually for each equivalent titration step. *LD* and normal absorption spectra were recorded with the two instruments calibrated in terms of wavelength range and data interval. LD^r spectra were calculated as described in section 3.3.

Polyvinyl alcohol (PVA) films for stretched film *LD* were prepared by dissolving low molecular weight PVA in pure water (10% w/v) and heating the resulting slurry to near boiling. The viscous solution (~5 mL) was then allowed to cool before a saturated solution of *t*-H_2P (0.1 cm^3) was added.[7] A reference film was also prepared in which pure water (0.1 cm^3) was added in place of *t*-H_2P. The mixture was cast onto a glass plate, any air bubbles removed, and the film allowed to dry in the dark over a period of two days. The dry films were removed from the plates with the aid of a scalpel and stretched in a mechanical film stretcher by a factor of two under heat from a hair dryer. *LD* and normal absorption spectra were recorded where the wavelength range and data interval of the two instruments were set to correspond.

4.2.5 Competition binding

DNA competition binding experiments were performed by initially preparing a solution of poly[d(G-C)]$_2$ (40 μM), *t*-H_2P (5 μM) and NaCl (20 mM) and recording normal absorption and *CD* spectra. An aliquot of poly[d(A-T)]$_2$ was then added together with an

equivalent volume of a solution containing poly[d(G-C)]$_2$, *t*-H_2P and NaCl at double their initial concentrations, such that the final concentration of solution components was poly[d(A-T)]$_2$ (40 μM), poly[d(G-C)]$_2$ (40 μM), *t*-H_2P (5 μM) and NaCl (20 mM). Normal absorption and *CD* spectra were recorded immediately and a further normal absorption spectrum was recorded 45 mins after the addition of poly[d(A-T)]$_2$. The experiment was then performed for an initial solution containing poly[d(A-T)]$_2$, to which poly[d(G-C)]$_2$ was subsequently added.

4.2.6 Spectroscopy

All porphyrin and DNA–porphyrin spectra were collected between 750 and 190 nm except *RLS* spectra which were measured between 700 and 200 nm. All DNA spectra were collected between 350 and 190 nm. Quartz cuvettes with a path length of 1 cm were used for all solution normal absorption, *CD* and *RLS* spectroscopy.

Normal absorption melting curves were measured on a Cary 1E spectrophotometer equipped with a temperature control unit and multiple sample holder. *CD* melting curves were collected on a Jasco J-715 spectropolarimeter equipped with a Peltier temperature control unit. All melting curve samples were placed in stoppered quartz cuvettes sealed with PTFE tape. Normal absorption spectra were collected on a Cary 1E or Jasco V-550 spectrophotometer. *CD* spectra were measured on a Jasco J-715 spectropolarimeter. *CD* data were averaged over eight scans collected at a scan rate of 100 nm min^{-1} with an averaging time of 1 s and a data interval of 0.5 nm. *CD* baselines were measured with identical parameters on pure water and subsequently subtracted from the sample spectra.

RLS spectra were collected on a Perkin-Elmer LS-50 luminescence spectrometer set to scan synchronously and modified to reduce background light scattering. Excitation and emission slit widths were set to 2.5 nm. Background light scattering was measured on pure water and subsequently subtracted from the sample spectra. *LD* spectra were measured on a Jasco J-715 spectropolarimeter adapted to produce alternating parallel and perpendicular plane polarised light. *LD* data were averaged over eight scans collected at a scan rate of 500 nm min^{-1} with an averaging time of 0.25 s and a data interval of 0.5 nm. A 1 mm path length couette flow cell was used to orient samples for flow *LD*. *LD* baselines were measured on pure water and subtracted from the sample spectra.

4.2.7 Molecular modelling

Molecular modelling was performed using a Silicon Graphics Indigo workstation. Quanta 97 (Quanta) from Molecular Simulations Inc. (MSI) was used to construct and visualise all molecular structures. A Pentium PC running the WebLab Viewer program (MSI) was also used to visualise molecular structures. Energy minimisation calculations were set up within Quanta and performed using molecular mechanics with CHARMm.[64] The CHARMm force field and a steepest descents minimisation algorithm were used throughout. Semi-empirical calculations to determine atomic charges prior to energy minimisations were performed with the MOPAC program.[65]

The molecular structure of *t*-H_2P was constructed using the Chemnote program within Quanta and minimised until the energy change between successive iterations was less than 0.01 kcal mol^{-1} $Å^{-1}$. Partial charges for the minimised *t*-H_2P geometry were

obtained from a semi-empirical MNDO calculation (specific details are given in Appendix 1). DNA dodecamers, one with alternating GC base pairs and the other with alternating AT base pairs, were generated using the nucleic acid sequence builder within Quanta. The DNA and *t*-H_2P were then docked in a variety of orientations and energy minimised over 6000 iterations. After preliminary searches for chemically reasonable binding modes, three binding geometries were examined for each DNA sequence. Firstly, *t*-H_2P was placed between the central base pairs of each dodecamer with one phenyl and one *N*-methylpyridiniumyl group protruding into the major groove, and the remaining two substituent groups in the minor groove but in close contact with the DNA backbone. Secondly, the porphyrin was placed end-on into the minor groove with one phenyl and one *N*-methylpyridiniumyl group buried in the groove. Thirdly, *t*-H_2P was placed in the major groove with a phenyl ring partially inserted between the central base pairs of each dodecamer and the *N*-methylpyridiniumyl groups in approximate van der Waals contact with the DNA backbone.

4.3 Results

4.3.1 Normal absorption titrations

In the absence of DNA, *t*-H_2P exhibits an intense Soret[3] absorption band at 418 nm. Less intense bands are observable in both the UV and visible regions of the spectrum. The form of the spectrum is dependent on the ionic strength. In the presence of NaCl a shoulder appears at 449 nm which intensifies as the concentration of salt is progressively increased. The appearance of the shoulder is accompanied by a decrease in the intensity

of the 418 nm Soret band (Figure 4.2). Furthermore, an isosbestic point is observed at 439 nm between 0 and 160 mM NaCl indicating the presence of exactly two spectroscopically distinct *t*-H_2P species. The identity of the 439 nm absorbing species is known to be a porphyrin aggregate and the 418 nm Soret band absorption arises from porphyrin monomers.[20] Thus NaCl promotes *t*-H_2P aggregation. Loss of the isosbestic point occurs at NaCl concentrations in excess of 160 mM.

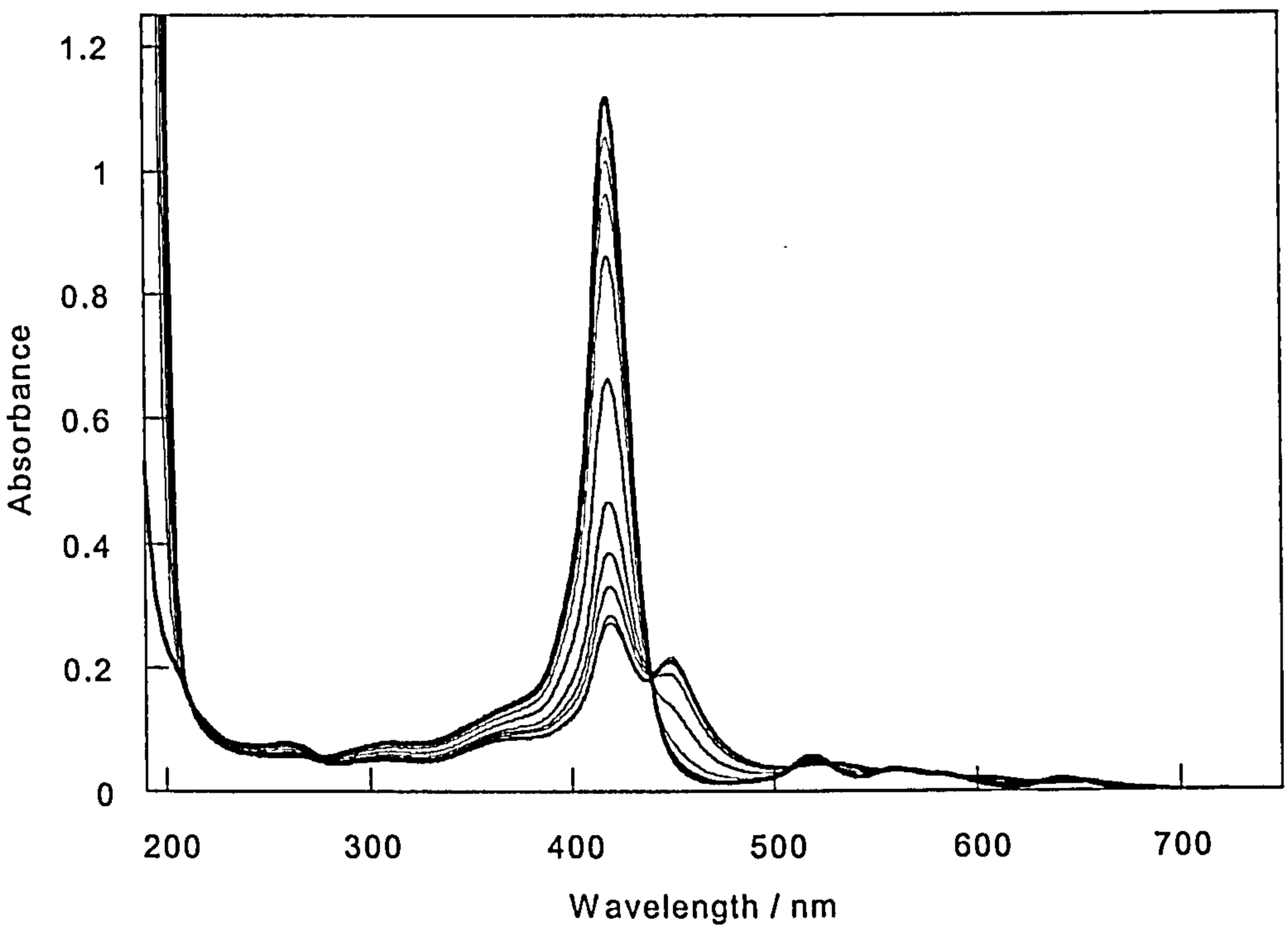

Figure 4.2 Normal absorption spectra of *t*-H_2P (5 μM) in pure water (bold line) and in the presence of NaCl (20 – 200 mM in 20 mM increments). The Soret intensity decreases with increasing NaCl concentration.

In the presence of DNA, the observed normal absorption spectra of the DNA–porphyrin complexes are very dependent on the relative DNA and *t*-H_2P concentrations, the ionic strength of the solution and the sequence composition of the DNA itself. When titrated against NaCl, qualitatively similar normal absorption spectra are obtained for the *t*-H_2P complexes with ct-DNA (Figure 4.3a) and poly[d(G-C)]$_2$ (Figure 4.3b). Both sets of spectra comprise a decreasing Soret intensity (422 nm for ct-DNA; 420 nm for poly[d(G-

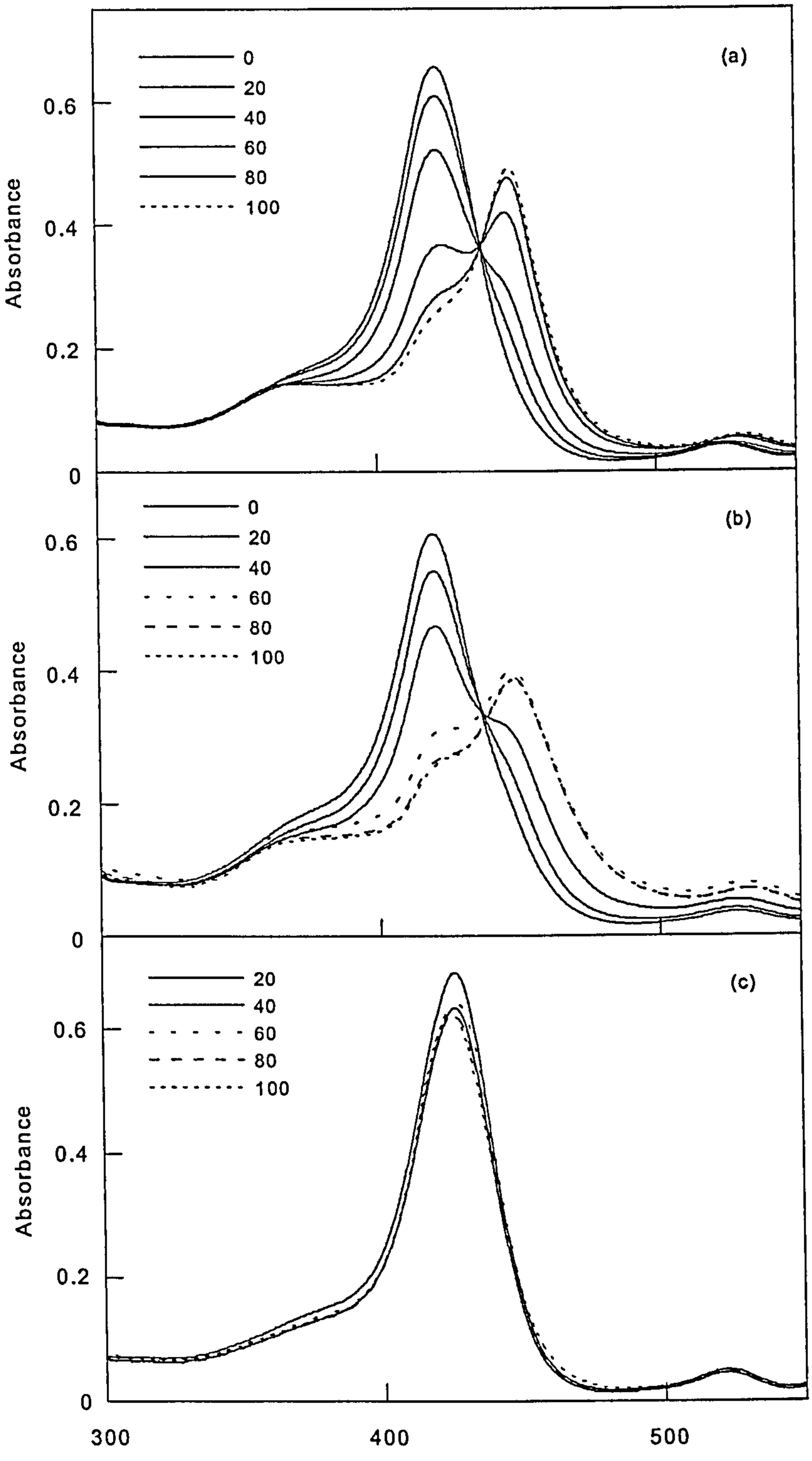

Figure 4.3 Normal absorption spectra of *t*-H_2P (5 μM), phosphate buffer (1 mM; pH 7), NaCl (see legend for mM concentrations) and (a) ct-DNA (40 μM), (b) poly[d(G-C)]$_2$ (40 μM) and (c) poly[d(A-T)]$_2$ (40 μM). Soret intensity decreases as NaCl concentration increases (solid lines).

C)]$_2$) with increasing NaCl concentration, and the gradual appearance of a shoulder (448 nm). At NaCl concentrations above 60 mM, the 448 nm band becomes the dominant feature of the spectra. Conversely, normal absorption spectra of the *t*-H_2P complex with poly[d(A-T)]$_2$, when titrated with salt (Figure 4.3c), exhibit the Soret absorption band (426 nm) only — a longer wavelength shoulder is notably absent. Small blue shifts in the Soret wavelength maximum are also observable at 80 mM (from 426 nm to 425 nm) and 100 mM (from 426 nm to 424 nm) NaCl, relative to the porphyrin spectra with no DNA present (Figure 4.2).

Normal absorption spectra measured as a function of *t*-H_2P concentration in the presence of DNA exhibit an expected progressive increase in intensity of the *t*-H_2P Soret absorption band as the concentration of porphyrin increases. The extent of the increase and the precise Soret band wavelength and shape, however, are dependent on the DNA sequence present and the DNA:porphyrin mixing ratio.

When *t*-H_2P is titrated against a constant concentration of ct-DNA (Figure 4.4a), the Soret maximum appears at 425 nm for 1 μM *t*-H_2P with a gradual blue shift to 421 nm as the concentration of porphyrin is raised to 8 μM. With poly[d(G-C)]$_2$ (Figure 4.4b) a very much smaller wavelength variation is observable in the Soret band (422 nm at 1 μM *t*-H_2P to 420 nm at 8 μM), but a more significant feature of this set of spectra is the presence of a shoulder (at ~ 440 nm) indicating the presence of porphyrin aggregates in this system. Since the aggregate band is absent from the corresponding ct-DNA and poly[d(A-T)]$_2$ (Figure 4.4c) spectra, and aggregation in the absence of DNA is undetectable in the visible spectrum at 20 mM NaCl (Figure 4.2), poly[d(G-C)]$_2$ may be

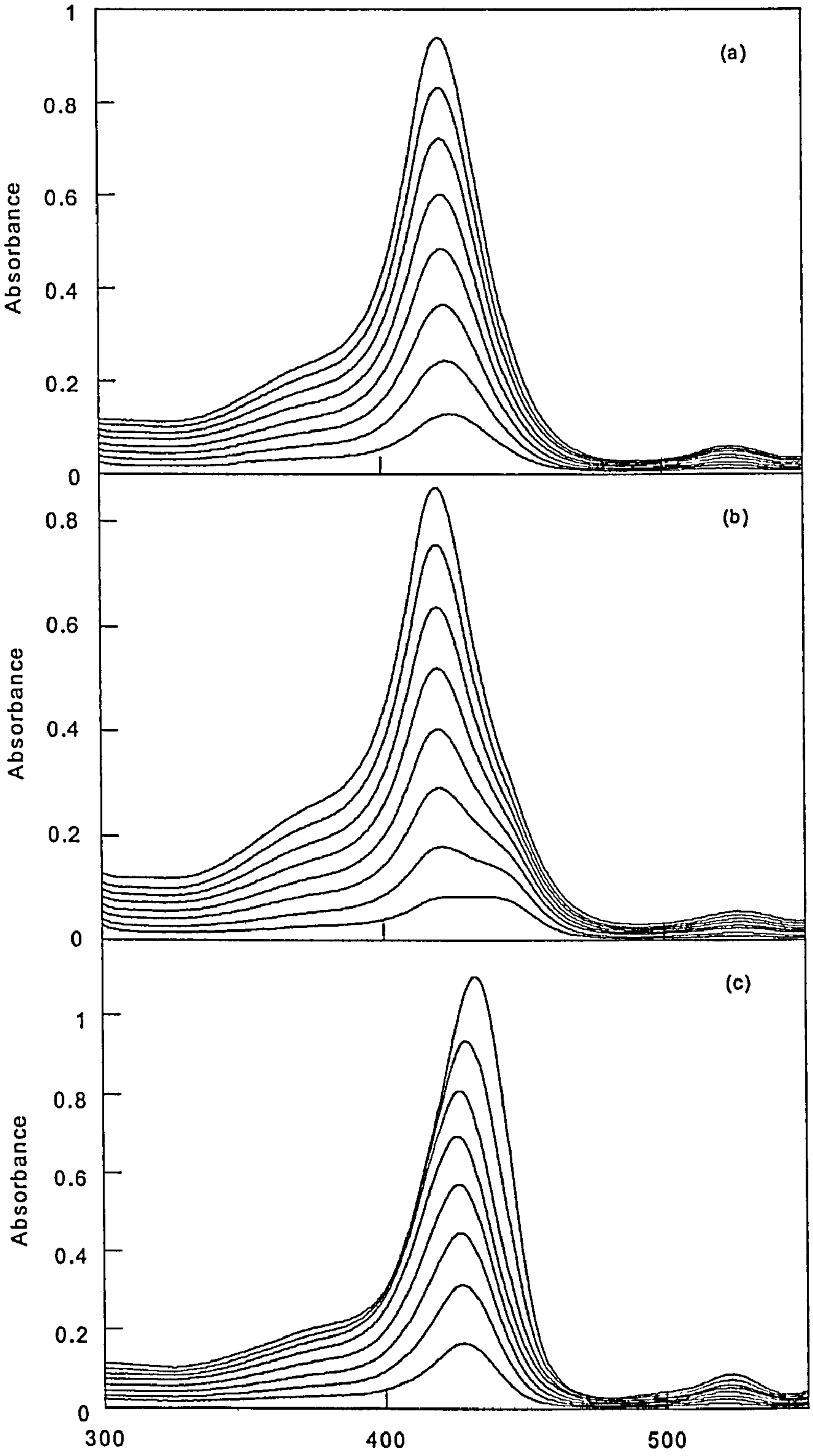

Figure 4.4 Normal absorption spectra of *t*-H_2P (1–8 μM in 1 μM increments; Soret intensity increases with *t*-H_2P concentration), NaCl (20 mM), phosphate buffer (1 mM; pH 7) and (a) ct-DNA (40 μM), (b) poly[d(G-C)]$_2$ (40 μM) and (c) poly[d(A-T)]$_2$ (40 μM).

considered to be promoting aggregate formation with the porphyrins aggregating on the DNA itself.

In the presence of poly[d(A-T)]$_2$, the Soret band wavelength is extremely dependent on the concentration of *t*-H_2P (Figure 4.4c). Large red shifts occur relative to the Soret wavelength of the free porphyrin in solution. At 1 μM *t*-H_2P the Soret appears at 428 nm and progressively shifts to 426 nm as the porphyrin concentration is raised to 5 μM. A shift to 432 nm then occurs over the 6, 7, and 8 μM *t*-H_2P titration steps.

4.3.2 Circular dichroism titrations

CD spectra of the DNA–porphyrin complexes comprise DNA bands at approximately 260 nm and induced porphyrin *CD* in the visible regions of the spectra. The observation of *ICD* at energies that correspond to porphyrin transitions confirms an interaction between the achiral porphyrin and DNA.

With ct-DNA, *t*-H_2P exhibits a small positive *CD* band (434 nm) (Figure 4.5a) when no salt is present. Addition of salt is accompanied by the appearance of a negative band (450 nm), the intensity of which increases as the concentration of salt is raised to 100 mM. Since the experiment was conducted at a constant *t*-H_2P concentration, the change in *CD* intensity could arise from either a change in the amount of porphyrin bound to DNA, or the occurrence of porphyrin–porphyrin interactions on DNA. Increasing the concentration of salt is unlikely to promote porphyrin binding (the *ICD* magnitude increases at higher salt concentrations) thus the increasing *ICD* is due to exciton interactions between bound

porphyrin molecules. Furthermore, the overall shape of the exciton *CD* band is constant implying the stacked binding mode is uniform over the salt concentration range studied. When the concentration of salt reaches 120 mM, the intensity of the 450 nm band decreases to below that corresponding to 100 mM NaCl, an observation consistent with the partial dissociation of porphyrin from the DNA.

In the presence of poly[d(G-C)]$_2$ and no salt, *t*-H_2P exhibits a very weak *CD* signal in the Soret region of the spectrum consisting of both negative (422 nm) and positive (438 nm) bands (Figure 4.5b). At 20 mM NaCl, positive (433 nm) and negative (454 nm) bands are also observed but combine to give a *CD* signature quite different in shape from that observed in the absence of salt. At higher salt concentrations (> 20 mM) the magnitude of the Soret *ICD* becomes extremely large (+330 mdeg at 432 nm; −600 at 456 nm for 40 mM NaCl). The observed form of the *ICD* spectrum, a positive (432 nm) and negative (456 nm) *ICD* both within the Soret band of the chromophore, and the enhanced magnitude of the signal are consistent with the exciton type *CD* associated with interactions between chromophores. The sudden appearance of the enhanced magnitude *ICD* signals between the 20 and 40 mM NaCl titration steps is suggestive of a highly cooperative porphyrin aggregation mechanism. Furthermore, the absence of further increases in *ICD* intensity beyond 60 mM NaCl, although partially due to porphyrin dissociation from the DNA at higher salt concentrations, is attributable to the bulk of the porphyrin being present in the aggregated form at this salt concentration. Thus no further increase in the state of porphyrin aggregation is possible.

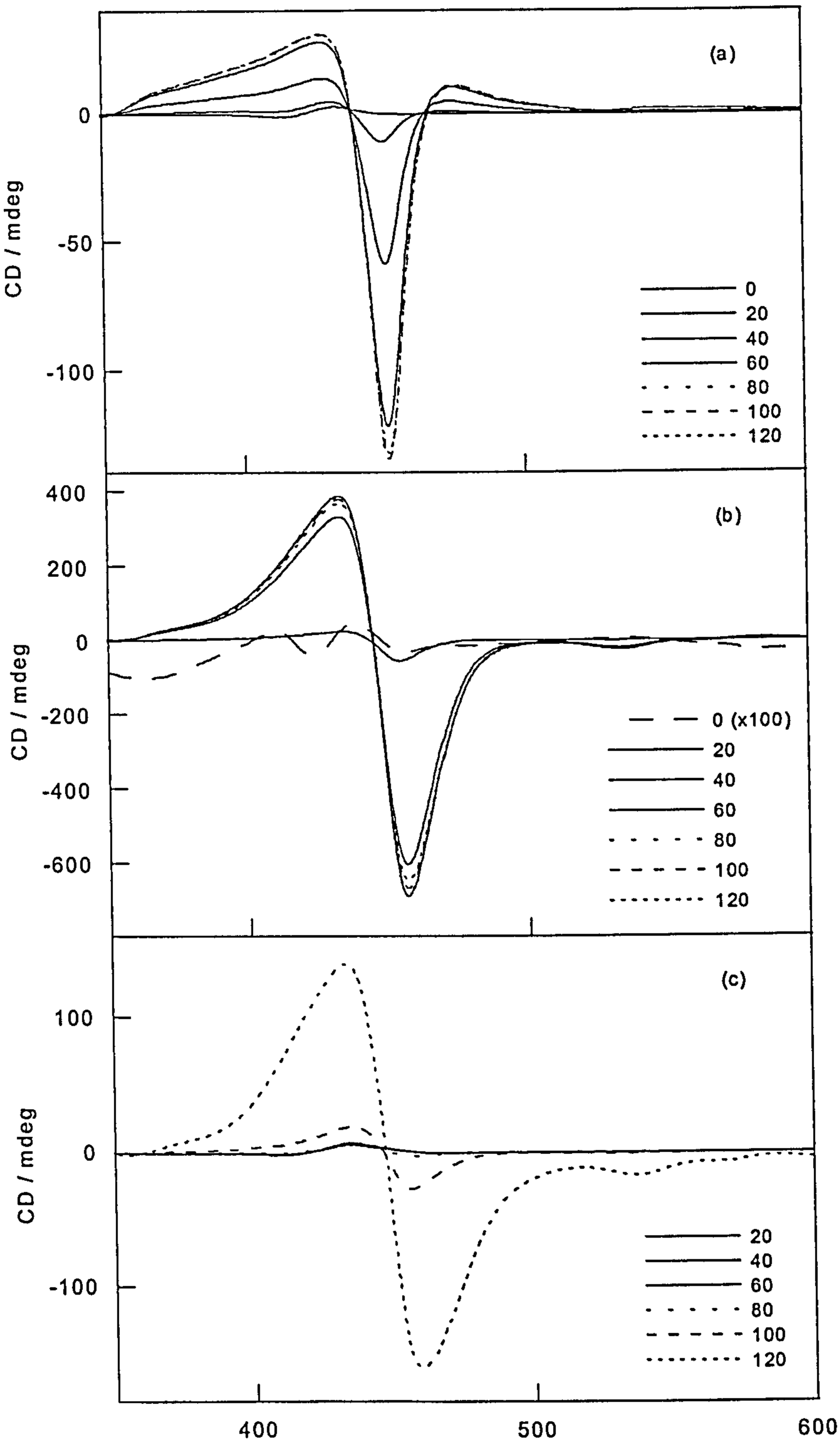

Figure 4.5 *CD* spectra of *t*-H_2P (5 μM), phosphate buffer (1 mM; pH 7), NaCl (see legend for mM concentrations) and (a) ct-DNA (40 μM), (b) poly[d(G-C)]$_2$ (40 μM) and (c) poly[d(A-T)]$_2$ (40 μM). *CD* intensity increases as NaCl concentration increases (solid lines).

When a poly[d(A-T)]$_2$ complex with *t*-H_2P (Figure 4.5c) is exposed to incrementally increasing concentrations of salt, a small positive band at 434 nm is observed between 20 and 60 mM NaCl. The shape and intensity of the *CD* band is constant thus a uniform binding regime is operative under the aforementioned conditions of salt concentration. A small negative band (456 nm) appears at 80 mM NaCl and at higher salt concentrations exciton *CD* is observed indicating the occurrence of porphyrin–porphyrin interactions on poly[d(A-T)]$_2$.

When the concentration of *t*-H_2P is varied in the presence of ct-DNA (Figure 4.7a), a *CD* signature consisting of two negative bands (413 nm; 457 nm) either side of a more intense positive band (433 nm) is observed in the Soret spectral region, except at a *t*-H_2P concentration of 1 μM where there is no negative *CD*. The intensity of the bands increases with *t*-H_2P concentration, an observation to be expected since the *ICD* intensity is dependent on the quantity of bound ligand. Moreover, a disproportionate increase in the magnitude of the *ICD* occurs as the porphyrin concentration is raised (Figure 4.6) suggesting the existence of porphyrin–porphyrin interactions, especially at the higher *t*-H_2P concentrations. Significantly, however, the shape of the *CD* signature is constant between 2 and 8 μM porphyrin concentration indicating a constant binding mode under these conditions.

With poly[d(G-C)]$_2$, *t*-H_2P exhibits a *CD* signature comprising positive (433 nm) and negative (452 nm) bands in the Soret region of the spectrum (Figure 4.7b). The increase in *ICD* intensity is disproportionately high for each incremental *t*-H_2P concentration increase (Figure 4.6) and the shape of the *CD* intensity versus *t*-H_2P concentration is

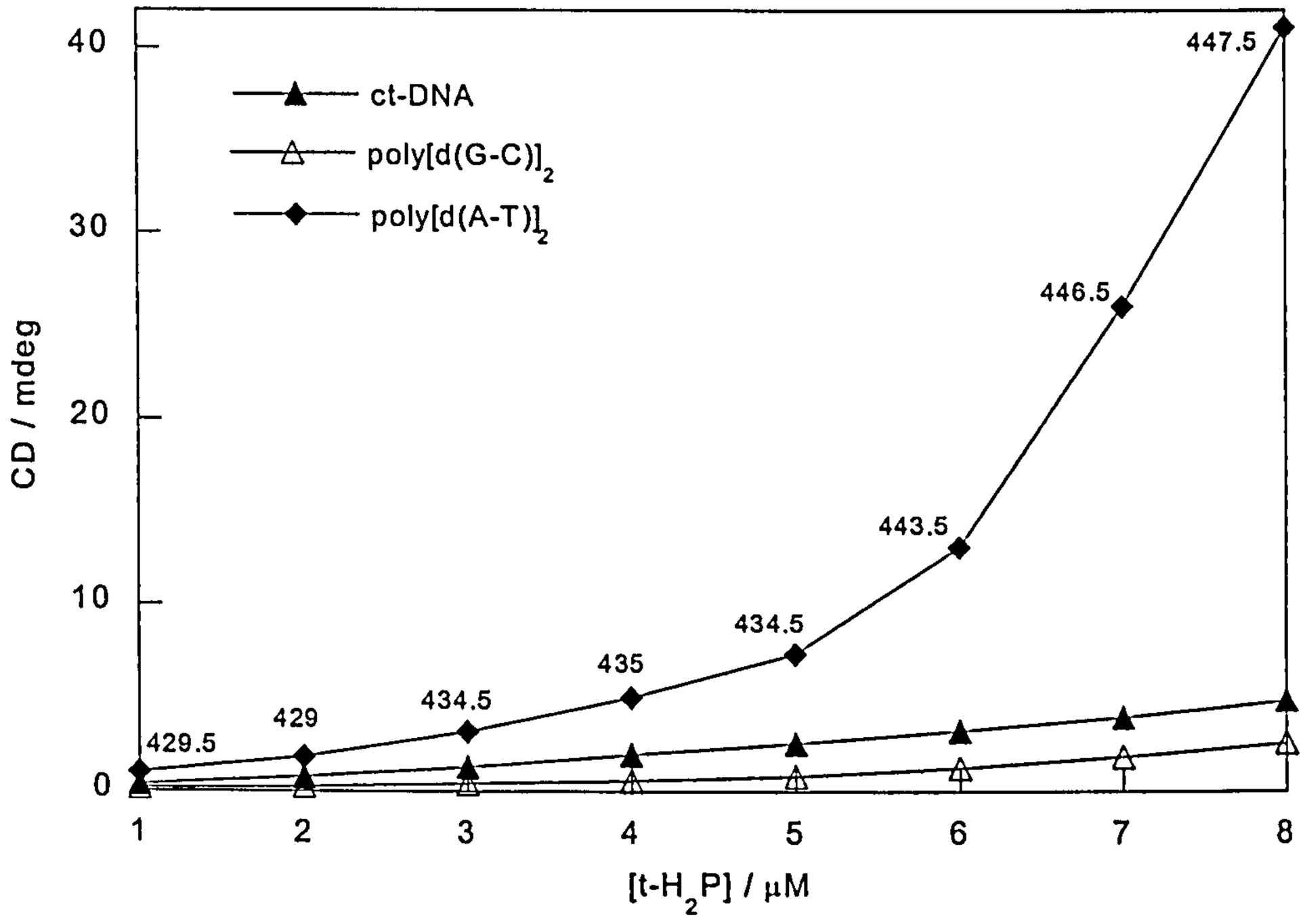

Figure 4.6 Variation in *CD* intensity with *t*-H_2P concentration for ct-DNA (433 nm), poly[d(G-C)]$_2$ (433 nm) and poly[d(A-T)]$_2$ (the wavelengths shown on the figure correspond to maximum *ICD* values).

consistent with the occurrence of porphyrin–porphyrin interactions on the DNA. The shape of the observed *CD* spectrum is thus due to exciton interactions between adjacently bound porphyrins.

In the presence of poly[d(A-T)]$_2$, incrementally increasing the concentration of *t*-H_2P generates complex *CD* spectra. In addition to the Soret band wavelengths (Figure 4.7c), the DNA region of the spectrum also yields *t*-H_2P concentration dependent *CD* (Figure 4.7d). With both ct-DNA and poly[d(G-C)]$_2$, the DNA region of the spectrum remains constant across the *t*-H_2P concentration range studied and indicates the absence of significant DNA structural changes. With poly[d(A-T)]$_2$ the *CD* signature in the DNA region of the spectrum is characteristic of B-DNA at low porphyrin concentrations, with a negative (247 nm) and positive (263 nm) band. As the porphyrin concentration is

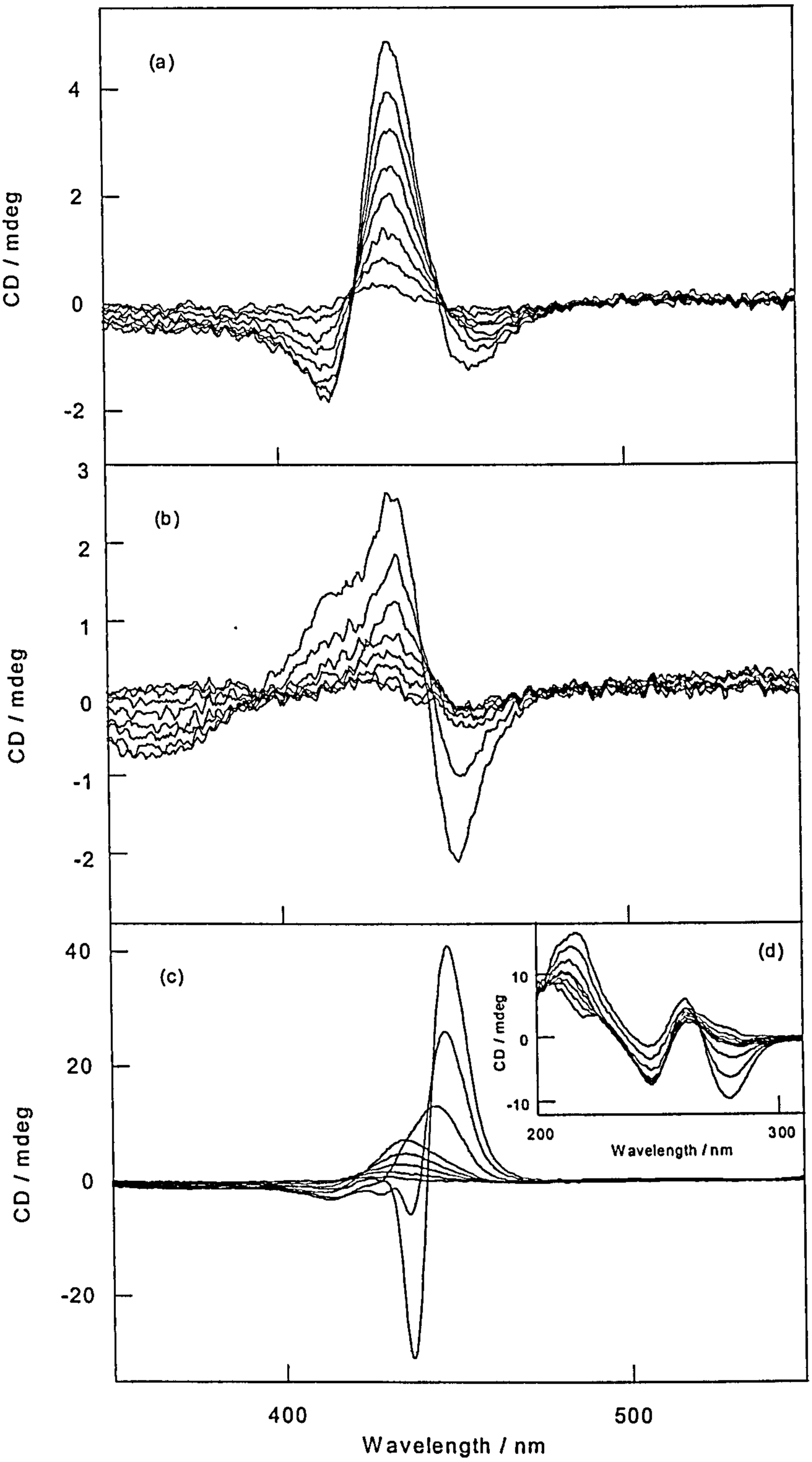

Figure 4.7 *CD* spectra of *t*-H_2P (1–8 μM in 1 μM increments; Soret intensity increases with *t*-H_2P concentration), NaCl (20 mM), phosphate buffer (1 mM; pH 7) and (a) ct-DNA (40 μM), (b) poly[d(G-C)]$_2$ (40 μM), (c) and (d) poly[d(A-T)]$_2$ (40 μM).

increased an additional negative band appears at 280 nm and is accompanied by a decrease in the intensity of the 247 nm band. Although the porphyrin does absorb in the UV region of the spectrum, the absorption is weak and 280 nm does not correspond to a specific maximum in the *t*-H_2P normal absorption spectrum. The observed changes in the DNA region of the *CD* spectrum are therefore likely to be the result of a DNA structural change induced by porphyrin binding. In the Soret region of the spectrum a small positive *ICD* (429 nm) is initially observed at 1 μM *t*-H_2P. As the porphyrin concentration is increased a red shift in the *ICD* is observed as is the gradual appearance of a negative *ICD* at 414 nm. At 7 and 8 μM *t*-H_2P the *CD* spectrum is strongly excitonic in character. The occurrence of porphyrin–porphyrin interactions is further supported by the shape of the *CD* intensity versus *t*-H_2P concentration plot for this system (Figure 4.6) which illustrates the disproportionately large *CD* increase with increasing porphyrin concentration.

4.3.3 Resonance light scattering titrations

When no DNA is present, *t*-H_2P exhibits *RLS* (455 nm) within the absorption envelope of the aggregated porphyrin species (Figure 4.8).[20] The intensity of the signal is dependent on the concentration of salt present. As the concentration of NaCl is raised the strength of the *RLS* signal also increases.

The observed *RLS* signal and its ionic strength dependence indicates several characteristics of *t*-H_2P aggregation in solution. *RLS* is sensitive to aggregate size and concentration such that larger aggregates produce more intense *RLS* signals. Furthermore, *RLS* only occurs for aggregated systems composed of arrays of extended chromophores.

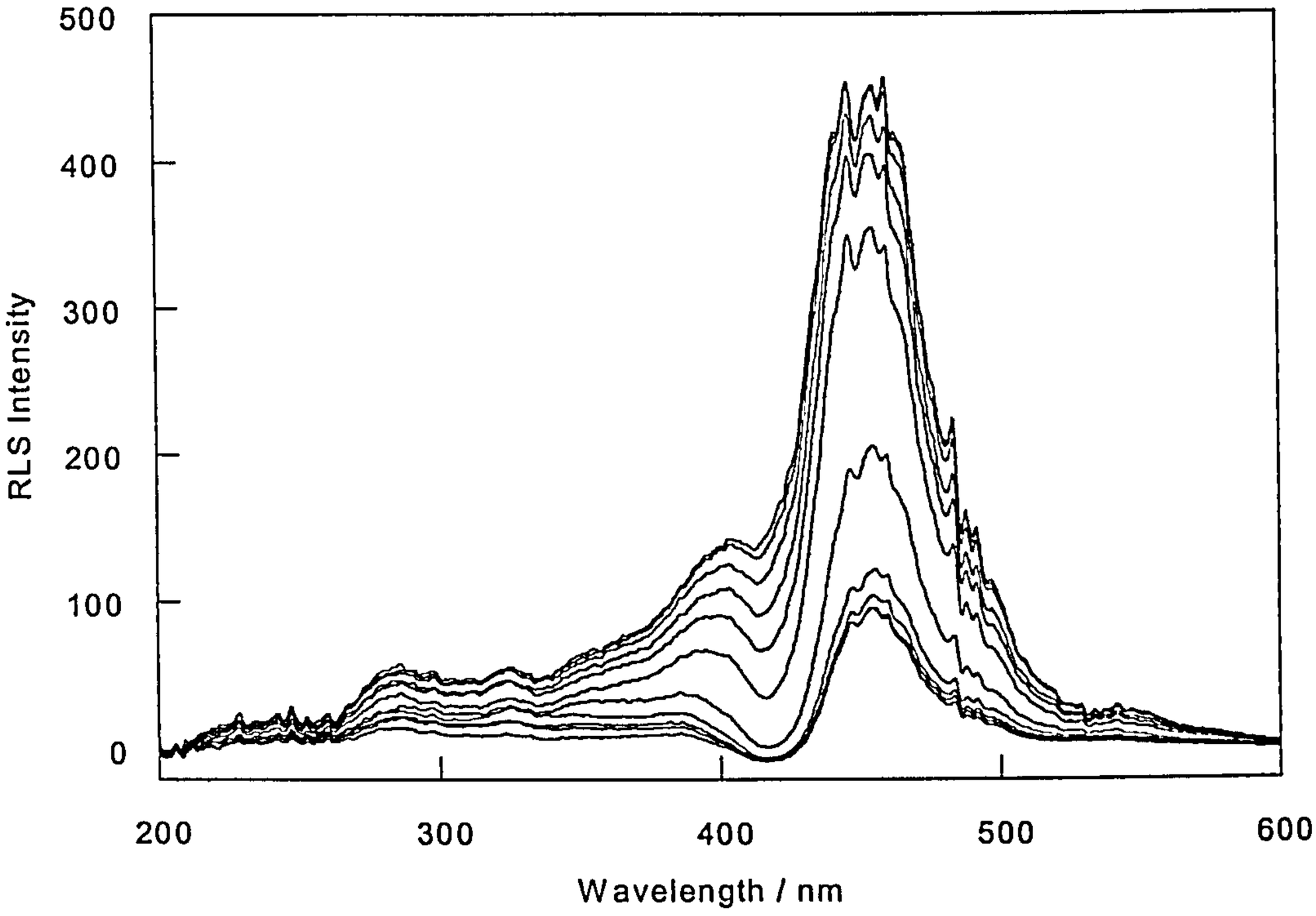

Figure 4.8 *RLS* spectra of *t*-H_2P (5 μM) in the presence of NaCl (0 – 200 mM in 20 mM increments). The *RLS* intensity increases with NaCl concentration.

The enhancement in the *t*-H_2P *RLS* observed with increasing NaCl concentration suggests not only the formation of extended *t*-H_2P aggregates but also that high ionic strengths promote the formation of larger aggregates rather than an increase in the number of aggregates present. The non-linear increase in the *RLS* magnitude with salt concentration (Figure 4.9) suggests porphyrin *t*-H_2P aggregation is a highly cooperative process. The shape of the *RLS* intensity versus NaCl concentration curve also correlates with the decrease in porphyrin monomer absorbance with increasing salt concentration (Figure 4.9), an observation consistent with the removal of porphyrin monomers from solution as aggregation occurs. The limiting factor in aggregate formation under these conditions would appear to the concentration of porphyrin present, since the change in aggregate size, as indicated by the *RLS* signal, with salt concentration starts to level off at NaCl concentrations in excess of a 100 mM.

When *t*-H_2P is titrated against NaCl in the presence of ct-DNA (Figure 4.10a), salt concentration dependent *RLS* is observed (455 nm). The *RLS* wavelength for this system matches that of *t*-H_2P in the absence of DNA (a small wavelength shift in the *RLS* maximum might reasonably have been expected if the aggregated porphyrin was interacting with the DNA). Where the ct-DNA *RLS* spectrum differs significantly from that of the free porphyrin is in the intensity of the signals. The *RLS* intensity at 455 nm of the 40 mM NaCl spectrum in the presence of ct-DNA is greater than that observed for 200 mM NaCl with no DNA present. Despite the lack of a wavelength shift, therefore, ct-DNA promotes *t*-H_2P aggregation and the corresponding *RLS* signal arises from DNA bound porphyrin arrays that are significantly more extended than in solution alone.

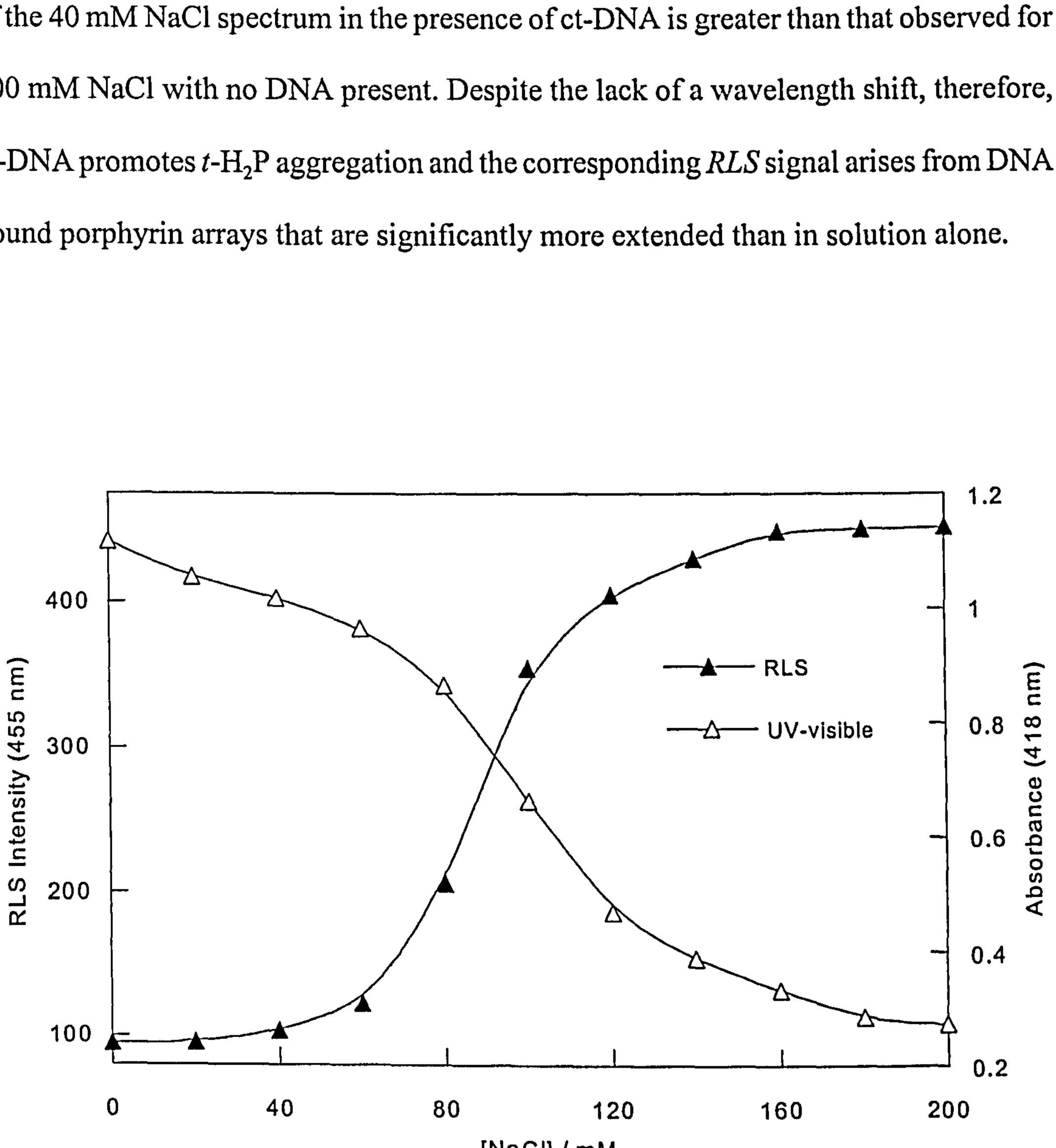

Figure 4.9 Variation in *RLS* intensity (455 nm) and normal absorbance (418 nm) of *t*-H_2P (5 μM) with NaCl concentration.

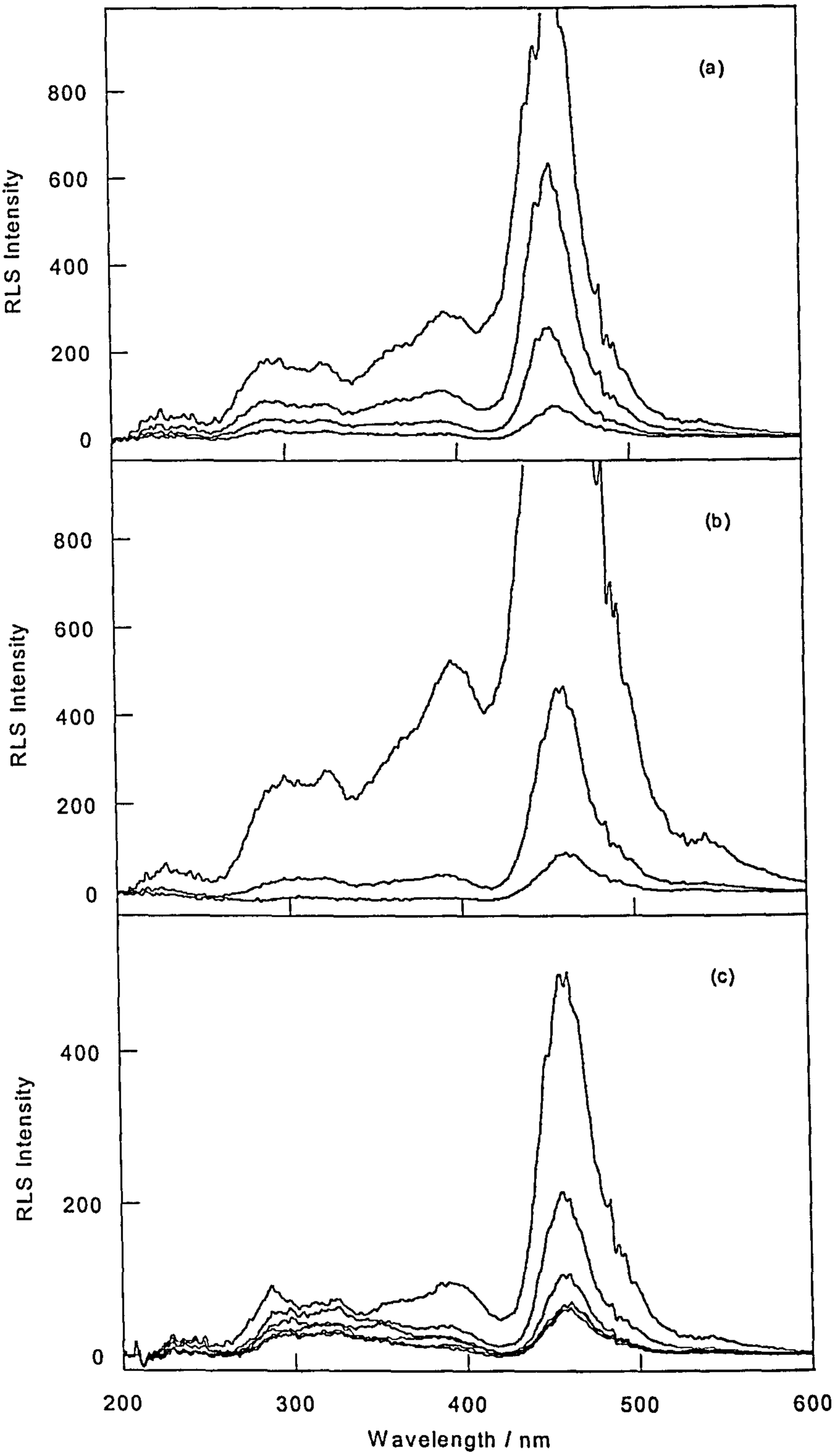

Figure 4.10 *RLS* spectra of *t*-H_2P (5 μM), phosphate buffer (1 mM; pH 7) and (a) ct-DNA (40 μM) and 0 – 60 mM NaCl (b) poly[d(G-C)]$_2$ (40 μM) and 0 – 40 mM NaCl and (c) poly[d(A-T)]$_2$ (40 μM) and 20 – 120 mM NaCl. *RLS* intensity increases as NaCl concentration increases.

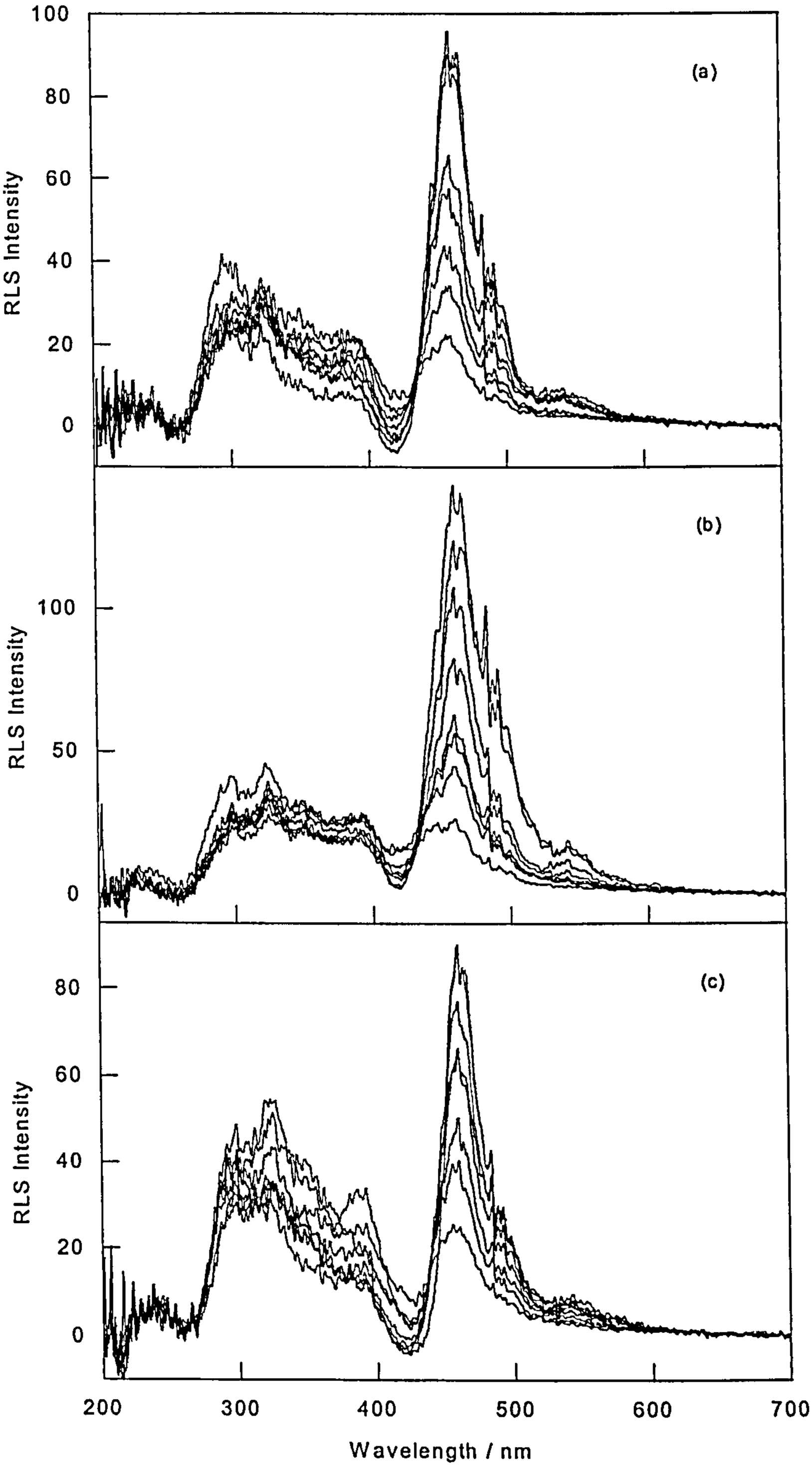

Figure 4.11 *RLS* spectra of *t*-H_2P (1–8 μM in 1 μM increments; *RLS* intensity increases with *t*-H_2P concentration), NaCl (20 mM), phosphate buffer (1 mM; pH 7) and (a) ct-DNA (40 μM), (b) poly[d(G-C)]$_2$ (40 μM), (c) poly[d(A-T)]$_2$ (40 μM).

With poly[d(G-C)]$_2$, extremely large *RLS* signals are observed (459 nm) even at low salt concentrations (Figure 4.10b). At a salt concentration of 20 mM NaCl with poly[d(G-C)]$_2$ the magnitude of the *RLS* is roughly equivalent to that at 200 mM NaCl in the absence of DNA. Thus the formation of extended *t*-H_2P aggregates in the presence of poly[d(G-C)]$_2$ is strongly favoured even at low ionic strengths. At 40 mM NaCl the *RLS* intensity exceeds the upper detection limit of the instrument.

RLS spectra of poly[d(A-T)]$_2$ and *t*-H_2P when titrated with salt remain constant over the 20 – 60 mM NaCl concentration range (Figure 4.10b). The *RLS* maximum appears at 457 nm but the intensity is weak compared to that observed for poly[d(G-C)]$_2$ and characteristic of a very low aggregate concentration or the presence of small aggregates. The *RLS* intensity then increases to an intensity indicative of extended aggregate formation at salt concentrations in excess of 60 mM NaCl. The lack of a significant *RLS* signal at low to medium ionic strengths suggests that *t*-H_2P is binding to the DNA as monomers and this monomer binding is sufficiently strong to disfavour subsequent *t*-H_2P aggregation. Furthermore, since *RLS* is sensitive to aggregation regardless of whether the aggregating species is bound to DNA, a high proportion of the porphyrin must be bound to poly[d(A-T)]$_2$ as any free ligand would aggregate in solution and lead to an observable *RLS* (Figure 4.8). The aggregated *t*-H_2P evident at higher ionic strengths is probably also predominantly bound to poly[d(A-T)]$_2$ as the *RLS* wavelength maximum is slightly shifted from that observed for *t*-H_2P aggregation in solution alone.

When the concentration of porphyrin is varied in the presence of ct-DNA at low NaCl concentration, the effect on the extent of aggregation of the system is small. Although

light scattering is detected (459 nm), its intensity is very weak (Figure 4.11a). The magnitude of the signal does increase slightly with *t*-H_2P concentration but not to a size comparable with that observed for the high salt concentration DNA–porphyrin complexes where extended aggregates are present. Similar effects are also observed in the presence of poly[d(G-C)]$_2$ (Figure 4.11b) and poly[d(A-T)]$_2$ (Figure 4.11c) where a weak *t*-H_2P concentration dependent light scattering appears at 461 nm and 460 nm respectively. With all three DNAs, the lack of an enhanced *RLS* indicates the non-formation of extended porphyrin aggregates. Any porphyrin stacking that occurs on the DNAs under these conditions therefore does so as dimers or small oligomers.

4.3.4 Film linear dichroism

In stretched PVA film the *t*-H_2P electronic transitions appear red shifted relative to the corresponding solution spectrum. The Soret band appears at 428 nm in the film spectrum (Figure 4.13a), 10 nm lower in energy than for the solution Soret. Similar red shifts are observed in the visible region of the spectrum. The *t*-H_2P film *LD* spectrum (Figure 4.13a) is predominantly positive in sign with just two weakly negative contributions at 265 nm and 646 nm. The Soret transition appears as an intense positive *LD* band centred at 427 nm. The fact that the observed *LD* is non-zero requires that the porphyrin is oriented in the film. The porphyrin was assumed to be uniaxially oriented along the long axis of the molecule (Figure 4.12). Previous stretched polymer film *LD* studies of porphyrins suggests that such an assumption is reasonable.[59,61] The film *LD* data were then interpreted in terms of a model for uniaxially oriented rod-like molecules, as described in section 3.3.1, to permit the determination of polarised absorbance spectra

and average transition polarisations. Polarised absorbance spectra were calculated with the TEM method (section 3.3.1) using a method analogous to that described in Appendix 2 for 9-OHE.

For an isolated transition of pure polarisation the LD^r is expected to be independent of wavelength across the absorption band. Variations in the LD^r magnitude across an absorption band arise from the presence of transitions with mixed polarisation or overlapping transitions with different polarisations. The symmetry of *t*-H_2P is strictly only C_s. Thus although well defined polarisation is expected for each in-plane transition, there are no symmetry based restrictions on allowed polarisations. The sloping LD^r across the *t*-H_2P Soret (Figure 4.13a) band region suggests the presence of transitions with mixed or overlapping polarisations.[7]

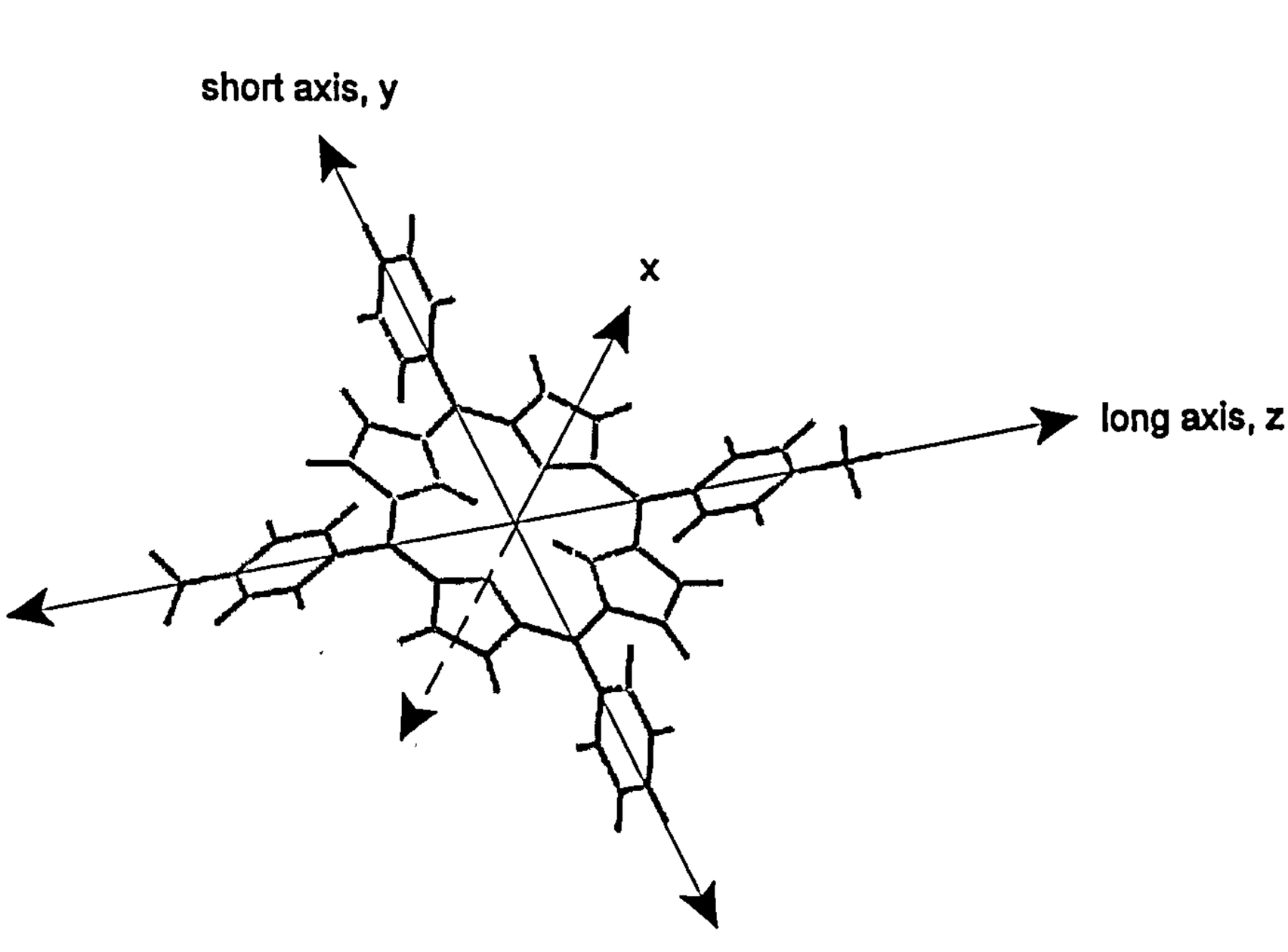

Figure 4.12 Definition of molecular axis system for *t*-H_2P. The long axis (*z*) intersects the two C_{meso}–*N*-methylpyridiniumyl bonds. The long and short axes lie in the plane of the porphyrin. Since the rod-like porphyrin is uniaxially oriented in the film, the *x* and *y* axes are effectively degenerate.

The positive LD^r over the Soret indicates the greater long axis character of this transition, a characteristic common to the majority of the *t*-H_2P electronic spectrum. The negative LD^r values observed at 265 nm and 646 nm denote the predominant short axis character of these transitions. Although the *z* component of the Soret absorption is the stronger, this transition also contains significant *y* axis character as evidenced by the calculated polarised absorption spectra (Figure 4.13b). These data also show the UV spectrum below 284 nm to be short axis polarised. The effective polarisation of the Soret transitionwas calculated to be 38 – 46° to the *t*-H_2P long axis although this figure represents the average polarisation of a number of transitions. Average or effective transition polarisations were also assigned for the UV and visible transitions of the *t*-H_2P electronic spectrum (Table 4.2; Figure 4.13c).

Wavelength / nm	α / deg
652	56
593 – 596	40 – 41
561	55
521	41
427 – 428	39
370 – 380	40 – 42
265	56

Table 4.2 Transition polarisation assignments for the electronic spectrum of *t*-H_2P from film *LD* data.

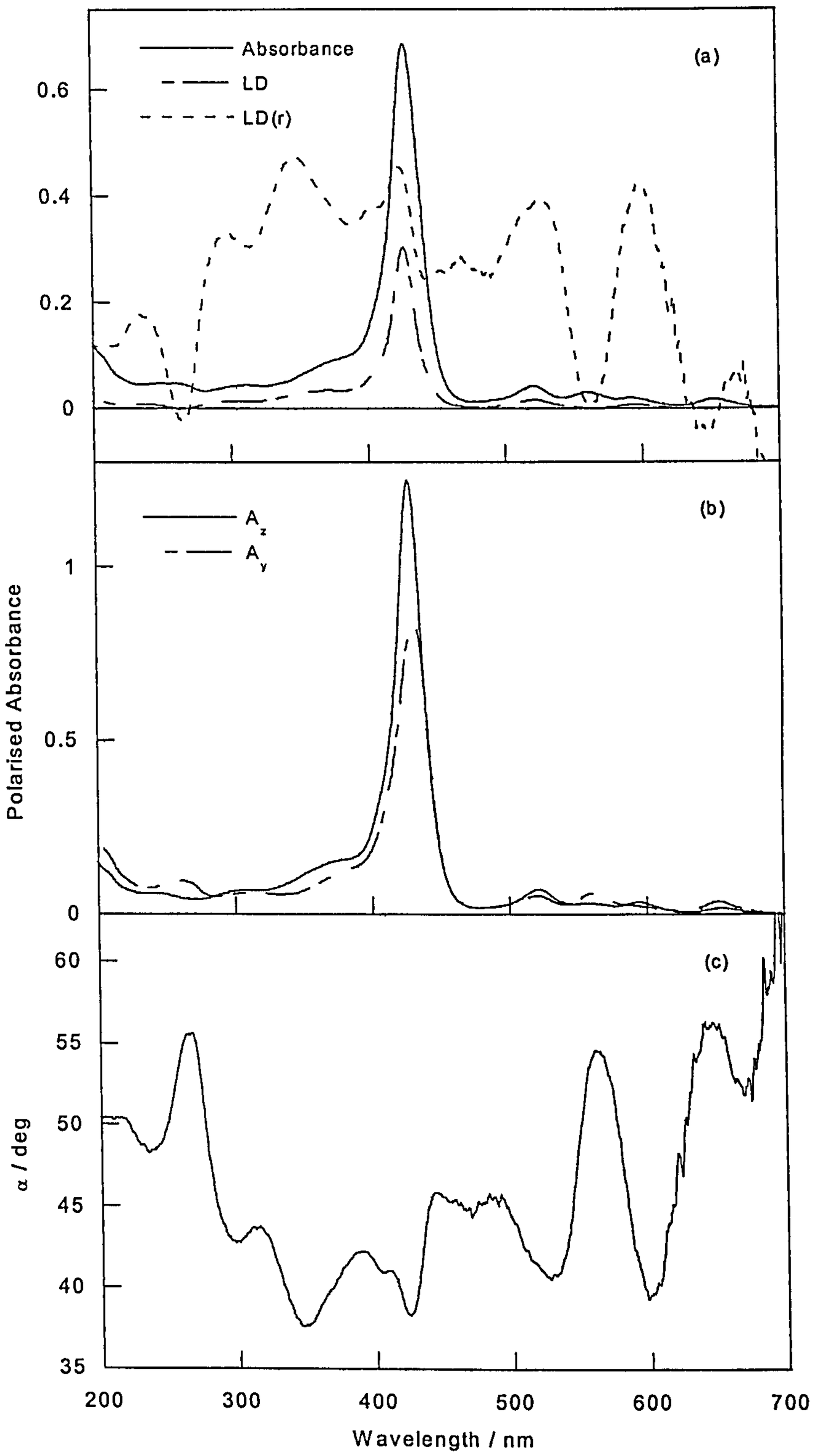

Figure 4.13 (a) Normal absorption, *LD* and *LD*^{r} spectra of *t*-H_2P oriented in PVA stretched (x2) film, (b) polarised absorbance spectra of *t*-H_2P calculated from PVA stretched film spectra (orientation parameters used were $S_{zz} = 0.36$ and $S_{yy} = -0.18$) and (c) calculated *t*-H_2P electronic transition polarisations.

4.3.5 Flow linear dichroism

Flow *LD* spectra of the DNA–porphyrin complexes consist of *t*-H_2P bands in the Soret region of the spectrum and a DNA band in the UV region at about 260 nm which overlaps with a weak porphyrin UV absorbance. The fact that *t*-H_2P *LD* is observed requires that the porphyrin is bound to DNA since unbound ligand does not orient in the solution flow. The degree of orientation achieved in the experiments was dependent on

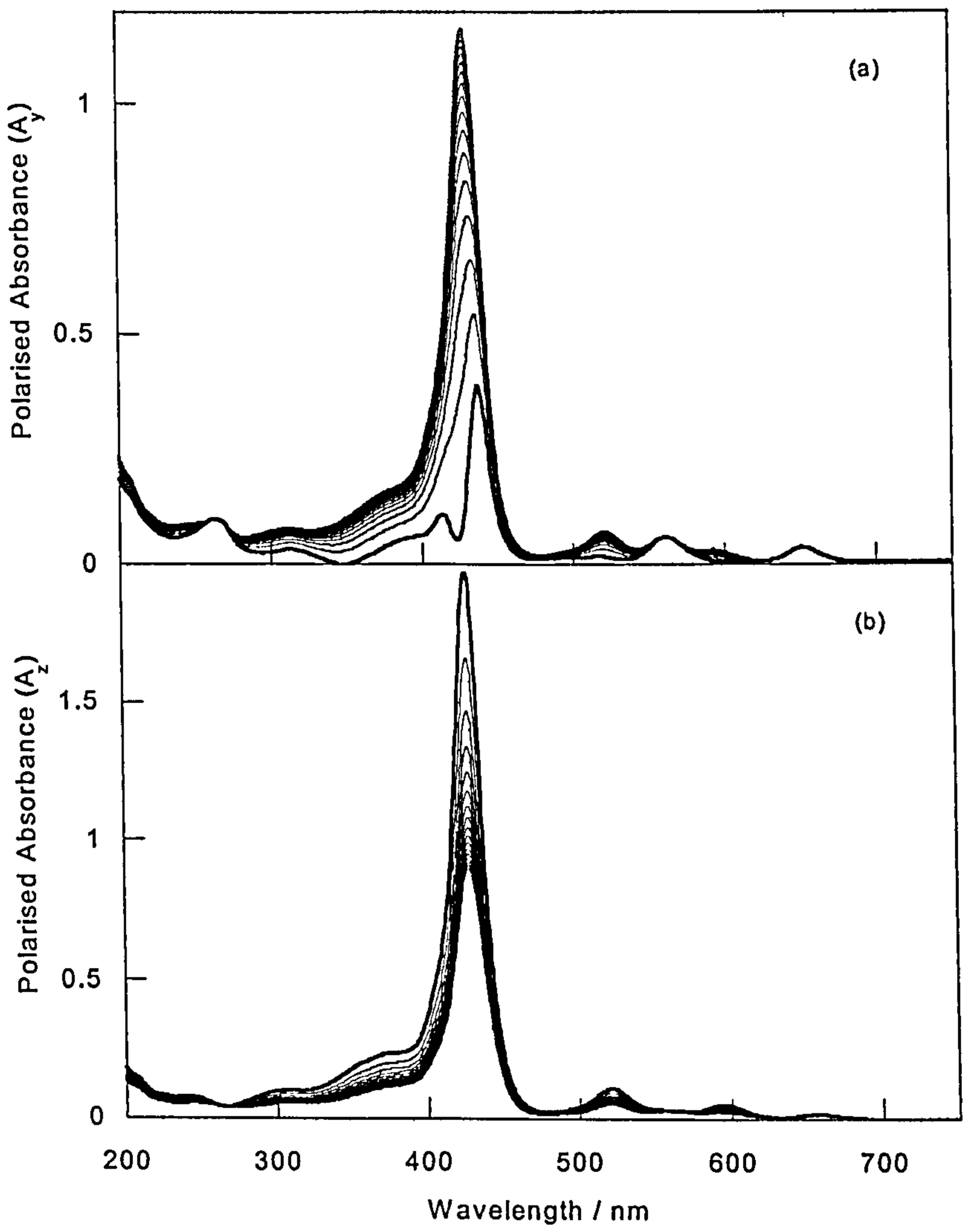

Figure 4.14 Polarised absorbance spectra resulting from TEM calculations on stretched film *LD* data for *t*-H_2P. Each spectrum corresponds to an adjustment of (a) −0.025 in S_{yy} from an initial value of −0.079 (thick line) and (b) 0.05 in S_{zz} from an initial value of 0.16 (thick line).

the length of the specific DNA. Significantly more efficient orientation was generally achieved for the longer, naturally occurring ct-DNA than for the shorter synthetic sequences poly[d(A-T)]$_2$ and poly[d(G-C)]$_2$.

When a complex of ct-DNA and *t*-H_2P is exposed to progressively increasing salt concentrations a change in both the DNA and Soret regions of the spectra are observed (Figure 4.15a). When no salt is present a single positive *LD* band (417 nm) is apparent. When the NaCl concentration is adjusted to 20 mM, the magnitude of the 417 nm band diminishes and a negative band (440 nm) appears. At higher salt concentrations a positive band (453 nm at 40 mM NaCl; 450 nm at > 40 mM NaCl) dominates the spectra. The 60, 80 and 100 mM NaCl *LD* spectra are also characterised by the appearance of a negative *LD* band at 359 nm. In the UV region of the spectrum, the negative *LD* (259 nm) of the DNA bases is observed. Raising the salt concentration reduces intensity of the 259 nm band.

LD indicates the orientation of electronic transition moments thus the observation of positive *LD* in the Soret region of the spectrum precludes an intercalative binding mode as the in-plane porphyrin transitions are aligned more perpendicular than parallel to those of the DNA bases. Furthermore, the change in intensity of the Soret bands in the *LD* spectra indicate a change in porphyrin binding geometry with each addition of salt. The wavelength of the Soret band with no salt present corresponds to the porphyrin monomer absorption wavelength and is quite different in terms of intensity and energy from that observed in the presence of salt. The monomer and aggregated porphyrin binding geometries are therefore dissimilar.

Quantitative data pertaining to the DNA–porphyrin binding geometry may be obtained from the LD^r, calculated according to equation 3.4. The Soret *LD* maxima of the ct-DNA complex with *t*-H_2P are slightly red shifted relative to the corresponding normal absorption peaks thus the corresponding LD^r (Figure 4.16a) is not flat across the Soret absorption band. In the case of a flow oriented DNA–ligand systems, the presence of unbound ligand may also contribute to LD^r variations within an absorption band since the unbound ligand contributes to the absorption spectrum and not the *LD*. For the ct-DNA complex with *t*-H_2P the LD^r spectrum is approximately flat across the DNA band at 258 nm. The LD^r magnitude is significantly larger for ct-DNA alone denoting a higher degree of orientation than when *t*-H_2P is present. Conversely, the LD^r is not constant across the porphyrin absorption band in the Soret region. The average angle between the Soret transition moments and the helix axis may be calculated from the LD^r spectrum, taking $\alpha = 86°$ for the DNA base transition moments,[15] according to equation 3.12 and using the procedure described in section 3.3.2. The results of these calculations for ct-DNA are shown in Table 4.3.

[NaCl] / mM	Orientation factor, *S*	Wavelength / nm	α / deg
0	0.0050	418 – 422	42 – 44
20	0.0037	440 – 443 413 – 422	61 – 62 51 – 53
40	0.0035	445 – 453 411 – 422	37 – 51 51 – 54
60	0.0042	358 – 366	57 – 58
80	0.0042	359 – 366	62 – 65
100	0.0040	359 – 366	64 – 67

Table 4.3 Calculated binding angles between the plane of the ct-DNA bases and *t*-H_2P transition moments.

The average Soret transition moment makes an angle of 42 – 44°(Table 4.3) with the DNA helix axis when no salt is present. This transition is in-plane polarised at 38 – 46° to the *t*-H_2P long axis. The calculated binding angle is thus consistent with groove binding and in any case preclusive of intercalation involving a co-planar alignment of the porphyrin ring with the plane of the DNA bases. At 20 and 40 mM NaCl the *z* and *y* polarised absorbing transition moments are on average oriented differently. There is also a slight difference in energy between the A_z and A_y Soret maxima (Figure 4.13b). Two angles were thus calculated for the Soret transitions of the porphyrin in the 20 and 40 mM NaCl binding modes since the two transition moments appear to be oriented differently. These angles are also consistent with groove binding although the plane of the porphyrin does not follow the pitch of the minor groove. Binding angles were also calculated for the ~360 nm *t*-H_2P transitions of the stacked binding modes (60 to 100 mM NaCl) and require that this transition, polarised at an average of 40 – 42° to the *t*-H_2P long axis, is oriented increasingly parallel to the bases as the extent of stacking increases.

When bound to poly[d(G-C)]$_2$ with no salt present (*t*-H_2P is not aggregated), *t*-H_2P exhibits both positive (414 nm) and negative (444 nm) *LD* in the Soret region of the spectrum (Figure 4.15b). Moreover, the negative DNA *LD* (258 nm) is almost comparable in terms of intensity to that corresponding to DNA alone. The observation of an *LD* band with both positive and negative elements in the Soret region of the spectrum is a consequence of the presence of two average transition moments with similar energies and oscillator strengths but different polarisations (Figure 4.13b) in the *t*-H_2P Soret that have very different alignments relative to the helix axis when bound to DNA. When NaCl is added a single positive band (456 nm at 20 mM NaCl; 459 nm at

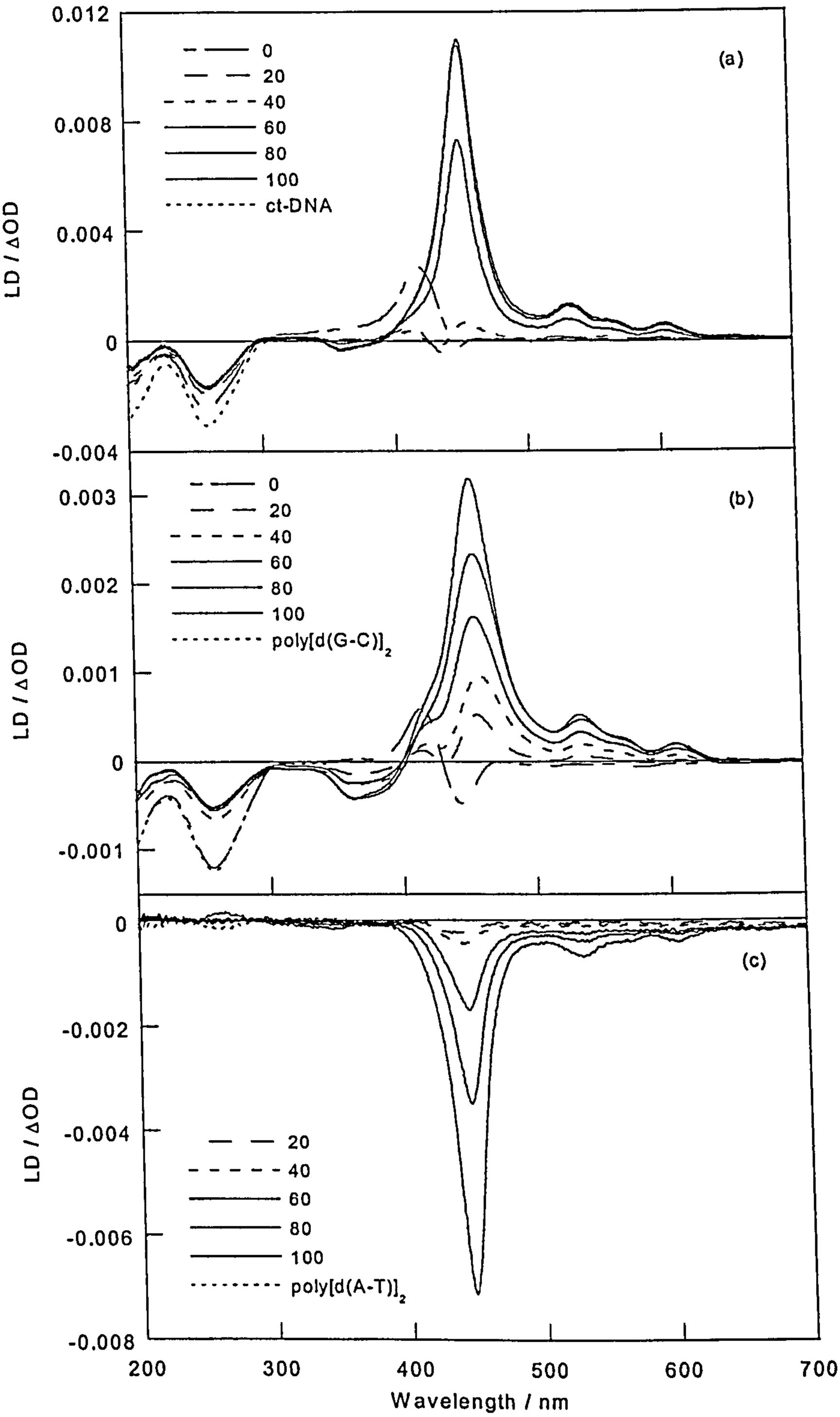

Figure 4.15 *LD* spectra of *t*-H_2P (5 μM), phosphate buffer (1 mM; pH 7), NaCl (see legend for mM concentrations) and (a) ct-DNA (40 μM), (b) poly[d(G-C)]$_2$ (40 μM) and (c) poly[d(A-T)]$_2$ (40 μM). Soret intensity increases as NaCl concentration increases (solid lines).

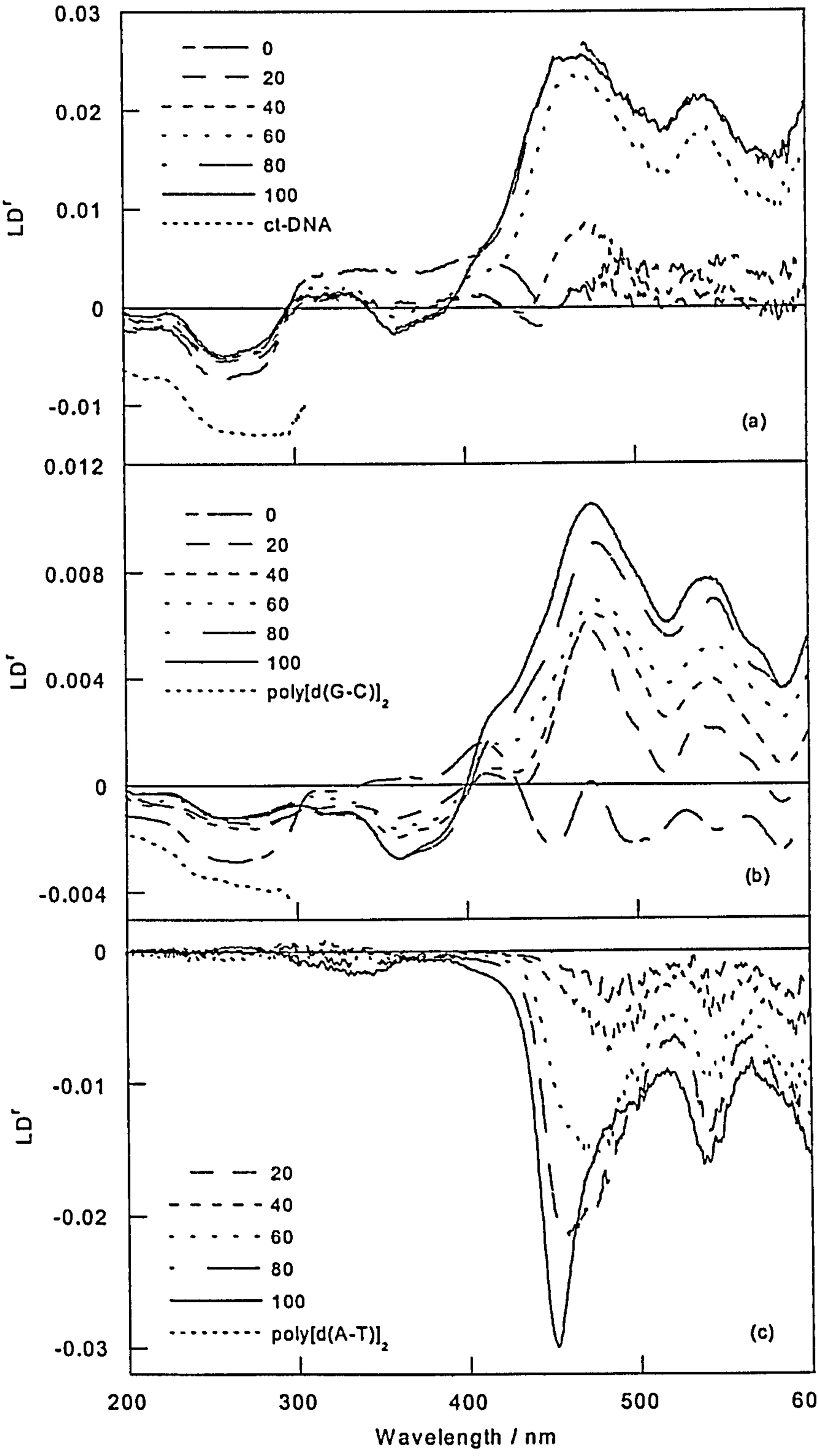

Figure 4.16 *LD*^{r} spectra of *t*-H_2P (5 μM), phosphate buffer (1 mM; pH 7), NaCl (see legend for mM concentrations) and (a) ct-DNA (40 μM), (b) poly[d(G-C)]$_2$ (40 μM) and (c) poly[d(A-T)]$_2$ (40 μM).

40 mM NaCl; 454 nm at 100 mM NaCl) appears in the Soret region indicating that both A_y and A_z in the Soret spectral region are oriented at less than 55° to helix axis. The intensity of this band increases with NaCl concentration and the precise wavelength maximum is also salt concentration dependent. The addition of salt is also accompanied by the appearance of a negative *LD* band (370 nm) outside the Soret region. The introduction of salt to the system reduces the intensity of the DNA spectral band, and therefore the degree of orientation of the system (this is not a pure salt effect and is porphyrin mediated).

With poly[d(A-T)]$_2$, a negative *LD* (442 nm at < 40 mM NaCl; 446 nm at > 40 mM NaCl) is observed in the Soret region with an intensity that increases as the NaCl concentration is raised. In the DNA region of the spectrum a solution of poly[d(A-T)]$_2$ gives only a very small negative *LD* and reflects the low degree of orientation of the polymer. In the presence of *t*-H_2P, the negative DNA band becomes undetectable, although the observation of *LD* in the Soret spectral region implies the system is oriented in the solution flow. Furthermore, at an NaCl concentration of 100 mM a small positive *LD* band is apparent in the DNA region of the spectrum. Since the system is oriented, the absence of a strong negative DNA *LD* is not due to the absence of DNA orientation. The origin of negative *LD* for the DNA base transitions is a perpendicular alignment of the bases relative to the helix axis along which the DNA is oriented. Deviation from this perpendicular alignment of base and helix axis would diminish the intensity of the DNA *LD*. The observed poly[d(A-T)]$_2$ *LD* spectrum in the presence of porphyrin could thus be due to disruption of the alignment of the DNA bases by bound porphyrin.

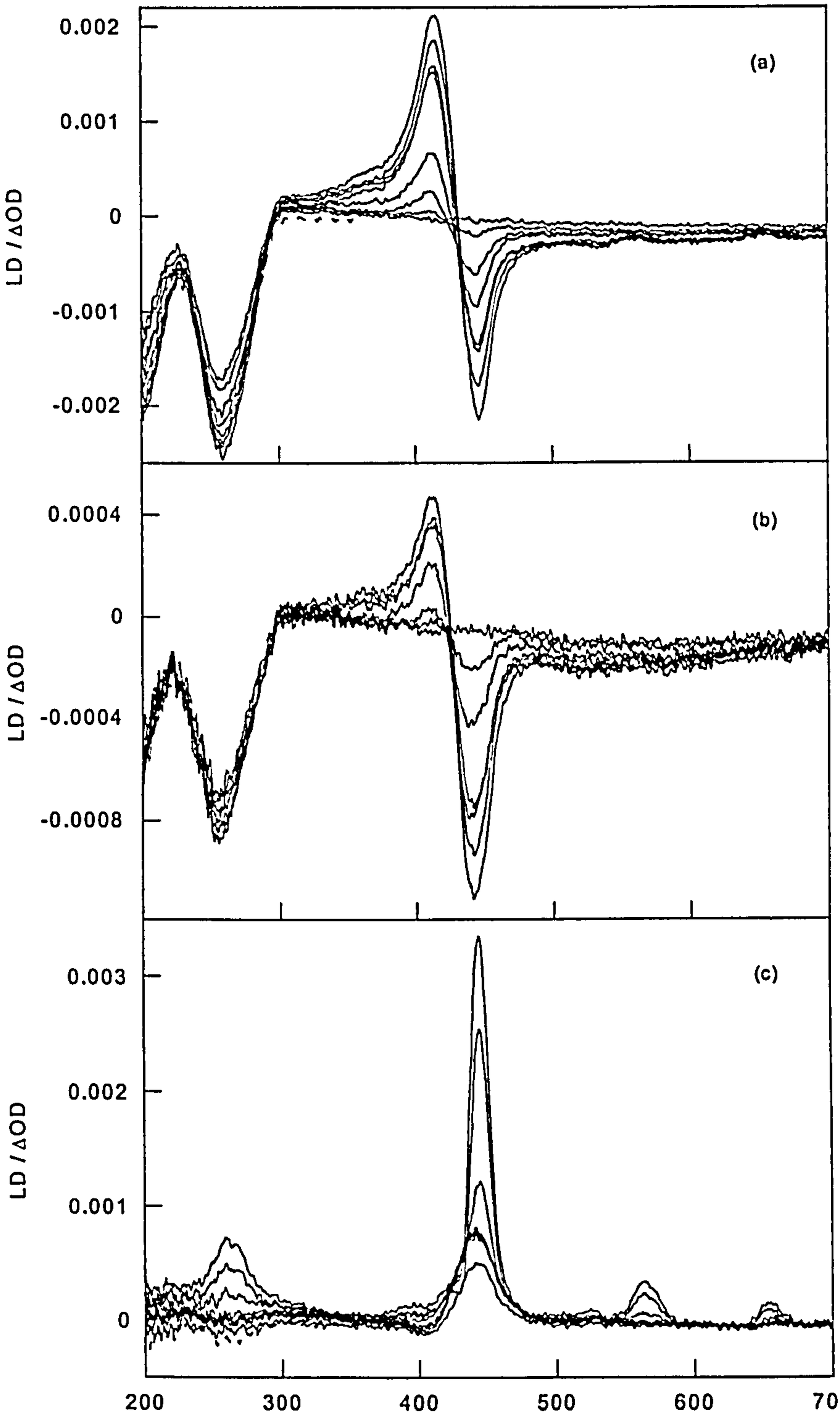

Figure 4.17 *LD* spectra of *t*-H_2P (1 – 8 μM; *LD* intensity increases with concentration), NaCl (20 mM), phosphate buffer (1mM; pH 7) and (a) ct-DNA (40 μM), (b) poly[d(G-C)]$_2$ (40 μM) and (c) poly[d(A-T)]$_2$ (40 μM). (- - -) DNA only spectra.

LD spectra of the ct-DNA complex with *t*-H_2P measured as a function of porphyrin concentration exhibit positive and negative *LD* in the Soret region of the spectrum (Figure 4.17a). The shape of the spectrum is reminiscent of that observed for the low salt porphyrin complexes of ct-DNA and poly[d(G-C)]$_2$ when titrated with NaCl. The positive maximum appears at 414 nm and the negative band is centred at 445 nm. The shape of the band is consistent at the different *t*-H_2P concentrations although the *LD* intensity increases with porphyrin concentration. Given that the in-plane $\pi \rightarrow \pi^*$ transitions of *t*-H_2P in the Soret region of the spectrum have considerable long and short axis polarisation, the observed *LD* indicates a binding orientation in which the Soret transition moments lie at angles of $\alpha > 55°$ for the negative *LD* band and $\alpha < 55°$ for the positive *LD* band (*LD* = 0 when $\alpha = 55°$). In the DNA region of the spectrum the negative *LD* of the ct-DNA bases appears at 259 nm at a progressively decreasing intensity as the porphyrin concentration increases. Thus the degree of orientation of the system is declining at progressively higher *t*-H_2P concentrations.

Porphyrin concentration dependent *LD* spectra of the *t*-H_2P complex with poly[d(G-C)]$_2$ (Figure 4.17b) are qualitatively very similar to those observed for *t*-H_2P and ct-DNA under analogous conditions. The positive *LD* appears at 410 nm and the negative band is centred at 440 nm in the Soret region of the spectrum. The same transition moment orientation effects that result in both positive and negative *LD* for the *t*-H_2P complex with ct-DNA, and discussed previously, are also apparent in *t*-H_2P binding to poly[d(G-C)]$_2$. The negative *LD* band has greater intensity than the positive band indicating a slightly different porphyrin orientation on poly[d(G-C)]$_2$ to that observed on ct-DNA. The DNA band appears at 256 nm and decreases in magnitude due to decreasing extent of

orientation as the concentration of *t*-H_2P increases.

When bound to poly[d(A-T)]$_2$, *t*-H_2P exhibits porphyrin concentration dependent *LD* spectra very different in form to those observed for ct-DNA and poly[d(G-C)]$_2$ (Figure 4.17c). The Soret band appears as a single, sharp positive peak at 441 nm at 1 μM porphyrin concentration but progressively shifts to 445 nm as the concentration of *t*-H_2P increases. In the UV region of the spectrum the DNA bases exhibit a weak negative *LD* at 262 nm and low porphyrin concentration but the signal becomes positive as the *t*-H_2P concentration increases. The positive DNA *LD* is consistent with significant disruption of the orientation of the DNA bases by the bound porphyrin. A positive *LD* contribution from the weak *t*-H_2P absorption in the UV spectral region may also contribute to the overall positive sign of the *LD* band. Assignment of the *t*-H_2P binding orientation from the Soret region is difficult given the uncertainty associated with the alignment of the bases in this DNA–porphyrin system.

4.3.6 Competition binding

In the presence of different DNAs, *t*-H_2P exhibits a *CD* signature characteristic of the DNA sequence to which it is bound. This spectroscopic property of the porphyrin can be exploited to qualitatively assess the relative binding affinity of *t*-H_2P to poly[d(G-C)]$_2$ versus poly[d(A-T)]$_2$. When bound to poly[d(A-T)]$_2$, the Soret maximum appears at 427 nm in the normal absorption spectrum and exhibits a positive *ICD* at 439 nm in the *CD* spectrum. Upon addition of poly[d(G-C)]$_2$ no change is observed in the wavelength maximum of the Soret in the normal absorption spectrum and the overall shape of the *CD*

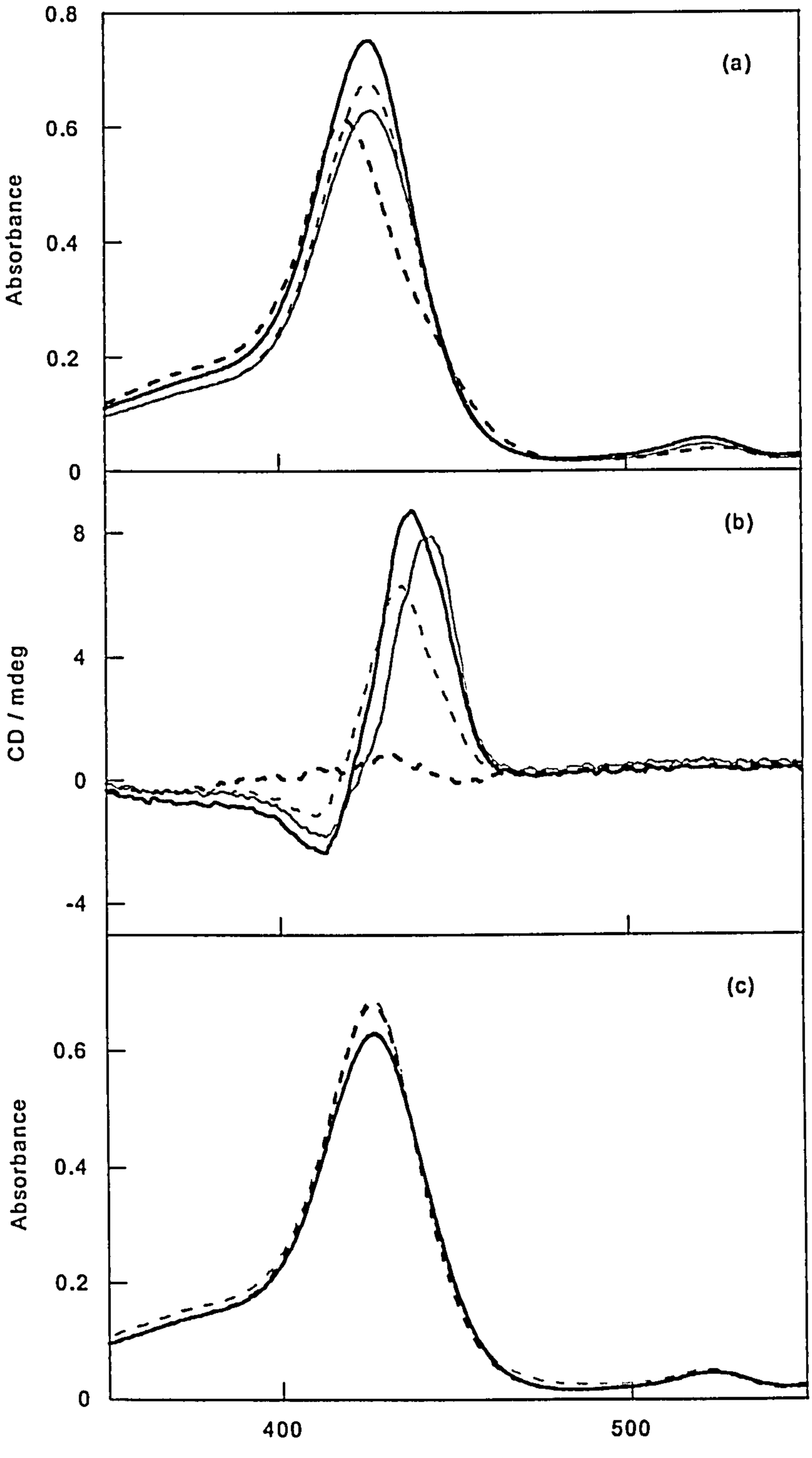

Figure 4.18 (a) Normal absorption spectra (b) *CD* spectra and (c) normal absorption spectra measured after 45 mins of *t*-H_2P (5 mM), NaCl (20 mM) and (thick line) poly[d(A-T)]$_2$ (40 mM), (thin line) poly[d(A-T)]$_2$ to which poly[d(G-C)]$_2$ was added, (thick broken line) poly[d(G-C)]$_2$ (40 mM) and (thin broken line) poly[d(G-C)]$_2$ to which poly[d(A-T)]$_2$ was added.

signature is retained, although the *CD* maximum shifts to 443 nm. Conversely, when poly[d(A-T)]$_2$ is added to a solution of poly[d(G-C)]$_2$, the Soret wavelength maximum shifts from 419 nm to 427 nm in the normal absorption spectrum and the weak positive *CD* band at 433 nm converts to the poly[d(A-T)]$_2$ characteristic *CD* signature with the positive maximum at 435 nm. After 45 minutes no further significant changes are observable in either the *t*-H_2P and poly[d(G-C)]$_2$ solution to which poly[d(A-T)]$_2$ was added, or the poly[d(A-T)]$_2$ and *t*-H_2P solution to which poly[d(G-C)]$_2$ was added. Thus *t*-H_2P preferentially binds to poly[d(A-T)]$_2$ over poly[d(G-C)]$_2$.

4.3.7 Normal absorption melting curves

Interaction with *t*-H_2P affects the thermal denaturation properties of poly[d(A-T)]$_2$. When no porphyrin is present a melting curve typical of the double stranded to single stranded DNA transition is observed (Figure 4.19c). At a salt concentration of 20 mM NaCl the melting temperature of poly[d(A-T)]$_2$ was measured to be 47.3 °C. The presence of *t*-H_2P increases both the melting temperature of the duplex DNA and the temperature range over which the DNA melting transition occurs. T_m increases with *t*-H_2P concentration thus the porphyrin stabilises the poly[d(A-T)]$_2$ duplex (Table 4.4).

r	[*t*-H_2P] / μM	T_m	T_a
0	0	47.3	47.2
0.025	1	50.5	49.7
0.1	4	61.9	60.7
0.2	8	71.9	70.8

Table 4.4 Effect of different *t*-H_2P concentrations on T_m and T_a of poly[d(A-T)]$_2$.

A pre-melting transition is apparent in the 8 μM *t*-H_2P melting curve (Figure 4.19f). Since the variation in the 260 nm absorbance of the porphyrin alone over the temperature range studied is only 5×10^{-3} absorbance units (Figure 4.19b), the observed low temperature transition is indicating a change in the structure of the DNA itself (the extent of *t*-H_2P aggregation is not significant under these conditions thus the 260 nm absorbance change is not an effect of extended porphyrin stacking). No pre-melting transitions are

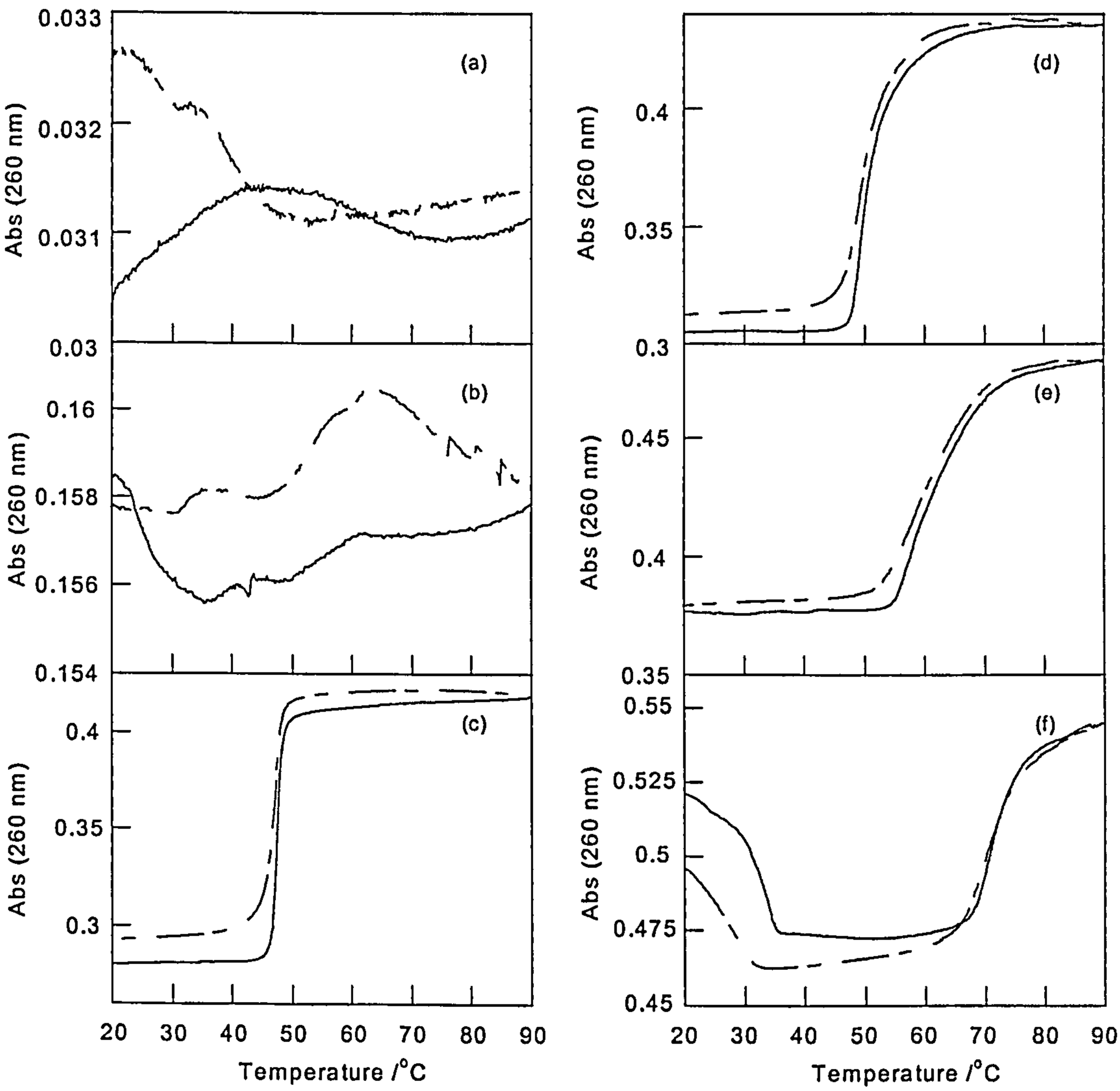

Figure 4.19 Normal absorbance measured at 260 nm as a function of temperature of (a) pure water, (b) *t*-H_2P (8 μM) and NaCl (20 mM), (c) poly[d(A-T)]$_2$ (40 μM) and NaCl (20 mM), (d) poly[d(A-T)]$_2$ (40 μM), *t*-H_2P (1 μM) and NaCl (20 mM), (e) poly[d(A-T)]$_2$ (40 μM), *t*-H_2P (4 μM) and NaCl (20 mM) and (f) poly[d(A-T)]$_2$ (40 μM), *t*-H_2P (8 μM) and NaCl (20 mM). (—) Melting curve and (- - -) annealing curve.

observable in either the 1 μM or 4 μM *t*-H_2P melting curves thus the DNA structural perturbation apparent at 8 μM *t*-H_2P occurs only as a result of a binding mode unique to the high porphyrin concentration. Hypochromicity of the DNA absorbance at 260 nm is usually a result of decreased base stacking interactions resulting from duplex melting or the formation of condensed DNA, in which case DNA absorbance decreases and light scattering above 300 nm are usually evident in the normal absorption spectrum. Thus it may be inferred from these data that the 8 μM *t*-H_2P binding mode decreases base stacking or condenses DNA. There is no evidence of light scattering outside the DNA region in the normal absorption spectrum to indicate the formation of condensed DNA thus a binding mode that disrupts the DNA stacking interactions is occurring. The hypochromic shift follows from a partial reversion to the standard duplex structure permitted by a decrease in the amount of bound porphyrin with increasing temperature.

4.3.8 Circular dichroism melting curves

The *CD* spectroscopy of *t*-H_2P when bound to DNA is temperature dependent. In the presence of poly[d(G-C)]$_2$ increasing the temperature inverts the sign of the initially positive Soret *ICD* at 425 nm (Figure 4.20a) thus temperature influences the mode of binding of *t*-H_2P to poly[d(G-C)]$_2$. No decrease in the overall *ICD* intensity is observed thus the change in binding mode is not a result of a decrease in the amount of bound ligand at high temperature. Furthermore, the poly[d(G-C)]$_2$ duplex remains intact over the temperature range studied, as evidenced by the invariant *CD* signature of the DNA in the absence of porphyrin (Figure 4.21a). The integrity of the poly[d(G-C)]$_2$ duplex is retained even in the presence of porphyrin, over the temperature range studied, since no

significant change is observed in the DNA *CD* of this system (Figure 4.20a). No normal absorption melting curves were measured for poly[d(G-C)]$_2$ due to its stability.

In the presence of poly[d(A-T)]$_2$, the shape and intensity of the Soret *ICD* of the porphyrin is strongly dependent on the temperature of the system (Figure 4.20b). The decrease in *ICD* intensity in the Soret region of the spectrum suggest the affinity of *t*-H_2P

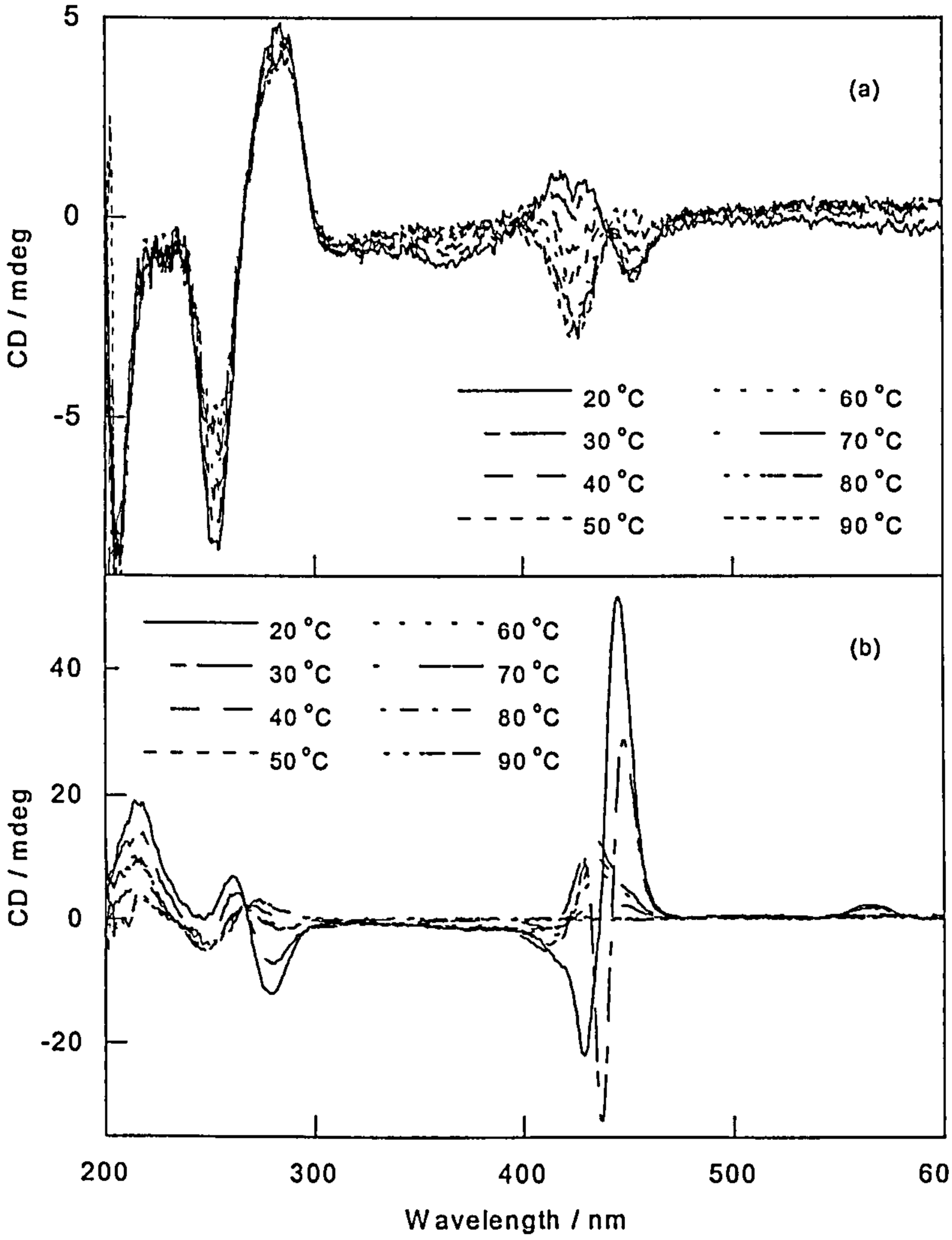

Figure 4.20 *CD* spectra measured as a function of temperature of (a) poly[d(G-C)]$_2$ (40 μM), *t*-H_2P (8 μM) and NaCl (20 mM) and (b) poly[d(A-T)]$_2$ (40 μM), *t*-H_2P (8 μM) and NaCl (20 mM).

for poly[d(A-T)]$_2$ is lower at higher temperature. Moreover, the observed change in *CD* signature with temperature implies a change in binding mode. This is presumably a consequence of the binding mode dependence on either concentration of bound porphyrin or temperature, since the change in Soret *CD* signal with deceasing temperature approximates that observed when the concentration of *t*-H_2P is increased in the presence of poly[d(A-T)]$_2$ at ambient temperature (Figure 4.7c). At low temperature an exciton *ICD* appears in the Soret spectral region, whereas at temperatures in excess of 40°C a single positive *ICD* is observed in the Soret region of the spectrum. No Soret *ICD*

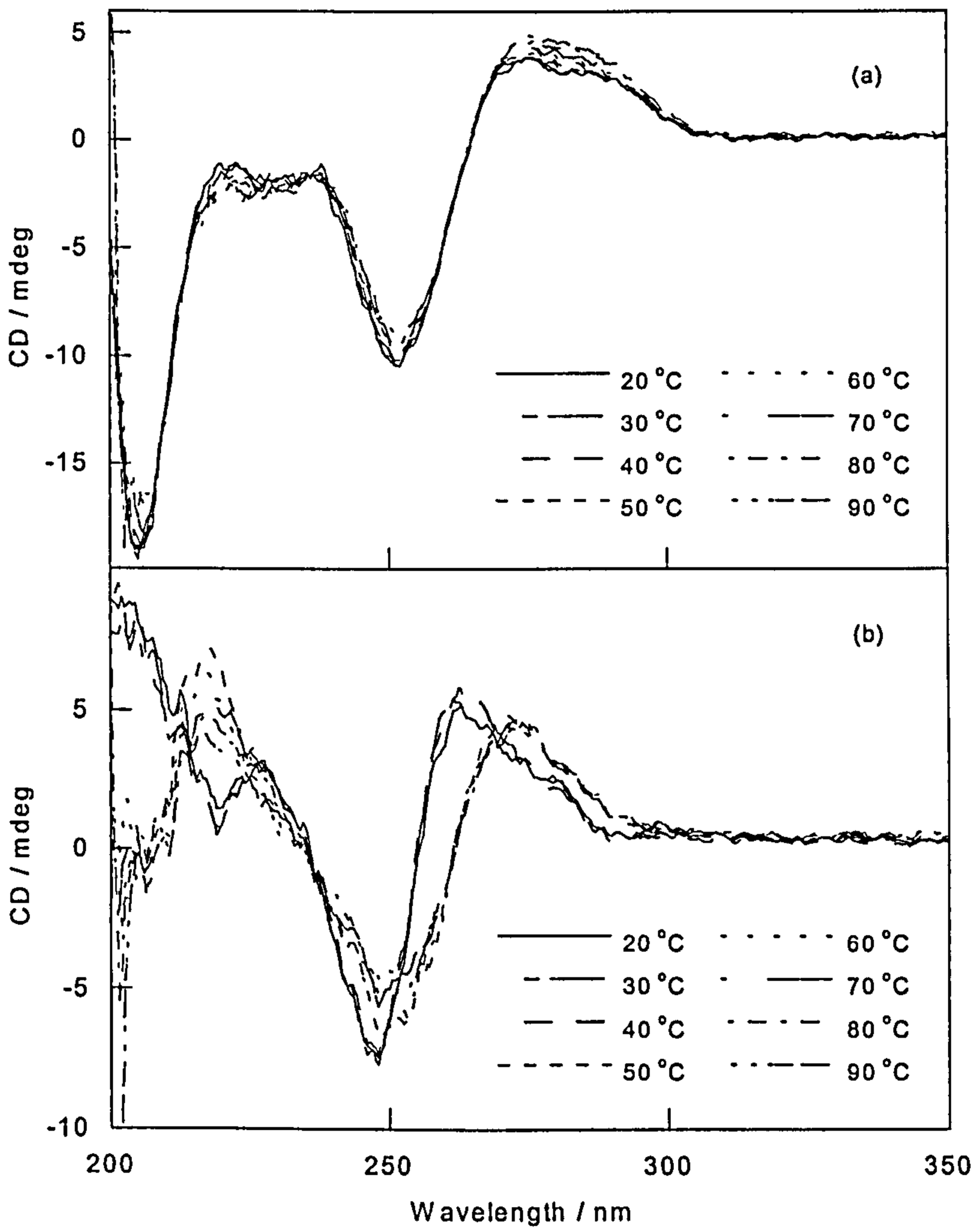

Figure 4.21 *CD* spectra measured as a function of temperature of (a) poly[d(G-C)]$_2$ (40 μM) and NaCl (20 mM) and (b) poly[d(A-T)]$_2$ (40 μM) and NaCl (20 mM).

appears in the *CD* spectrum above T_m (71.9°C; Figure 4.19f) for this system.

The temperature dependent behaviour of *t*-H_2P binding to poly[d(A-T)]$_2$ implies that the porphyrin–porphyrin stacking interactions that occur on poly[d(A-T)]$_2$ are disfavoured at higher temperature where predominant monomer binding is observed. No porphyrin *ICD* is detectable above T_m for this system (71.9°C). Apparently then, *t*-H_2P does not bind to single stranded poly[d(A-T)]$_2$ at high temperature.The DNA region of the *CD* spectrum indicates a porphyrin induced change in the structure of poly[d(A-T)]$_2$ at low temperature. The porphyrin induced DNA structure is characterised by a positive peak at 261 nm and a negative *CD* at 279 nm. The DNA structural effect is favoured at lower temperatures where the porphyrin binds in a stacked binding mode since the poly[d(A-T)]$_2$ B-DNA *CD* signature is observed at higher temperatures where the stacked binding mode is lost.

4.3.9 Molecular modelling

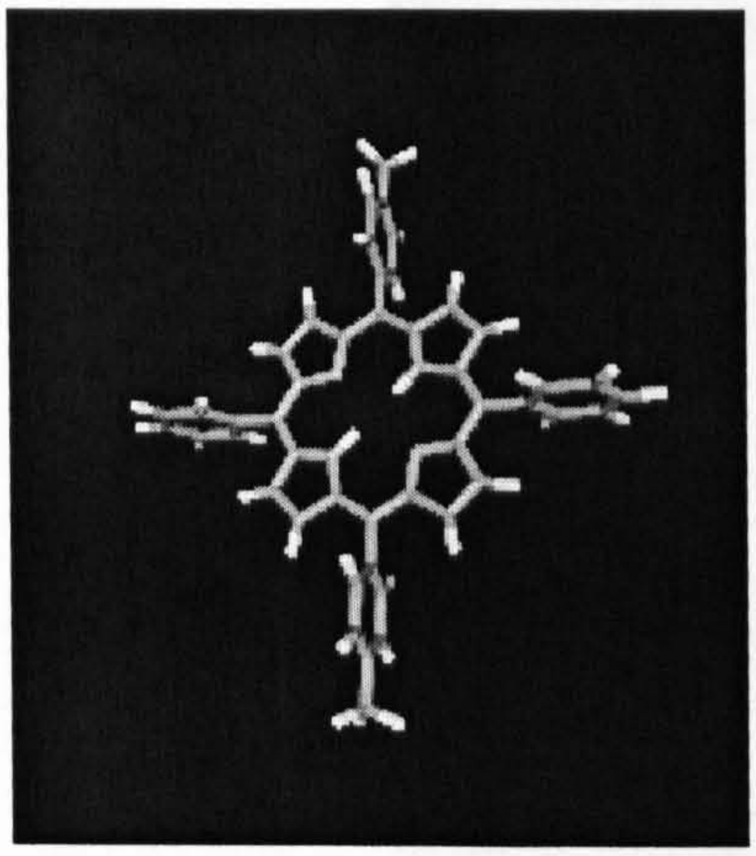

Figure 4.22 Energy minimised structure of *t*-H_2P.

Energy minimisation of *t*-H_2P resulted in a planar arrangement of the central porphyrin ring with the peripheral meso-substituents aligned perpendicular to the ring (Figure 4.22). The results of the MOPAC single point energy MNDO calculation, used to compute partial charges on the porphyrin, are detailed in Appendix I together with other relevant information pertaining to this calculation.

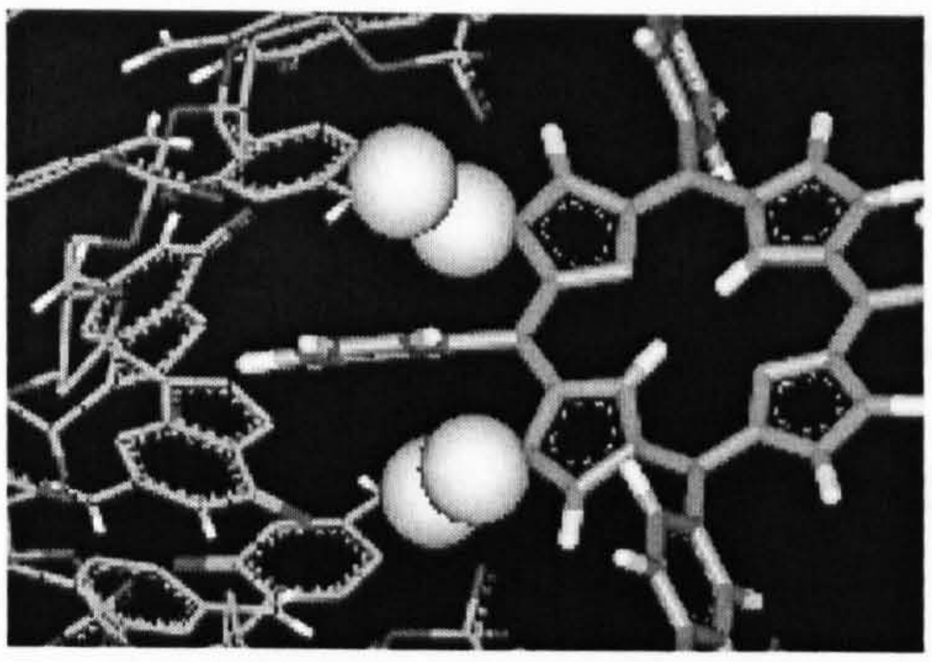

Figure 4.23 Steric clashes between cytosine C4 amino group and *t*-H_2P C_β protons.

Energy minimisation of the DNA–porphyrin complexes (as described in section 4.2.7) resulted in sterically acceptable structures for all the binding geometries studied. Energy minimisation of the partially intercalated major groove *t*-H_2P binding geometry with the GC dodecamer (Figure 4.24) resulted in small distortions in the structure of both DNA and porphyrin. The intercalated phenyl ring pushed the adjacent bases apart although the Watson–Crick hydrogen bonding pattern was retained at the intercalation site in the energy minimised structure. The porphyrin ring is slightly twisted in this binding geometry and the intercalated phenyl is rotated relative to the ring to be roughly co-planar with the DNA bases. The porphyrin plane lies at approximately 18° to the helix axis allowing electrostatic interactions between the *N*-methylpyridiniumyl porphyrin groups and the

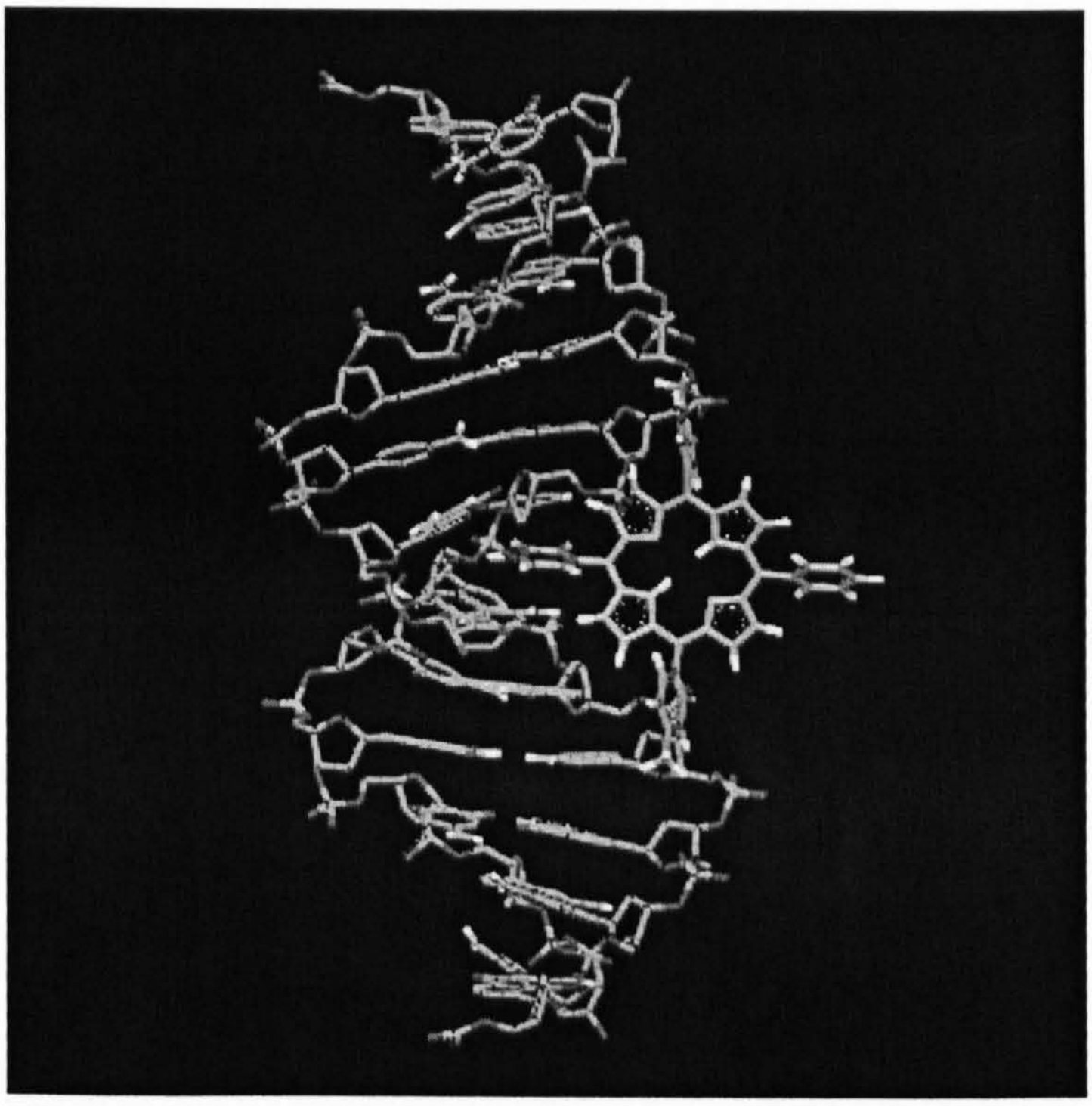

Figure 4.24 Energy minimised structure of *t*-H_2P partially intercalated into a GC dodecamer from the major groove.

DNA backbone. Analysis of CPK structures (as defined by the van der Waals radii for each constituent atom of the molecule) for this molecular model indicate that steric clashes occur between the amino group protons at C4 on cytosine and the porphyrin C_β protons pointing towards the floor of the groove (Figure 4.23). The binding site size of this geometry is six base pairs.

The porphyrin may also be accommodated in the GC dodecamer minor groove (Figure 4.25). This binding modes involves the insertion of two meso substituents into the DNA groove such that the plane of the porphyrin ring follows the 45° pitch of the groove. The GC dodecamer minor groove appears to accommodate *t*-H_2P without significant structural perturbation to DNA or porphyrin. The groove bound phenyl and *N*-methylpyridiniumyl groups of the porphyrin are rotated to 61° and 74° respectively to the porphyrin plane. The *N*-methylpyridiniumyl group external to the helix is tilted

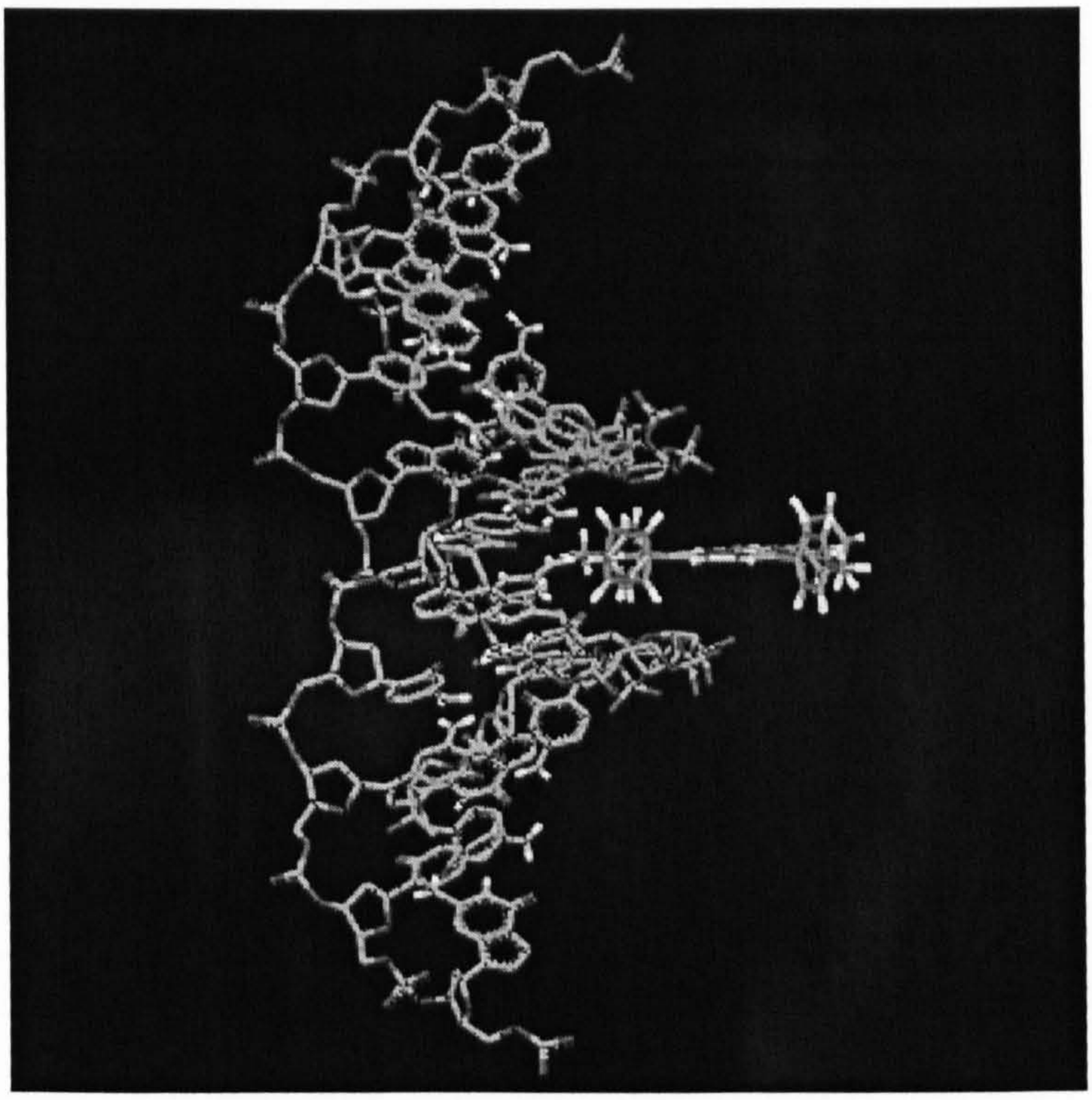

Figure 4.25 Energy minimised structure of *t*-H_2P bound in the minor groove of a GC dodecamer.

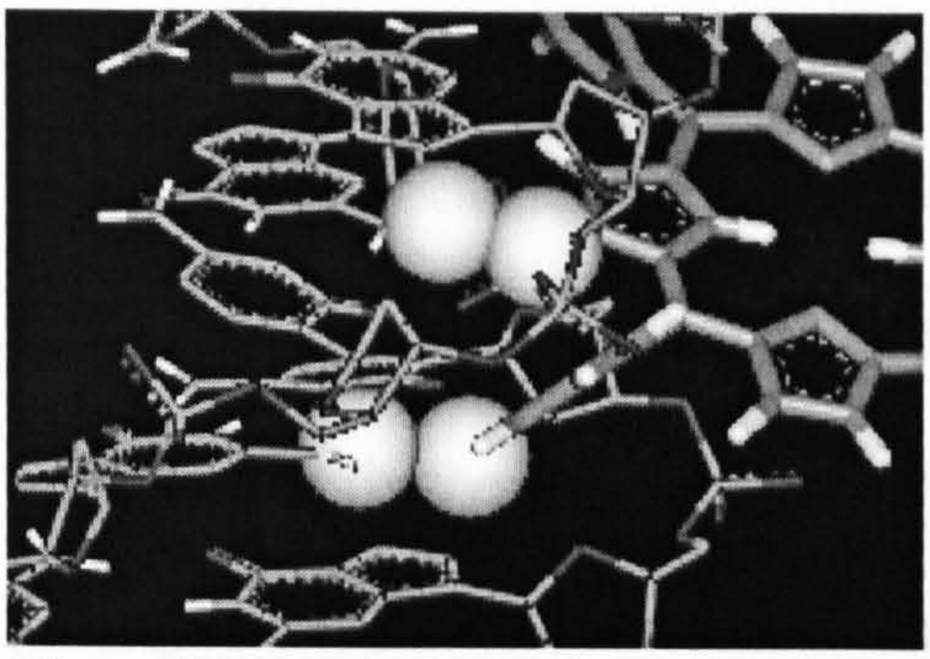

Figure 4.26 Steric clashes between guanine C2 amino group and *t*-H_2P C_β protons.

towards the DNA backbone, presumably the result of electrostatic interactions between the oppositely charged moieties. Analysis of CPK structures suggest that porphyrin insertion into the GC dodecamer minor groove is hindered by steric clashes between the exocyclic amino group at C2 on guanine and the porphyrin protons at C_β and the meta position on phenyl (Figure 4.26). The porphyrin spans three base pairs in this binding geometry.

The energy minimised molecular model of *t*-H_2P fully intercalated into the GC dodecamer (Figure 4.27) reveals porphyrin insertion between the DNA base pairs to be at least sterically feasible. The porphyrin ring lies in the centre of the helix in a geometry in which *t*-H_2P and the DNA bases are approximately co-planar. The substituent groups

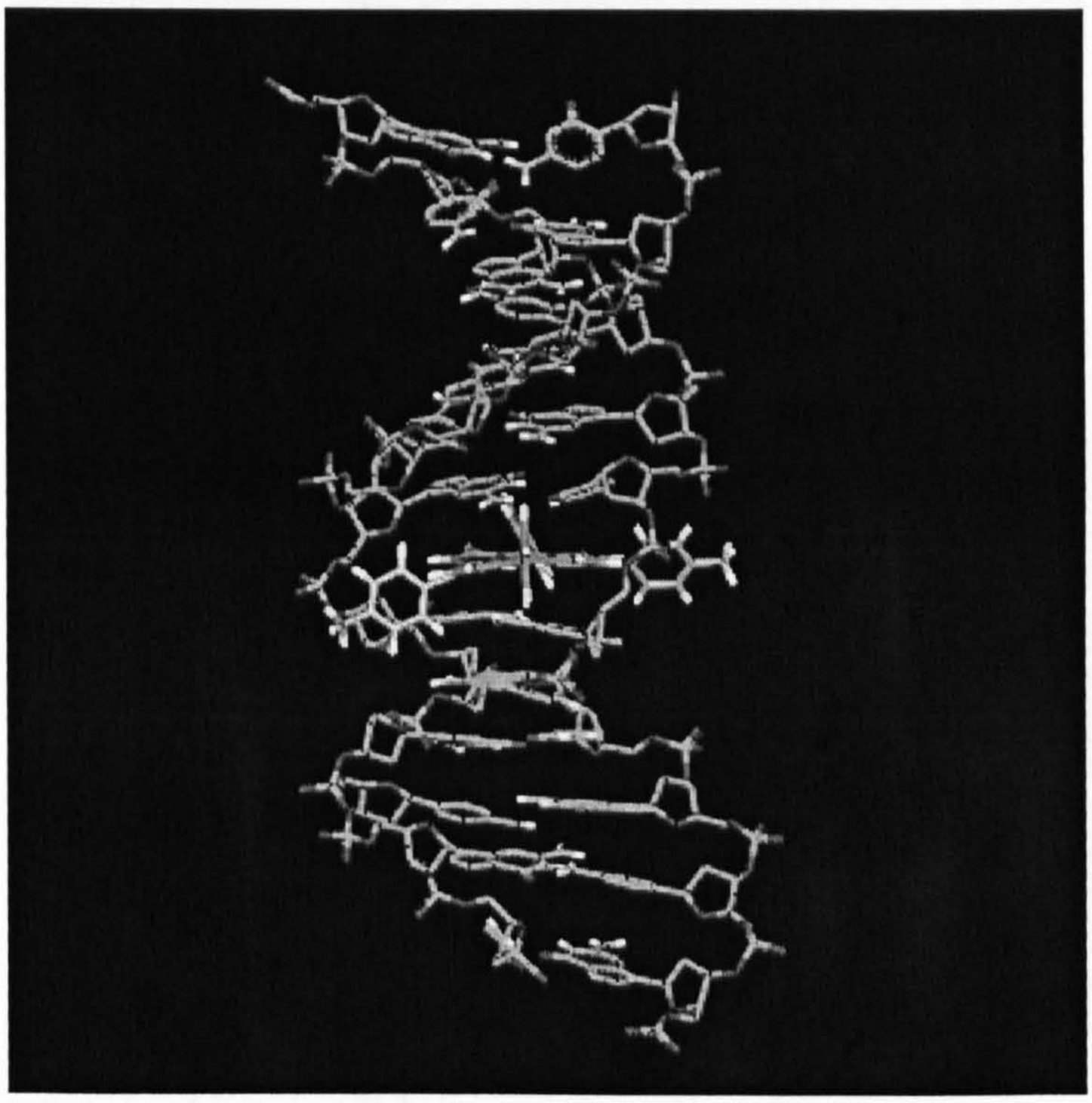

Figure 4.27 Energy minimised structure of *t*-H_2P fully intercalated into a GC dodecamer.

protrude into the DNA grooves, two of which are accommodated in each groove. The presence of intercalated porphyrin forces the adjacent base pairs apart, although there is no significant increase in length of the dodecamer. The *N*-methylpyridiniumyl groups further perturb the duplex structure by deforming the local DNA backbone. The porphyrin itself adopts a distorted conformation in which the central ring system is twisted and the phenyl and minor groove *N*-methylpyridinumyl groups lie tilted above and below the mean porphyrin plane respectively.

The computed energy minimised geometry for partial porphyrin intercalation from the major groove of an AT dodecamer (Figure 4.28) resulted in the expected separation of adjacent base pairs at the intercalation site. Disruption of the base stacking, induced by the presence of the intercalated porphyrin phenyl group, was not sufficient to prevent the

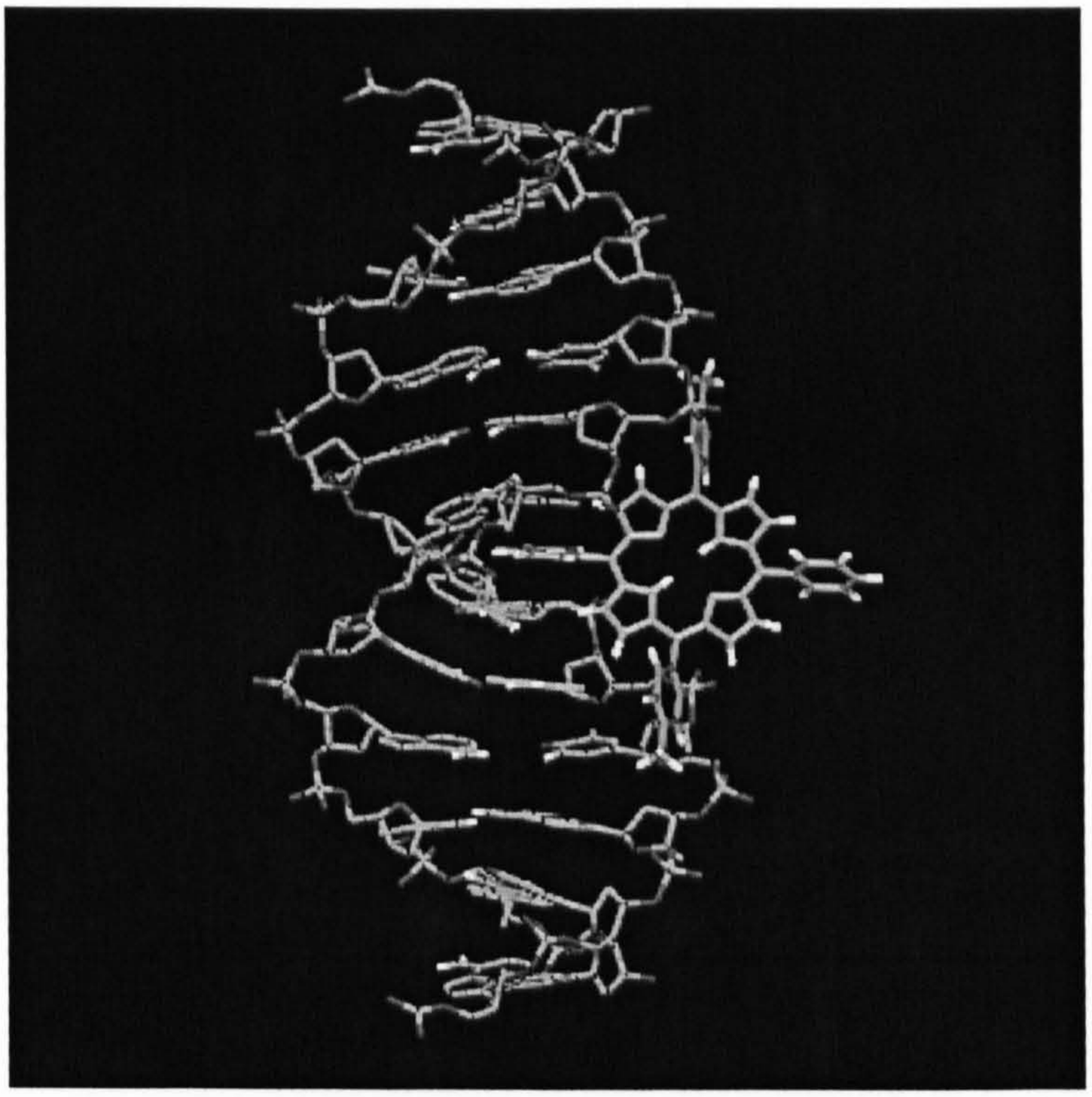

Figure 4.28 Energy minimised structure of *t*-H_2P partially intercalated into an AT dodecamer from the major groove.

formation of Watson–Crick base pairs. The porphyrin plane lies across the major groove and makes an angle of approximately 26° with the helix axis. This binding geometry permits electrostatic interactions between the cationic *N*-methylpyridiniumyl porphyrin groups and anionic phosphate groups of the DNA backbone. The only significant alteration to the porphyrin structure when bound to the DNA is the rotation of the intercalated phenyl group to a position co-planar with the base pairs. No close contacts between atoms of porphyrin and DNA are observed. The porphyrin occupies a binding site spanning six base pairs.

The minor groove of an AT dodecamer easily accommodates *t*-H_2P in an edge-on binding geometry in which one phenyl and one *N*-methylpyridiniumyl group are buried deep in the groove (Figure 4.29). In the energy minimised molecular model of this geometry the

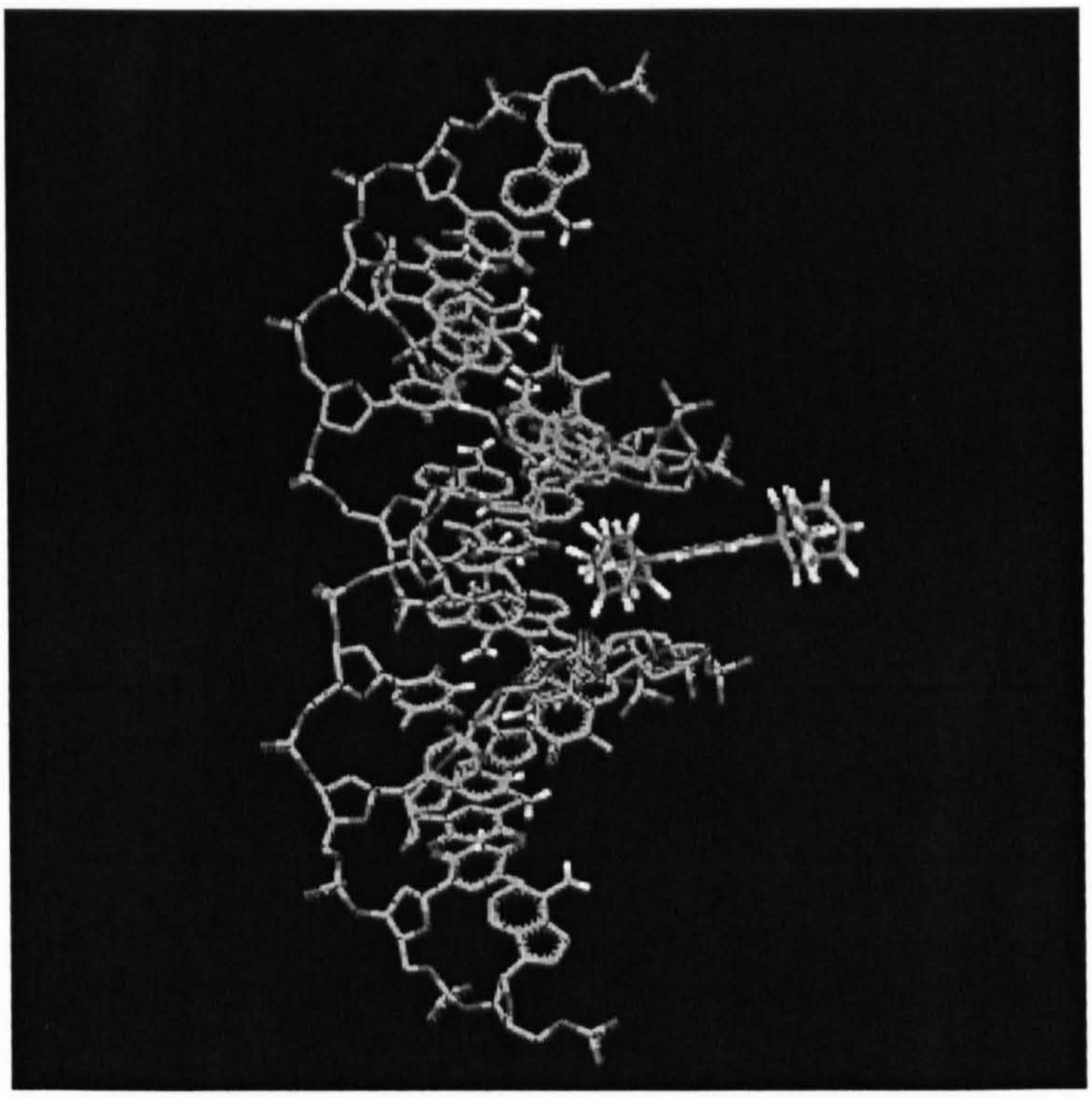

Figure 4.29 Energy minimised structure of *t*-H_2P bound in the minor groove of an AT dodecamer.

tilt of the porphyrin plane matches the pitch of the minor groove. The model is lacking in significant structural perturbation to the DNA dodecamer. The only discernable porphyrin deformation is to the *N*-methylpyridiniumyl external to the DNA helix which is tilted towards the DNA groove, an observation explained by the mutual electrostatic attraction experienced between two oppositely charged bodies. The absence of steric clashes between atoms of porphyrin and DNA further characterise this minor groove binding geometry. The porphyrin binding site is three base pairs.

Full intercalation of *t*-H_2P between the central base pairs of an AT dodecamer (Figure 4.30) forces the base pairs apart resulting in a co-planar arrangement of porphyrin plane and DNA bases. The porphyrin meso-substituted groups are accommodated by the DNA grooves, with two groups in each groove. The minor groove situated *N*-

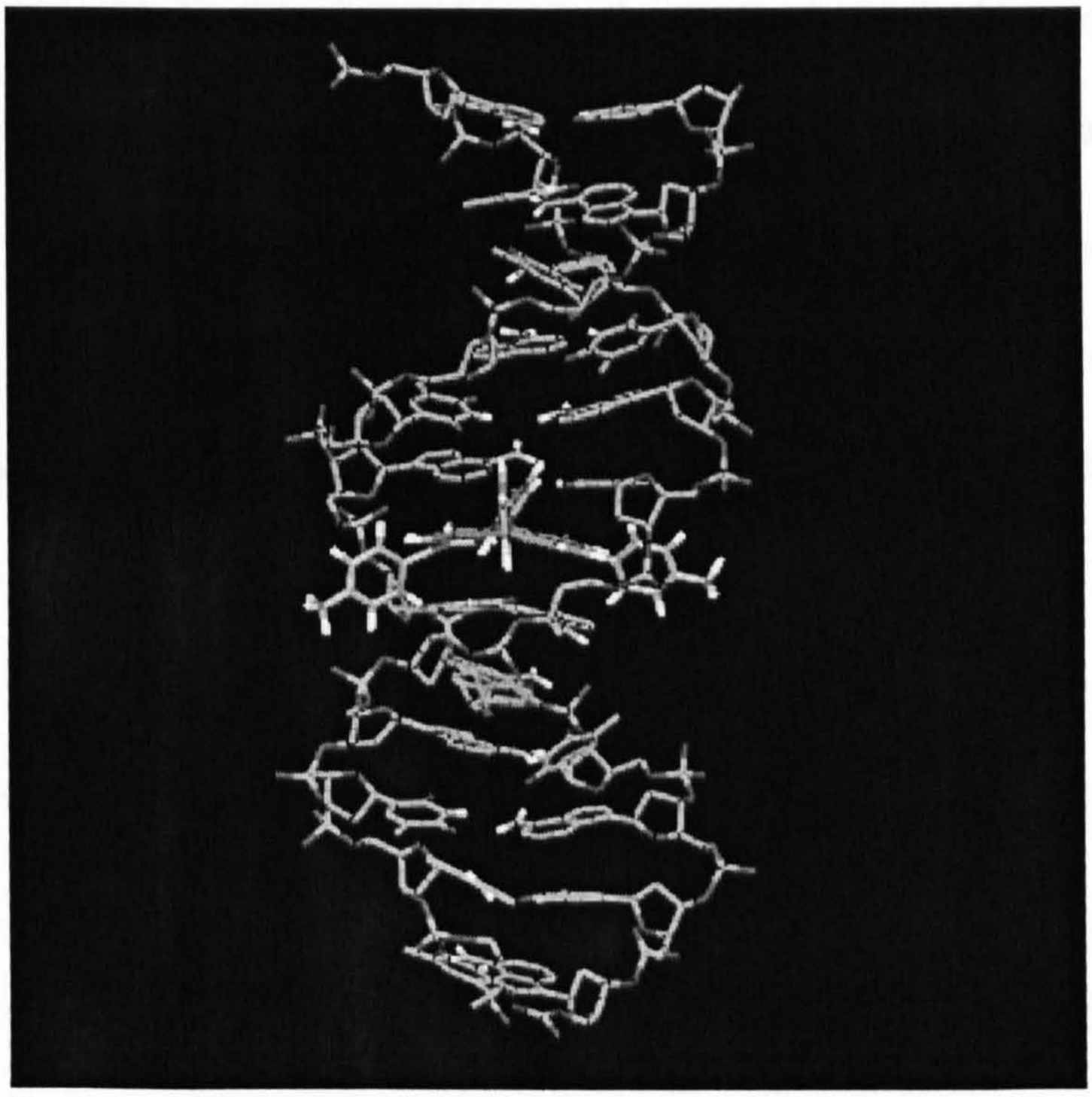

Figure 4.30 Energy minimised structure of *t*-H_2P fully intercalated into an AT dodecamer.

methylpyridiniumyl group is tilted towards the centre of the groove resulting a twist to the central porphyrin ring. This effect also occurs in the major groove although to a lesser extent, and further contributes to the porphyrin twist. The overall effect of the intercalative binding is the induction of a saddle type distortion into the porphyrin ring.

4.4 Discussion

The binding of *t*-H_2P to DNA has been studied as a function of a number of variables by means of four spectroscopic techniques and molecular modelling. The study of the binding mode dependence on NaCl concentration enabled the interaction of porphyrin aggregates with DNA to be observed. *RLS* was particularly useful in this case as a sensitive probe of the state of porphyrin aggregation. The porphyrin also interacts with DNA in the monomer form and *CD* and *LD* data measured at various porphyrin/DNA mixing ratios permitted analysis of this binding behaviour. DNA sequence was an important determinant in the type of *t*-H_2P binding that occurs, an observation facilitated by the differential study of porphyrin interaction with ct-DNA, poly[d(G-C)]$_2$ and poly[d(A-T)]$_2$ across the experimental conditions. The spectroscopic data, *LD* in particular, was supplemented with a molecular modelling study and enabled molecular level interpretation of the DNA–porphyrin binding modes.

4.4.1 Interaction of *t*-H_2P with ct-DNA

The spectroscopic data collectively show that *t*-H_2P is capable of interacting with ct-DNA in a number of different ways. Prominent differences in the modes of DNA binding exist

between the monomeric and aggregated porphyrin forms. Binding studies with the synthetic DNAs reveal monomer binding to readily occur at AT sites whereas GC tracts promote aggregated binding. In the absence of salt the ct-DNA binding mode is characterised by a *CD* signature that corresponds in terms of wavelength maximum and band shape to that observed for monomer binding to poly[d(A-T)]$_2$. The monomer interaction with ct-DNA is therefore likely to occur at AT rich tracts at low salt concentrations with the aggregated binding mode dominating at GC rich binding sites at high salt concentrations. The monomer binding mode occurs preferentially on ct-DNA only at low salt and low porphyrin concentrations, with the onset of aggregation occurring rapidly as either the salt or porphyrin concentration increases (the high porphyrin concentration binding modes involves stacking but the stack is not extended). Accordingly, the concentration of binding sites in ct-DNA to which strong monomer binding may occur is probably low, but the population of these sites may ultimately inhibit the formation of very long range porphyrin aggregates on ct-DNA at high salt concentrations, in contrast to the situation for poly[d(G-C)]$_2$.

Geometric considerations further differentiate the porphyrin monomer and aggregate binding modes. The observation of a $42-44°$ angle between the porphyrin Soret average transition moments and the DNA helix axis for monomer binding is strongly suggestive of an interaction via a DNA groove. The experimental binding angle is consistent with that observed in the molecular models of *t*-H_2P bound in the DNA minor groove. The narrow minor groove is an unlikely binding site for a bulky porphyrin aggregate and in any case the *LD* data suggest the aggregate binding geometry is very different from that observed for monomer binding. Such binding could only occur in the major groove or

externally to the phosphate backbone, in a geometry that allowed efficient face–face π-stacking interactions between the aggregated porphyrin molecules.[66,67]

4.4.2 Interaction of *t*-H_2P with poly[d(G-C)]$_2$

Analysis of the spectroscopic data pertaining to the interaction of *t*-H_2P with poly[d(G-C)]$_2$ reveals a strong preference for the formation of DNA bound extended porphyrin aggregates. Although *t*-H_2P aggregates in solution in the absence of DNA, comparison of the *RLS* magnitudes observed for *t*-H_2P in both the presence and absence of poly[d(G-C)]$_2$ show the DNA to actively promote porphyrin aggregation. Larger porphyrin aggregates are observed at lower salt concentrations when poly[d(G-C)]$_2$ is present. The mechanism of the observed DNA enhanced porphyrin aggregation likely involves poly[d(G-C)]$_2$ acting as a template for aggregation to occur. The collective spectroscopic data suggest the nucleic acid structure remains relatively unperturbed by the presence of bound aggregated porphyrin. The high cooperativity of the aggregation process on poly[d(G-C)]$_2$ therefore arises from favourable porphyrin–porphyrin interactions rather than significant DNA structural changes or allosteric effects.

The occurrence of efficient face–face π-stacking interactions is an important prerequisite for the stability of any aggregated porphyrin array in solution.[66] When bound to DNA, the geometry dependence of the stacking interactions would constrain the aggregated binding mode to one for which the efficiency of the π-stack was retained at least to some extent. Of further significance to the geometry of the *t*-H_2P interaction with poly[d(G-C)]$_2$ is the lack of porphyrin hydrogen bond donating and accepting groups. Although the

poly[d(G-C)]$_2$ major groove is easily capable of accommodating a ligand stack, the molecular models of *t*-H_2P interactions with a GC dodecamer resulted in steric clashes occurring between the porphyrin C_β protons and DNA base protons in both the major and minor grooves. The molecular models also suggested a preference for an electrostatic interaction between the *N*-methylpyridiniumyl groups of *t*-H_2P and the backbone of the DNA. Therefore, the dominant interaction in *t*-H_2P binding to poly[d(G-C)]$_2$ could be between the DNA backbone and the cationic porphyrin substituents, resulting in a binding mode in which the porphyrin is partially free of the geometric constraints imposed by the DNA grooves to form an efficiently π-stacked long range aggregate. Such a binding mode would still adopt a well defined orientation due to porphyrin–porphyrin stacking interactions and DNA backbone geometry constraints.

On the basis of normal absorption and *CD* data, *t*-H_2P has been previously reported to be capable of intercalating into poly[d(G-C)]$_2$ under conditions of low ionic strength.[49] The intercalated binding mode was characterised by a weak, broad negative *CD* signature with two maxima in the Soret spectral region. A qualitatively similar *CD* signature is observed here for the interaction of *t*-H_2P with poly[d(G-C)]$_2$ in the complete absence of salt. *LD* permits further characterisation of this binding mode and the observation of an *LD* band with both positive and negative components in the Soret region of the spectrum precludes full porphyrin intercalation as a likely binding mode since these transitions are $\pi \rightarrow \pi^*$ polarised in the plane of the porphyrin. The *LD* data is consistent with a binding mode in which one porphyrin transition moment lies parallel with the plane of the DNA bases, hence giving negative *LD*, with the positive component of the spectrum arising from a second porphyrin transition moment aligned more parallel than perpendicular to

the helix axis. Such a geometry could involve partial intercalation in which the plane of the porphyrin ring lies across a DNA groove with a peripheral phenyl group inserted between the DNA base pairs as discussed section 4.3.9. Furthermore, in support of this interpretation of the data, the DNA *LD* for this binding mode lacks a decrease in intensity, relative to poly[d(G-C)]$_2$ alone, typically observed for with non-intercalated DNA–porphyrin complexes. Intercalated ligands lengthen and stiffen the DNA helix leading to more efficient flow orientation and larger DNA *LD* signals. The molecular model of *t*-H_2P partially intercalated into a GC dodecamer from the major groove suggests that such a binding geometry is not unfeasible.

4.4.3 Interaction of *t*-H_2P with poly[d(A-T)]$_2$

The interaction of *t*-H_2P with poly[d(A-T)]$_2$ differs fundamentally from that observed with either poly[d(G-C)]$_2$ or ct-DNA. Although *t*-H_2P binding to poly[d(A-T)]$_2$ occurs as either monomers or aggregates depending on the environment to which the DNA–porphyrin complex is exposed, a strong preference for the monomer binding mode is expressed at low to moderate salt concentrations. At high salt concentrations, an aggregated porphyrin binding mode does occur on poly[d(A-T)]$_2$, but the extent of the *t*-H_2P stacking is small compared to that observed for poly[d(G-C)]$_2$ and ct-DNA as shown by *RLS* and *CD* data. Furthermore, the competition binding experiments indicated a higher *t*-H_2P binding affinity for poly[d(A-T)]$_2$ than for poly[d(G-C)]$_2$. The formation of a thermodynamically stable groove bound *t*-H_2P complex with poly[d(A-T)]$_2$ at low salt concentrations would disfavour the subsequent aggregation of the bound porphyrins. Although a binding geometry could not be extracted from *LD* data for the porphyrin

complex with poly[d(A-T)]$_2$, the low salt binding mode probably involves the minor groove where the tilt of porphyrin plane matches the pitch of the groove. Since the *CD* signatures for the salt free complexes of *t*-H_2P with both ct-DNA and poly[d(A-T)]$_2$ are similar, it is reasonable to assume that the two binding modes are very similar. Therefore, the assignment of the porphyrin binding geometry to poly[d(A-T)]$_2$ as being minor groove may be made by analogy with the corresponding ct-DNA complex which was determined to interact via the minor groove from *LD* data. The molecular model of *t*-H_2P bound in the minor groove of an AT dodecamer suggests that the porphyrin fits easily into the groove without steric clashes between atoms of porphyrin and DNA.

The *CD* signature relating to the binding of porphyrin extended aggregates to poly[d(A-T)]$_2$ is qualitatively similar to that observed for poly[d(G-C)]$_2$. Therefore, the binding geometry of aggregated *t*-H_2P on the two DNAs may be concluded to be similar. Extended aggregate formation on poly[d(A-T)]$_2$ would thus require the reorganisation of the groove bound low salt porphyrin complex into an externally bound stack in contact with the phosphate backbone. Such a process is consistent with the requirement of high salt concentrations for aggregation to occur on poly[d(A-T)]$_2$.

At low salt concentration and high porphyrin/DNA mixing ratio porphyrin–porphyrin interactions also occur on poly[d(A-T)]$_2$, but the associated exciton type *CD* signature is dissimilar to the one corresponding to the high salt aggregated binding mode. Since high salt concentrations would appear to be required for external long range porphyrin stacking to occur on poly[d(A-T)]$_2$, the stacked binding mode indicated by the high porphyrin/DNA mixing ratio exciton *CD* signature occurs in a binding geometry different

from that observed at high salt. This binding mode is also characterised by changes in the DNA *CD* signature which may reflect a DNA structural change. Given that the affinity of *t*-H_2P for poly[d(A-T)]$_2$ is high and the porphyrin/DNA mixing ratio is high, the observed stacked binding mode could be the result of poly[d(A-T)]$_2$ minor groove saturation where subsequent *t*-H_2P binding requires a DNA structural change. Alternatively, the stacked binding mode may occur in the poly[d(A-T)]$_2$ major groove. In either case, the presence of a high concentration of bound *t*-H_2P perturbs the poly[d(A-T)]$_2$ structure.

4.5 Conclusions

The interaction of *t*-H_2P with ct-DNA, poly[d(G-C)]$_2$ and poly[d(A-T)]$_2$ has been studied with spectroscopic techniques and molecular modelling. The electronic spectrum of *t*-H_2P in PVA stretched film was also studied and the approximate, average polarisations for the in-plane $\pi \rightarrow \pi^*$ transition moments were assigned. The effects of salt concentration, ligand concentration and temperature on the DNA binding of *t*-H_2P were considered. The DNA binding modes of both aggregated and non-aggregated porphyrin were investigated; *CD* and *RLS* data permitted detection of any aggregated binding and *LD* and molecular modelling enabled analysis of the binding geometries.

The porphyrin was shown to preferentially bind to poly[d(A-T)]$_2$ by competition binding and the reduced tendency of *t*-H_2P to aggregate on poly[d(A-T)]$_2$ was then explained by the formation of a strongly bound complex between monomeric porphyrin and poly[d(A-T)]$_2$. The low salt *t*-H_2P complex with poly[d(G-C)]$_2$ has been tentatively concluded to

involve partial intercalation where a phenyl group is intercalated and the plane of the porphyrin lies along the major groove. The aggregated complexes with poly[d(G-C)]$_2$ and poly[d(A-T)]$_2$ probably bind in a mode where the cationic substituents interact with the DNA backbone. A third binding mode was observed for poly[d(A-T)]$_2$ at low salt but high *t*-H_2P concentrations in which dimers or small porphyrin oligomers form on the DNA and disrupt the base stacking. Porphyrin binding to ct-DNA was shown to involve monomer groove binding at low salt and low *t*-H_2P concentration, dimer or small oligomer binding at low salt and high *t*-H_2P concentration and extended aggregate formation at high salt concentrations. The observed binding to ct-DNA was explained in terms of the binding mode dependence on the DNA base sequence composition of the binding sites.

5 Spectroscopic Studies of Hoechst 33258 Binding to DNA

5.1 Introduction

Hoechst (Figure 5.1) is one of a number of small molecules that bind to the B-DNA minor groove with a marked specificity for AT rich regions.[68,69] The interaction of Hoechst with DNA has been intensively studied, mainly to provide a basis for the rational design of ligands capable of targeting and binding to a specific DNA sequence.[70] The development of such ligands would provide potential antiviral and anticancer agents with the ability to interact with a predetermined DNA sequence.

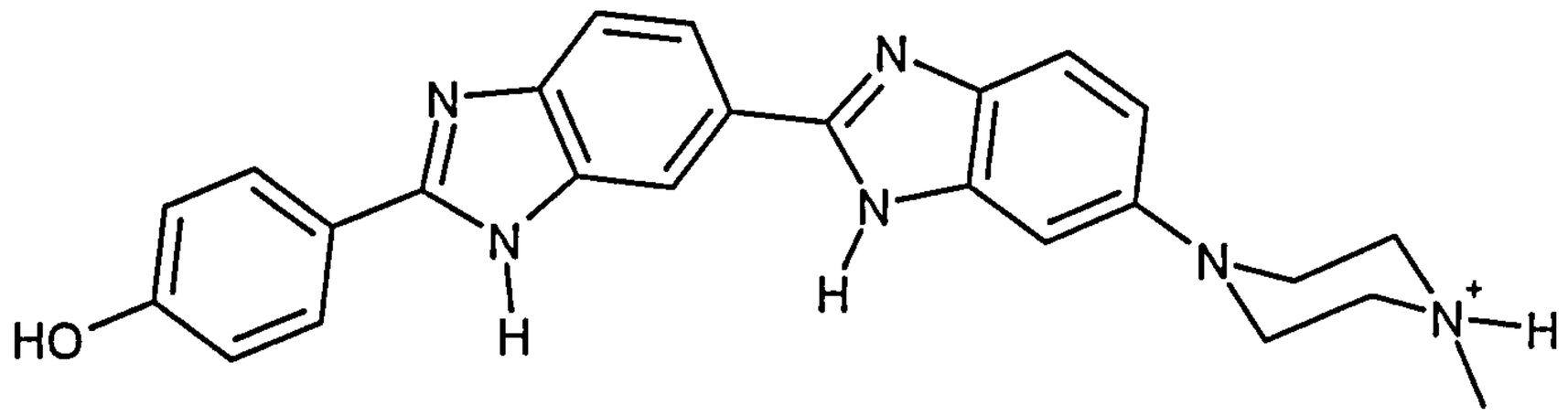

Figure 5.1 Structure of Hoechst 33258 (2'-(4-hydroxyphenyl)-5-(4-methyl-1-piperazinyl)-2,5'-bi-1H-benzimidazole).

The study of DNA–Hoechst interactions has elucidated important principles pertaining to GC over AT discrimination in small molecule binding to DNA. Hoechst was originally developed with the belief that the incorporation of a bulky *N*-methylpiperazine ring into an otherwise AT specific molecule might induce a GC reading element into the DNA binding, since this group is too wide to be accommodated in the minor groove of AT tracts.[71] Subsequent structural characterisation of oligonucleotide–Hoechst complexes, by means of both X-ray crystallography[71–74] and NMR spectroscopy,[75–78] revealed not

only a tolerance to the presence of a GC at one end of the binding site, but also interaction with an AT tract alone. The ability of Hoechst to tolerate either a GC or AT at the *N*-methylpiperazine end of the binding site arises from the presence of two Hoechst solution conformers. One of these conformers permits the *N*-methylpiperazine ring to remain external to the minor groove upon DNA binding, allowing an interaction with AT only.[71,79,80] Thus Hoechst is only weakly selective for GC tracts.

In an effort to develop DNA binding ligands with improved GC recognition features, various analogues of Hoechst have been synthesised and their DNA binding properties investigated.[81–86] The rationale employed[87,88] was similar in many ways to that applied to the AT specific DNA binding ligand netropsin, which resulted in the development of the lexitropsin class of ligands. The lexitropsins were also designed to exhibit predictable GC selectivity but the resulting compounds were typically indiscriminate in their DNA binding, interacting at a variety of sites composed of mixtures of AT and GC.[89–91] Similarly, analogues of Hoechst have generally displayed an increased tolerance to the presence of GC tracts at their binding sites rather than any selectivity for GC tracts. Apparently then, an improved understanding of the fundamentals of DNA–ligand interactions is needed if sequence specific DNA binding ligands are to be successfully developed.

Although DNA-Hoechst interactions have been intensively studied, the details of certain aspects of the binding remain unclear. In particular, the mode of interaction of Hoechst with GC rich binding sites is not fully known or understood. Similarly, a binding mode involving ligand stacking is thought to occur at high concentrations of bound ligand at

both AT and GC tracts, but the structural details of the binding modes are undetermined.[71,92] A more complete picture of Hoechst binding to DNA may enhance the suitability of the ligand as a model for the design of sequence specific DNA binding analogues. The further characterisation of Hoechst binding to GC rich sites would appear to be a particularly important objective given current interest in building GC recognition features into DNA binding ligands.

Several plausible binding modes have been suggested for Hoechst binding to GC rich DNAs. A binding mode involving ligand stacking in the major groove at GC sites was tentatively proposed on the basis of measured binding stoichiometries.[93,94] *CD* data have also suggested a binding mode where dimerisation or stacking occurs along the DNA polymer.[95] However, electric *LD* measurements combined with a competition binding study with the known intercalator proflavin provided evidence for Hoechst intercalation at GC binding sites. The authors speculated that simultaneous stacking and intercalation was possible if Hoechst bound in a mode in which part of the molecule was intercalated and part was located in the GC major groove.[92] The results from subsequent spectroscopic studies using electric *LD*[96–98] and combining flow *LD* measurements with *CD* and fluorescence data,[99] were interpreted as being consistent with such a binding mode in which part of the molecule intercalates and part is located in the GC major groove.

In the work presented here, spectroscopic techniques are used to investigate the binding, at medium to high *r* values, of Hoechst to poly[d(A-T)]$_2$ and poly[d(G-C)]$_2$ to permit analysis of the sequence dependent binding characteristics of the ligand. Spectroscopic

data from *CD*, flow *LD* and fluorescence experiments are complemented with *RLS* measurements to permit the detection and characterisation of ligand stacking on DNA.[20] Specific emphasis has been placed on the binding of Hoechst to poly[d(G-C)]$_2$ and on the ligand stacking interactions that occur at both AT and GC binding sites when the concentration of bound ligand is high.

5.2 Experimental

5.2.1 Materials

Hoechst was purchased from Sigma as the trichloride salt and used without further purification. Solution concentrations were determined in pure water using $\varepsilon = 4.2 \times 10^4$ $M^{-1}\,cm^{-1}$ for the 343 nm absorption band.[93] Hoechst was stored as the dry powder at −20°C in the dark until required. DNAs were purchased from Sigma and used as previously described (Section 4.2.1).

5.2.2 Spectroscopic titrations

Normal absorption, *CD*, *RLS* and fluorescence titrations were each performed according to an identical experimental protocol to permit direct comparison between the data sets. The titrations were performed at a constant concentration of Hoechst and repeated for both poly[d(G-C)]$_2$ and poly[d(A-T)]$_2$. Hoechst interaction with DNA was observed over a range of ligand/DNA mixing ratios by incrementally reducing the concentration of DNA during the course of the titration. An initial solution of DNA (100 μM), Hoechst

(20 μM), NaCl (20 mM) and phosphate buffer (1 mM; prepared as described in Section 4.2.2) was prepared along with a stock solution containing identical components but without DNA. The concentration of DNA was then reduced by making stepwise additions of the stock solution to give a range of ligand/DNA mixing ratios. A normal absorption, *CD*, *RLS* and fluorescence spectrum were recorded after each addition of stock solution. Solution volumes, the actual DNA concentrations and ligand/DNA mixing ratios used are detailed in Table 5.1.

[DNA] / μM	Total Solution Volume / μL	Added Stock Solution Volume / μL	*r* / Ligand per DNA Base
100	1500	0	0.2
80	1875	375	0.25
66.7	2250	375	0.3
57.1	2625	375	0.35
50	3000	375	0.4
44.4	3375	375	0.45
40	3750	375	0.5

Table 5.1 Experimental parameters for DNA–Hoechst spectroscopic titrations.

5.2.3 Linear dichroism

Flow *LD* spectra were measured on samples with identical DNA and Hoechst concentrations to those given in Table 5.1. Solutions for flow *LD* were prepared individually for each analogous titration step and normal absorption and *LD* spectra were recorded. The *LD* spectropolarimeter and UV–visible spectrometer were set to

correspond in terms of wavelength range and data interval prior to measurement of spectra.

5.2.4 Spectroscopy

Hoechst and DNA-Hoechst samples were scanned from 500 to 200 nm for normal absorption, *CD* and *LD* spectra. *RLS* and fluorescence emission spectra were recorded over a wavelength range of 600 to 200 nm, with an excitation wavelength of 343 nm for fluorescence measurements. DNA samples were scanned between 350 and 200 nm. Normal absorption spectra were collected on a Cary 1E UV-visible spectrophotometer. A Perkin-Elmer LS-50 luminescence spectrometer was used for *RLS* and fluorescence data collection. The excitation and emission slit widths used were 2.5 nm. The LS-50 was set to scan synchronously for *RLS* data collection. *CD* and *LD* spectra were measured on a Jasco J-715 spectropolarimeter.

CD data were averaged over eight 100 nm min^{-1} scans each measured with an averaging time of 1s and a data interval of 0.5 nm. *LD* data were also averaged over eight scans but an averaging time of 0.25 s, data interval of 0.5 nm and scan rate of 500 nm min^{-1} were used. Quartz fluorescence cuvettes with a 1 cm path length were employed for all spectroscopic measurements except flow *LD* spectrum measurement where a couette flow cell was used. Baseline measurements were made on pure water for *CD*, *LD* and *RLS* spectra and subsequently subtracted from the appropriate sample spectra. Excessively noisy *CD* spectra were smoothed used a Fourier transform noise reduction routine, ensuring that no distortion of λ_{max} occurred.

5.3 Results

5.3.1 Normal absorption titrations

The normal absorption spectrum of free Hoechst comprises absorption bands with maxima centred at 343, 264 and 209 nm. In the presence of DNA the Hoechst UV absorption band at 264 nm overlaps with the DNA transition at 260 nm and a single,

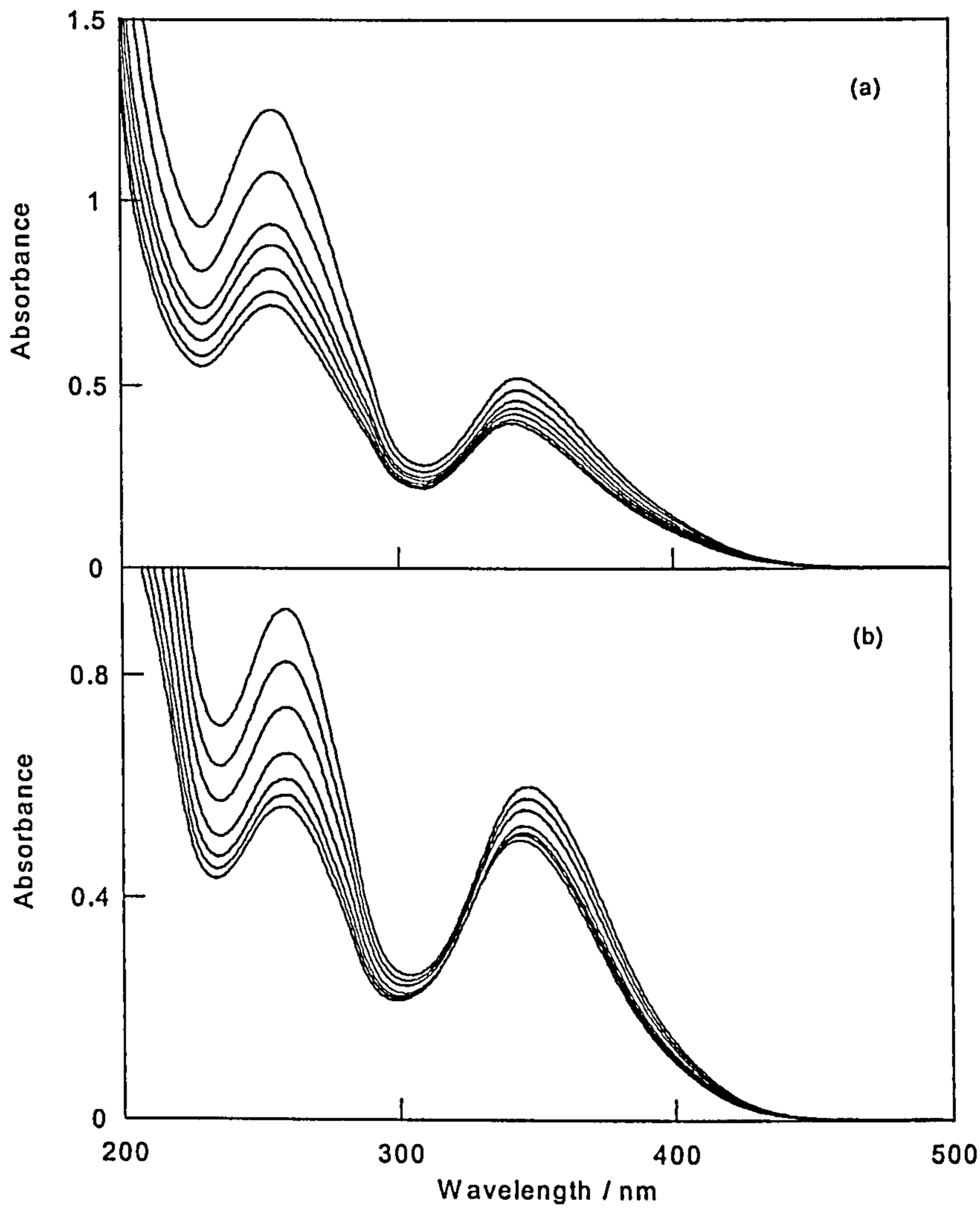

Figure 5.2 Normal absorption spectra of Hoechst (20 μM), NaCl (20 mM), phosphate buffer (1mM; pH 7) with (a) poly[d(G-C)]$_2$ (40 – 100 μM) and (b) poly[d(A-T)]$_2$ (40 – 100 μM) at variable *r* (0.2 – 0.5 in 0.05 increments; absorbance increases with *r*).

broad UV band is observed. Moreover, strong absorbance contributions from the presence of NaCl in the DNA-Hoechst systems masks the 209 nm Hoechst transition in the normal absorption spectrum. The spectra were collected at a constant Hoechst concentration thus spectral changes above 300 nm reflect DNA–Hoechst interactions. The Hoechst transition at 343 nm indicates changes in the electronic spectrum of Hoechst alone upon binding to DNA.

The normal absorption spectrum of the Hoechst complex with poly[d(G-C)]$_2$ (Figure 5.2a) comprises absorption bands at approximately 345 and 254 nm at $r = 0.2$. Thus the absorption band of free Hoechst (343 nm) is red shifted on binding to poly[d(G-C)]$_2$. As r increases, a blue shift in this band occurs and is consistent with increasing contribution from unbound ligand. Hypochromicity is also present in the lower energy Hoechst absorption on binding to poly[d(G-C)]$_2$, an effect that increases with r. Hypochromicity is usually observed in the absorption bands of aggregated or intercalated chromophores thus stacking effects may explain the observed decrease in the intensity of the 344 nm Hoechst band with increasing r.

The absorption spectrum of the Hoechst complex with poly[d(A-T)]$_2$ consists of two bands centred at 259 and 347 nm at $r = 0.2$. A greater hypochromic shift in the 347 nm band compared to that for Hoechst binding to poly[d(G-C)]$_2$ is observed and is consistent with the established higher binding affinity of Hoechst for poly[d(A-T)]$_2$. This band is red shifted by 4 nm relative to the free ligand wavelength maximum but the extent of the shift is reduced at higher r. As for the Hoechst complex with poly[d(G-C)]$_2$, a higher concentration of unbound ligand is the likely cause of the decreasing extent of red

shifting. As for Hoechst with poly[d(G-C)]$_2$, increasing hypochomicity at 347 nm is observed at higher *r* values and may indicate the presence of ligand stacking.

5.3.2 Circular dichroism titrations

CD spectra of the DNA-Hoechst complexes comprise *ICD* bands at wavelengths corresponding to the energy of Hoechst electronic transitions. The observation of an *ICD* for the achiral Hoechst transitions indicates the molecule is bound to DNA. The UV region of the *CD* spectra also contains contributions from the DNA. Thus the observed *CD* signature in the spectral region below 300 nm is a combination of the Hoechst *ICD* and the DNA *CD*.

CD spectra of the Hoechst complex with poly[d(G-C)]$_2$ (Figure 5.3a) comprise *CD* maxima at 334 nm and 274 nm. *CD* minima appear at 373 nm, 252 nm and 206 nm. Significant features of the spectra are that the same spectral form occurs for the *CD* bands across the range of *r* values. The observed independence of the form of the *CD* spectrum from *r* implies that the mode of Hoechst binding to poly[d(G-C)]$_2$ is constant over the conditions studied. Variations in the intensities of the *CD* spectra between *r* values are due to the decrease in DNA concentration at each successive titration step. *CD* intensity for an achiral ligand such as Hoechst in the presence of DNA is a function of the amount of that ligand bound to DNA. Unbound ligand does not contribute to the *CD* spectrum. Since the concentration of DNA decreases as the mixing ratio increases, the concentration of bound Hoechst also decreases. Thus the diminishing *CD* intensity observed for the Hoechst complex with poly[d(G-C)]$_2$ with increasing *r* is attributable to

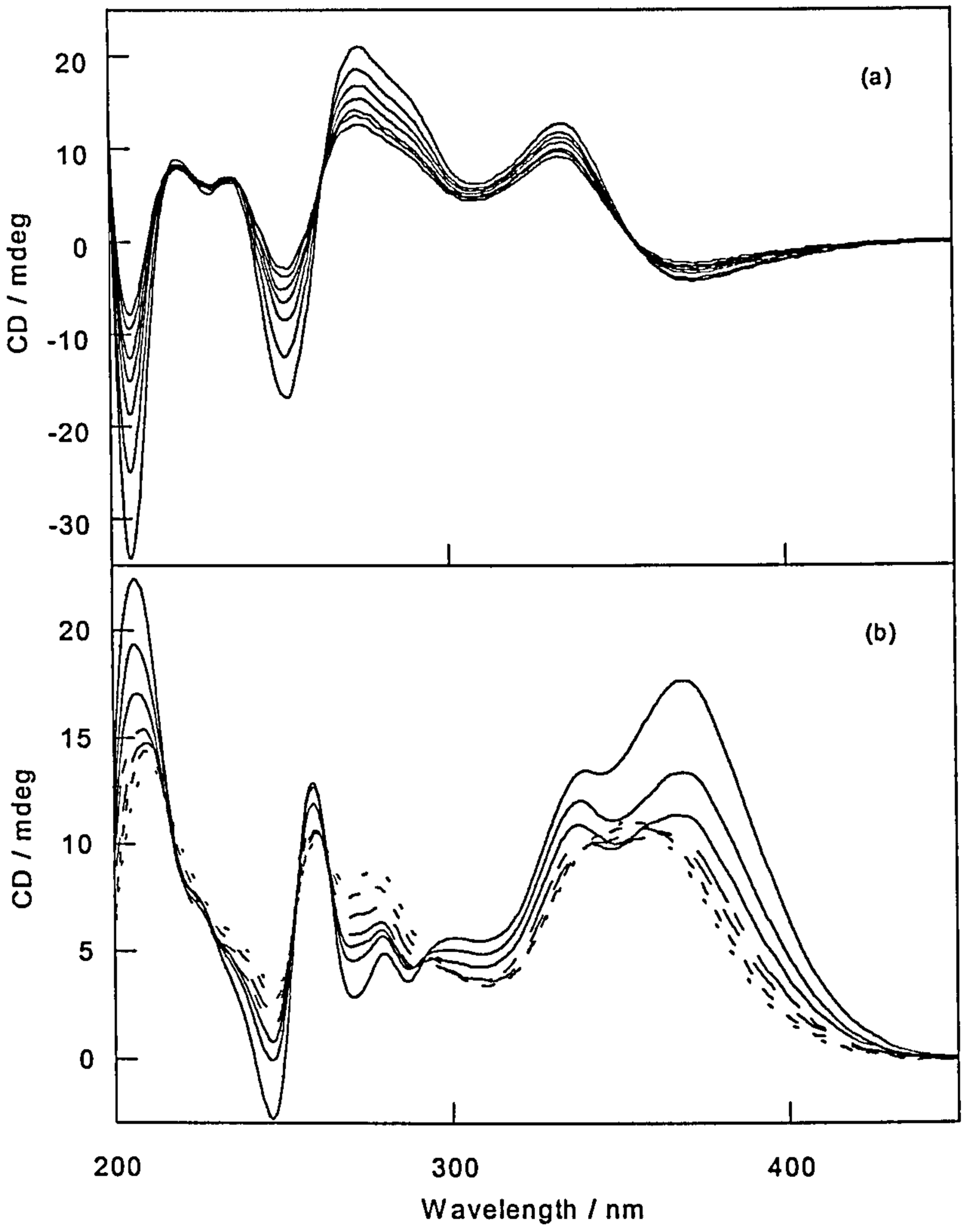

Figure 5.3 *CD* spectra of Hoechst (20 μM), NaCl (20 mM), phosphate buffer (1 mM; pH 7) and (a) poly[d(G-C)]$_2$ (40-100 μM) at variable r (0.2-0.5 in 0.05 increments; *CD* intensity decreases as r increases) and (b) poly[d(A-T)]$_2$ (40-100 μM), (——; *CD* intensity decreases with increasing r) $r = 0.2$-0.3; (– —) $r = 0.35$; (— —) $r = 0.4$; (– –) $r = 0.45$; (- - -) $r = 0.5$.

a decreasing concentration of both poly[d(G-C)]$_2$ and bound ligand. However, the shape of the *CD* spectrum above 300 nm is strongly reminiscent of that observed when exciton coupling occurs between stacked ligands. Exciton *CD* is usually characterised by disproportionately large increases in the ligand *ICD* intensity with increasing ligand concentration. Since the overall concentration of Hoechst remains constant and the concentration of bound Hoechst is decreasing as r increases, the occurrence of stacking

interactions between DNA bound Hoechst molecules cannot be detected with any certainty in these *CD* data. A similar situation is encountered in the UV region of the spectrum. The *CD* band shape is also consistent with a ligand-ligand exciton interaction but spectral overlap between absorption bands of Hoechst and DNA inhibit the clear observation of any such effects.

In the presence of poly[d(A-T)]$_2$ Hoechst exhibits an *r* dependent *ICD* signature (Figure 5.3b). The wavelength maxima and *CD* band shapes of the Hoechst transition above 300 nm exhibit significant variation with *r*. At $r = 0.2$ a positive *ICD* band with maxima at 369 nm and 355 nm is observed. This band shape is roughly retained albeit with progressively diminishing *CD* intensity and wavelength shifts (Table 5.2) through to $r = 0.35$. The $r = 0.4$ *CD* spectrum is quite different in shape from that observed at $r < 0.4$ and is characterised by a single wavelength maximum at approximately 355 nm. Additionally, a small increase in *CD* intensity is observed at this wavelength relative to the $r = 0.35$ spectrum and further increases are observed through to $r = 0.5$ with no variation in *CD* band shape. The initial decreases in *ICD* intensity at low *r* arise from the decrease in concentration of DNA bound Hoechst as the concentration of the DNA itself is reduced. The subsequent increase in the magnitude of the *ICD* could be the result of exciton *CD* due to ligand–ligand interactions on poly[d(A-T)]$_2$ since the *CD* intensity increase occurs despite a probable reduction in the concentration of bound Hoechst. The *ICD* spectrum above 300 nm thus suggests the operation of at least two binding modes, one of which may involve ligand stacking. The spectra below 300 nm contain overlapping DNA and Hoechst transitions. Positive *CD* bands are observed at 259 nm and 207 nm in the UV region of the spectrum with negative *CD* at 246 nm. The

intensities of the bands diminish with increasing *r* primarily as a consequence of the associated decreasing contribution from DNA absorption in this spectral region.

	ICD band with double maxima				*ICD* exciton band	
r / ligand per DNA base	*CD* / mdeg	λ_{max} / nm	*CD* / mdeg	λ_{max} / nm	*CD* / mdeg	λ_{max} / nm
0.2	17.7	369	13.5	341	–	–
0.25	13.4	369	12.0	339	–	–
0.3	11.3	367	10.9	338	–	–
0.35	10.5	363	10.1	340	–	–
0.4	–	–	–	–	10.7	355
0.45	–	–	–	–	10.9	355
0.5	–	–	–	–	11.2	355

Table 5.2 *CD* spectroscopic data for Hoechst complexes with poly[d(A-T)]$_2$.

5.3.3 Fluorescence titrations

The fluorescence spectrum of free Hoechst contains a single, broad emission band centred at 491 nm following excitation of the longer wavelength absorption band at 343 nm. In the presence of poly[d(G-C)]$_2$ the form of the fluorescence emission spectrum is *r* dependent (Figure 5.4a). At $r = 0.2$ the spectrum exhibits a blue shifted emission band (maximum at 486 nm) relative to the free Hoechst fluorescence wavelength. Furthermore, the intensity of the fluorescence emission is approximately 5 times less intense than that observed for an identical concentration of free Hoechst. A shorter wavelength fluorescence shoulder (approximately 389 nm) with weak intensity is also apparent in the emission spectrum. As *r* is increased, the 486 nm band progressively decreases in

intensity and shifts to higher energy (482 nm at $r = 0.5$). Increasing r is also accompanied by an increase in the intensity of the 389 nm shoulder. At $r = 0.5$ the shoulder intensity is approximately half that of the 482 nm band compared with only one tenth relative intensity at $r = 0.2$.

Since the fluorescence properties of any fluorophore are dependent on environment, the differences in the fluorescence characteristics of Hoechst in the presence of poly[d(G-C)]$_2$

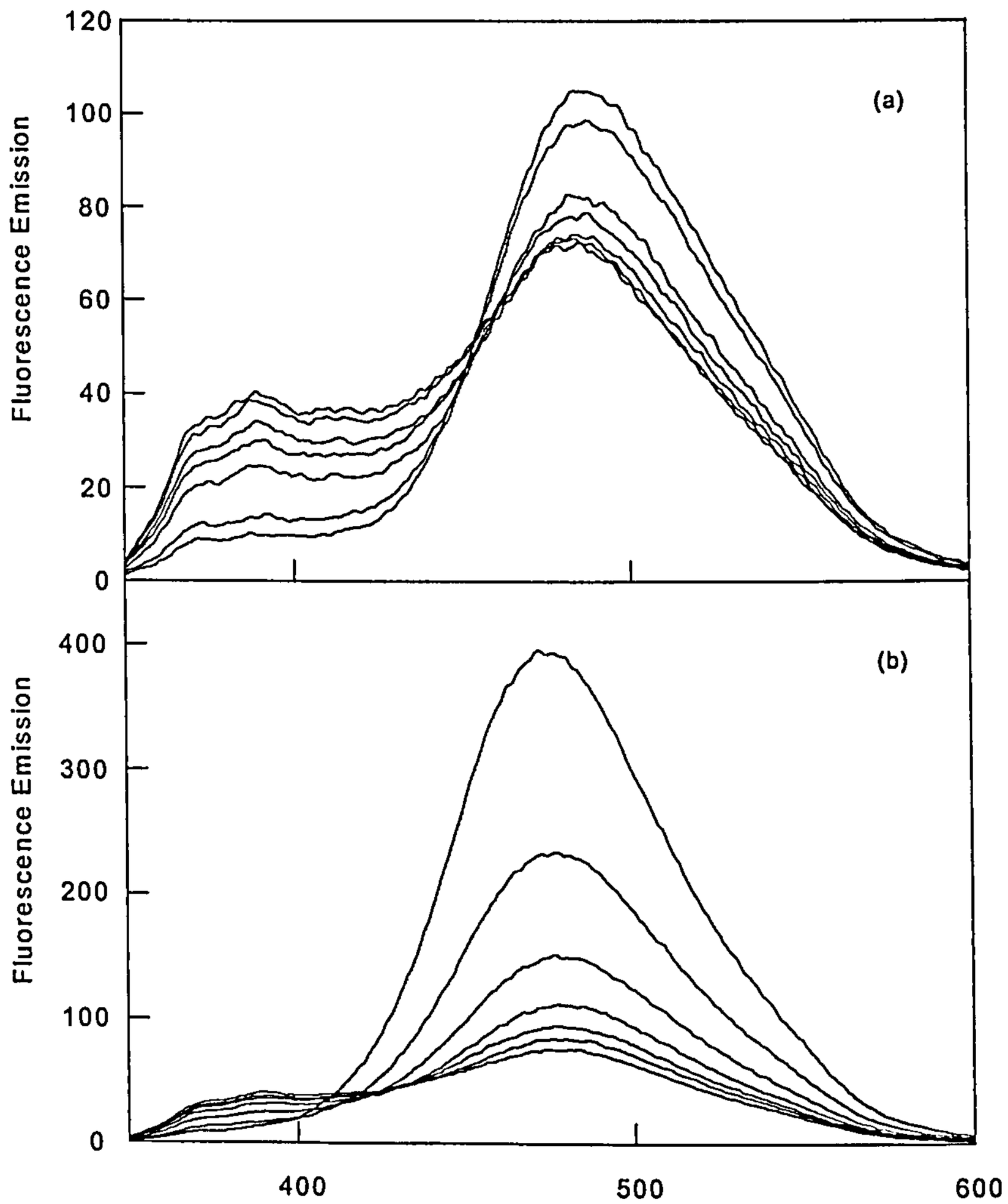

Figure 5.4 Fluorescence emission spectra of Hoechst (20 μM), NaCl (20 mM), phosphate buffer (1 mM; pH 7) and (a) poly[d(G-C)]$_2$ (40-100 μM), ($r = 0.2$-0.5 in 0.05 increments; ~476 nm fluorescence intensity decreases as r increases) and (b) poly[d(A-T)]$_2$ (40-100 μM), ($r = 0.2$-0.5 in 0.05 increments; ~486 fluorescence intensity decreases as r increases).

relative to the free ligand arise from DNA binding. The degree of fluorescence quenching is greater for DNA bound Hoechst than for free Hoechst in solution. This observation in itself is significant. Ligands such ethidium and DAPI (Figure 2.3) exhibit a large fluorescence enhancement upon binding to DNA because their binding sites provide protection from the fluorescence quenching solvent.[9,18] For the latter ligand the extent of the fluorescence enhancement was reduced upon binding to GC sequences in a stacked binding mode since exciton coupling between the electronic transitions of the stacked DAPI molecules quenched the fluorescence. Fluorescence enhancement is not always observed on DNA binding even in the absence of ligand–ligand exciton effects. For example, the observed fluorescence quenching of anthracene-9-carbonyl-N^1-spermine on binding to DNA was attributed to strong electronic coupling of the bound ligand to the DNA bases.[100,101] These fluorescence data therefore suggest that the Hoechst binding mode to poly[d(G-C)]$_2$ is one which may involve either ligand–ligand coupling interactions, strong coupling to the DNA bases or a combination of the two effects.

The observed fluorescence shoulder cannot easily be explained in terms of solvent or binding site quenching effects. The appearance of a fluorescence spectral feature unique to DNA bound Hoechst implies the formation of a Hoechst species unique to DNA bound Hoechst. Such a species is likely to involve the formation of dimers or more extensively stacked ligands on DNA.[99] The observed increase in the fluorescence shoulder intensity with r indicates the increased tendency of the DNA bound ligands to stack at high r. The occurrence of Hoechst stacking would also contribute to the observed quenching of the monomer fluorescence band. The extent of the stacking cannot be extracted from the measured fluorescence data.

In the presence of poly[d(A-T)]$_2$ Hoechst exhibits a fluorescence band at 476 nm at r = 0.2, 15 nm higher in energy than that observed for free Hoechst (Figure 5.4b). A small wavelength shift (the maximum appears at 478 nm at r = 0.5) and a diminishing intensity are observed in this fluorescence emission band across the range of r values. The r = 0.2 fluorescence intensity is lower than the equivalent free ligand emission intensity but only a factor of approximately one third, in contrast to the case for Hoechst binding to poly[d(G-C)]$_2$. However, as r increases the ~476 nm fluorescence intensity falls off rapidly such that the r = 0.5 emission band has approximately 15% of the intensity of the r = 0.2 band. The decrease is accompanied by the appearance and subsequent increase in intensity of a higher energy fluorescence shoulder with a maximum at approximately 390 nm. The shoulder is very weak but nonetheless detectable in the r = 0.2 spectrum and significantly stronger in the r = 0.5 spectrum.

The observed fluorescence quenching on DNA binding relative to the free solution fluorescence intensity suggests that Hoechst under these conditions is not bound to the poly[d(A-T)]$_2$ minor groove in a mode where Hoechst is buried deep in the groove. This minor groove binding mode has been well established as leading to a large fluorescence enhancement on binding to AT rich regions of DNA.[69] The presence of the 390 nm emission band and the quenching in the long wavelength band suggest the occurrence of ligand–ligand exciton interactions in the presence of poly[d(A-T)]$_2$. The stacked binding mode is present at r = 0.2 but is favoured at higher r values. The fall off in the intensity of the ~476 nm emission band reflects the formation of ligand stacks at the expense of the monomer binding mode as r increases. The observation that ligand stacking occurs at the expense of, rather than in addition to, monomer binding is significant. Although

this finding is to some extent unsurprising given the very high affinity of Hoechst for poly[d(A-T)]$_2$, it does suggest the monomer and stacked binding modes are related in terms of DNA binding site location. The effect of changes in ligand environment, such as hydrophobic interactions with the DNA binding site versus hydrophilic interactions with the solvent, also contribute to the observed fluorescence quenching of the ~476 nm emission band relative to the free ligand, as previously discussed.

5.3.4 Resonance light scattering titrations

Before performing an analysis of the *RLS* behaviour of Hoechst-DNA systems, it was first necessary to establish that when a Hoechst-DNA solution is scanned synchronously with a standard fluorimeter that the origin of the resulting signal is an enhanced light scattering effect. There are no literature data available describing the *RLS* phenomenon occurring for any systems other than porphyrins,[20] 9-hydroxyellipticine (see chapter 6)[102] and metal complexes with terpyridine ligands[57,58] thus a specific precedent for the observation of Hoechst *RLS* is lacking. Hoechst is fluorescent and the possibility exists that a synchronous scan may also detect fluorescence emission in addition to or instead of the *RLS*. In the absence of DNA the measured fluorescence emission intensity is higher than that corresponding to Hoechst bound to DNA. If the spectral features in the synchronous scan spectra of the DNA–Hoechst complexes were due to fluorescence rather than *RLS* then a solution of free Hoechst would be expected to exhibit those same spectral features with at least equivalent intensity, since Hoechst does not aggregate in solution. No large magnitude spectral feature is observed when free Hoechst is synchronously scanned, nor is there any signal at ~480 nm where the fluorescence is

large, thus synchronous scanning in this case is insensitive to fluorescence and the DNA–Hoechst signal is indeed due to enhanced light scattering.

The *RLS* spectra of Hoechst in the presence of poly[d(G-C)]$_2$ (Figure 5.5a) exhibit peaks at 393 nm and 305 nm across the range of *r* values. The intensity of the signal shows only small variation with *r* and generally decreases in intensity as *r* increases. The observation of an *RLS* signal indicates the formation of extended Hoechst aggregates since no signal

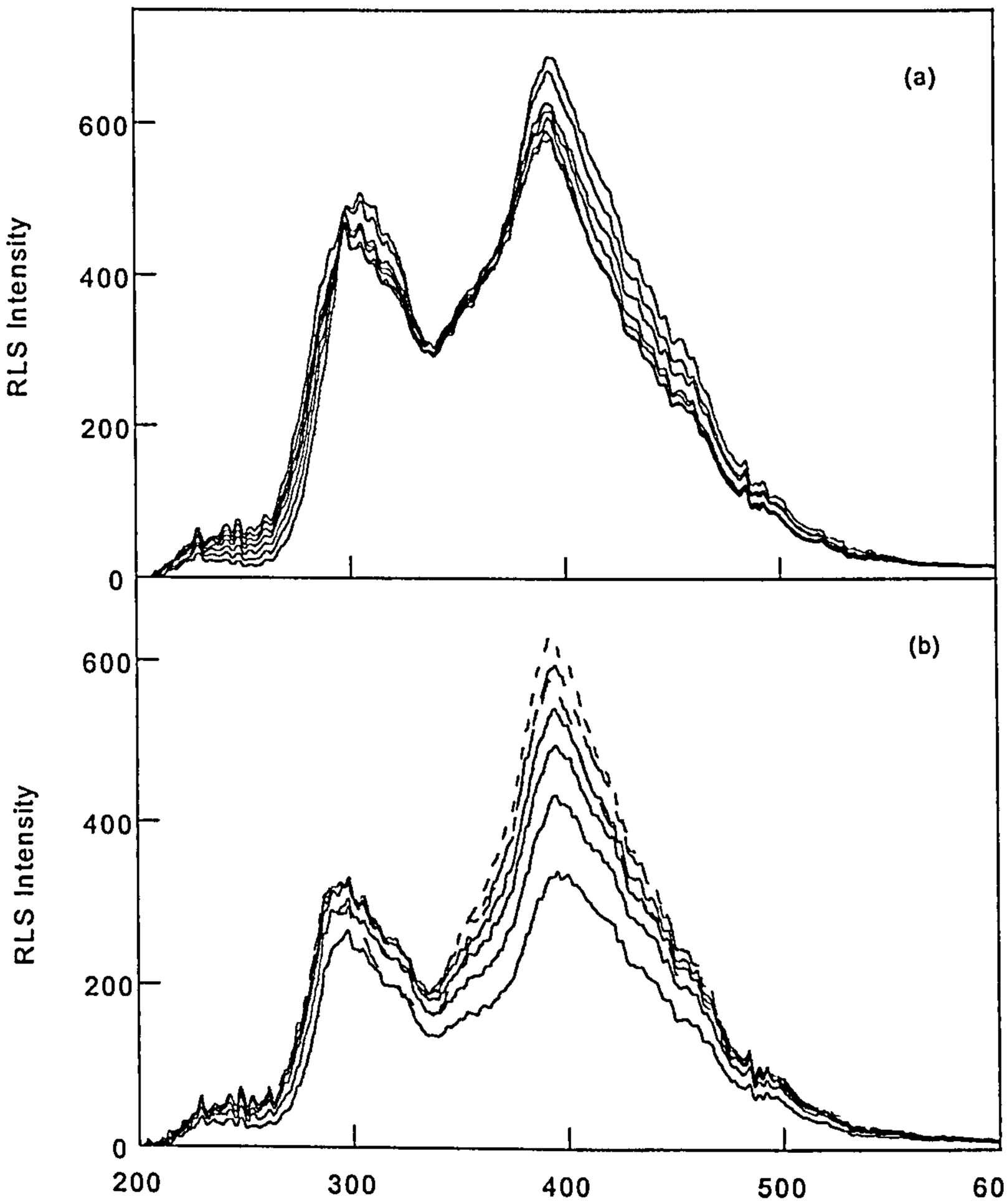

Figure 5.5 *RLS* spectra of Hoechst (20 μM), NaCl (20 mM), phosphate buffer (1 mM; pH 7) and (a) poly[d(G-C)]$_2$ (40-100 μM) $r = 0.2, 0.25, 0.35, 0.3, 0.5, 0.4, 0.45$ in order of decreasing intensity at 393 nm, and (b) poly[d(A-T)]$_2$ (40-100 μM) (——) $r = 0.2$-0.35 in order of increasing intensity at 397 nm, (— –) $r = 0.4$, (– –) $r = 0.45$ and (- - -) $r = 0.5$.

would be expected if Hoechst stacked to form dimers or small oligomers. However, the observed *RLS* maxima do not correspond to any Hoechst absorption maximum as would be expected in the *RLS* spectrum of extended aggregated chromophores.[20] Moreover, a dip in the spectrum occurs at 338 nm, close to the Hoechst 343 absorption band maximum.

The Hoechst-DNA system differs in one fundamental respect from previously reported aggregate systems that have been studied with *RLS*. Only the DNA bound Hoechst component of the system is aggregated and any unbound Hoechst remains as a monomer in solution. In both porphyrin and terpyridine aggregation the stacking occurs for both the DNA bound and unbound forms of the ligands. This results in the entire ligand component of these systems contributing to the *RLS* spectrum. In the case of Hoechst aggregation, however, any monomer absorption contributes to the *RLS* spectrum by reducing the intensity of the measured light scattering across the Hoechst absorption envelope. The observed *RLS* spectrum is therefore the net result of enhanced light scattering by aggregated Hoechst minus absorption by Hoechst monomers. The presence of Hoechst dimers or oligomers too small to exhibit *RLS* would also contribute to the absorption component of the spectrum. The peaks in the *RLS* spectrum therefore do not correspond to the true *RLS* maximum because this maximum overlaps with a Hoechst absorption band. Since the experiments were conducted at a constant Hoechst concentration and the absorption contribution to the *RLS* spectrum is approximately the same for all values of *r*, the *RLS* intensity outside the Hoechst absorption band is still a good indicator of aggregate size. Thus, extended aggregates are forming on poly[d(G-C)]$_2$ and there appears to be little variation in aggregate size across the range of *r* values.

In the presence of poly[d(A-T)]$_2$, Hoechst *RLS* spectra (Figure 5.5b) exhibit monomer absorption versus aggregate enhanced light scattering effects, as previously discussed for poly[d(G-C)]$_2$. The *RLS* peaks occur at 395 and 297 nm with a dip at 336 nm. The observation of an *RLS* signal for this system indicates the occurrence of extended Hoechst aggregate formation on poly[d(A-T)]$_2$. The *RLS* intensifies significantly with *r* and indicates the increased tendency of Hoechst to form extended aggregates on poly[d(A-T)]$_2$ as *r* increases at constant ligand concentration.

5.3.5 Linear dichroism

Flow *LD* spectra of Hoechst-DNA complexes exhibit an *LD* band corresponding to the 343 nm Hoechst normal absorption band and a UV band containing absorption contributions from both DNA and Hoechst. The observation of an *LD* signal for the Hoechst electronic transitions indicates the Hoechst is bound to the flow oriented DNA.

Flow *LD* spectra of the Hoechst complex with poly[d(G-C)]$_2$ exhibit negative bands at 347 nm and 255 nm (Figure 5.6a). The observed wavelength maxima are independent of *r*. The *LD* spectrum is negative across the entire wavelength range and for all *r* values. A negative *LD* is expected for the DNA absorption band since the bases are approximately perpendicular to the helix axis along which the DNA is oriented, but the sign of the *LD* corresponding to the Hoechst transitions is ligand orientation dependent. Although the sign of the Hoechst component of the 255 nm *LD* band is not directly

observable due to absorption overlap with the DNA bases, the Hoechst transition is making a negative contribution to the net *LD* band. The 255 nm transition moment is approximately long axis polarised.[99] Since the 347 nm transition moment also has approximate long axis polarisation[99] both the 255 and 347 nm transitions would be expected to exhibit the same sign in the *LD* spectrum unless the binding orientation was such that the Hoechst plane was near 55° to the helix axis. Since the 347 nm transition exhibits a strong negative *LD* (thus is unlikely to lie close 55° where $LD = 0$) the 255 nm

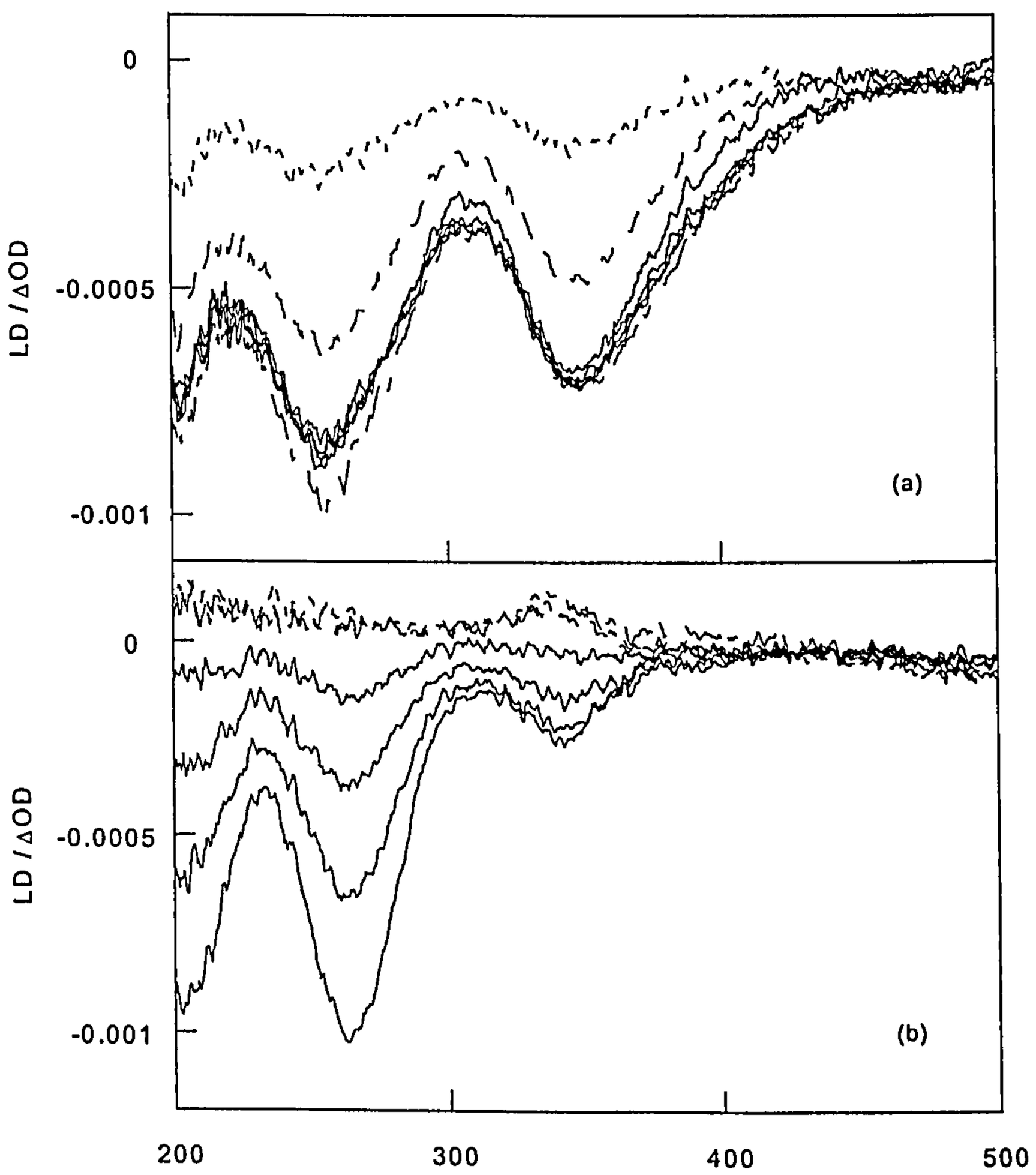

Figure 5.6 Flow *LD* spectra of Hoechst (20 μM), NaCl (20 mM), phosphate buffer (1mM; pH7), (a) poly[d(G-C)]$_2$ (40-100 μM), (— –) $r = 0.2$, (——) $r = 0.25$-0.4, (– – –) $r = 0.45$, (- - - -) $r = 0.5$ and (b) poly[d(A-T)]$_2$ (40-100 μM), (——) $r = 0.2$-0.35 (decreasing negative *LD* at 263 nm as r increases), (— –) $r = 0.4$, (– – –) $r = 0.45$, (- - - -) $r = 0.5$.

is also making a negative contribution to the spectrum.

The negative *LD* observed for the Hoechst transitions at 255 and 347 nm indicates the orientation of these in-plane $\pi \rightarrow \pi^*$ transition moments is closer to the plane of the DNA bases than to the helix axis. The magnitude of the *LD* bands are approximately constant between $r = 0.2 - 0.4$ for the 437 nm band and between $r = 0.25 - 0.4$ for the 255 nm band. This observation is significant since the decrease in DNA concentration with each successive *r* increase would be expected to decrease the DNA *LD*. There are two plausible explanations for the observed *LD* behaviour. Firstly, the *LD* signal size is dependent on the degree of orientation thus an increase in the extent of DNA orientation with *r* would offset the absorption loss associated with a lower DNA and bound Hoechst concentration. Such an effect would be expected for an intercalated binding mode in which Hoechst insertion between the base pairs lengthened and stiffened the DNA helix leading to better orientation in the solution flow and larger negative *LD*. Secondly, a change in binding mode in which the orientation of the bound Hoechst transition moments align more perpendicular to the DNA helix axis as *r* increases would also lead to larger *LD* signals. The two effects cannot be differentiated on the basis of these *LD* data alone (as both Hoechst and DNA absorb at ~260 nm it is not possible to determine the extent of the DNA orientation decrease). However, the sign of the *LD* is suggestive of a binding geometry in which the Hoechst plane lies close to that of the DNA bases.

Flow *LD* spectra of the Hoechst complex with poly[d(A-T)]$_2$ exhibit *r* dependent *LD* (Figure 5.6b). A negative *LD* band is observed over $r = 0.2$-0.3 at 342 nm. There is no net *LD* at this wavelength at $r = 0.35$ but a positive *LD* band is apparent between $r = 0.4$-

0.5 at 336 nm. The observation of a negative *LD* band at $r = 0.2$ that diminishes in intensity and becomes positive as *r* increases indicates a change in binding geometry with *r*. At $r = 0.2$ Hoechst is bound in an orientation in which the 342 nm transition moment is oriented more perpendicular than parallel to the helix axis. However, the intensity of the negative *LD* is weak and is not comparable in magnitude with that observed in the UV region of the spectrum. Thus the Hoechst plane is probably not aligned closely with the plane of the DNA bases as would be expected for an intercalated binding mode. The presence of a near zero *LD* for the 342 nm Hoechst absorption band when $r = 0.35$ is interesting since zero *LD* corresponds to an average angle of 55° between the DNA helix axis (orientation axis) and the absorbing Hoechst transition moment. Since the 342 nm transition is approximately long axis polarised, the molecule is aligned such that its average long axis is approximately 55° to the helix axis at $r = 0.35$. The positive *LD* bands apparent at $r = 0.4 - 0.5$ indicate a binding mode in which the Hoechst transition moments are aligned more parallel to the DNA helix axis than perpendicular. The observed positive *LD* at high *r* precludes intercalation as a possible binding mode.

In the UV region of the *LD* spectrum the observed *LD* (263 nm) is strongly negative at $r = 0.2$ but the intensity of the band diminishes rapidly as *r* increases. At $r = 0.4 - 0.5$ no net *LD* appears in the UV spectral region. The rapid fall off in the intensity of the *LD* band is due to a combination of effects. A decreasing DNA concentration with increasing *r* reduces the DNA contribution to the 263 nm *LD* and the change in Hoechst binding geometry also partially diminishes the 236 nm *LD* intensity. At $r \geq 0.4$ the lack of an observed *LD* is due to a positive Hoechst contribution to the *LD* cancelling the negative

DNA *LD* [it is not due to a lack of orientation since the longer wavelength has *LD* (Figure 5.6b)].

5.4 Discussion

Spectroscopic techniques have been applied to study the binding of Hoechst to the synthetic DNA polymers poly[d(A-T)]$_2$ and poly[d(G-C)]$_2$. The medium to high *r* binding modes were examined to permit investigation of ligand stacking effects on DNA and the related Hoechst binding modes to both GC and AT rich binding sites. Analysis of *CD* data has highlighted the sequence dependent interactions of Hoechst with DNA and the other techniques facilitated further characterisation of the binding modes. *RLS* and fluorescence spectroscopies were primarily used to detect and characterise the stacked binding modes and were complemented by *LD* data to provide Hoechst-DNA binding geometry information.

5.4.1 Interaction of Hoechst with poly[d(G-C)]$_2$

The collective spectroscopic results suggest that Hoechst binds to poly[d(G-C)]$_2$ in a single binding geometry over the concentration range studied. A significant feature of the binding is the occurrence of ligand stacking on the DNA. However, the precise extent of the stacking is dependent on *r*. Although the *RLS* data did not require an increase in the absolute concentration of stacked Hoechst or even in the extent of the stacking, data from the fluorescence experiments were suggestive of an increase in the relative concentration of the aggregated component of the system. The small *RLS* intensity decrease with *r* can

therefore be attributed to the net result of increased extent of stacking versus decrease in concentration of stacked Hoechst caused by DNA dilution during the course of the titration experiments. The same effect is responsible for the uncertainty over the occurrence of exciton effects in the *CD* spectra of the Hoechst complex with poly[d(G-C)]$_2$. The fact that *RLS* is observed at all is proof that the biphasic *CD* signature of the Hoechst 343 nm absorption band is due to exciton coupling effects. Thus the extent of Hoechst stacking increases as the concentration of bound ligand relative to the DNA concentration increases, although extended aggregates are present over the entire concentration range studied.

The presence of extended stacks at all *r* values has important implications for the likely binding geometry of Hoechst to poly[d(G-C)]$_2$. No change in binding geometry was obvious from analysis of the *LD* data, where changes in concentration and the degree of flow orientation explained the observed *LD* intensity changes. The lack of intensity decrease in the UV *LD* band is probably due to better DNA orientation caused by helix lengthening since the observation of an invariant *CD* signature for all *r* values suggests no change in Hoechst binding mode occurs. DNA helix lengthening usually occurs upon ligand intercalation. The requirements of the binding geometry of Hoechst to poly[d(G-C)]$_2$ are that the average Hoechst plane lies more parallel than perpendicular to the plane of the DNA bases and that some part of the molecule is probably intercalated (full intercalation is not sterically possible for Hoechst[99]). The binding orientation must also permit the occurrence of ligand–ligand interactions and the formation of extended Hoechst stacks along the DNA helix. The result of the collective binding geometry constraints is that the most probable binding mode for Hoechst to poly[d(G-C)]$_2$, on the

basis of the spectroscopic data presented here, is one where the molecule partially intercalates and forms extended aggregates in one of the DNA grooves. The *N*-methylpiperazine group is too bulky to intercalate thus the hydroxyphenyl would be the intercalating group. It is conceivable that this group alone when intercalated would not perturb the DNA bases to the extent of causing significant helix lengthening. Thus at least part of the adjacent benzimidazole group may also intercalate, leaving the second benzimidazole to interact with adjacently bound Hoechst molecules in a DNA groove. The DNA helical twist or the intrinsic crescent shape of the ligand may be important in preventing steric clashes between the adjacent *N*-methylpiperazine groups. The steric constraints of such a binding mode would favour the major groove, however, no direct evidence for major over minor groove binding is extractable from the spectroscopic data in this work.

5.4.1 Interaction of Hoechst with poly[d(A-T)]$_2$

Hoechst binds poly[d(A-T)]$_2$ in an *r* dependent mode. The spectroscopic data indicate the increasing prominence of ligand–ligand interactions at higher *r* values when Hoechst binds poly[d(A-T)]$_2$. In the presence of poly[d(A-T)]$_2$ Hoechst exhibits a much broader extent of stacking over the range of *r* values than is observed for poly[d(G-C)]$_2$. The weak *RLS* observed at $r = 0.2$ for Hoechst binding to poly[d(A-T)]$_2$ suggests Hoechst binds DNA as monomers, dimers or small oligomers under these conditions. The observation of a weak but detectable shoulder in the DNA–Hoechst fluorescence spectrum even at $r = 0.2$ is consistent with the presence of DNA bound dimers or oligomers too small to cause an enhanced light scattering. The progressively increased

extent of stacking at higher *r* values involves the formation of extended Hoechst stacked along the poly[d(A-T)]$_2$ helix. Comparison of the *RLS* magnitudes observed for Hoechst binding to poly[d(A-T)]$_2$ and poly[d(G-C)]$_2$ indicates the size of the aggregates to be similar on both DNAs at $r = 0.5$ although the *r* dependence of aggregate size is much greater for poly[d(A-T)]$_2$.

Combined *CD* and *LD* spectroscopic data suggest the binding mode of Hoechst to poly[d(A-T)]$_2$ differs considerably from that observed for poly[d(G-C)]$_2$ over the conditions studied. The gradual loss of the double maxima *CD* signature characterising the medium *r* Hoechst binding mode to poly[d(A-T)]$_2$, in favour of the exciton mode, delineates a difference in binding orientation between the small oligomer and extended stack binding modes. *LD* facilitates assignment of the likely binding geometries for these two modes. At low *r*, the binding of Hoechst to AT tracts is well established as minor groove in which the average Hoechst plane follows the pitch of the groove. A positive *LD* band would be observed for this binding mode in which the plane of the molecule makes an approximately 45° angle with the DNA helix axis. The observation of negative *LD* at $r = 0.2$ indicates the very different nature of the medium *r* binding mode. The negative *LD* magnitudes measured for Hoechst binding to poly[d(A-T)]$_2$ are inconsistent with intercalation (the Hoechst complex with poly[d(G-C)]$_2$ is probably partially intercalated and the corresponding *LD* magnitudes are larger). Thus the average Hoechst plane lies more perpendicular than parallel to the helix axis in the presence of poly[d(A-T)]$_2$ but not to the extent of being coplanar with the plane of the DNA bases. In the absence of intercalation such a binding orientation is unlikely if Hoechst were bound in the poly[d(A-T)]$_2$ minor groove. The groove is only just wide enough to accommodate

the molecule at 45° thus any other minor groove orientation is improbable. Only a binding geometry in which Hoechst lies in the poly[d(A-T)]$_2$ major groove is consistent with the measured *LD* data. The major groove binding orientation would then permit an alignment increasingly parallel to the helix axis as the extent of the Hoechst stacking increases. The exact geometry of the extended stack in terms of the relative alignment of adjacent Hoechst molecules is difficult to determine from these data. A binding mode in which the Hoechst molecules were aligned in a head to tail arrangement up the major groove would permit interaction between the π systems of the stacked Hoechst and avoid steric clashes between adjacent *N*-methylpiperazine groups.

5.5 Conclusions

The medium to high *r* binding modes of Hoechst to poly[d(G-C)]$_2$ and poly[d(A-T)]$_2$ have been studied with *CD*, *LD*, *RLS*, fluorescence and normal absorption spectroscopy. The spectroscopic data show a strong dependence of binding mode on DNA sequence. Hoechst binds to poly[d(G-C)]$_2$ in a mode independent of the *r* values studied, that requires both intercalation and stacking, as evidenced by the observation of an enhanced *RLS* and negative *LD*. These results would therefore appear to support the proposal that Hoechst partially intercalates with part of the molecule stacked in the poly[d(G-C)]$_2$ major groove.[96,99] The observed *RLS* provides the first direct evidence for the formation of extended ligand stacks for Hoechst binding to DNA.

Hoechst binds poly[d(A-T)]$_2$ in an *r* dependent mode. Significantly, the previously well characterised minor groove binding geometry of Hoechst to poly[d(A-T)]$_2$ was not

observed at the relatively high *r* values studied in this work. Instead, Hoechst binds in an orientation in which the average Hoechst plane is significantly more perpendicular to the helix axis than would be expected for an exclusively minor groove binding geometry. The absence of the minor groove binding mode is attributed to the formation of Hoechst dimers or small oligomers at the lower *r* values studied and the formation of extended stacks at the higher *r* values. This binding mode is proposed to occupy the poly[d(A-T)]$_2$ major groove on the basis of steric considerations.

6 Spectroscopic Studies of 9-hydroxyellipticine binding to DNA

6.1 Introduction

9-OHE (Figure 6.1b) is one of a number of ellipticine (Figure 6.1a) derivatives that exhibit anticancer activity in cell lines.[5] The mode of action of ellipticine and various derivatives has been established as being via interaction with DNA.[103] Structural investigations of the DNA–ellipticine complexes have determined intercalation to be the therapeutically active binding mode.[104] DNA bound ellipticine interferes with the action of topoisomerase II though a mechanism that induces either an enhanced forward rate of DNA cleavage by the enzyme or illegitimate DNA recombination events following strand cleavage.[105] Since ellipticine is present in both charged (protonated) and uncharged forms under physiological conditions, initial complex formation occurs through binding to DNA in the case of the charged form and to topoisomerase II for the neutral form of the ligand.[106] In either case, ellipticine is present upon enzyme complexation with DNA.

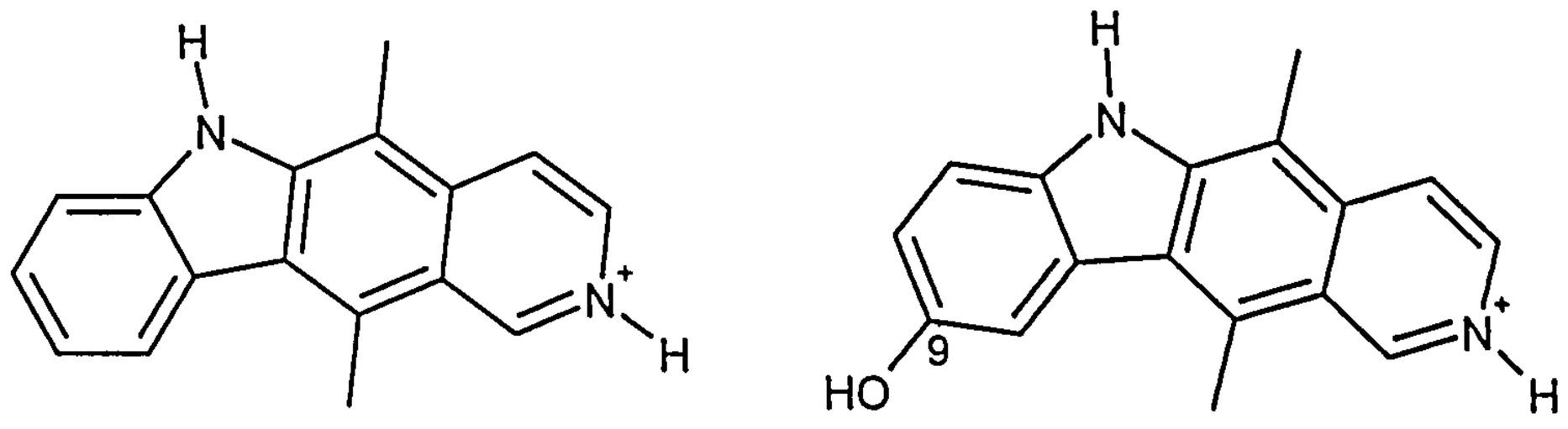

(a) (b)

Figure 6.1 Structures of (a) ellipticine and (b) 9-hydroxyellipticine

In an effort to develop ellipticine based drugs with enhanced anticancer activity and improved specificity for cancerous cells, several ellipticine analogues have been synthesised and their interactions with DNA and topoisomerase II investigated.[107-111] One rationale was to enhance the DNA binding by the placement of an electrophilic substituent at C9 on ellipticine to enable an interaction with the anionic oxygen of the DNA phosphate backbone.[112] This particular strategy was based on the assumption that bound ellipticine is oriented with its long axis parallel to the long axis of the intercalation site. Accordingly, the binding constant of 9-OHE to DNA is an order of magnitude higher than that of ellipticine with intercalation observed as the preferential binding mode. The presence of the 9-hydroxyl group also stabilises the DNA–topoisomerase–ellipticine complex.[113]

Although enhanced DNA binding and anticancer activity was observed for 9-OHE, evidence to support the occurrence of the initially assumed binding geometry for ellipticine, and the retention of this binding orientation for 9-OHE, was lacking. The results from a spectroscopic study of the binding of 9-OHE derivatives to DNA suggested that intercalation, groove binding and external binding with ligand stacking could occur.[114,115] The spectroscopic data were further concluded to be consistent with an intercalated binding orientation in which the 9-OHE derivatives' long axes were parallel to the dyad axis rather than the long axis of the intercalation site. However, this conclusion was drawn by analogy with transition moment polarisation data for methylene blue.[116] Without a knowledge of the 9-OHE transition moment polarisations the assignment of the orientation of the transition moments relative to those of the DNA bases is not possible with any degree of certainty.

Although the potential of ellipticines as anticancer and antiviral agents is high, their relatively low solubility has inhibited their progression to clinical trials. The limited extent of therapeutic use of ellipticine derivatives includes the treatment of advanced breast cancer with elliptinium acetate (Celiptium),[117] 2-methyl-9-hydroxyellipticine and 2-(diethylamino)ethyl-9-hydroxyelliptcine.[118] 2*N*-methyl-hydroxyelliptcine has also been used in the treatment of AIDS. Additionally, various 9-substituted ellipticines and N2 quaternized ellipticine derivatives exhibit selective cytotoxicity for leukemia cells[119] and human brain tumour cell lines[120] respectively. A more complete understanding of the mode of action of the ellipticines may enable the full therapeutic potential of this class of drugs to be realised. Improved pharmacokinetic properties would appear to be a particularly important prerequisite for new ellipticine analogues intended for clinical use.

Since 9-substitution has proved effective in enhancing the toxicity of ellipticine for cancerous cells,[112] the purpose of this study was to address the remaining uncertainties regarding 9-OHE binding to DNA. The binding of 9-OHE to ct-DNA, poly[d(G-C)]$_2$ and poly[d(A-T)]$_2$ in solution was studied to permit the analysis of the DNA sequence dependence of the binding. The transition moment polarisations of 9-OHE were determined with stretched film *LD* to enable the orientation of 9-OHE within the DNA intercalation site to be determined. Flow *LD* was applied to probe the orientation of both the intercalated and non-intercalated binding modes and thus facilitate assignment of the likely DNA binding sites for these modes. Flow *LD* has been employed previously to demonstrate coplanarity between various ellipticine analogues and the bases of DNA.[121] Previous studies have also used molecular modelling to analyse the binding of intercalated ellipticines.[122,123] The stacked binding mode was detected and studied in this

work with *RLS*, [20] to determine the extent of the ligand–ligand stacking interactions on DNA.

6.2 Experimental

6.2.1 Materials

9-OHE was provided by Sanofi Chimie, Sisteron at 99.6% purity and used without further purification. The Beer Lambert Law was used to determine the extinction coefficient for 9-OHE from accurately weighed samples. 9-OHE concentration was determined in all subsequent experiments spectroscopically in pure water using ε_{304} = 27,000 mol^{-1} dm^3 cm^{-1}. Synthetic DNAs were purchased from Pharmacia Biotech and ct-DNA highly polymerized sodium salt from Sigma. The DNAs were dissolved initially in water and used without further purification. They were diluted for use so that final solutions were all 20 mM NaCl (SigmaUltra) and 1 mM phosphate buffer (pH 7.0) (Fluka Chemicals, > 99.5% purity). DNA concentrations were also determined spectroscopically using ε_{254} = 8400 mol^{-1} dm^3 cm^{-1} for poly[d(G-C)]$_2$, ε_{262} = 6600 mol^{-1} dm^3 cm^{-1} for poly[d(A-T)]$_2$ and ε_{258} = 6600 mol^{-1} dm^3 cm^{-1} for ct-DNA. Polyvinyl alcohol Type III low molecular weight hot water soluble, purchased from Sigma Chemical Company, was used to make the stretched films.

6.2.2 Spectroscopic titrations

Spectroscopic titrations were performed in which normal absorption and *RLS* spectra

were collected as a function of 9-OHE concentration for solutions containing DNA (100 μM), 9-OHE (1 – 15 μM), NaCl (20 mM) and phosphate buffer (1 mM; pH 7). The concentrations of DNA, salt and buffer were held constant during the course of the titrations by adding equal volumes of two stock solutions, one containing ellipticine and the other containing DNA (200 μM), NaCl (40 μM) and phosphate buffer (2 μM; pH 7). The required volume of added stock solution for each titration step, dependent on the concentration of the ellipticine stock solution used, was computed from equation 4.2 as previously described (section 4.2.2). Normal absorption and *RLS* spectra were recorded after each addition of solution. Precise solution volumes and concentrations for an example titration are listed in Table 6.1. The titrations were repeated for each DNA sequence.

r / Ligand per DNA Base	[9-OHE] / μM	Total 9-OHE Volume / μL	Total Volume / μL	Added Volume / μL
0.01	1	27.8	1555.6	27.8
0.025	2.5	73.5	1647.1	45.8
0.05	5	163.0	1826.1	89.5
0.075	7.5	274.4	2048.8	111.3
0.1	10	416.7	2333.3	142.3
0.15	15	865.4	3230.8	448.7

Table 6.1 Example experimental parameters for DNA–9-OHE spectroscopic titrations. $[9\text{-OHE}]_{stock}$ = 56 μM. Initial volume = 1500 μL. Calculations based on equation 4.2.

A titration was also performed in which *CD* and *RLS* spectra of ct-DNA (40 μM), 9-OHE (10 μM), NaCl (20 mM), and phosphate buffer (1 mM; pH 7) were measured as a function of increasing concentrations of $[Co(NH_3)_6]^{3+}$ (0 – 60 μM in 10 μM increments). The concentrations of all solution components except $[Co(NH_3)_6]^{3+}$ were held constant

during the course of the titration, as described above.

6.2.3 Linear dichroism

Flow *LD* spectra were collected on DNA–9-OHE solutions prepared individually but made up to correspond in terms of component concentrations to those used for the spectroscopic titrations. A normal absorption spectrum was recorded along with each *LD* spectrum. The normal absorption and *LD* spectra were collected at an identical data interval and over the same wavelength range. LD^r spectra were then calculated as previously described (section 3.3).

PVA stretched films containing 9-OHE were prepared for film *LD* using a procedure identical to that described in section 4.2.4.

6.2.4 Spectroscopy

All spectra were collected over a wavelength range of 600 – 200 nm. *CD* and flow *LD* spectra were collected on a Jasco J-715 spectropolarimeter using a data interval, scan rate and averaging time identical to those described in section 5.2.4. Data were averaged over eight successive scans. A couette flow cell was used for flow *LD* solutions. Solution normal absorption spectra were collected on a Cary 1E UV–visible spectrophotometer and the stretched film normal absorption spectrum was collected on a Jasco V-550 spectrophotometer. A Perkin–Elmer LS–50 in synchronous scan mode was used for *RLS* data collection with the excitation and emission slit widths set to 2.5 nm. Quartz

fluorescence cuvettes with a 1 cm path length were used for all solution *CD*, *RLS* and normal absorption data acquisition. Baseline measurements were recorded and applied as described previously (section 5.2.4).

6.3 Results

6.3.1 Normal absorption titrations

The normal absorption spectrum of free 9-OHE exhibits absorption maxima in both the UV (244 nm, 275 nm and 304 nm) and visible (375 nm and 342 nm) regions of the spectrum. In the presence of DNA the ~260 nm DNA band dominates the UV region of the spectrum and a single absorbance band at ~250 nm is observed composed of DNA and 9-OHE transitions. The 9-OHE absorption spectrum outside the DNA absorption envelope exhibits wavelength shifts and hypochromicity to an extent dependent on the 9-OHE binding mode to DNA.

In the presence of all three DNA sequences, red shifts and hypochromicity are observed in the absorption bands of 9-OHE (Figure 6.2). The effect is most apparent for the 304 nm absorption band which shifts to 323 nm with ct-DNA and poly[d(G-C)]$_2$ regardless of the 9-OHE concentration. In the poly[d(A-T)]$_2$ spectrum the wavelength shift is dependent on the 9-OHE concentration where red shifts to 325 nm and 322 nm are observed for the 1 μM and 15 μM 9-OHE spectra respectively relative to the free 9-OHE absorption band maximum. The observed hypochromicities are not significantly different for poly[d(G-C)]$_2$ and ct-DNA but noticeably less for poly[d(A-T)]$_2$.

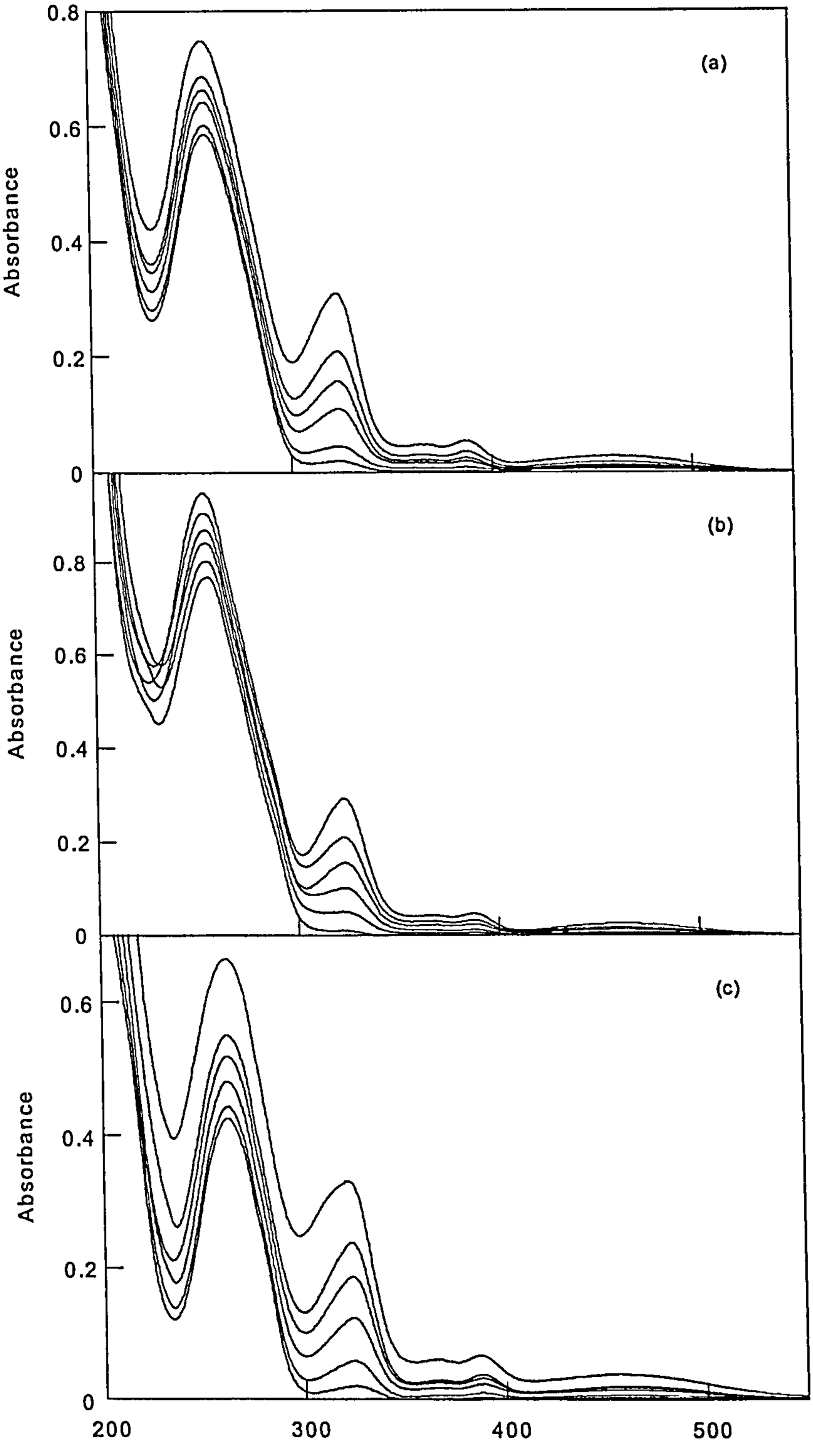

Figure 6.2 Normal absorption spectra of 9-OHE (1 – 10 μM in 2.5 μM increments and 15 μM. 255 nm absorbance increases with 9-OHE concentration), NaCl (20 mM), phosphate buffer (1 mM; pH 7) and (a) ct-DNA (100 μM), (b) poly[d(G-C)]$_2$ (100 μM) and (c) poly[d(A-T)]$_2$ (100 μM).

6.3.2 Film linear dichroism

The film UV-visible spectrum of 9-OHE exhibits sharpened and blue shifted bands relative to the corresponding solution spectrum. The main UV transition appears at 300 nm in the film spectrum compared to 304 nm in water. The broad transition at 441 nm in water shifts to 408 nm in PVA film.

The film *LD* spectrum of 9-OHE is entirely positive with the exception of a small negative feature at 428 nm. As 9-OHE is comparable in shape to tetracene, for example, it is reasonable to assume rotational averaging about the 9-OHE long (*z*) axis in the film.[7] This implies that the electronic transitions of 9-OHE are predominantly long axis polarized. The 9-OHE film LD^r spectrum exhibits the strongest positive feature at 300 nm thus the polarization of this transition possesses the greatest long axis character. Conversely, negative LD^r at 428 nm reflects the short axis character of this transition.

For a transition of pure polarization in an oriented sample a flat LD^r is expected across the entire absorbance envelope. The absence of any flat feature in the film LD^r spectrum of 9-OHE indicates that transitions overlap in all regions of the spectrum.[7] All $\pi \rightarrow \pi^*$ transitions are polarized in the plane of the 9-OHE, however, their polarization is not restricted to pure *y* and *z* polarization as a result of the low symmetry the molecule. Due to the partial orientation of the stretched film sample it was necessary to resolve the film *LD* spectrum into long and short axis components in order to determine the polarizations of different transitions. The data were analysed according to a model for uniaxially oriented rods, as described in section 3.3.1. The polarised absorbance spectra calculated

from TEM analysis are shown in Figure 6.4 and full details this calculation are given in Appendix 2.

The 9-OHE polarised absorbance spectra clearly show the dominant *z* polarized nature of the 9-OHE absorbance spectrum with the exception of the 428 nm band where the *y* component absorbance is stronger. The 9-OHE transition polarizations were calculated to be 24° from the long axis at 300 nm and 56° from the long axis at 430 nm. Transition polarization assignments were also made for the remaining transitions (Table 6.2). These reflect a considerable amount of averaging due to overlap between absorbance bands. The long axis of the molecule is illustrated in Figure 6.5.

Transition Wavelength / nm	Transition Polarisation Angle / deg
430	56
370 – 380	38 – 40
355	33
340	32
300	24
280	28
240	40
205 – 215	46 – 47

Table 6.2 Transition polarisation angle assignments for 9-OHE from stretched film data. Angles are relative to the 9-OHE orientation axis.

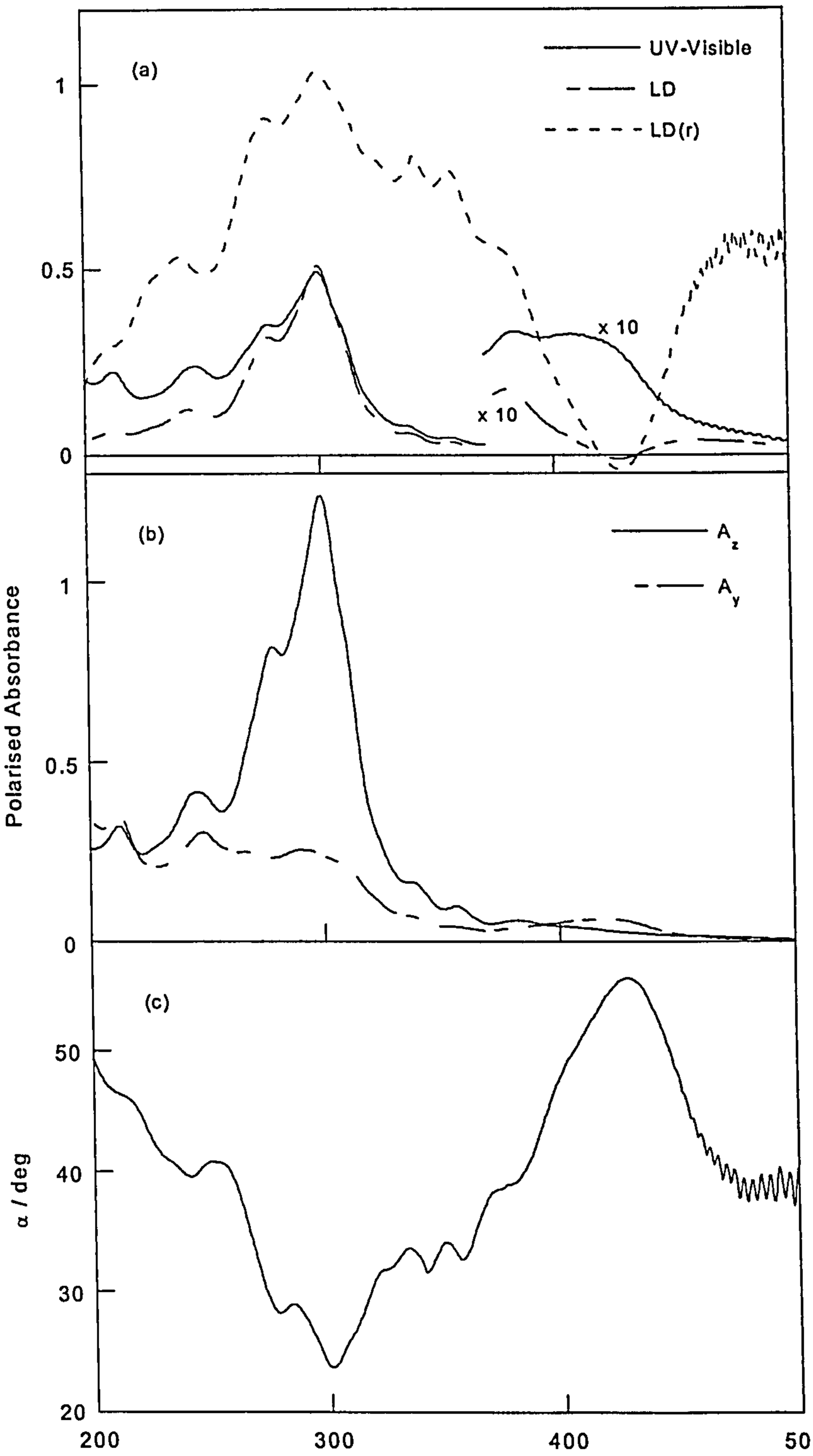

Figure 6.3 (a) Film normal absorption, film *LD* and film LD^r spectra of 9-OHE oriented in PVA stretched film, (b) polarised absorbance spectra of 9-OHE oriented in PVA stretched film. Orientation parameters used were $S_{zz} = 0.45$ and $S_{yy} = -0.23$. (c) Calculated transition moment polarisation angles for 9-OHE.

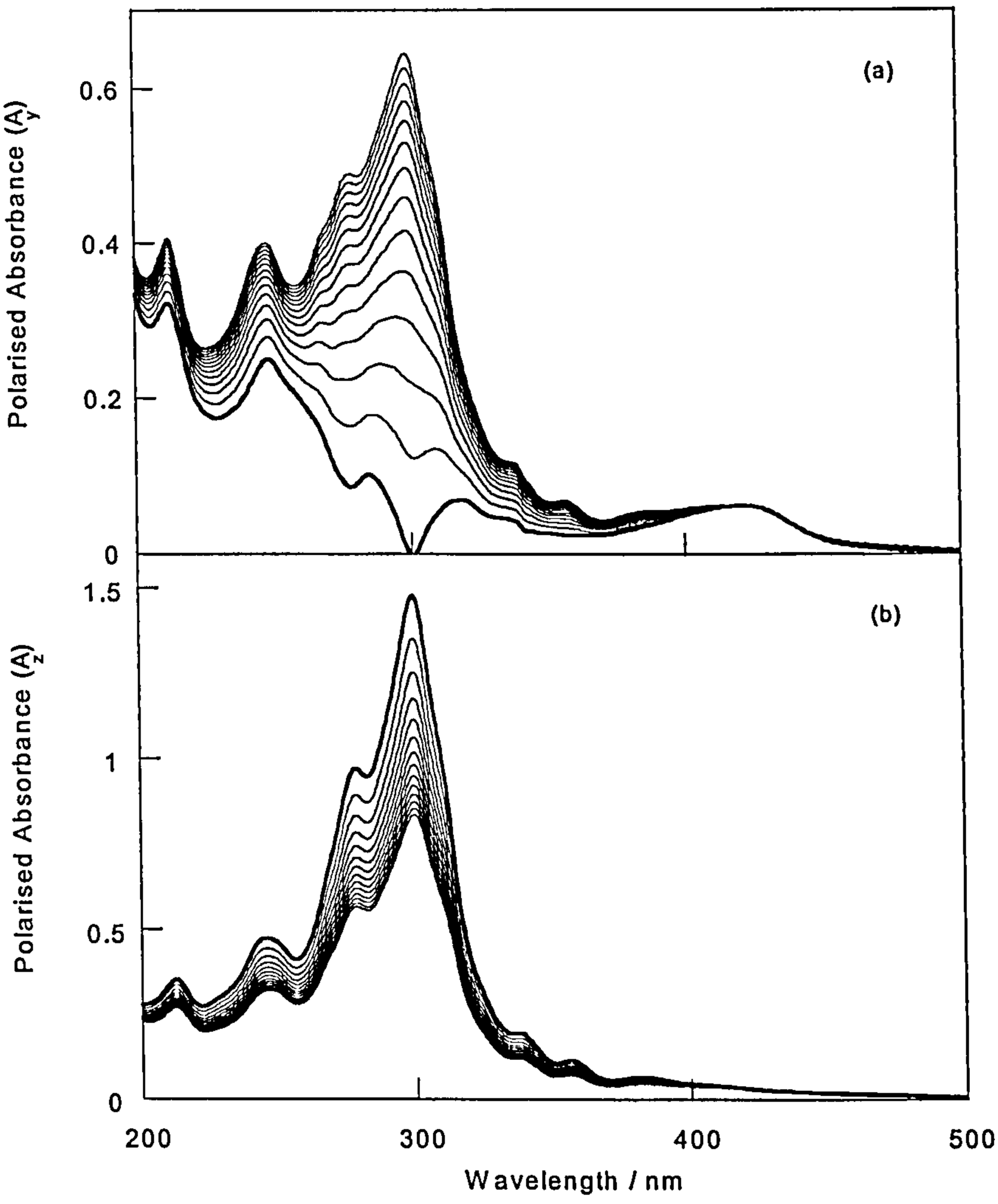

Figure 6.4 Polarised absorbance spectra from TEM calculations on 9-OHE stretched film *LD* data. Each spectrum corresponds to an adjustment of (a) −0.025 in S_{yy} from an initial value of −0.172 (thick line) and (b) 0.05 in S_{zz} from an initial value of 0.344 (thick line).

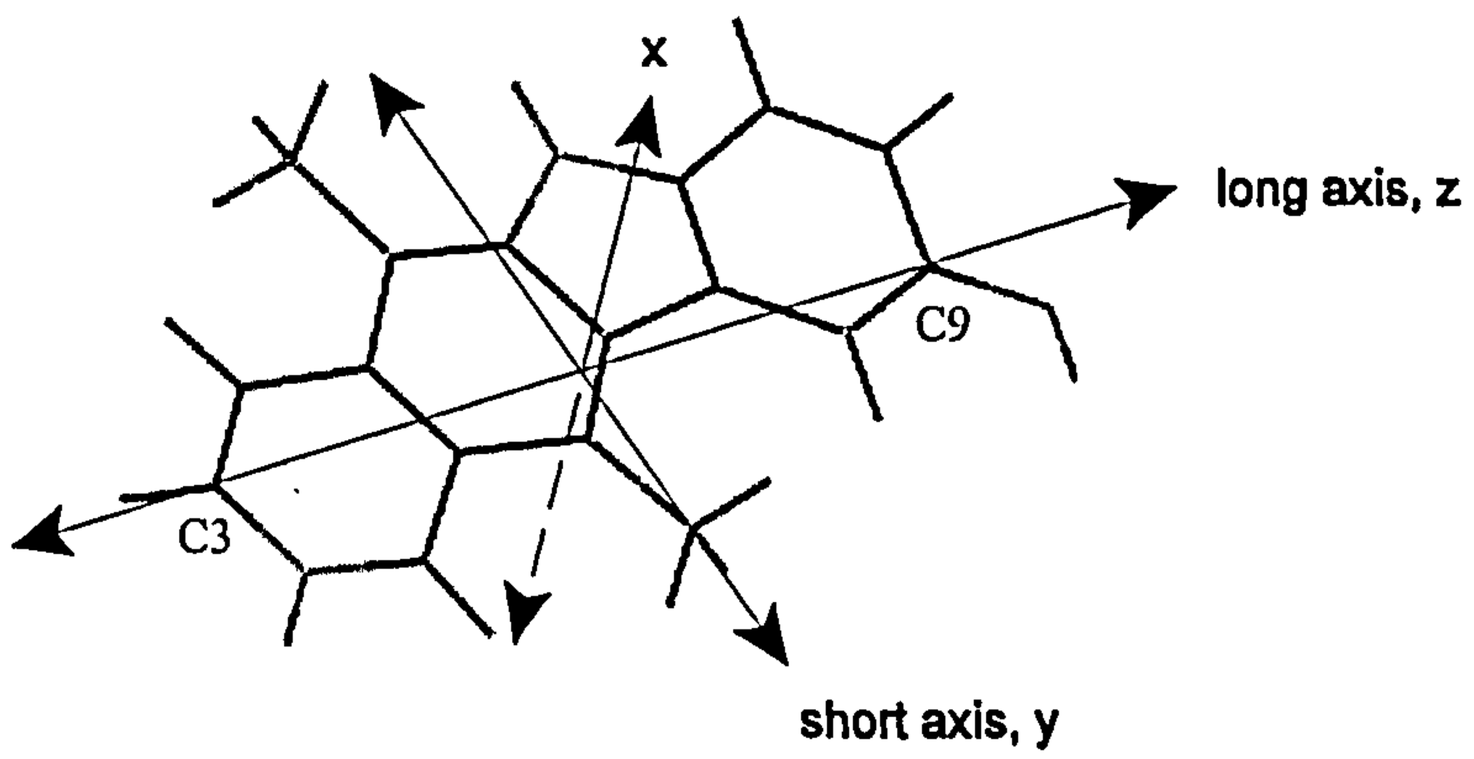

Figure 6.5 Definition of molecular axis system for 9-OHE. The long (*z*) axis intersects C3 and C9. The orientation axis will be on or near this axis. The long and short (*y*) axes lie in the plane of the molecule.

6.3.3 Flow linear dichroism

Uncomplexed DNAs have a negative flow *LD* signal for all the base in-plane $\pi \rightarrow \pi^*$ transitions. Flow oriented ct-DNA gives larger *LD* signals than those observed for poly[d(G-C)]$_2$ or poly[d(A-T)]$_2$ due to more efficient orientation of the long natural DNA compared to the shorter synthetic DNAs.

The fact that an *LD* signal is observed indicates the DNA–9-OHE complex is macroscopically oriented under the experimental conditions and the observation of an *LD* band for the 9-OHE transitions indicates the ligand is binding to DNA. Although a complete quantitative interpretation of the flow *LD* spectra of the DNA–9-OHE complexes is not possible, due primarily to the overlap of 9-OHE and DNA absorbance bands at 260 nm and local stiffening of the DNA duplex around intercalation sites, empirical and qualitative analysis of the *LD* data is both useful and informative.

Flow *LD* spectra of the ct-DNA–9-OHE complex exhibit four negative bands at 258, 324, 389 and 467 nm (Figure 6.6a). The intensity of the bands increases with 9-OHE concentration although the 467 nm band is undetectable in the 1 and 2.5 μM 9-OHE *LD* spectra. The *LD* spectrum is negative across the wavelength range for all 9-OHE concentrations. The 9-OHE in-plane $\pi \rightarrow \pi^*$ transitions at 324, 389 and 467 nm, for which the *LD* is due to pure 9-OHE absorption, are thus aligned closer to the plane of the DNA bases than parallel to the helix axis. The 258 nm *LD* band contains absorption contributions from both the DNA bases and 9-OHE (the sign of the 9-OHE component is still negative since the intensity of the band increases with 9-OHE concentration).

LD^r data for this system (Figure 6.7a) provide further insight into the binding orientation of 9-OHE to ct-DNA. The increasing LD^r magnitude in the DNA region of the spectrum implies better DNA orientation due to lengthening and stiffening of the ct-DNA helix as the concentration of 9-OHE increases. The LD^r corresponding to the 324 nm absorption band is greater in magnitude than the DNA region LD^r for all concentrations of 9-OHE. However, the intensities of the 389 and 467 nm LD^r relative to that observed in the DNA region are dependent on the 9-OHE concentration. Both transitions exhibit a shift from lower relative intensity at a 9-OHE concentration of 5 μM to a higher relative intensity at 15 μM 9-OHE. Thus the orientation of the 9-OHE plane is changing with respect to the plane of the DNA bases as a function of 9-OHE concentration.

The 9-OHE complex with poly[d(G-C)]$_2$ exhibits negative *LD* at 324 and 255 nm for all 9-OHE concentrations except the 1 and 2.5 μM 9-OHE spectra where the lower energy 9-OHE *LD* maximum appears at 326 nm (Figure 6.6b). The 389 and 476 nm bands observed for the ct-DNA–9-OHE complex are undetectable in the 9-OHE complex with poly[d(G-C)]$_2$ *LD* spectra, probably because of the low degree of orientation intrinsic to the short, synthetic DNA polymer. A weakly negative *LD* band is present at 387 nm for the 15 μM 9-OHE spectrum. As for ct-DNA, a requirement of the observed negative *LD* is that 9-OHE when complexed to poly[d(G-C)]$_2$ is bound in an orientation where the ligand plane is more perpendicular than parallel the DNA helix axis.

LD^r data are less satisfactory for 9-OHE binding to poly[d(G-C)]$_2$ (Figure 6.7b) than for the ct-DNA–9-OHE system, due mainly to the lower degree of flow orientation obtainable for short, synthetic DNAs leading to a lower signal to noise ratio. More

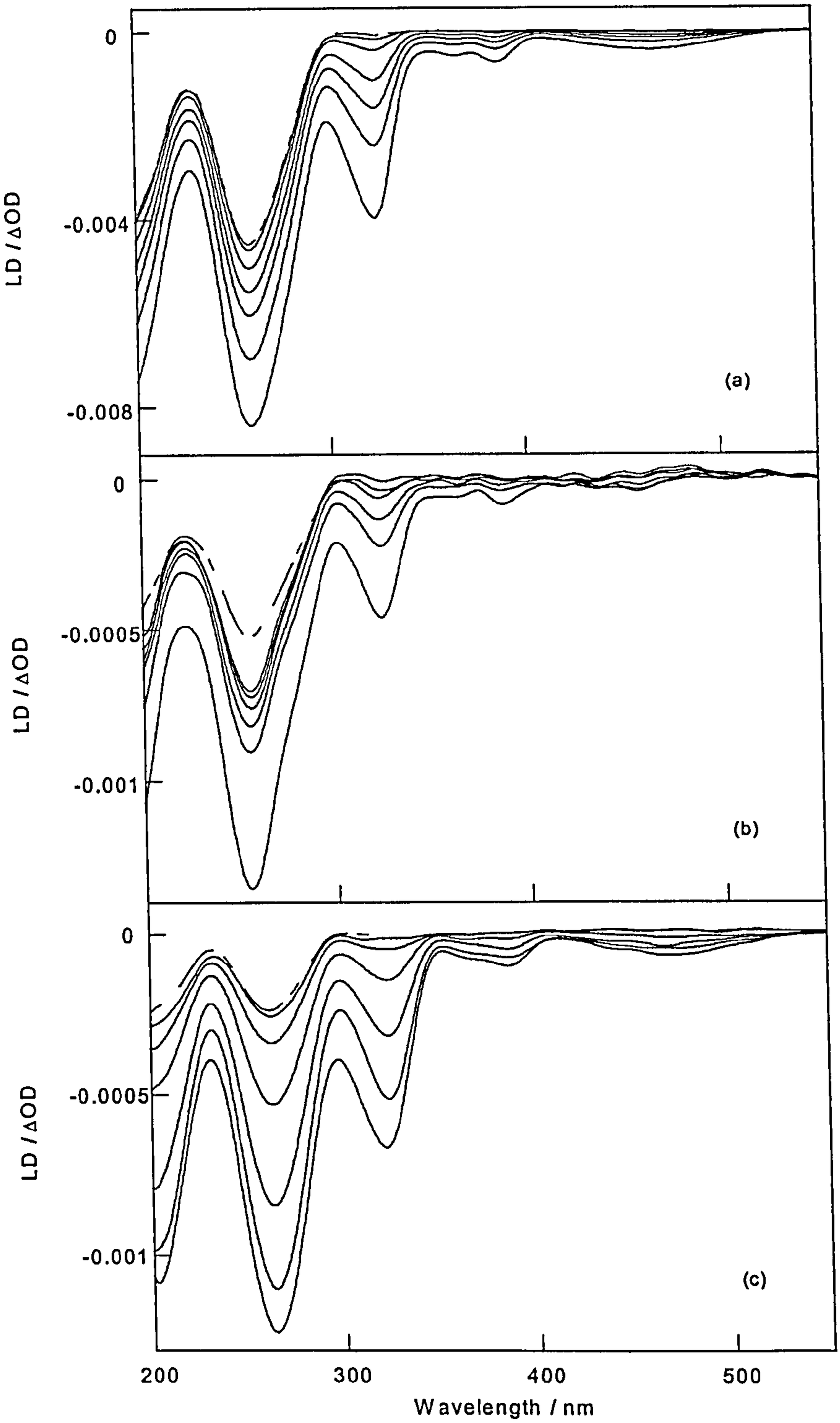

Figure 6.6 Flow *LD* spectra of 9-OHE (1 – 10 μM) in 2.5 μM increments and 15 μM. *LD* intensity increases with 9-OHE concentration), NaCl (20 mM), phosphate buffer (1 mM; pH 7) and (a) ct-DNA (100 μM), (b) poly[d(G-C)]$_2$ (100 μM) and poly[d(A-T)]$_2$ (100 μM). (– —) DNA (100 μM), NaCl (20 mM) and phosphate buffer (1 mM; pH 7).

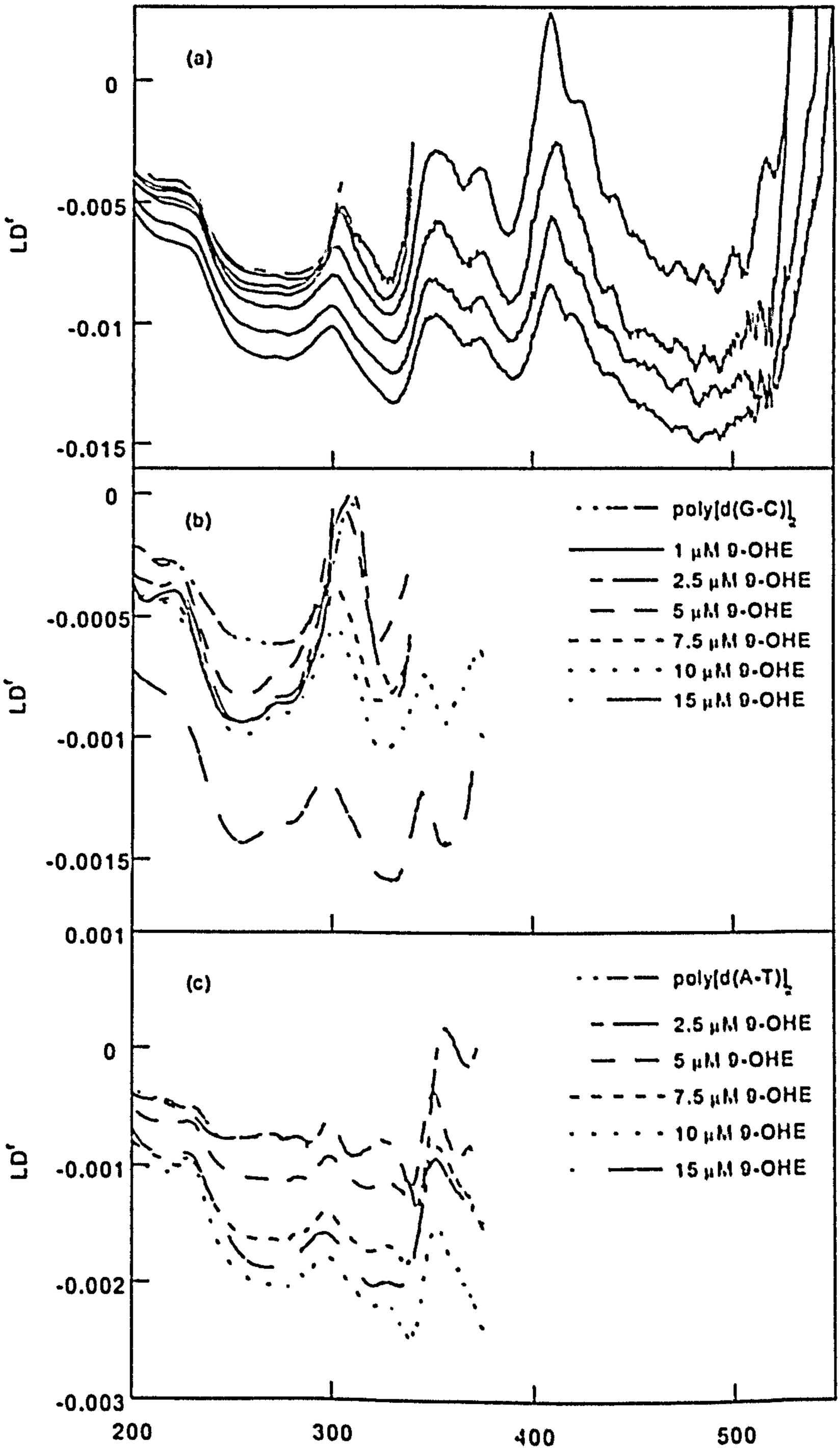

Figure 6.7 *LD'* spectra of (a) ct-DNA (100 μM) and 9-OHE (1 – 10 μM in 2.5 μM increments and 15 μM. *LD'* magnitude increases with 9-OHE concentration), (b) poly[d(G-C)]$_2$ (100 μM) and 9-OHE (concentrations indicated on figure) and (c) poly[d(A-T)]$_2$ (100 μM) and 9-OHE (concentrations indicated on figure).

efficient flow orientation due to stiffening and lengthening of the poly[d(G-C)]$_2$ duplex is evident from an increasing LD^r magnitude in the DNA region with increasing 9-OHE concentration. The intensity of the 324 nm LD^r relative that observed for the DNA region of the spectrum indicates a concentration dependent change in 9-OHE orientation relative to the DNA bases.

Flow *LD* of the 9-OHE complexes with poly[d(A-T)]$_2$ exhibit negative *LD* bands at 263, 322, 386 and 467 nm (Figure 6.6c). As for ct-DNA and poly[d(G-C)]$_2$, the sign of the *LD* spectrum is negative across the wavelength range and for all 9-OHE concentrations. The 322, 386 and 467 nm 9-OHE absorbances are undetectable, or extremely weak in the case of the 322 nm absorbance, at low 9-OHE concentration (1 and 2.5 μM 9-OHE). The negative sign of the *LD* suggests a binding orientation qualitatively similar to that observed for 9-OHE binding to ct-DNA and poly[d(G-C)]$_2$.

Calculation of meaningful LD^r spectra for 9-OHE binding to poly[d(A-T)]$_2$ was only possible for energies down to 322 nm, and for a limited range of 9-OHE concentrations (Figure 6.7c). As observed for 9-OHE binding to both ct-DNA and poly[d(G-C)]$_2$, 9-OHE stiffens and lengthens the poly[d(A-T)]$_2$ duplex causing more efficient flow orientation. No concentration dependent change in the orientation of DNA bound 9-OHE is obvious from analysis of the DNA and 9-OHE LD^r signals.

6.3.4 Resonance light scattering titrations

RLS spectra of the ct-DNA–9-OHE complex (Figure 6.8a) contain two distinct peak

shapes. The first of these is a broad maximum centred at approximately 345 nm. This scattering profile occurs for samples containing between 1 and 5 μM 9-OHE. There is no linear correlation between the intensity of scattered light and the 9-OHE concentration. The second observable scattering profile comprises a dip at 323 nm and weak intensity scattering at 350 nm. This scattering profile appears for samples containing between 7.5 and 15 μM 9-OHE. Significantly, no enhanced magnitude resonance light scattering is observed. The light scattering spectrum of the ct-DNA–9-OHE system is dominated by absorption effects. At low concentrations of 9-OHE the low level of ligand absorption does not significantly reduce the intensity of the scattering profile. At higher 9-OHE concentrations ligand absorption contributes to the scattering profile by reducing the intensity of measured scattered light at the 323 nm absorption maximum. Since the dip appears at the absorption wavelength of DNA bound 9-OHE, and no *RLS* is observed, the ligand is not forming extended stacks on the DNA.

The form of the *RLS* spectra for 9-OHE in the presence of poly[d(G-C)]$_2$ and poly[d(A-T)]$_2$ is qualitatively similar to the high 9-OHE concentration ct-DNA scattering profile. The dip due to 9-OHE absorption appears at 322 nm for poly[d(G-C)]$_2$ and 324 nm for poly[d(A-T)]$_2$. Thus extended ligand stacks are not forming on either poly[d(G-C)]$_2$ or poly[d(A-T)]$_2$.

Although the absence of *RLS* is consistent with 9-OHE binding to DNA in a mode where extended stacking does not occur, the limited amount of *RLS* data in the literature constitutes insufficient support for such a qualitative conclusion. Measurement of 9-OHE *RLS* under conditions where extended stacking would be expected to occur was therefore

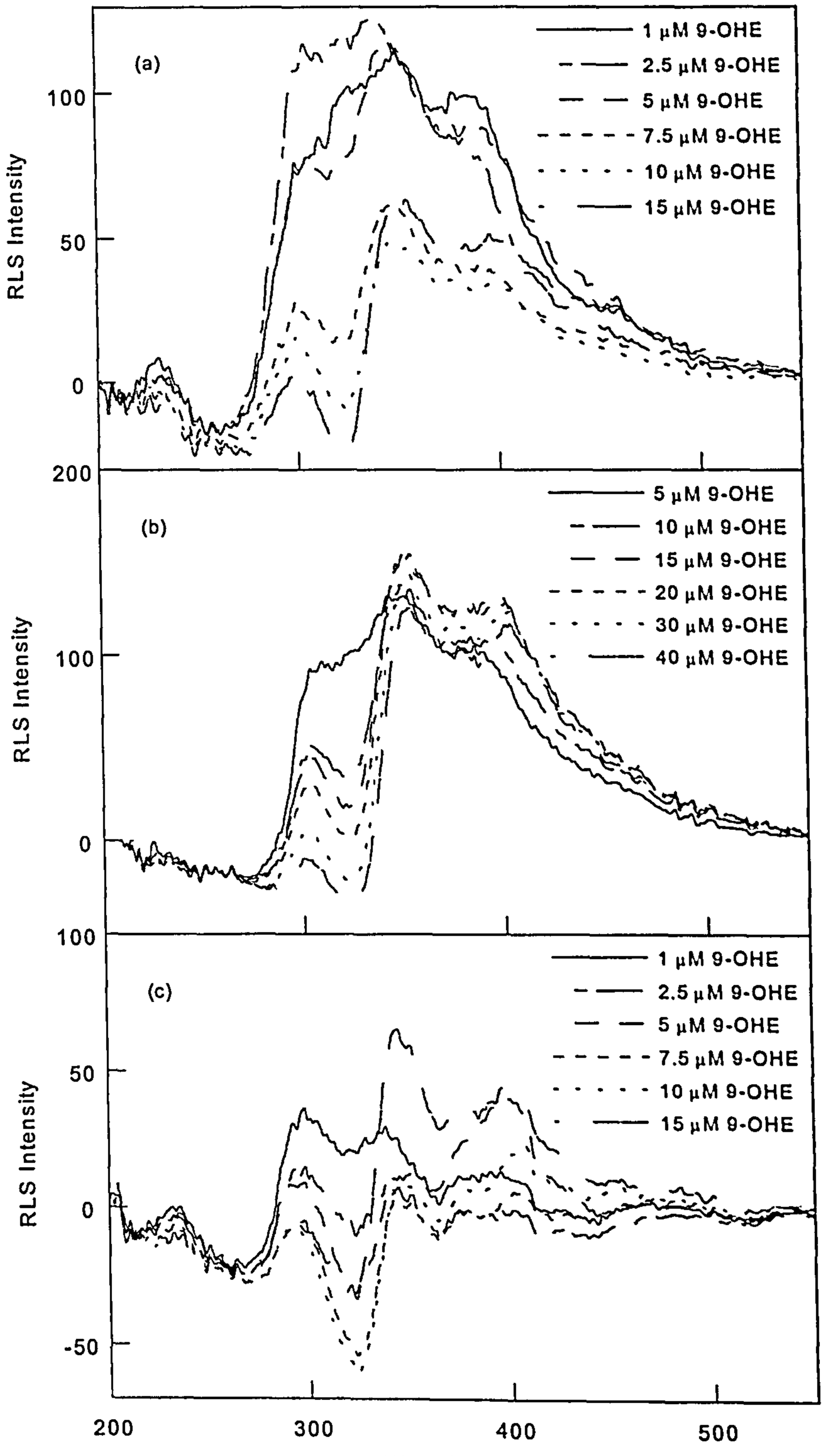

Figure 6.8 *RLS* spectra of 9-OHE (concentrations indicate on figure), NaCl (20 mM), phosphate buffer (1 mM; pH 7) and (a) ct-DNA (100 μM), (b) poly[d(G-C)]$_2$ (200 μM) and (c) poly[d(A-T)]$_2$ (100 μM).

necessary. When DNA is condensed with $[Co(NH_3)_6]^{3+}$ the presence of bound non-intercalated ligand leads to the formation of extended stacks of that ligand. Under such conditions an *RLS* would be expected for 9-OHE.

When $[Co(NH_3)_6]^{3+}$ is added to a complex of ct-DNA and 9-OHE an enhanced *RLS* appears at 340 nm (Figure 6.9b). The intensity of the measured *RLS* increases with $[Co(NH_3)_6]^{3+}$ concentration. The $[Co(NH_3)_6]^{3+}$ induced *RLS* is up to 3.5 times larger than

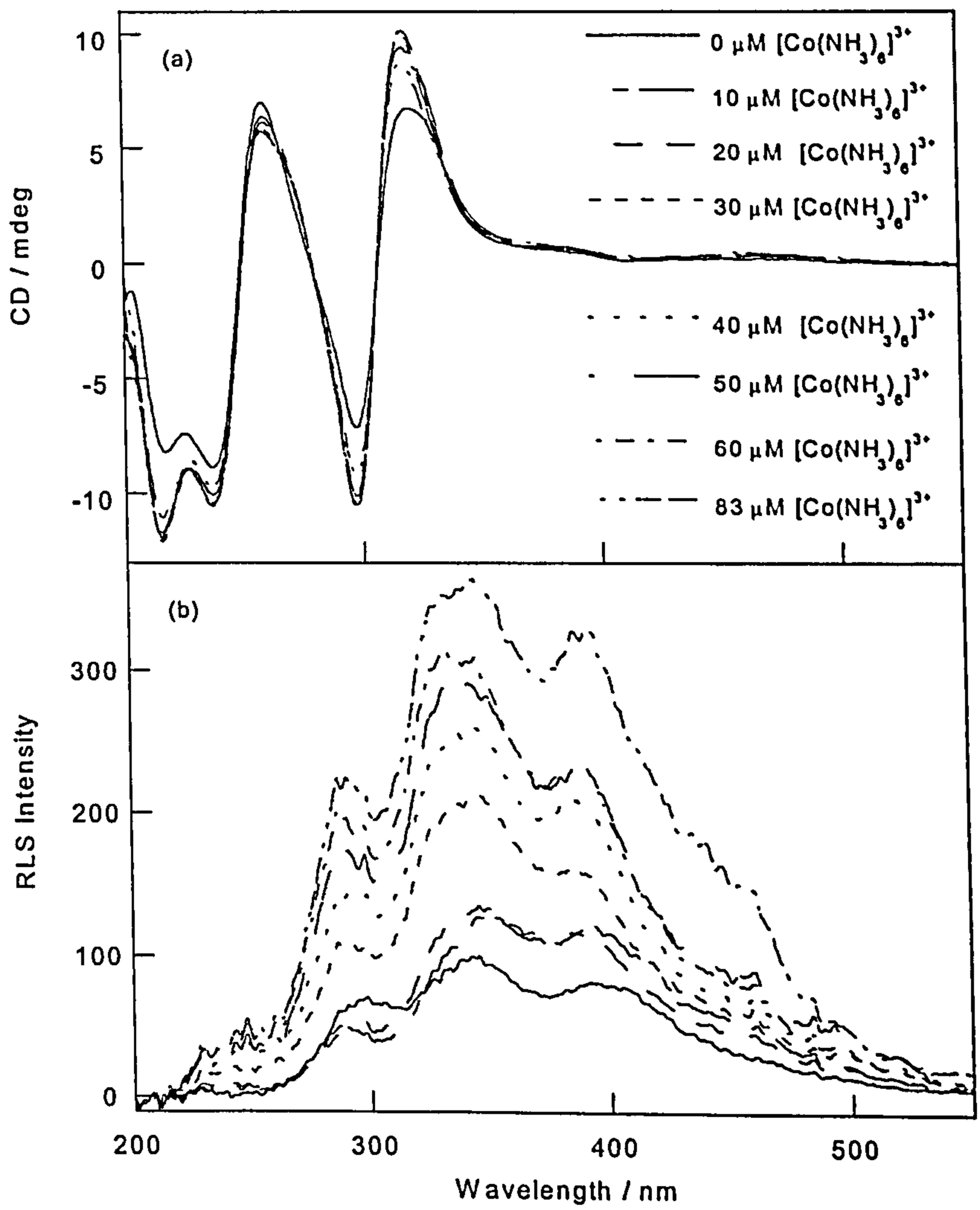

Figure 6.9 (a) *CD* spectra and (b) *RLS* spectra of 9-OHE (10 μM), ct-DNA (40 μM), NaCl (20 mM), phosphate buffer (1 mM; pH 7) and $[Co(NH_3)_6]^{3+}$ (concentrations indicated on figure).

that observed for 9-OHE binding to uncondensed DNA and is consistent with the formation of extended 9-OHE stacks on the condensed ct-DNA template.

The 9-OHE aggregation process was also monitored with *CD* spectroscopy. The stacked binding mode is characterised by exciton coupling in the 9-OHE *ICD* (297 nm negative band and 318 nm positive band; Figure 6.9a). The intensity of the *ICD* exciton band for 9-OHE is less intense in the absence of $[Co(NH_3)_6]^{3+}$, although the magnitude of the *ICD* exciton band upon addition of $[Co(NH_3)_6]^{3+}$ is only weakly dependent on $[Co(NH_3)_6]^{3+}$ concentration. The observed *CD* spectra are thus consistent with the initial formation of extended 9-OHE stacks upon $[Co(NH_3)_6]^{3+}$ addition and subsequent increase in the extent of the stacking, since *CD* is considerably less sensitive to aggregate size than *RLS*. The observation of an *ICD* exciton band in the absence of $[Co(NH_3)_6]^{3+}$, albeit at reduced intensity, suggests the formation of oligomer 9-OHE stacks too small to give an enhanced *RLS*.

6.4 Discussion

Flow *LD* and *RLS* spectroscopies have been applied to study the binding of 9-OHE to three DNA sequences. Flow *LD* permits analysis of the binding geometries of 9-OHE to the different DNAs while *RLS* is a sensitive probe of the state of aggregation of the DNA bound ligand. In addition to the solution spectroscopy the electronic spectrum of 9-OHE in PVA stretched film was investigated to permit the assignment of the transition moment polarisations for 9-OHE. Interpretation of the spectroscopic results presented in this thesis are aided by reference, in the following discussion, to *CD* data pertaining to this

study of 9-OHE binding to DNA, but presented elsewhere (see Appendix 3).[102]

The collective *LD* data indicate intercalation to occur across the range of 9-OHE concentrations studied and for all three DNAs. Intercalated ligands force the DNA base pairs apart and lead to an overall increase in length of the DNA. Local duplex stiffening around the intercalation sites is also a characteristic of intercalated binding modes. Such effects are consistent with the increase in LD^r magnitude observed for the absorption bands of the DNAs.

The LD^r of ct-DNA–9-OHE enables the orientation of the ligand transitions to be analysed relative to the plane of the DNA bases. The precise orientation of 9-OHE is dependent on ligand concentration, implying the presence of a second binding mode at higher 9-OHE concentrations in addition to intercalation. The long axis polarised 9-OHE transition at ~324 nm is oriented more perpendicular to the helix axis than the average DNA base, an observation explained by the local duplex stiffening associated with intercalated ligands. At intermediate 9-OHE concentrations, the 389 and 467 nm transitions, polarised at approximately 40 and 56° to the 9-OHE long axis, are slightly less perpendicular to the helix axis than the average DNA base. Thus the plane of the 9-OHE is tilted relative to the plane of the bases within the intercalation site. These transitions could not be analysed for the lowest 9-OHE concentrations due to the poor quality of the LD^r spectrum. At high 9-OHE concentrations, where exciton coupling effects are observed in the *ICD* spectrum of 9-OHE and suggest ligand stacking,[102] the *LD* that the ligand transitions are aligned more perpendicular to the helix axis than the average DNA base. Although the *LD* and LD^r spectra are averaged over the 9-OHE

orientations of the intercalative and stacked binding modes, the stacked mode still has negative *LD* for which the LD^r indicates the 9-OHE orientation relative to the DNA bases. The observed 9-OHE orientation for the stacked mode is inconsistent with a minor groove binding geometry, for which a positive *LD* would be expected.

Ligand stacking also occurs at high 9-OHE concentrations for 9-OHE binding to poly[d(A-T)]$_2$ and poly[d(G-C)]$_2$, as evidenced by exciton effects in the *CD* spectra of these systems.[102] This stacked binding mode for all three DNAs has been further characterised by the *RLS* data. While ligand–ligand interactions are detectable as exciton effects in the *CD* bands of the ligands, this technique is usually insensitive to the extent of the stacking. The observed exciton couplings could arise from dimers, oligomers or extended stacks. *RLS*, however, is only observed when extended aggregates are present. The absence of enhanced light scattering in the *RLS* spectra of the DNA–9-OHE complexes thus requires that the ligand stacking detected in the *CD* spectra of these systems is due to the presence of 9-OHE dimers or small oligomers. The lack of extended 9-OHE stacking on DNA could be related to the presence of intercalated ligand. Since the LD^r of the stacked ligand exceeds that of the average DNA base, 9-OHE stacking may require an intercalated ligand as a step to initiate a short stack. If the extent of the stack could not continue past the next intercalated ligand, no extended stack could occur. Such a binding mode would populate the major groove and is consistent with the observed *RLS* and *LD* data.

6.5 Conclusions

The binding of 9-OHE to ct-DNA, poly[d(G-C)]$_2$ and poly[d(A-T)]$_2$ has been studied by means of *LD*, *RLS* and normal absorption spectroscopy. 9-OHE has been shown to bind by intercalation to the three DNAs by analysis of *LD* and LD^r data. *RLS* data shows the stacked 9-OHE binding mode to involve dimers or small oligomers rather than extended ligand stacks. *LD* data shows the geometry of the stacked binding mode to involve an arrangement in which the 9-OHE plane is more parallel than perpendicular to the plane of the average DNA base and thus to require a binding site other than the minor groove. Additionally, the transition moment polarisations of the electronic spectrum of 9-OHE have been assigned from stretched film *LD* data. The data was used to aid interpretation of the flow *LD* spectra of the DNA–ligand complexes.

7 Conclusions

The collective application of different spectroscopic techniques has been demonstrated to be a useful approach to the study of DNA–ligand interactions. The ability of each technique to provide complementary information on the DNA–ligand systems was intrinsic to the effectiveness of the method. *CD* was generally employed to identify the occurrence of different binding modes. The binding orientation of the various ligands to DNA was then analysed with *LD* and, in the case of the porphyrin, molecular modelling. The use of film *LD* to assign ligand transition moment polarisations was particularly effective. In addition to facilitating interpretation of the flow *LD* studies in this work, the transition polarisations assigned for 9-OHE and *t*-H_2P may be useful in future studies involving these molecules. Fluorescence, *RLS* and normal absorption provided supplementary information. *RLS*, a relatively new technique, was a useful means of detecting extensively stacked binding modes. The use of *RLS* to study 9-OHE and Hoechst binding to DNA constitutes the first application of the technique to chromophores that aggregate exclusively in the presence of DNA. Previous applications of the technique were to systems that readily self-assemble in solution in addition to when bound to DNA.

This thesis has described the DNA binding properties of three small molecules with therapeutic potential. The ligands were similar in that they each bind to DNA tightly but non-covalently and their binding modes were dependent on the base composition of the binding site and the ligand load on the DNA. A propensity to bind as aggregates at high ligand load was another property common to the DNA binding behaviour of the ligands.

In each case, the aggregated binding modes occurred most readily at binding sites composed of GC base pairs.

Most groove binding small molecules interact preferentially with DNA at AT minor groove binding sites thus the development of ligands that are selective for GC tracts constitutes a significant challenge. Although small molecules generally preferentially bind to AT sequences, they are mostly capable of interacting with GC (often with the major groove) albeit with a reduced binding affinity. Since the AT binding modes occurred more readily they were initially the subject of most research on DNA–ligand interactions. The development of GC specific ligands therefore proceeded based largely on a knowledge of AT specific binding modes. That established minor groove binders may interact with DNA in a sequence and ligand load dependent mode is now universally accepted, but the problem of developing effective GC selective ligands remains.

Thus the results presented in this thesis, where at least equal emphasis was placed on binding to GC as AT, may prove useful in the design of ligands capable of binding to DNA at a predetermined sequence of bases. The prevalence of stacking interactions at GC sites could in some way be exploited to engineer GC specific DNA binding ligands. Given current interest in supramolecular chemistry and the concomitant development and understanding of novel molecular architectures, one can envisage the possible development of such complexes, based on established knowledge of DNA groove binders, that mimic the behaviour of aggregated ligands and preferentially bind to DNA at GC sites (porphyrins, for example, readily accommodate metals ions at their centres and can be assembled into higher order structures[124, for example]). The potential of such

ligands in medical applications is significant. DNA sequences rich in GC have been mapped across the human genome and suggested to be important for biological processes such as proliferation.[125] Sequence specific drugs or ligands will be required to exploit effectively this genetic information at the molecular level in therapeutic and medical applications.

References

The referencing convention of the *Journal of the American Chemical Society* has been adopted for the presentation of references in this thesis.

(1) Watson, J. D.; Crick, F. H. C. *Nature* **1953**, *171*, 737–738.

(2) Saenger, W. *Principles of Nucleic Acid Structure*; Springer-Verlag: New York, 1984.

(3) Falk, J. E. *Porphyrins and Metalloporphyrins*; Elsevier Publishing Company: New York, 1964; pp 73–80.

(4) Stryer, L. *Biochemistry*; W. H. Freeman and Company: New York, 1988; pp 7–14.

(5) Le Pecq, J.-B.; Xuong, N.-D.; Gosse, C.; Paoletti, C. *Proc. Natl. Acad. Sci. USA* **1974**, *71*, 5078–5082.

(6) Calladine, C. R.; Drew, H. R. *Understanding DNA: The Molecule and How it Works*; Academic Press: Cambridge, 1992.

(7) Rodger, A.; Nordén, B. *Circular Dichroism and Linear Dichroism*; Oxford University Press: Oxford, 1997.

(8) Lavery, R.; Pullman, B. *Int. J. Quantum Chem.* **1981**, *20*, 259–272.

(9) Kim, S. K.; Eriksson, S.; Kubista, M.; Nordén, B. *J. Am. Chem. Soc.* **1993**, *115*, 3441–3447.

(10) Matsuoka, Y.; Nordén, B. *J. Phys. Chem.* **1982**, *86*, 1378–1386.

(11) Thulstrup, E. W.; Michl, J.; Eggers, J. H. *J. Phys. Chem.* **1970**, *74*, 3869–3874.

(12) Pariser, R.; Parr, R. G. *J. Chem. Phys.* **1953**, *21*, 466–471.

(13) Rodger, A. *Methods in Enzymology*; Academic Press: New York, 1993; pp 232–258.

(14) Nordén, B.; Kubista, M.; Kurucsev, T. *Q. Rev. Biophys.* **1992**, *25*, 51–170.

(15) Matsuoka, Y.; Nordén, B. *Biopolymers* **1982**, *21*, 2433–2452.

(16) Matsuoka, Y.; Nordén, B. *Biopolymers* **1983**, *22*, 1731–1746.

(17) Tinoco, I. Jr. *Adv. Chem. Phys.* **1962**, *4*, 113–160.

(18) Lakowicz, J. R. *Principles of Fluorescence Spectroscopy*; Plenum Press: New York, 1986; pp 4.

(19) Atkins, P. W. *Physical Chemistry*; Oxford University Press: Oxford, 1990; pp 693–698.

(20) Pasternack, R. F.; Bustamante, C.; Collings, P. J.; Giannetto, A.; Gibbs, E. J. *J. Am. Chem. Soc.* **1993**, *115*, 5393–5399.

(21) Pasternack, R. F.; Schaefer, K. F.; Hambright, P. *Inorg. Chem.* **1994**, *33*, 2062–2065.

(22) Pasternack, R. F.; Collings, P. J. *Science* **1995**, *269*, 935–939.

(23) Parkash, J.; Robblee, J. H.; Angnew, J.; Gibbs, E.; Collings, P.; Pasternack, R. F.; dePaula, J. C. *Biophys. J.* **1998**, *74*, 2089–2099.

(24) Haung, C. Z.; Li, K. A.; Tong, Y. T. *Anal. Chem.* **1997**, *96*, 514–520.

(25) Haung, C. Z.; Li, K. A.; Tong, Y. T. *Anal. Chem.* **1996**, *68*, 2259–2263.

(26) Haung, C. Z.; Li, Y. F.; Mao, J. G.; Tan, D. G. *Analyst* **1998**, *123*, 1401–1406.

(27) Marzilli, L. G. *New J. Chem.* **1990**, *14*, 409–420.

(28) Pottier, R. *Photosensitisation: Molecular, Cellular and Medical Aspects*; Springer-Verlag: Berlin, 1988, pp 2.

(29) Diamond, I.; Granelli, S. G.; McDonaugh, A. F. *Biochem. Med.* **1977**, *17*, 121–127.

(30) Fiel, R. J. *J. Biomol. Struct. Dyn.* **1989**, *6*, 1259–1274.

(31) Fiel, R. J.; Howard, J. C.; Mark, E. H.; Datta-Gupta, N. *Nucleic Acids Res.* **1979**, *6*, 3093–3120.

(32) Pasternack, R. F.; Gibbs, E. J.; Villafranca, J. J. *Biochemistry* **1983**, *22*, 2406–2414.

(33) Mauro, E. D.; Saladino, R.; Tagliatesta, V. D. S.; Negri, R. *J. Mol. Biol.* **1998**, *282*, 43–57.

(34) Kuroda, R.; Takahashi, E.; Austin, C. A.; Fisher, L. M. *FEBS* **1990**, *262*, 293–298.

(35) Scheider, H.-J.; Wang, M. *J. Org. Chem.* **1994**, *59*, 7473–7478.

(36) Verchère-Béaur, C.; Perrée-Fauvet, M.; Tarnaud, E.; Anneheim-Herbelin, G.; Bône, N.; Gaudemer, A. *Tetrahedron* **1996**, *52*, 13589–13604.

(37) Koningstein, J. A.; Liu, Y. *J. Phys. Chem.* **1993**, *97*, 6155–6160.

(38) Uno, T.; Hamasaki, K.; Tanigawa, M.; Shimabayashi, S. *Inorg. Chem.* **1997**, *36*, 1676–1683.

(39) Yun, B. H.; Jeon, S. H.; Cho, T.-S.; Yi, S. Y.; Sehlstedt, U.; Kim. S. K. *Biophys. Chem.* **1998**, *70*, 1–10.

(40) Kuroda, R.; Tanaka, H. *J. Chem. Soc. Chem. Commun.* **1994**, 1575–1576.

(41) Sehlstedt, U.; Kim, S. K.; Carter, P.; Goodisman, J.; Vollano, J. F.; Nordén, B.; Dabrowiak, J. C. *Biochemistry* **1994**, *33*, 417–426.

(42) Geacintov, N. E.; Ibanez, V.; Rougee, M.; Bensasson, R. V. *Biochemistry* **1987**, *26*, 3087–3092.

(43) Marzilli, L. G.; Banville, D. L.; Zon, G.; Wilson, W. D. *J. Am. Chem. Soc.* **1986**, *108*, 4188–4192.

(44) Carvlin, M. J.; Fiel, R. J. *Nucleic Acids Res.* **1983**, *11*, 6121–6139.

(45) Marzilli, L. G.; Petho, G.; Lin, M.; Kim, M. S.; Dixon, D. W. *J. Am. Chem. Soc.* **1992**, *114*, 7575–7577.

(46) Sari, M. A.; Battioni, J. P.; Mansuy, D.; Le Pecq, J. B. *Biochem. Biophys. Res. Commun.* **1986**, *141*, 643–649.

(47) Sari, M. A.; Battioni, J. P.; Dupre, D.; Mansuy, D.; Le Pecq, J. B. *Biochem. Pharmacol.* **1988**, *37*, 1861–1862.

(48) Lipscomb, L. A.; Zhou, F. X.; Presnell, S. R.; Woo, R. J.; Peek, M. E.; Plaskon, R. R.; Williams, L. D. *Biochemistry* **1996**, *35*, 2818–2823.

(49) Gibbs, E. J.; Tinoco I. Jr.; Maestre, M. F.; Ellinas, P. A.; Pasternack, R. F. *Biochem. Biophys. Res. Commun.* **1988**, *157*, 350–358.

(50) Pasternack, R. F.; Giannetto, A. *J. Am. Chem. Soc.* **1991**, *113*, 7799–7800.

(51) Mukundan, N. E.; Pethö, G.; Dixon, D. W.; Marzilli, L. G. *Inorg. Chem.* **1995**, *34*, 3677–3687.

(52) Mukundan, N. E.; Pethö, G.; Dixon, D. W.; Kim, M. S.; Marzilli, L. G. *Inorg. Chem.* **1994**, *33*, 4676–4687.

(53) McClure, J. E.; Baudouin, L.; Mansuy, D.; Marzilli, L. G. *Biopolymers* **1997**, *42*,

203–217.

(54) Pasternack. R. F.; Gibbs, E. J.; Collings, P. J.; dePaula, J. C.; Turzo, L. C.; Terracina, A. *J. Am. Chem. Soc.* **1998**, *120*, 5873–5878.

(55) Pasternack, R. F.; Goldsmith, J. I.; Szép, S.; Gibbs, E. J. *Bioplys. J.* **1998**, *75*, 1024–1031.

(56) Depaula, J. C.; Robblee, J. H.; Pasternack, R. F. *Bioplys. J.* **1995**, *68*, 335–341.

(57) Casomento, M.; Arena, G. E.; LoPasso, C.; Pernice, I.; Romeo, A.; Scolaro, L. M. *Inorg. Chim. Acta* **1998**, *276*, 242–249.

(58) Arena, G.; Scolaro, L. M.; Pasternack, R. F.; Romeo, R. *Inorg. Chem.* **1995**, *34*, 2994–3002.

(59) Nordén, B.; Davidsson, Å. *Chem. Plys. Lett.* **1976**, *37*, 433–437.

(60) Gale, R.; Peacock, R. D.; Samori, B. *Chem. Plys. Lett.* **1976**, *37*, 430–432.

(61) Gryczynski, Z.; Paolesse, R.; Smith, K. M.; Bucci, E. *J. Plys. Chem.* **1994**, *98*, 8813–8816.

(62) Ford, K. G.; Neidle, S. *Bioorg. Med. Chem.* **1995**, *3*, 671–677.

(63) Colowick, S. P.; Kaplan, N. O. *Methods in Enzymology*; Academic Press: New York, 1955; pp 138–146.

(64) Brooks, B. R.; Bruccoleri, R. E.; Olafson, B. D.; States, D. J.; Swaminathan, S.; Karplus, M. *J. Comp. Chem.* **1983**, *4*, 187–217.

(65) Stewart, J. J. P. *J. Comput.-Aided Mol. Design* **1990**, 4, 1–45.

(66) Hunter, C. A.; Sanders, J. K. M. *J. Am. Chem. Soc.* **1990**, *112*, 5525–5534.

(67) Hunter, C. A.; Meah, M. N.; Sanders, J. K. M. *J. Am. Chem. Soc.* **1990**, *112*, 5773–5780.

(68) Dervan, P. B. *Science* **1986**, *232*, 464–471.

(69) Müller, W.; Gautier, F.; *Eur. J. Biochem.* **1975**, *54*, 385–394.

(70) Lown, J. W. *Anti-Cancer Drug Design* **1988**, *3*, 25–40.

(71) Pjura, P. E.; Grzeskowiak, K.; Dickerson, R. E. *J. Mol. Biol.* **1987**, *197*, 257–271.

(72) Teng, M.-K.; Usman, N.; Frederick, C. A.; Wang, A. H.-J. *Nucleic Acids Res.* **1988**, *16*, 2671–2690.

(73) Quintana, J. R.; Lipanov, A. A.; Dickerson, R. E. *Biochemistry* **1991**, *30*, 10294–10306.

(74) Vega, M. C.; García-Sáez, I.; Aymamí, J.; Eritja, T.; van der Marcel, G. A.; van Boom, J. H.; Rich, A.; Coll, M. *Eur. J. Biochem.* **1994**, *222*, 721–726.

(75) Searle, M. S.; Embrey, K. J. *Nucleic Acids Res.* **1990**, *18*, 3753–3762.

(76) Parkinson, J. A.; Barber, J.; Douglas, K. T.; Rosamond, J.; Sharples, D. *Biochemistry* **1990**, *29*, 10181-10190.

(77) Fede, A.; Labhardt, A.; Bannwarth, W.; Leupin, W. *Biochemistry* **1991**, *30*, 11377-11388.

(78) Embrey, K. J.; Searle, M. S.; Craik, D. J. *Eur. J. Biochem.* **1993**, *211*, 437–447.

(79) Embrey, K. J.; Craik, D. J. *J. Phys. Chem.* **1995**, *99*, 4831–4836.

(80) Vega, M. C.; Coll, M.; Alemán, C. *Eur. J. Biochem.* **1996**, *239*, 376–383.

(81) Robles, J.; Rajur, S. B.; McLaughlin, L. W. *J. Am. Chem. Soc.* **1996**, *118*, 5820–5821.

(82) Guan, L. L.; Zhao, R.; Lown, J. W.; *Biochem. Biophys. Res. Commun.* **1997**, *231*, 94–98.

(83) Wiederholt, K.; Rajur, S. B.; Giuliano, J. Jr.; O'Donnell, M. J.; McLaughlin, L. W. *J. Am. Chem. Soc.* **1996**, *118*, 7055–7062.

(84) Parkinson, J. A.; Ebrahimi, S. E.; McKie, J. H.; Douglas, K. T. *Biochemistry* **1994**, *33*, 8442–8452.

(85) Clark, G. R.; Squire, C. J.; Gray, E. J.; Leupin, W.; Neidle, S. *Nucleic Acids Res.* **1996**, *24*, 4882–4889.

(86) Parkinson, J.; Sadat-Ebrahimi, S.; Wilton, A.; McKie, J. H.; Andrews, J; Douglas, K. T. *Biochemistry* **1995**, *34*, 16240–16244.

(87) Kumar, S.; Joseph, T.; Singh, M. P.; Bathini, Y.; Lown, J. W. *J. Biomol. Struct.*

Dyn. **1992**, *9*, 853–880.

(88) Kumar, S.; Bathini, Y.; Zimmermann, J.; Pon, R. T.; Lown, J. W. *J. Biomol. Struct. Dyn.* **1990**, *98*, 331–357.

(89) Kopka, M. L.; Yoon, C.; Goodsell, D.; Pjura, P.; Dickerson, R. E. *Proc. Natl. Acad. Sci. USA* **1985**, *82*, 1376–1380.

(90) Kopka, M. L.; Yoon, C.; Goodsell, D.; Pjura, P.; Dickerson, R. E. *J. Mol. Biol.* **1985**, *183*, 553–563.

(91) Lown J. W.; Krowicki, K.; Balzarini, J.; de Clercq, E. *J. Med. Chem.* **1986**, *29*, 1210–1214.

(92) Bailly, C.; Colson, P.; Hénichart, J.-P.; Houssier, C. *Nucleic Acids Res.* **1993**, *21*, 3705–3709.

(93) Loontiens, F. G.; Refenfuss, P.; Zechel, A.; Dumortier, L.; Clegg, R. M. *Biochemistry* **1990**, *29*, 9029–9039.

(94) Loontiens, F. G.; McLaughlin, L. W.; Diekmann, S.; Clegg, R. M. *Biochemistry* **1991**, *30*, 182–189.

(95) Jorgenson, K. F.; Varshney, U.; van de Sande, J. H. *J. Biomol. Struct. Dyn.* **1988**, *5*, 1005–1023.

(96) Bailly, C.; Colson, P.; Houssier, C.; Wang, H. Y.; Bathini, Y.; Lown, J. W. *J. Biomol. Struct. Dyn.* **1994**, *12*, 173–181.

(97) Colson, P; Houssier, C.; Bailly, C. *J. Biomol. Struct. Dyn.* **1995**, *13*, 351–366.

(98) Colson, P; Houssier, C.; Bailly, C. *Biophys. Chem.* **1996**, *58*, 125–140.

(99) Moon, J. H.; Kim, S. K.; Sehlstedt, U.; Rodger, A; Nordén, B. *Biopolymers* **1996**, *38*, 593–606.

(100) Rodger, A.; Blagbrough, I. S.; Adlam, G.; Carpenter, M. L. *Biopolymers* **1994**, *12*, 1583–1593.

(101) Rodger, A.; Taylor, S.; Adlam, G.; Blagbourgh, I. S.; Haworth, I. S. *Bioorg. Med. Chem.* **1995**, *3*, 861–872.

(102) Ismail, M. A.; Sanders, K. J.; Fennell, G. C.; Latham, H. C.; Wormell, P. Rodger, A. *Biopolymers* **1998**, *46*, 127–143.

(103) Kohn, K. W.; Waring, M. J.; Glaubiger, D.; Friedman, C. A. *Cancer Res.* **1975**, *35*, 71–76.

(104) Patel, N.; Bergman, J.; Gräslund, A. *Eur. J. Biochem.* **1991**, *197*, 507–604.

(105) Ferguon, L. R.; Baguley, B. C. *Environmental and Molecular Mutagenesis* **1994**, *24*, 245–261.

(106) Froelichammon, S. J.; Patchan, M. W.; Osheroff, N.; Thompson, R. B. *J. Biol. Chem.* **1995**, *270*, 14998–15004.

(107) Jones, R. A.; Pastor, J.; Siro, J.; Voro, T.N. *Tetrahedron* **1997**, *53*, 479–486.

(108) Kennedy, G. D.; Krishnan, G.; Karim, M.; Harden, D. *Heterocycl. Commun.* **1996**, *2*, 125–128.

(109) Devraj, R.; Cushman, M. *Bioorg. Med. Chem. Lett.* **1997**, *7*, 369-372.

(110) Moinet-Hedin, V.; Tabka, T.; Sichel, F.; Gauduchon, P.; Le Talaer, J. Y.; Saturnino, C.; Letois, B.; Lancelot, J. C.; Robba, M. *Eur. J. Med. Chem.* **1997**, *32*, 113–122.

(111) Jain, S. C.; Bhandary, K. K.; Sobell, H. M. *J. Mol. Biol.* **1979**, *135*, 813–840.

(112) Le Pecq, J.-B.; Xuong, N.-D.; Gosse, C.; Paoletti, C. *Proc. Natl. Acad. Sci. USA* **1974**, *71*, 5078–5082.

(113) Fosse, P.; Charra, M.; Paoletti, C.; Saucier, J. M.; Rene, B. *Bulletin du Cancer* **1994**, *81*, 194–202.

(114) Monnot, M.; Mauffret, O.; Simon, V.; Lescot, E.; Psaume, B.; Saucier, J.-M.; Charra, M.; Belehradek, J. Jr.; Fermandjian, S. *J. Biol. Chem.* **1991**, *266*, 1820–1829.

(115) Monnot, M.; Mauffret, O.; Simon, V.; Lescot, E.; Psaume, B.; Saucier, J-M.; Belehradek, J. Jr.; Fermandjian, S. *FEBS Lett.* **1990**, *273*, 71–74.

(116) Lyng, R.; Härd, T.; Nordén, B. *Biopolymers* **1987**, *26*, 1327–1345.

(117) Martindale, Rouesse, J.; Spielmann, M.; Turpin, F.; Lechevalier, T.; Azab, M.; Mondesir, J. M. *Eur. J. Canc.* **1993**, *29A*, 856–859.

(118) Osashi, M.; Oki, T. *Expert Opin. Therp. Patents* **1996**, *6*, 1285–1294.

(119) Devraj, R.; Cushman, M. *Bioorg. Med. Chem. Lett.* **1997**, *7*, 369–372.

(120) Acton, E. M.; Narayanan, V. L.; Risbood, P. A.; Shoemaker, R. H.; Vitica, D. T.; Boyd, M. R. *J. Med. Chem.* **1994**, *37*, 2185–2189.

(121) Behravan, G.; Leijon, M.; Sehlstedt, U.; Nordén, B.; Vallberg, H.; Bergman, J.; Graslund, A. *Biopolymers* **1994**, *34*, 599–609.

(122) Elcock, A. H.; Rodger, A.; Richards, W. G. *Biopolymers* **1996**, *39*, 309–326.

(123) Shimamoto, T.; Imajo, S.; Honda. T.; Satomichi, Y.; Ishiguro, M. *Bioorg. Med. Chem. Lett.* **1996**, *6*, 1331–1334.

(124) Burrell, A. K.; Officer, D. L.; Reid, D. C. W.; Wild, K. Y. *Angew. Chem., Int. Ed. Engl.* **1998**, *37*, 114–117.

(125) Mattes, W. B.; Hartley, J. A.; Kohn, K. W.; Matheson, D. W. *Carcinogenesis* **1988**, *9*, 2065–2072.

A1 Porphyrin Molecular Modelling

Input data for MOPAC calculation on *t*-H_2P

```
MNDO 1SCF T=24.0H DUMP=60.0M NOXYZ NOINTER GRAPH GEO-OK CHARGE=2 SINGLET
MOPAC Calculation from Cerius2
```

N	0.0000000	0	0.0000000	0	0.0000000	0	0	0	0
C	1.3436475	1	0.0000000	0	0.0000000	0	1	0	0
C	1.3915972	1	122.7217391	1	0.0000000	0	2	1	0
C	1.3802509	1	119.5601031	1	0.0176577	1	3	2	1
C	1.4921523	1	120.9755271	1	-179.9153028	1	4	3	2
C	1.4326771	1	120.5521222	1	88.8075825	1	5	4	3
N	1.3594964	1	128.2567105	1	-179.9177533	1	6	5	4
C	1.3600246	1	105.9149607	1	-179.9679775	1	7	6	5
C	1.4323055	1	128.4750622	1	-179.9760159	1	8	7	6
C	1.4341996	1	118.4779348	1	0.0079109	1	9	8	7
N	1.3647750	1	128.9641808	1	-0.0079017	1	10	9	8
C	1.3639620	1	105.6081039	1	179.9845678	1	11	10	9
C	1.4344682	1	128.6949656	1	179.9582995	1	12	11	10
C	1.4326365	1	118.6515845	1	-0.0308473	1	13	12	11
N	1.3594465	1	128.2586257	1	0.0049342	1	14	13	12
C	1.3600086	1	105.9102948	1	-179.9846624	1	15	14	13
C	1.4322596	1	128.4715666	1	-179.9630577	1	16	15	14
C	1.4341994	1	118.4797909	1	0.0188578	1	17	16	15
N	1.3647875	1	128.9619986	1	-0.0282224	1	18	17	16
C	1.3639810	1	105.6087558	1	179.9505257	1	19	18	17
C	1.4172231	1	111.3404206	1	-179.9919210	1	20	19	5
C	1.4155499	1	111.3983649	1	-179.9517458	1	18	19	17
H	1.0806497	1	128.8820697	1	179.9808839	1	22	18	21
H	1.0794841	1	129.7472846	1	-179.9740013	1	21	20	22
C	1.4947966	1	120.6330912	1	-179.9760545	1	17	16	18
C	1.3836210	1	120.6832992	1	-90.0223889	1	25	17	16
C	1.3941635	1	120.9987114	1	179.9714603	1	26	25	17
C	1.3898161	1	120.1309958	1	0.0011485	1	27	26	25
C	1.3898011	1	119.0863105	1	-0.0125938	1	28	27	26
C	1.3836291	1	120.6629382	1	179.9603963	1	25	17	26
H	1.0826609	1	119.4970107	1	179.9673664	1	30	25	29
H	1.0837249	1	119.2826632	1	-179.9781497	1	29	28	30
H	1.0839860	1	120.4621384	1	-179.9882108	1	28	27	29
H	1.0836997	1	120.5872632	1	-179.9787113	1	27	26	28
H	1.0826435	1	119.4981821	1	-179.9672951	1	26	25	27
C	1.4156861	1	111.3517202	1	179.9633637	1	16	15	17
C	1.4175251	1	111.2723276	1	179.9883609	1	14	15	13
H	1.0797011	1	129.7519596	1	179.9869240	1	37	14	36
H	1.0808039	1	128.8595620	1	-179.9909327	1	36	16	37
H	0.9871287	1	127.2212443	1	-179.9885622	1	15	14	16
C	1.4920823	1	120.8114810	1	179.9709690	1	13	12	14
C	1.3802327	1	120.9755761	1	-89.2894414	1	41	13	12
C	1.3915510	1	119.5564791	1	-179.9550822	1	42	41	13
N	1.3436235	1	122.7237177	1	-0.0200015	1	43	42	41
C	1.3436723	1	117.4280557	1	0.0839484	1	44	43	42
C	1.3802380	1	121.0092547	1	-179.9093597	1	41	13	42
H	1.0833427	1	120.2931313	1	-179.9584949	1	46	41	45
H	1.0847988	1	119.5315213	1	179.9086875	1	45	44	46
C	1.4828174	1	121.2781439	1	179.7708790	1	44	43	45
H	1.0917661	1	111.2550705	1	150.0688109	1	49	44	43
H	1.0917769	1	111.2499123	1	-119.7843687	1	49	44	50
H	1.0914226	1	110.4857809	1	120.1136447	1	49	44	50
H	1.0848128	1	119.5355186	1	-179.9099336	1	43	44	42
H	1.0833439	1	120.2892932	1	179.9486605	1	42	41	43
C	1.4172220	1	111.3418474	1	-179.9566981	1	12	11	13
C	1.4155085	1	111.3989435	1	-179.9863983	1	10	11	9

H	1.0806402	1	128.8762128	1	-179.9974362	1	56	10	55
H	1.0794817	1	129.7545880	1	179.9683276	1	55	12	56
C	1.4948269	1	120.6341011	1	-179.9868595	1	9	8	10
C	1.3836140	1	120.6643301	1	89.9130738	1	59	9	8
C	1.3941269	1	121.0040596	1	-179.9609762	1	60	59	9
C	1.3897828	1	120.1286173	1	-0.0022650	1	61	60	59
C	1.3897895	1	119.0876224	1	0.0079775	1	62	61	60
C	1.3836570	1	120.6849903	1	-179.9549102	1	59	9	60
H	1.0826242	1	119.4936749	1	-179.9671190	1	64	59	63
H	1.0837134	1	119.2758848	1	179.9795964	1	63	62	64
H	1.0839625	1	120.4559892	1	179.9846384	1	62	61	63
H	1.0837047	1	120.5844716	1	179.9788236	1	61	60	62
H	1.0826469	1	119.4906418	1	179.9709533	1	60	59	61
C	1.4156939	1	111.3479243	1	179.9823801	1	8	7	9
C	1.4175386	1	111.2682613	1	179.9614920	1	6	7	5
H	1.0797119	1	129.7578809	1	-179.9600938	1	71	6	70
H	1.0808103	1	128.8590170	1	-179.9992621	1	70	8	71
H	0.9871259	1	127.2133620	1	179.9840917	1	7	6	8
C	1.3802470	1	118.0104037	1	179.9652724	1	4	3	5
C	1.3436469	1	117.4263581	1	-0.0860088	1	1	2	3
H	1.0847924	1	119.5250955	1	-179.9309959	1	76	1	75
H	1.0833101	1	120.2977801	1	-179.9649594	1	75	4	76
H	1.0833433	1	120.1453147	1	-179.9822211	1	3	2	4
H	1.0848222	1	119.5312667	1	179.9387680	1	2	1	3
C	1.4828504	1	121.2858177	1	-179.8118791	1	1	2	76
H	1.0917786	1	111.2420500	1	-150.0318346	1	81	1	2
H	1.0914381	1	110.5076511	1	-120.1178031	1	81	1	82
H	1.0917768	1	111.2445060	1	119.7666241	1	81	1	82

Results from MOPAC calculation on *t*-H_2P

SUMMARY OF MNDO CALCULATION

VERSION 6.00

C44 H34 N6

16-Feb-96

MNDO 1SCF T=24.0H DUMP=60.0M NOXYZ NOINTER GRAPH GEO-OK CHARGE=2 SINGLET
MOPAC Calculation from Cerius2

1SCF WAS SPECIFIED, SO BFGS WAS NOT USED
SCF FIELD WAS ACHIEVED

HEAT OF FORMATION	=	746.660055 KCAL
ELECTRONIC ENERGY	=	-80245.465028 EV
CORE-CORE REPULSION	=	72923.333236 EV
DIPOLE	=	0.00000 DEBYE
NO. OF FILLED LEVELS	=	119
CHARGE ON SYSTEM	=	2
IONIZATION POTENTIAL	=	11.286388 EV
MOLECULAR WEIGHT	=	646.793
SCF CALCULATIONS	=	1
COMPUTATION TIME =	1 MINUTES AND	3.224 SECONDS

FINAL GEOMETRY OBTAINED CHARGE
MNDO 1SCF T=24.0H DUMP=60.0M NOXYZ NOINTER GRAPH GEO-OK CHARGE=2 SINGLET
MOPAC Calculation from Cerius2

N	0.0000000	0	0.000000	0	0.000000	0	0	0	0	-0.1136

C	1.3436475	1	0.000000	0	0.000000	0	1	0	0	0.1033
C	1.3915972	1	122.721739	1	0.000000	0	2	1	0	-0.0631
C	1.3802509	1	119.560103	1	0.017658	1	3	2	1	0.1353
C	1.4921523	1	120.975527	1	-179.915303	1	4	3	2	-0.0989
C	1.4326771	1	120.552122	1	88.807582	1	5	4	3	0.0833
N	1.3594964	1	128.256710	1	-179.917753	1	6	5	4	-0.1219
C	1.3600246	1	105.914961	1	-179.967977	1	7	6	5	0.0273
C	1.4323055	1	128.475062	1	-179.976016	1	8	7	6	0.0929
C	1.4341996	1	118.477935	1	0.007911	1	9	8	7	0.0102
N	1.3647750	1	128.964181	1	-0.007902	1	10	9	8	-0.2989
C	1.3639620	1	105.608104	1	179.984568	1	11	10	9	0.0572
C	1.4344682	1	128.694966	1	179.958299	1	12	11	10	-0.0989
C	1.4326365	1	118.651584	1	-0.030847	1	13	12	11	0.0833
N	1.3594465	1	128.258626	1	0.004934	1	14	13	12	-0.1218
C	1.3600086	1	105.910295	1	-179.984662	1	15	14	13	0.0273
C	1.4322596	1	128.471567	1	-179.963058	1	16	15	14	0.0928
C	1.4341994	1	118.479791	1	0.018858	1	17	16	15	0.0102
N	1.3647875	1	128.961999	1	-0.028222	1	18	17	16	-0.2990
C	1.3639810	1	105.608756	1	179.950526	1	19	18	17	0.0572
C	1.4172231	1	111.340421	1	-179.991921	1	20	19	5	-0.1566
C	1.4155499	1	111.398365	1	-179.951746	1	18	19	17	-0.0516
H	1.0806497	1	128.882070	1	179.980884	1	22	18	21	0.0978
H	1.0794841	1	129.747285	1	-179.974001	1	21	20	22	0.0706
C	1.4947966	1	120.633091	1	-179.976054	1	17	16	18	-0.0935
C	1.3836210	1	120.683299	1	-90.022389	1	25	17	16	-0.0327
C	1.3941635	1	120.998711	1	179.971460	1	26	25	17	-0.0556
C	1.3898161	1	120.130996	1	0.001148	1	27	26	25	-0.0289
C	1.3898011	1	119.086310	1	-0.012594	1	28	27	26	-0.0556
C	1.3836291	1	120.662938	1	179.960396	1	25	17	26	-0.0328
H	1.0826609	1	119.497011	1	179.967366	1	30	25	29	0.0614
H	1.0837249	1	119.282663	1	-179.978150	1	29	28	30	0.0749
H	1.0839860	1	120.462138	1	-179.988211	1	28	27	29	0.0783
H	1.0836997	1	120.587263	1	-179.978711	1	27	26	28	0.0749
H	1.0826435	1	119.498182	1	-179.967295	1	26	25	27	0.0615
C	1.4156861	1	111.351720	1	179.963364	1	16	15	17	-0.0332
C	1.4175251	1	111.272328	1	179.988361	1	14	15	13	-0.1388
H	1.0797011	1	129.751960	1	179.986924	1	37	14	36	0.0842
H	1.0808039	1	128.859562	1	-179.990933	1	36	16	37	0.1106
H	0.9871287	1	127.221244	1	-179.988562	1	15	14	16	0.2731
C	1.4920823	1	120.811481	1	179.970969	1	13	12	14	0.1352
C	1.3802327	1	120.975576	1	-89.289441	1	41	13	12	-0.0629
C	1.3915510	1	119.556479	1	-179.955082	1	42	41	13	0.1033
N	1.3436235	1	122.723718	1	-0.020001	1	43	42	41	-0.1135
C	1.3436723	1	117.428056	1	0.083948	1	44	43	42	0.1033
C	1.3802380	1	121.009255	1	-179.909360	1	41	13	42	-0.0629
H	1.0833427	1	120.293131	1	-179.958495	1	46	41	45	0.1266
H	1.0847988	1	119.531521	1	179.908687	1	45	44	46	0.1295
C	1.4828174	1	121.278144	1	179.770879	1	44	43	45	0.1641
H	1.0917661	1	111.255070	1	150.068811	1	49	44	43	0.0541
H	1.0917769	1	111.249912	1	-119.784369	1	49	44	50	0.0541
H	1.0914226	1	110.485781	1	120.113645	1	49	44	50	0.0536
H	1.0848128	1	119.535519	1	-179.909934	1	43	44	42	0.1295
H	1.0833439	1	120.289293	1	179.948660	1	42	41	43	0.1267
C	1.4172220	1	111.341847	1	-179.956698	1	12	11	13	-0.1565
C	1.4155085	1	111.398943	1	-179.986398	1	10	11	9	-0.0517
H	1.0806402	1	128.876213	1	-179.997436	1	56	10	55	0.0978
H	1.0794817	1	129.754588	1	179.968328	1	55	12	56	0.0706
C	1.4948269	1	120.634101	1	-179.986859	1	9	8	10	-0.0935
C	1.3836140	1	120.664330	1	89.913074	1	59	9	8	-0.0327
C	1.3941269	1	121.004060	1	-179.960976	1	60	59	9	-0.0556
C	1.3897828	1	120.128617	1	-0.002265	1	61	60	59	-0.0288
C	1.3897895	1	119.087622	1	0.007977	1	62	61	60	-0.0556
C	1.3836570	1	120.684990	1	-179.954910	1	59	9	60	-0.0327
H	1.0826242	1	119.493675	1	-179.967119	1	64	59	63	0.0614
H	1.0837134	1	119.275885	1	179.979596	1	63	62	64	0.0749
H	1.0839625	1	120.455989	1	179.984638	1	62	61	63	0.0782
H	1.0837047	1	120.584472	1	179.978824	1	61	60	62	0.0749
H	1.0826469	1	119.490642	1	179.970953	1	60	59	61	0.0615
C	1.4156939	1	111.347924	1	179.982380	1	8	7	9	-0.0332
C	1.4175386	1	111.268261	1	179.961492	1	6	7	5	-0.1387
H	1.0797119	1	129.757881	1	-179.960094	1	71	6	70	0.0842
H	1.0808103	1	128.859017	1	-179.999262	1	70	8	71	0.1106
H	0.9871259	1	127.213362	1	179.984092	1	7	6	8	0.2731

C	1.3802470	1	118.010404	1	179.965272	1	4	3	5	-0.0628
C	1.3436469	1	117.426358	1	-0.086009	1	1	2	3	0.1033
H	1.0847924	1	119.525095	1	-179.930996	1	76	1	75	0.1295
H	1.0833101	1	120.297780	1	-179.964959	1	75	4	76	0.1267
H	1.0833433	1	120.145315	1	-179.982221	1	3	2	4	0.1266
H	1.0848222	1	119.531267	1	179.938768	1	2	1	3	0.1295
C	1.4828504	1	121.285818	1	-179.811879	1	1	2	76	0.1641
H	1.0917786	1	111.242050	1	-150.031835	1	81	1	2	0.0537
H	1.0914381	1	110.507651	1	-120.117803	1	81	1	82	0.0544
H	1.0917768	1	111.244506	1	119.766624	1	81	1	82	0.0537

A2 9-Hydroxyellipticine Film Linear Dichroism

Calculation of polarised absorbance spectra for 9-OHE

Deconvolution of the measured film normal absorption spectrum of 9-OHE into long (z) and short (y) axis component was required to extract the transition moment polarisations. Since no feature in the 9-OHE LD^r spectrum could be identified that belonged to a single isolated transition, direct calculation of S was not possible from the LD^r spectrum. The TEM method was therefore employed to determine polarised spectra.[7,11]

The LD^r maximum at 300 nm (Figure 6.3a) was initially assumed to belong to an isolated transition of pure polarisation and S_{zz} and S_{yy} determined from equations 3.6 and 3.8 respectively. The calculated values for S_{zz} and S_{yy} were then incrementally varied by 0.05 and −0.025 respectively. A total of 14 sets of polarised spectra were calculated from[7]

$$A_z(\lambda) = \frac{3S_{yy}A(\lambda) - LD(\lambda)}{S_{yy} - S_{zz}} \qquad \text{(A2.1)}$$

and

$$A_y(\lambda) = \frac{3S_{zz}A(\lambda) - LD(\lambda)}{S_{zz} - S_{yy}} \qquad \text{(A2.2)}$$

using each of the adjusted S values. The results of these calculations are shown in Figure

6.4. Polarised absorbance spectra with 'good shape' were determined by inspection to be near the $S_{zz} = 0.344$, $S_{yy} = -0.172$ set of spectra. The process of incremental variation was thus repeated using a further 14 steps of 0.005 and −0.0025 in S_{zz} and S_{yy} respectively to calculate the spectra shown in Figure A2.1. The $S_{zz} = 0.453$, $S_{yy} = -0.227$ set of polarised spectra were then used to calculate the transition moment polarisations from equation 3.9.

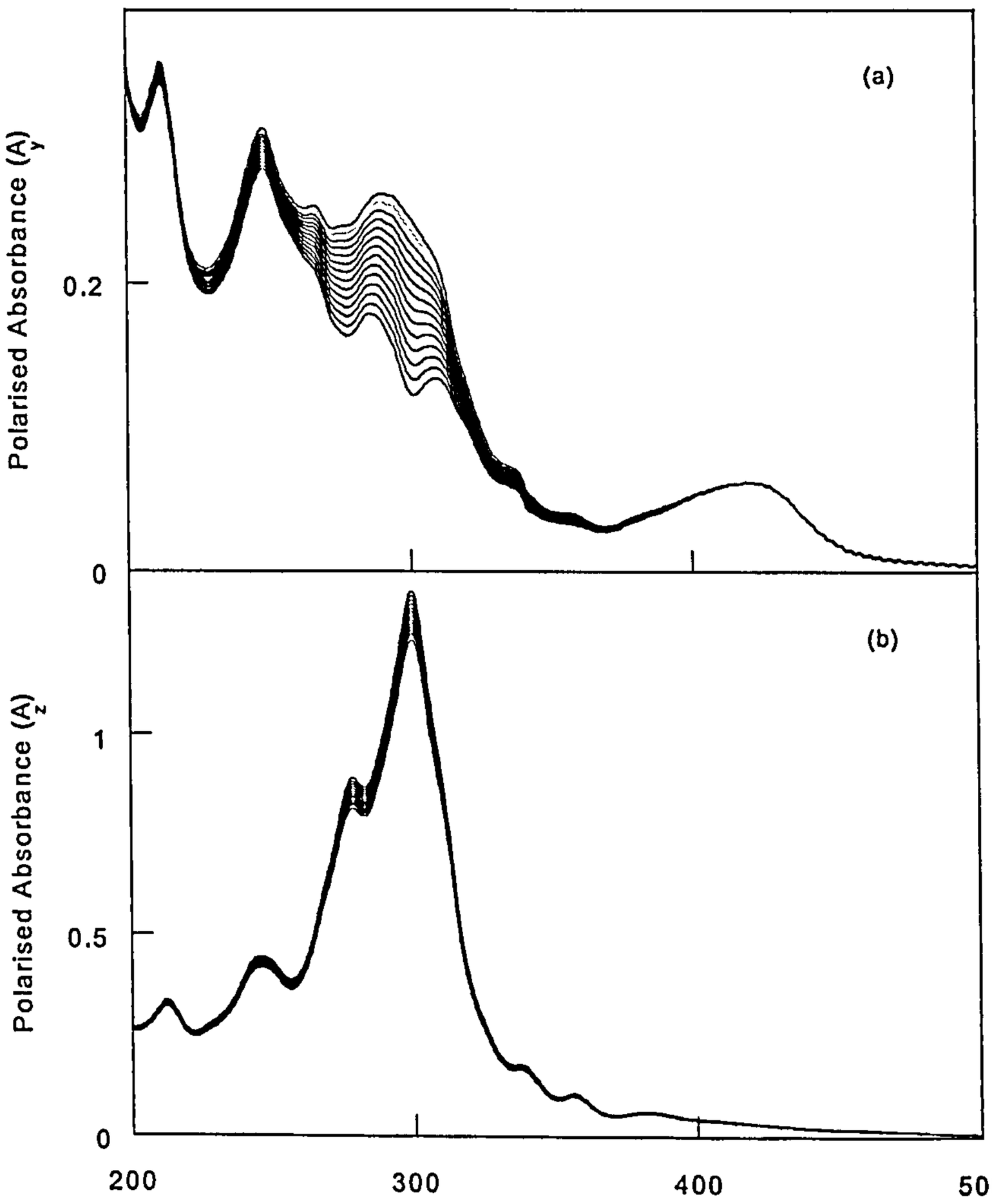

Figure A2.1 Polarised absorbance spectra resulting from TEM calculations on stretched film *LD* data for 9-OHE. Each spectrum corresponds to an adjustment of (a) −0.0025 in S_{yy} from an initial value of −0.197 and (b) 0.005 in S_{zz} from an initial value of 0.394. Grey lines indicate spectra used for calculation of α.